BNL 51801
UC-28
(Particle Accelerators and High Voltage Machines — TIC-4500)

BNL--51801

DE85 002610

RHIC AND QUARK MATTER

PROPOSAL
for a
RELATIVISTIC HEAVY ION COLLIDER
at
BROOKHAVEN NATIONAL LABORATORY

August 1984

BROOKHAVEN NATIONAL LABORATORY
ASSOCIATED UNIVERSITIES, INC.

UNDER CONTRACT NO. DE-AC02-76CH00016 WITH THE
UNITED STATES DEPARTMENT OF ENERGY

Preface

This document describes the Brookhaven National Laboratory Proposal for the construction of a Relativistic Heavy Ion Collider (RHIC). The construction of this facility represents the natural continuation of the laboratory's role as a center for nuclear and high-energy physics research and extends and uses the existing AGS, Tandem Van de Graaff and CBA facilities at BNL in a very cost effective manner. The Administration and Congress have approved a project which will provide a link between the Tandem Van de Graaff and the AGS. Completion of this project in 1986 will provide fixed target capabilities at the AGS for heavy ions of about 14 GeV/amu with masses up to ~30 (sulfur). The addition of an AGS booster would extend the mass range to the heaviest ions (A~200, e.g. gold); its construction could start in 1986 and be completed in three years. These two new AGS experimental facilities can be combined with the proposed Relativistic Heavy Ion Collider to extend the energy range to 100x100 GeV/amu for the heaviest ions. BNL proposes to start construction of RHIC in FY 86 with completion in FY 90 at a total cost of 134 M$.

A task force to prepare the RHIC proposal was established by Associate Director P. J. Reardon in November 1983 with M. Q. Barton as chairman and H. Hahn as technical coordinator. Senior members included A. Ruggiero (Fermilab), G. Young (Oak Ridge National Laboratory), D. Barton, Y. Y. Lee, T. Ludlam, R. Shutt, P. Thieberger and L. Turf. The essential specifications of the collider were established by a separate task force chaired by T. Ludlam and A. Schwarzschild which convened at Brookhaven in August 1983. The collider specifications were re-examined in December 1983 by an ad-hoc panel of physicists, most of whom had participated in the August study. The accelerator design aspects of the collider were reviewed in two subsequent meetings in April 1984 by the RHIC Technical Committee chaired by W. Willis. The desirability and suitability from the physics point of view was examined in May 1984 by the RHIC Review Board with D. Allan Bromley as chairman. Having obtained the endorsement from both committees, the RHIC Task Force now under the direction of R. R. Rau proceeded with the completion of the present proposal.

Brookhaven National Laboratory has distinct advantages and unique assets for constructing a Relativistic Heavy Ion Collider facility at a low cost not possible at any other site. The flexibility of fixed target operation as well as beam-beam collisions covering the entire energy range up to 100x100 GeV/amu and the full range of ion species from protons to gold would provide a unique, dedicated, world-class facility which meets the criteria for scientific excellence which the United States should support. Brookhaven National Laboratory, its scientific and technical staff, and its Director have complete confidence in the scientific merit of this machine and in their ability to build a superb facility for use by the nuclear as well as the high-energy physics community.

Nicholas P. Samios
Director
Brookhaven National Laboratory

TABLE OF CONTENTS

TABLE OF CONTENTS (Cont.)

TABLE OF CONTENTS (Cont.)

I. SUMMARY

I.1. Introduction

With the introduction of the quark model, speculation began on the possibility of creating a form of matter in which the recognizable components are not the familiar neutrons and protons, but are quarks. The development of Quantum Chromodynamics (QCD) as a fundamental theory of strong interactions provided confident predictions, rather than speculations. An international community has since developed among nuclear and particle physicists with a common interest in the possibility of creating this matter by colliding heavy nuclei at extremely high energies.

As interest has mounted in this new field of physics, conferences and workshops have been organized with increasing frequency, including a series of international meetings at Darmstadt (Oct. 1980), Bielefeld (May 1982), and Brookhaven (Sept. 1983). Until the Brookhaven meeting, discussions of experimental facilities centered mainly on ways to graft a limited heavy ion capability onto existing proton accelerators. Likely candidates were the ISR and SPS at CERN, and a series of workshops at Brookhaven resulted in a scenario for heavy ion beams in the proposed CBA. During the summer of 1983 the way became clear for realistic discussions of a dedicated machine optimized for the physics of nuclear beams.

In July 1983, the Nuclear Science Advisory Committee advised DOE "...that the United States should proceed with the planning for the construction of this relativistic heavy ion collider facility expeditiously, and we see it as the highest priority new scientific opportunity within the purview of our science." Shortly thereafter, on September 26-30, "Quark Matter '83, the Third International Conference on Ultra-Relativistic Nucleus-Nucleus Collisions, was

held at Brookhaven National Laboratory. This meeting may well be remembered as that moment when theory and experimental information reached a critical state, exciting nuclear and high energy physicists to push forward on a dedicated high energy relativistic heavy ion collider facility. The significant growth in physics understanding and in general interest between the Bielefeld meeting in 1982 and the Brookhaven meeting was impressive.

The physics questions to be addressed by high-energy heavy ion collisions range from the continuation of current studies of relativistic heavy ion reaction mechanisms and dynamics to the formation of fundamentally distinct forms of matter. Quantum Chromodynamics (QCD) appears to describe very well indeed the quark-gluon behaviour inside of hadrons which have volumes of about 1 fm^3. In effect, quarks and gluons are confined within hadron boundaries. This description and the predictions of QCD are well matched by experimental data from very high energy hadron collisions, neutrino interactions, and electron-positron collisions. In short, quarks and gluons always appear to be confined within hadrons. However there are theoretical and some experimental signs (from α-α collisions at the ISR and cosmic ray events) that with the collisions of heavy nuclei at energies in the 10 to 100 GeV/amu range a very much larger volume ($\sim$10's fm^3) would be heated to sufficient temperature ($\sim$200-300 MeV) and/or acquire sufficient quark density ($5/fm^3$ rather than $0.5/fm^3$ in cold hadrons) that the entire volume might temporarily be deconfined and quarks and gluons would exist as a plasma. Such conditions should have prevailed in the early universe, a few microseconds after the "Big Bang."

Such tempting speculation and the promise of an entirely new regime in experimental and theoretical physics are now attracting a growing number of nu-

clear and high-energy physicists to think about and plan for high-energy heavy ion physics experiments. There is also interest from astrophysicists as well.

Brookhaven National Laboratory has distinct advantages and attractive assets for developing a dedicated heavy ion collider facility in the range up to 100 GeV/amu energy per beam. Briefly these are: a complete injection system will exist independently of the collider; the injection tunnels from the AGS, the main tunnel, support buildings, three completed experimental areas (three additional undeveloped experimental areas also exist), and a central control building, are available from the CBA project; a cryogenic refrigerator system is complete and will soon undergo acceptance tests. Brookhaven has an experienced superconducting magnet group and very large facilities exist for constructing, assembling, and testing superconducting magnets.

The top beam energy ($\sim$100 GeV/amu for beams of gold ions) arises naturally and simply from the circumference of the existing tunnel ($\sim$4 km), the availability of a very large cryogenic refrigerator facility, and by selecting a very modest, conservative, magnetic bending field of $\sim$3.5 T. This relatively low field allows a much simpler magnet design than those used in the FNAL Doubler, or those designed for CBA or the electron-proton collider, HERA. With this Collider facility, a wide and continuous range of equivalent beam energies, in the center of mass frame, is available: from $\sim$1.5 GeV/amu to 100 GeV/amu. This range would be attained by using the AGS for fixed target experiments (1.5 GeV/amu to 2.5 GeV/amu); one Collider beam striking a gas jet or wire target (2.5 GeV/amu to 7 GeV/amu); and the colliding beams of the Collider itself (7 GeV/amu to 100 GeV/amu). This range of energies, the flexibility of having fixed target operation as well as beam-beam collisions, and the full range of ion species from protons to gold, would provide a unique dedicated, world class

facility, which meets the criteria for scientific excellence which the United States should support.

I.2. Description of the Facility and Performance

The complete Relativistic Heavy Ion Collider (RHIC) facility is a complex set of accelerators and beam transfer equipment connecting them. A very significant portion of the total facility either exists, is under construction, or funds have been requested for them. Only the high-energy collider itself will be requested through this proposal.

Fig. I.1 is a site plan showing all of the major components. The two existing, very efficient Tandem Van de Graaff accelerators will serve for the initial ion acceleration. It is proposed that two-stage operation be employed with the negative ion source at ground potential. Both Tandems will be available in parallel, so that a spare source of particles will exist. The negative ions, with charge -1, are accelerated from ground to +15 MV potential. They pass through a stripping foil in the high voltage terminal, leaving with a most probable charge, $+Q_T$, which is a function of the element being accelerated. (Ions considered specifically for this proposal are deuterium, carbon, sulfur, copper, iodine and gold. Other species are not ruled out.) The partially stripped ions are accelerated back to ground potential, increasing their energy by 15 Q_T MeV. Exiting from the Van de Graaff, they pass through a second stripping foil; for example carbon, 20 $\mu g/cm^2$ thick, for gold ions.

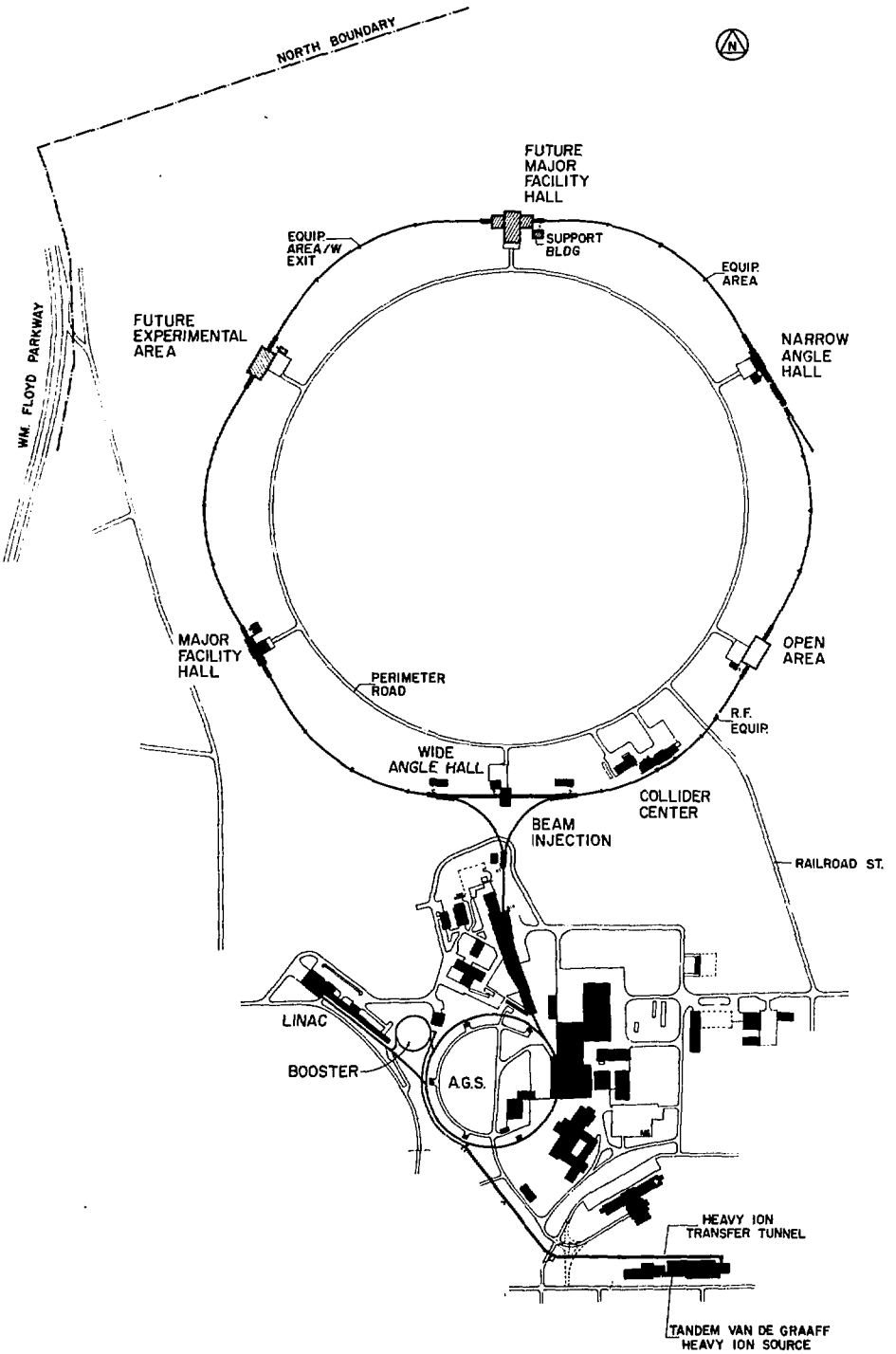

Figure I.1. Layout of RHIC Project - Collider & Source

From this point, the ions will traverse a long (~2,000 ft.) transfer line* to the AGS tunnel, where the transfer line will enter the tunnel for about 120°, then exit and proceed to be injected into the Booster accelerator.

The Booster† will be located between the existing 200 MeV proton linac and the northwest quadrant of the AGS (see Fig. I.1). Its circumference will be one quarter of that of the AGS.

Beam from the Tandem is injected into the Booster and stacked in betatron phase space by filling the machine with some number, ($n \gtrsim 8$), of consecutive turns corresponding to a total number of particles N_B. The beam intensity will be limited by the available Tandem ion currents for ions up to copper. For iodine and gold the beam will be space charged limited. For gold we take N_B to be ~2 x 10^9 ions, while for deuterium $N_B = 10^{11}$.

The beam is captured in the Booster using an rf system with harmonic number = 1, i.e., only one bunch is used and all particles (N_B) are in that bunch. For gold the acceleration period is 0.6 sec and the overall cycle period of the Booster is 1.2 sec.

At the end of the acceleration cycle, the particle bunch length has contracted so that it will match the length of the rf buckets in the AGS. At a field of 1.2 T, gold ions will have a kinetic energy of 320 MeV/amu; $\beta\gamma = 0.893$.

After extraction from the Booster, the ions pass through one more stripping target (about 70 mg/cm^2 for gold ions), become completely stripped and

*This transfer line, which is to start construction in FY 1984, will be completed in 1986 and will be used to inject heavy ions (up to sulfur) into the AGS for experimentation at energies up to ~13 GeV/amu.

†Brookhaven has requested funds for the Booster and expects to begin construction in FY 86. It would initially be used for improving the AGS experimental program. If funded it will be operational in 1988.

are then injected into the AGS. Since the ions are completely stripped upon entering the AGS, no improvements in the AGS vacuum or its rf system are needed.

Each particle bunch transferred from the Booster to the AGS is accelerated to the top AGS energy (28 GeV for protons; 11 GeV/amu for gold) and then transferred to the Collider by a magnet system installed in the existing transfer line tunnels. Bunch injection is repeated 57 times for each ring (box car beam stacking). Filling time per ring will be about 1 minute. The circumference of the Collider, 3833.8 m, is determined by the existing tunnel. For gold, as an example, there will be $\sim 1.1 \times 10^9$ ions/bunch or $\sim 6 \times 10^{10}$ ions in 57 bunches in each ring. For light ions approximately 10^{11} protons/bunch can be stored in the machine as presently designed. Acceleration will take approximately 60 seconds. Bending and focusing of the ion beams is achieved with superconducting magnets. Given the existing tunnel, cost optimization indicates that filling the circumference with lower field magnets is most economical. At a magnetic field of about 3.5T, the maxiumum energy is $\sim$100 GeV/amu for gold and 250 GeV for protons. The cost estimate is based upon single layer $\cos\theta$ magnets, in a dual configuration, i.e., magnetically separate magnets in a common vacuum vessel. The beams will be 30 cm apart. The cold bore beam tube aperture was chosen to be 65.8 mm diameter, by considering the requirements due to intrabeam scattering.

We have considered two crossing angles (α) at which the beams collide. It will be possible to produce head on collisions ($\alpha = 0$) and crossing at $\alpha = 2$ mrad. Other crossing angles can be accommodated. The free space around the intersecting point is ± 10 m. Peak luminosity naturally depends on the ion species and the angle at which the beams collide. For example, for head-on collisions with gold ion beams, we expect a maximum luminosity of $\sim 1.2 \times 10^{27} \text{cm}^{-2}$

sec^{-1}. For protons the expected value should be $\sim 1.2 \times 10^{31} cm^{-2} sec^{-1}$. These maximum values will be decreased a factor of ~ 4 using the beam crossing angle of 2 mrad. Good luminosity should be possible for at least 10 hours for ion energies from $\gamma = 12$ to 100. For head-on collisions the interaction region length will vary from ±35 cm to ±106 cm rms over 10 hours at 100 GeV/amu. For a crossing angle of 2 mrad this interaction length is ±14 cm rms.

It must be recalled that the CBA construction provided 6 beam interaction points. Three completed experimental halls located around the tunnel at clock positions 2, 6, and 8 o'clock already exist. (These halls, as well as interior views of the tunnel, the cryogenic wing, and the Collider Center, are shown in Figures I.2 through I.8). The area at 4 o'clock is open, but has a completed concrete floor and an auxiliary building. The 10 and 12 o'clock experimental areas were left totally undeveloped when the CBA project was terminated. This proposal includes funds only to allow the rings to be completed through these areas, including radiation shielding. They will not be available as useable experimental areas. That option is open for the future.

I.3. Cost and Schedule

The following table summarizes the costs for constructing the relativistic heavy ion collider, making use of all existing resources at Brookhaven National Laboratory. We assume a conservative schedule of 4 years for magnet production (including 1 year of R&D and tooling fabrication prior to the start of the 3 year magnet production proper) and 5 years for overall project completion. Fig. VI.2 is the construction timeline for RHIC. Based upon this schedule, initial experimentation could begin about September 1, 1990. Complete details are found in Section VI.

Table I.1. RHIC Cost Estimate Summary

Accelerator systems		88.3
Magnets	46.8	
Other	41.5	
Completion of conventional facilities		3.7
Architect-Engineer		0.5
Engineering, Design, Inspection, Adm.		25.0
Sub Total		117.5
Contingency		16.9
TOTAL (FY 84 M$)		134.4

Figure I.2. Interior view of narrow angle hall at 2 o'clock, showing arch-shaped extension of the experimental area, leading to the tunnel proper.

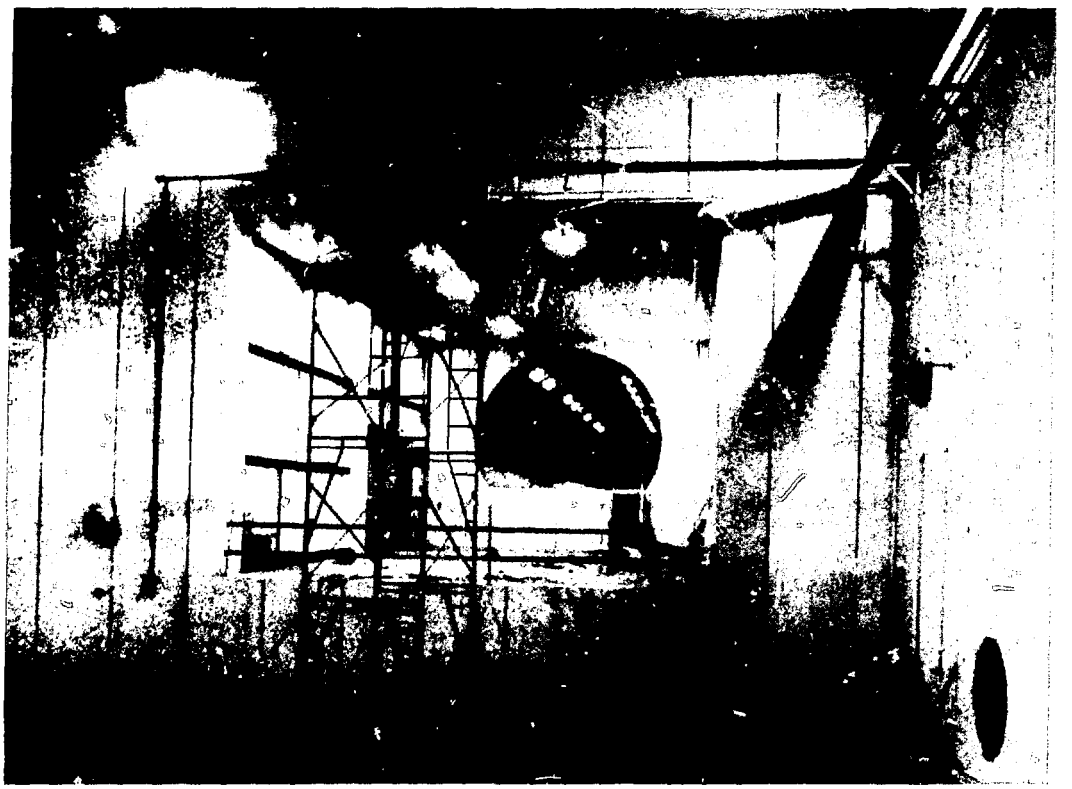

Figure I.3. View from the major facility hall at 8 o'clock, showing one of the side halls, and an enlarged section of the tunnel leading to the magnet enclosure.

Figure I.4. The wide angle hall at 6 o'clock, with adjoining support building.

Figure I.5. Enlarged section of the tunnel near 6 o'clock. In the background can be seen the transition structure leading to the wide angle hall (left) and the west injection tunnel from the AGS (right).

Figure I.6. Inside the magnet enclosure.

Figure I.7. Interior view of the cryogenic wing. The ends of the five cold boxes of the refrigerator are barely discernible behind the cryogenic piping.

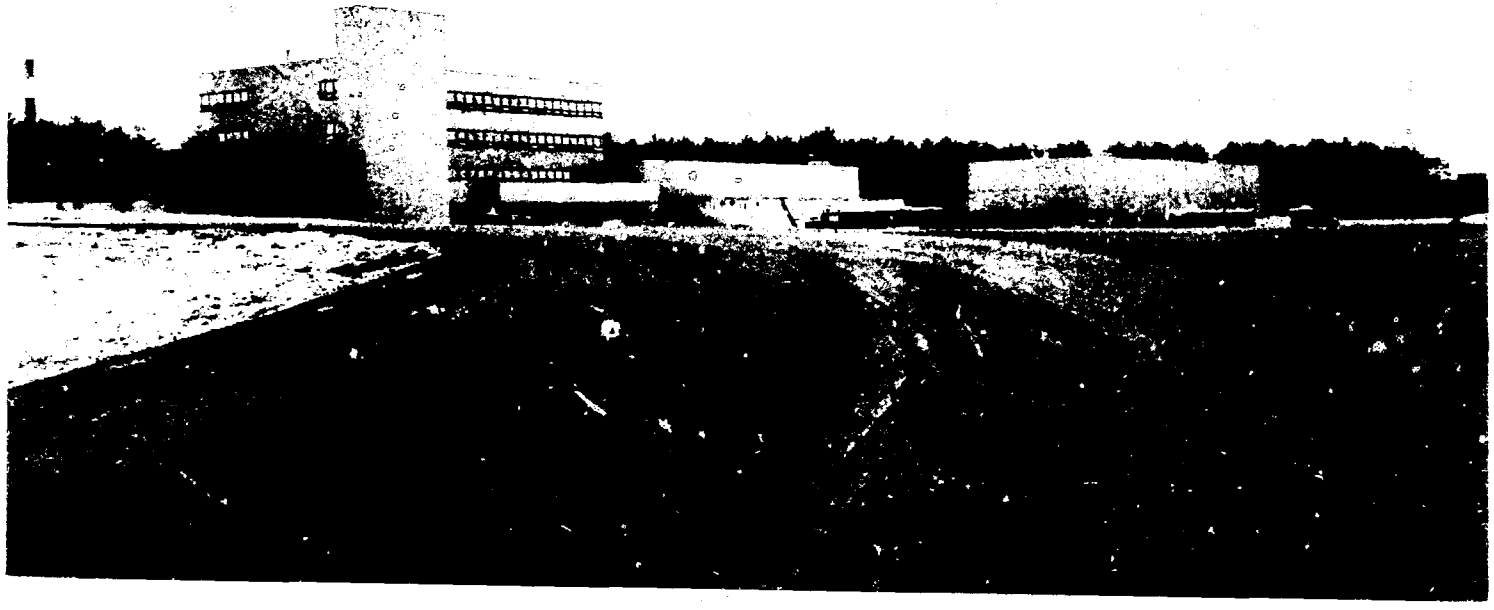

Figure I.8. The Collider Center, as seen from inside the RHIC Ring. From Left to Right: Main Control Building, Cryogenic Wing, Compressor Structure, and Cooling Towers.

II. PHYSICS AT RHIC

II.1. Scope of Physics

The essential motivation for colliding heavy nuclei at ultrarelativistic energies is the production of nuclear matter at extreme conditions of temperature and baryon density: extended volumes of hadronic matter with energy densities greater than 10 times that of the nuclear ground state should be realizable. There is little direct knowledge about what to expect under such conditions as they have not been approached in the laboratory nor detected anywhere in the known universe. Thus the proposed facility represents a venture into a completely unknown regime for the study of fundamental properties of matter.

While the leap into the unknown is perhaps the most compelling attraction for experimenters, it is also true that very specific goals for discovery and exploration can be defined within our present understanding of Quantum Chromodynamics (QCD)--as developed from high energy collisions of elementary particles--and the low energy behavior of bulk nuclear matter. The parameters of the proposed machine complex will allow the experimenter to make contact with both regimes in the systematic study of new phenomena.

The specific motivation from QCD is the belief that we can assemble macroscopic volumes of nuclear matter at such extreme thermodynamic conditions as to overcome the forces that confine constituents in normal hadrons, creating a new form of matter in an extended confined plasma of quarks and gluons. The physics issues underlying the production and detection of this new state of matter have been the subject of many recent conferences and workshops.[1-4] Studies with a variety of theoretical methods have led to increased confidence in the basic expectation that a phase transition between hadrons and a "deconfined"

state* of quarks and gluons is achieved at an energy density of $\gtrsim 1$ GeV/fm^3. These theoretical expectations are illustrated on the phase diagram of nuclear matter shown in Fig. II.1.

Calculations based on the measured properties of high energy hadron-hadron and hadron-nucleus interactions, as well as information from high energy nucleus-nucleus collisions observed in cosmic ray data, show that energy densities of this order can be reached, over the range of temperature and density conditions exhibited in Fig. II.1, in accelerator produced collisions of heavy nuclei.

Recent theoretical results indicate a second phase transition, coupled to the deconfinement transition but probably at somewhat higher energy density, in which chiral symmetry is restored. Inducing this transition would bring us yet closer to the elementary states of matter, as it is the spontaneous breaking of chiral symmetry in ordinary hadronic states which gives the pion a nonzero mass.

From the point of view of QCD, ultra-relativistic collisions of heavy ions offer the means of studying the fundamental theory of strong interactions in the high density limit and observing directly the parameters of the predicted phase transitions. We will also be able to study the physical properties of the QCD vacuum state and the mechanism of quark confinement, both of which reflect manifestly long-range phenomena,[5] over large distance scales which cannot be realized in collisions of elementary particles.

Between the conditions of normal nuclear matter and quark-gluon plasma lies unexplored territory. Many as yet unseen phenomena have been predicted,

*Deconfined is used in the sense of not being a part of a normal hadron, but in fact confined within a large plasma.

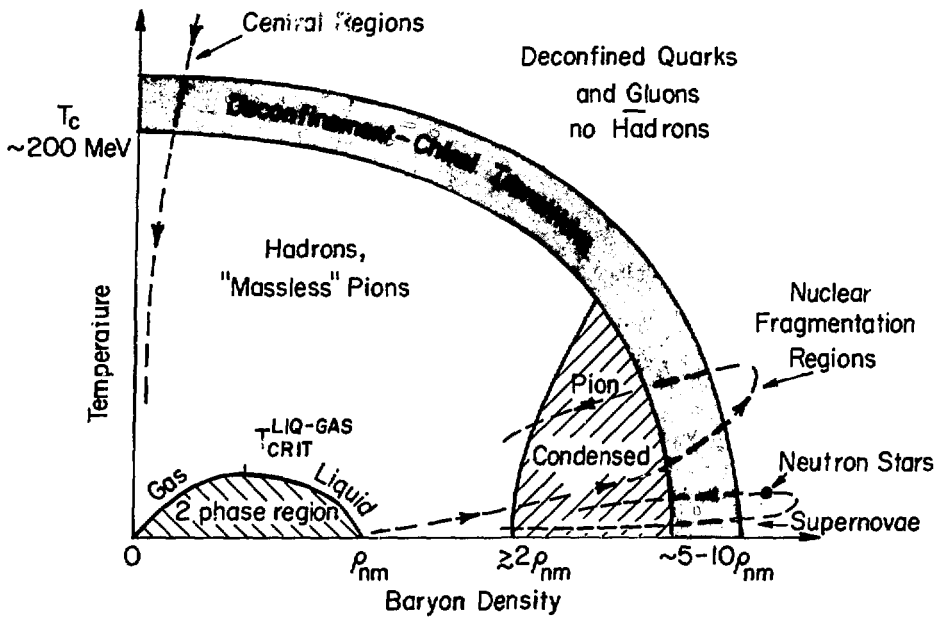

Fig. II.1 Phase diagram of Nuclear Matter (G. Baym, ref. 3). Temperature is plotted vs. net baryon density for an extended volume of nuclear matter in thermal equilibrium. Normal nuclear matter appears at the point ρ_{nm} at zero temperature, and this is the neighborhood explored by low energy nuclear physics. The region of the phase transitions corresponding to deconfinement (at temperature T_C) and chiral symmetry restoration is indicated T_F. The two critical temperatures may well be coincident. The confinement force couples quarks to form hadrons. The chiral force binds the collective excitation to Goldstone bosons. Above T_C, hadrons dissolve into quarks and gluons. Above T_F quarks are massless. The indicated trajectories show two avenues for probing the quark-gluon plasma with high energy nucleus-nucleus collisions: by reaching high baryon densities among the hot, compressed fragments of the colliding nuclei, and at very high temperatures in the central rapidity region among thermally produced particles where conditions may approximate those of the early universe.

some of which are shown schematically in Fig. II.1. There is ample room for the unforeseen.

In addition to addressing directly problems of nuclear and elementary particle physics, these experiments will provide essential new information for use in astrophysics and cosmology. For example, there is presently no direct knowledge of the equation of state of nuclear matter at densities relevant to the interiors of neutron stars. Measurements of ultra-relativistic heavy ion collisions could provide an upper limit for masses of neutron stars, as well as providing new information to complement surface temperature measurements from x-ray telescopes for understanding the evolution of these objects. It may be, in fact, that deconfined matter exists in the dense cores of neutron stars which are left as the remnants of supernovae.

With ion collisions at very high beam energies we expect to achieve not only extreme baryon density (moving out along the horizontal axis of Fig. II.1), but also to produce the case of extremely high temperature at near-zero baryon density (moving along the vertical axis of Fig. II.1). The latter conditions approximate those which existed a few microseconds after the big bang, as the cooling cosmos condensed from one of quarks to one of hadrons. Direct experimental measurement of this process will have application for understanding the early stages and subsequent evolution of our universe.

In the following sections we examine these physics questions, and some of the important experimental probes, to see how they affect the choice of basic parameters for a heavy ion collider: in particular the range of beam energies, accessible ion species, and the collision rate.

II.2. Quark Matter

Experiments with nuclei under ordinary conditions reveal them to be made up of neutrons and protons, not quarks and gluons. Nonetheless particle physics experiments persuade us that quarks exist, that they are normally confined within hadrons, and that the confining forces are such that isolated quarks are never observed. The expectation that quarks and gluons should become free of confinement into hadrons under conditions of sufficiently high temperature and density is a consequence of asymptotic freedom in QCD theory: as the distances between quarks become very small, as in very high energy interactions, the forces that bind them tend to zero.

A QCD picture of normal nuclear matter is shown in Fig. II.2.a, in which the ordinary hadrons exist as quarks and gluons confined to small cavities ("bags") imbedded in the ground state, nonperturbative vacuum. This ground-state vacuum is not simply empty space, but a complex physical medium[5,6] which excludes the color field just as a perfect dielectric excludes electric fields. An isolated quark has infinite mass in this medium. Inside a hadron the presence of quarks and gluons transforms the vacuum to a higher energy state--the perturbative, or "simple" vacuum--in which color fields can be established and quarks and gluons propagate freely. In the bag models of hadrons, the higher energy density of the perturbative vacuum is treated as a pressure exerted on the confining volume (the bag) by the outside vacuum.

We know that the bags can be penetrated, dislodging the constituent quarks and gluons. In high energy hadron-hadron collisions we observe "hard scattering" events at large P_T in which quarks and gluons are knocked free of the bags, then rehadronize and are seen as jets. The formation of quark matter in nuclear collisions is expected to occur when the density of bulk nuclear mat-

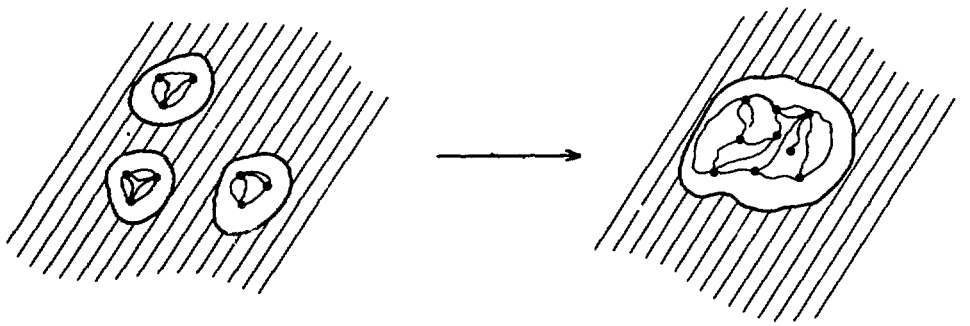

(a) (b)

Fig. II.2 Phase transition of the QCD vacuum: (a) quarks and coloer fields confined inside the observable hadrons. The confining medium (shaded) is the ground-state vacuum. (b) At high temperature and density the hadrons coalesce into an extended volume of confinement containing many quarks.

ter is increased to such an extent, either by increasing the nucleon density or by thermally producing more hadrons, that the bags begin to interpenetrate, overlapping one another until the entire volume is filled with the simple, perturbative vacuum. The quarks are then no longer locally confined, but are free to roam over the entire volume (Fig. II.2.b). Colorless hadronic matter has undergone a phase transition to a color conducting plasma of quarks and gluons: quark matter.

Until recently, calculations of the critical parameters for this transition have begun with the a priori assumption of two phases, using phenomenological models (bag models) for the hadronic phase and perturbative QCD for the deconfined quark phase. One then parameterizes the thermodynamic behavior in both phases in terms of temperature, chemical potential (baryon density), volume and pressure (energy density) and interprets the parameters at which the two pictures merge as being the critical parameters for a phase transition. The phase transition is thus obtained by construction. These calculations (for an example see Ref. 7) give self-consistent results, and lead to rather confident predictions that a (first-order) phase transition should occur in the range of temperatures and densities indicated in Fig. II.1, corresponding to an energy density $\varepsilon = 0.5 - 1$ GeV/fm^3.

During the past three or four years these results have been reinforced by studies of the phase structure of QCD using the calculational techniques of lattice gauge theory.[7,8] Here one is able to derive both the critical behavior and the limiting phases from a single fundamental description. Figure II.3 shows one such result,[7] the energy density of an SU(2) Yang-Mills system evaluated on a space-time lattice and normalized to the value for an ideal gas, as a function of the temperature. The phase transition is dramatically evident, in

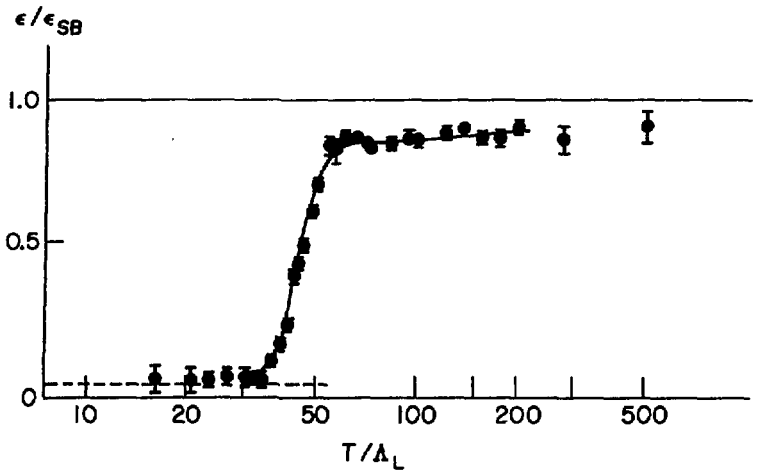

Fig. II.3 Energy density of the Yang-Mills system for SU(2) color group, as a function of the temperaure. Monte Carlo techniques are used to evaluate the partition function on a finite space-time lattice; hence the calculation appears as discrete points with statistical errors. The energy density ϵ is normalized to the ideal gas form ϵ_{SB} calculated on the same lattice. The lattice scale, Λ_L, is approximately equal to 5 MeV. (ref. 7)

this case corresponding to a noninteracting gas of gluons at high temperature, freezing into hadrons (glueballs) at a temperature T_c = 200 MeV.

Rapid progress is being made to extend and improve such calculations. The inclusion of quarks does not appear to alter the critical parameters significantly (see Polonzi, et al., ref. 8), and there is a broad consensus among the practitioners that a color deconfining phase transition at $T_c \simeq 200$ MeV and energy densities in the range .5 - 1 GeV/fm^3 is a firm prediction of the thermodynamics of finite temperature QCD.

Figure II.4 shows a computer simulation in SU(3) gauge theory in which a second phase transition appears corresponding to the restoration of chiral symmetry.[8] In this case there are three phases: the hadron gas; an intermediate phase in which the quarks and gluons are deconfined, but chiral symmetry is still spontaneously broken; and the high temperature quark-gluon plasma. In the intermediate phase pions and pionic resonances still exist, and it is predicted that resonance masses are shifted downward by the mean field of the quark-gluon plasma. These resonances then melt away as the second phase transition is approached.

If QCD is a correct description of the interaction dynamics, the parameters of a deconfining phase transition appear to be well constrained. The indicated temperatures and energy densities should be accessible to laboratory measurements in high energy collisions of heavy nuclei, a matter we take up in the following section.

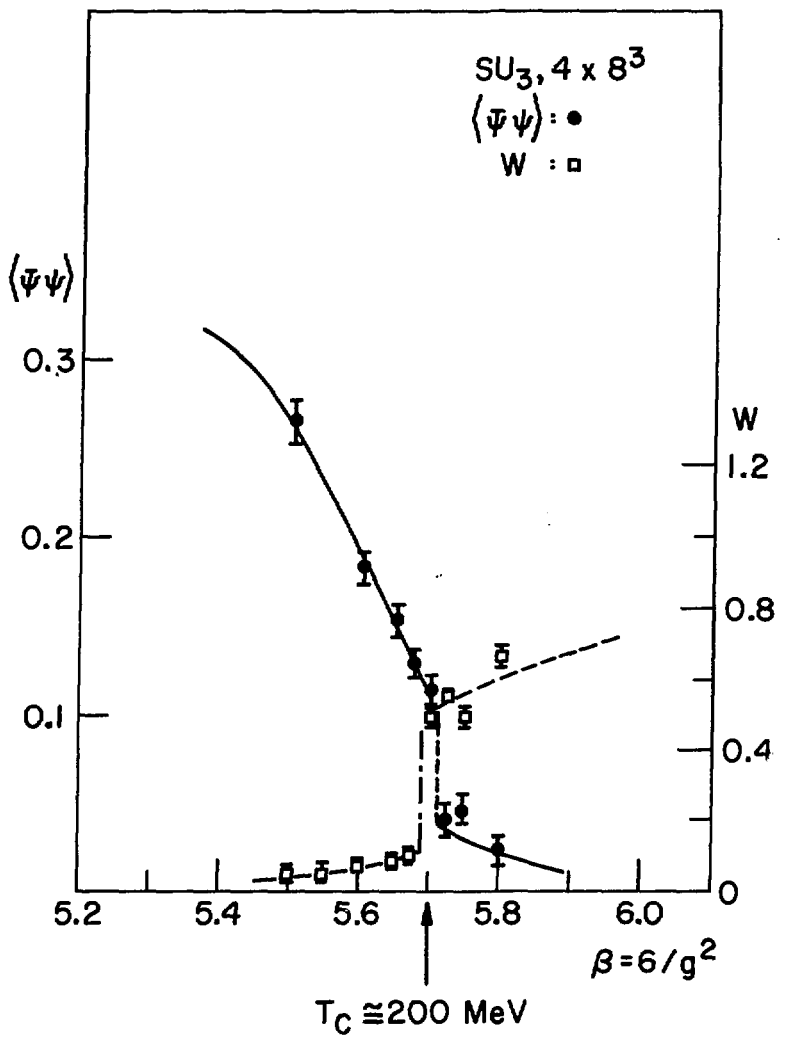

Fig. II.4 Lattice calculation for SU(3) gauge theory showing a coupled, first-order transition in the order parameters for the Chiral force ($\bar{\psi}\psi$) the confining force (W). (ref. 8)

II.3. Characteristics of High Energy Nucleus-Nucleus Collisions: Energy Deposition and Thermalization

The belief that a thermodynamic environment capable of developing the quark-gluon plasma is achievable in high energy collisions is based on estimates of energy densities and characteristic space-time volumes as a function of the energy and mass of the colliding nuclei. These estimates follow from the observed particle production in proton-proton and proton-nucleus collisions.[6] The few examples of direct observation provided by cosmic ray events give additional input and are satisfactorily consistent with expectations. Here we sketch the essential features of these arguments and address the question of what beam conditions--energy and size of colliding nuclei--are required for sensitive experiments.

The detailed manner of energy deposition in head-on (zero impact parameter) collisions of equal mass nuclei is not known from direct measurement. Much can be inferred, however, from what we do know of hadron-hadron and hadron-nucleus collisions. The central concept is that of "nuclear transparency" (or, alternatively, "nuclear stopping power"): when hadrons collide at high energy they rarely bring each other to rest, instead they pass through one another with most of the final-state energy carried by leading particles. In nucleon-nucleus collisions the spectrum of leading baryons in the final state gives a measure of the nuclear stopping power,[9] and this can be related to the way energy is deposited in nucleus-nucleus collisions. The picture which emerges is sketched in Fig. II.5. At low energies the colliding nuclei bring each other to rest, while at very high energies they bore through each other, producing two hot, baryon-rich fireballs moving off in opposite directions at large rapidity (the fragmentation regions), and inelastically produced

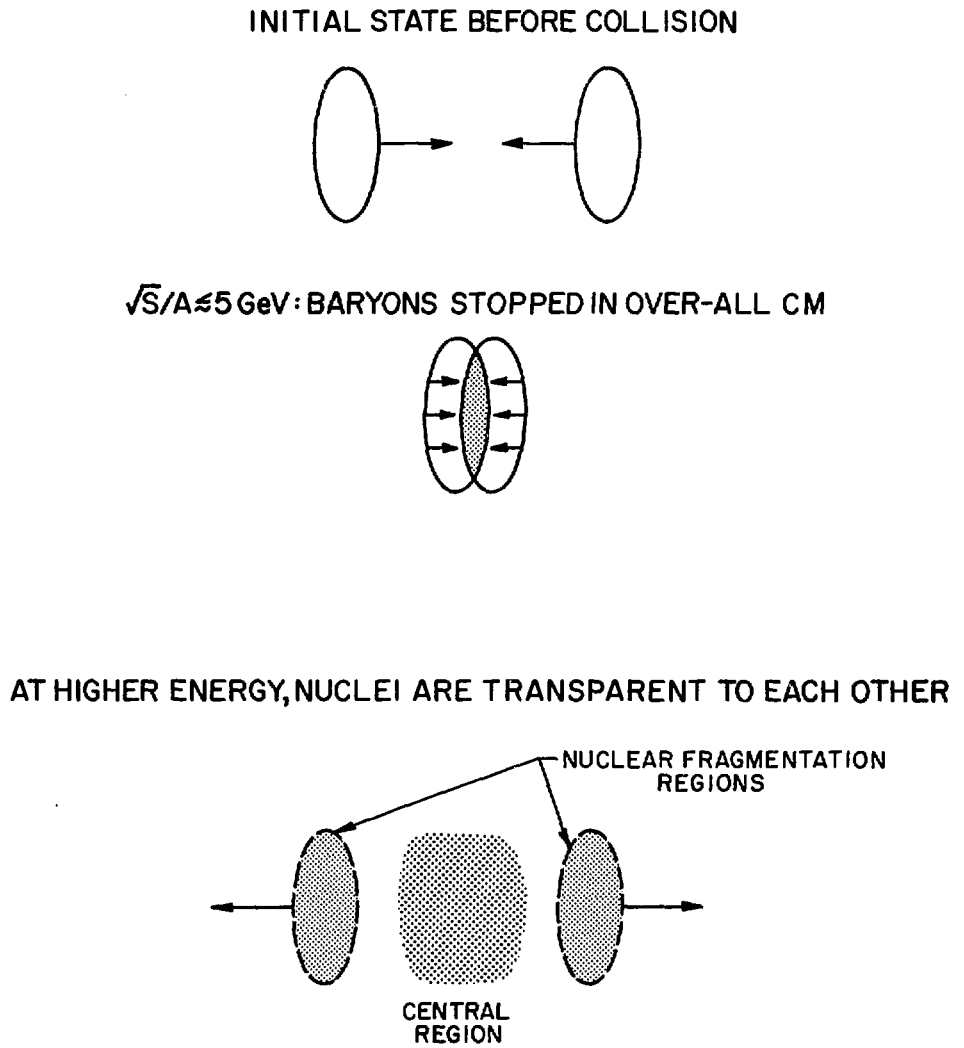

Fig. II.5 Schematic illustration of nuclear transparency in high energy collisions at zero impact parameter.

pions populate the central rapidity range. The energy at which transparency sets in, i.e., the maximum collision energy at which the two nuclei are (in some average sense) brought to rest, is currently estimated to be $\sim$5 GeV/nucleon in the center of mass.[9] At this point the energy density in the fragmentation regions has reached its asymptotic, maximum value. An important consequence of transparency is that the formation of hot nuclear matter is confined to local regions of coordinate and momentum space. We do not expect the entire nuclear volume to establish overall equilibrium, as in simple hydrodynamical models. Rather, we must look separately at the excitation of nuclear matter in the central and fragmentation regions.

In the fragmentation regions compression and heating of the incident nuclei result in large energy density at a very high density of baryons (see trajectory sketched in Fig. II.1). For collision energies at or beyond the threshold for transparency, the predicted value for the energy density depends only on the size of the colliding nuclei, as shown in Fig. II.6. Energy densities approaching 2 GeV/fm^3 are expected for the heaviest nuclei.[10]

At collision energies significantly beyond the threshold for transparency the central rapidity region develops as indicated in Fig. II.5, and we have the possibility of exploring two regions of the phase diagram in Fig. II.1, with the production of quark matter in both. The two fragmentation regions are flying apart, carrying the net baryon density of the system with the energy density described above. Lying between these in phase space is the central region in which the net baryon number is small--tending to zero at very high energies--and a high density of particles, mostly pions, is thermally produced from the Fermi sea of the QCD vacuum. It is at high energy densities in this central region

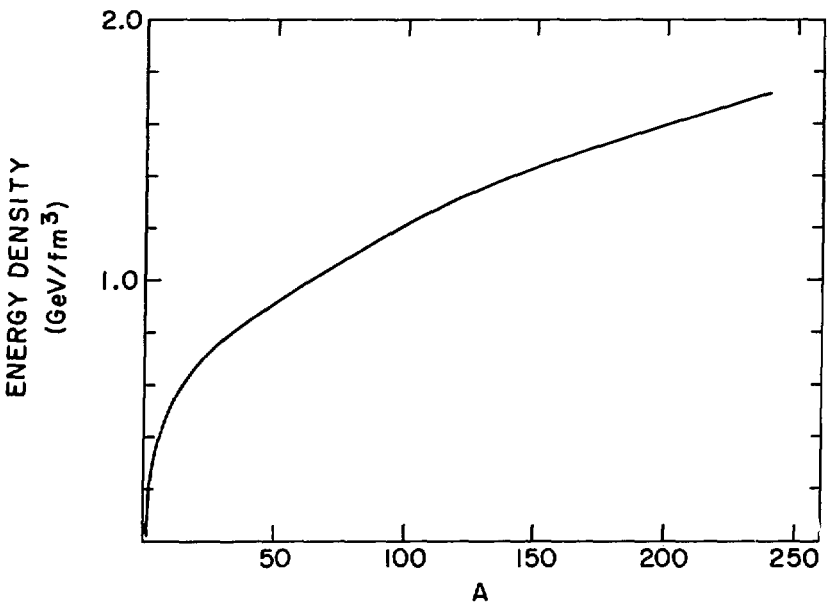

Fig. II.6 Predicted energy density in the fragmentation regions as a function of the atomic mass number (A) of the colliding nuclei (ref. 10). The functional form is

$$\varepsilon \simeq .15(2A^{1/3} - 1)\text{GeV/fm}^3.$$

This result applies for zero impact parameter and collision energies $\sqrt{s}/A \geq 5$ GeV/nucleon, corresponding to maximum baryon density.

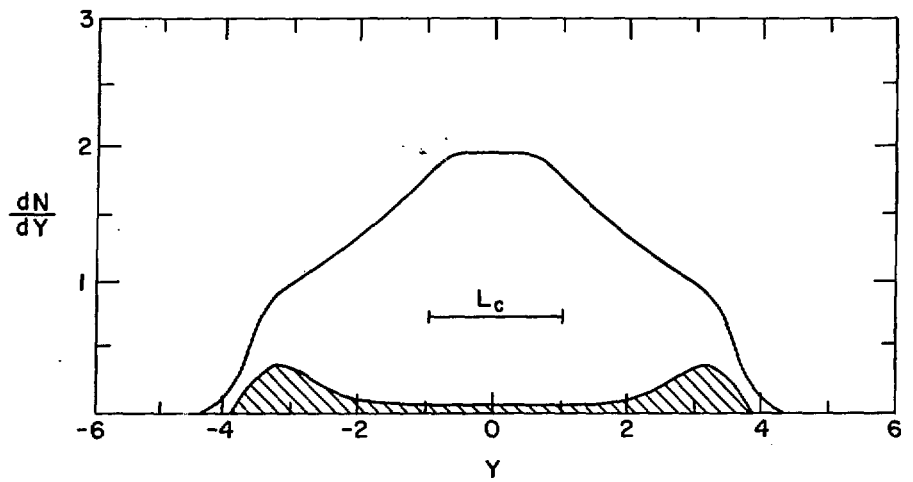

Fig. II.7 Rapidity spectrum of charged particles as measured at the CERN ISR in 30 + 30 GeV proton-proton collisions. The rapidity density is shown for all charged particles. The shaded area shows the net density of protons (protons minus antiprotons). Particle pairs emitted in the central region are found to be strongly correlated--either because of resonances or through multiperipheral dynamics--and the characteristic correlation length is indicated as L_c.

that we may approximate in the laboratory the strong interaction physics that took place microseconds after the big bang.

The measured features of charged particle production in proton-proton collisons at the CERN ISR ($\sqrt{s}$ = 30 + 30 GeV) are illustrated in Fig. II.7. The available rapidity interval $\left[y_{max} \simeq \ell n \sqrt{s}\ (\text{GeV})\right]$ is ± 4 units. Near y = 0 the rapidity density of charged particles is ~ 2 per unit of rapidity, of which the net number of baryons (protons minus antiprotons) constitutes a few percent. At this collision energy the central rapidity region extends over an interval of $\pm 1\frac{1}{2}$ units. Beyond the central region one observes the fragmentation regions, each about 2 units wide, where the density of baryons is comparable to or exceeds the pion density. At the ISR energy the width of the central region is comparable to the correlation length, L_c, characteristic of short-range multiperipheral dynamics and the decay kinematics of low-mass resonances. Thus, at the ISR energy a central region has just begun to develop in proton-proton collisions.

The energy dependence of the main features of particle production is well established: as the collision energy is increased the width of the central region grows logarithmically with energy; the particle density in the fragmentation region remains fixed; and the density of charged particles at y = 0 grows slowly (logarithmically) with energy. Figure II.8, comparing data from the two CERN colliders, illustrates these trends.

We can extrapolate the proton-proton data to infer the energy density which should be achieved in the central rapidity region for heavy ion collisions. Here the energy density has been estimated in terms of the density of final-state pions:[11]

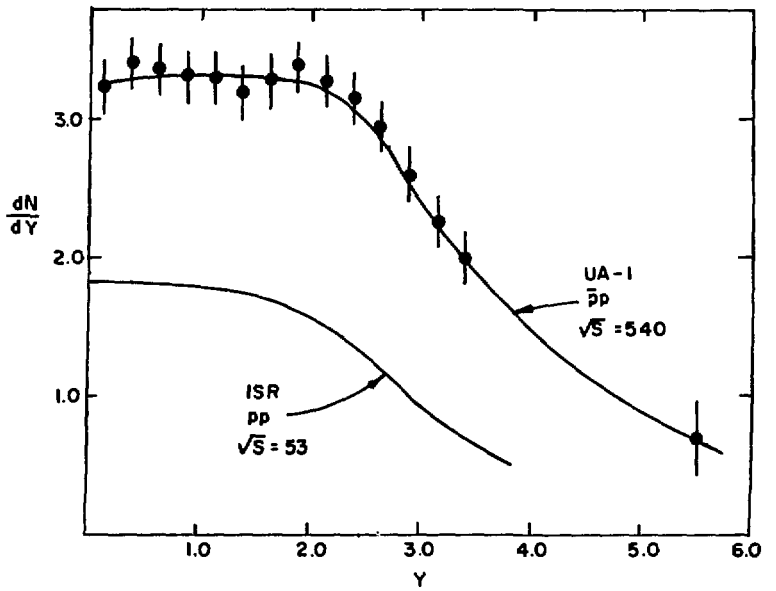

Fig. II.8.a

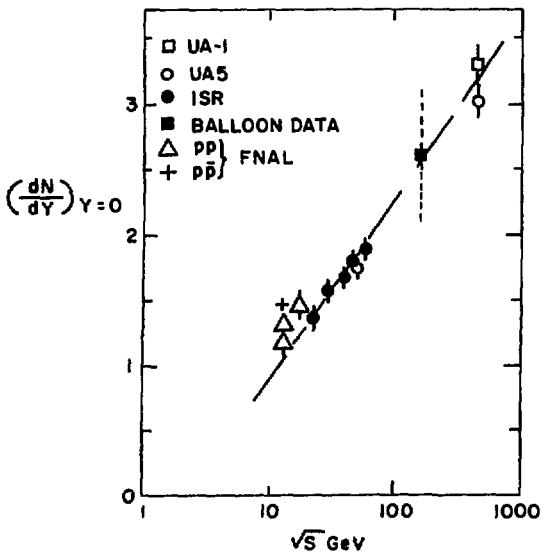

Fig.II.8.b

Fig. II.8 Measured charged particle production at the CERN ISR and SPS colliders, showing the energy dependence.

$$\epsilon \simeq \frac{0.1}{t} A^{-2/3} (dn/dy)_{AA} \text{ GeV/fm}^3 \qquad (3.1)$$

Here $(dn/dy)_{AA}$ is the total number of pions per unit rapidity at $y = 0$, for colliding nuclei of mass A, and t is the time measured in fermi.

Assuming the final pion density grows roughly in proportion with A, and taking the energy dependence shown in Fig. II.8, we have

$$(dn/dy)_{AA} \simeq A(dn/dy)_{pp} \simeq A \ln(\sqrt{s}/A) \ . \qquad (3.2)$$

Thus, for the largest values of A we have, even for times several fermi after the formation of the central region, energy densities >1 GeV/fm^3. These results correspond to extremely high particle multiplicities: $(dn/dy)_{AA} > 500$. That this is in fact to be expected is confirmed in cosmic ray data,[12] where researchers using emulsion stacks in balloon flights above the atmosphere are amassing a growing library of events with c.m. energies in excess of 50 GeV/nucleon and many hundreds of charged particles in the final state. In Fig. II.9 we show the central region energy density as given by the above estimate, and the energy densities computed from Eq. 3.1 for some measured cosmic ray events (which, it should be noted, involve relatively light ions).

If the heaviest nuclei are brought into collision at energies high enough to develop a central rapidity region, we may be confident of achieving the required conditions for a phase transition. In estimating the "correct" energy for exploiting the central region physics we can at best identify a regime in which there is a good probability for nuclear transparency--noting that the important parameters become more favorable as the energy is increased. We are not aware of sharp thresholds for this process. The estimates discussed here all refer to averages over a range of conditions within which there will be

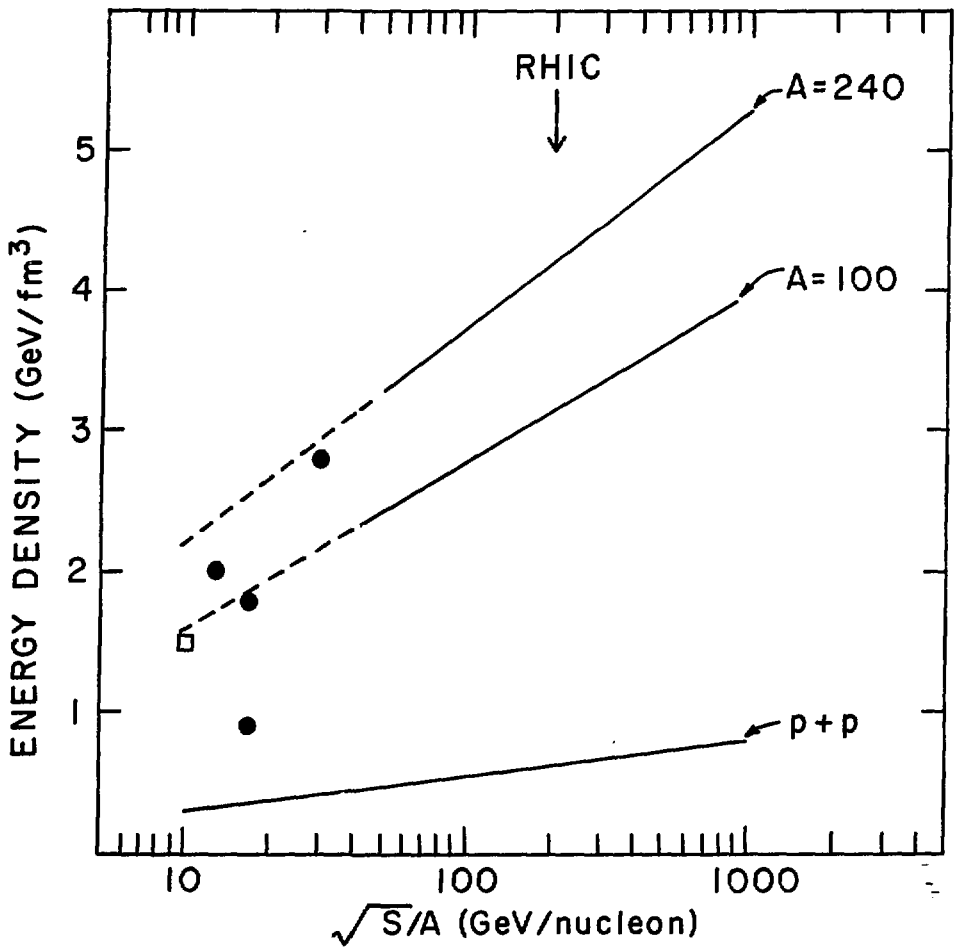

Fig. II.9 Predicted energy density in the central region as a function of collision energy, for various masses of colliding nuclei. The data points are from cosmic ray events. The colliding nuclei were Si + Ag (round points) and Ar + Pb (square point).

large fluctuations. Ideally we prefer to work with a central region much wider than that shown in Fig. II.7, so that long-range correlations are not masked by "trivial" short-range correlations which dominate the nucleon-nucleon interaction. On the other hand, we expect the fragmentation regions to be considerably broader in nuclear collisions than in the proton-proton case. Present data[9] indicate that the target and projectile fragments each will occupy $\sim$4 units of rapidity--leaving no room for a central region at the collision energy shown in Fig. II.7.

Figure II.10 illustrates the expected average behavior for Au + Au collisions at three different energies, assuming the multiplicity grows in proportion to A and incorporating the results of Ref. 9 for the nuclear stopping power. At 100 + 100 GeV/amu two units of rapidity are added to the available phase space in each of the fragmentation regions (compared to the ISR data), and there is a substantial interval around y = 0 where the mean baryon density is small compared to the pion density. We have chosen this energy as desirable and quite feasible for the RHIC facility.

Figure II.11 shows the range of energies and kinematic terrain covered by the AGS and RHIC complex. Exploiting fixed target as well as collider modes, the coverage extends from below the energies of maximum baryon density up to and including the very high energies where cosmic ray data show spectacular multiplicities, central region physics is accessible, and hard-scattering phenomena (jets) stand out clearly in nucleon-nucleon interactions.

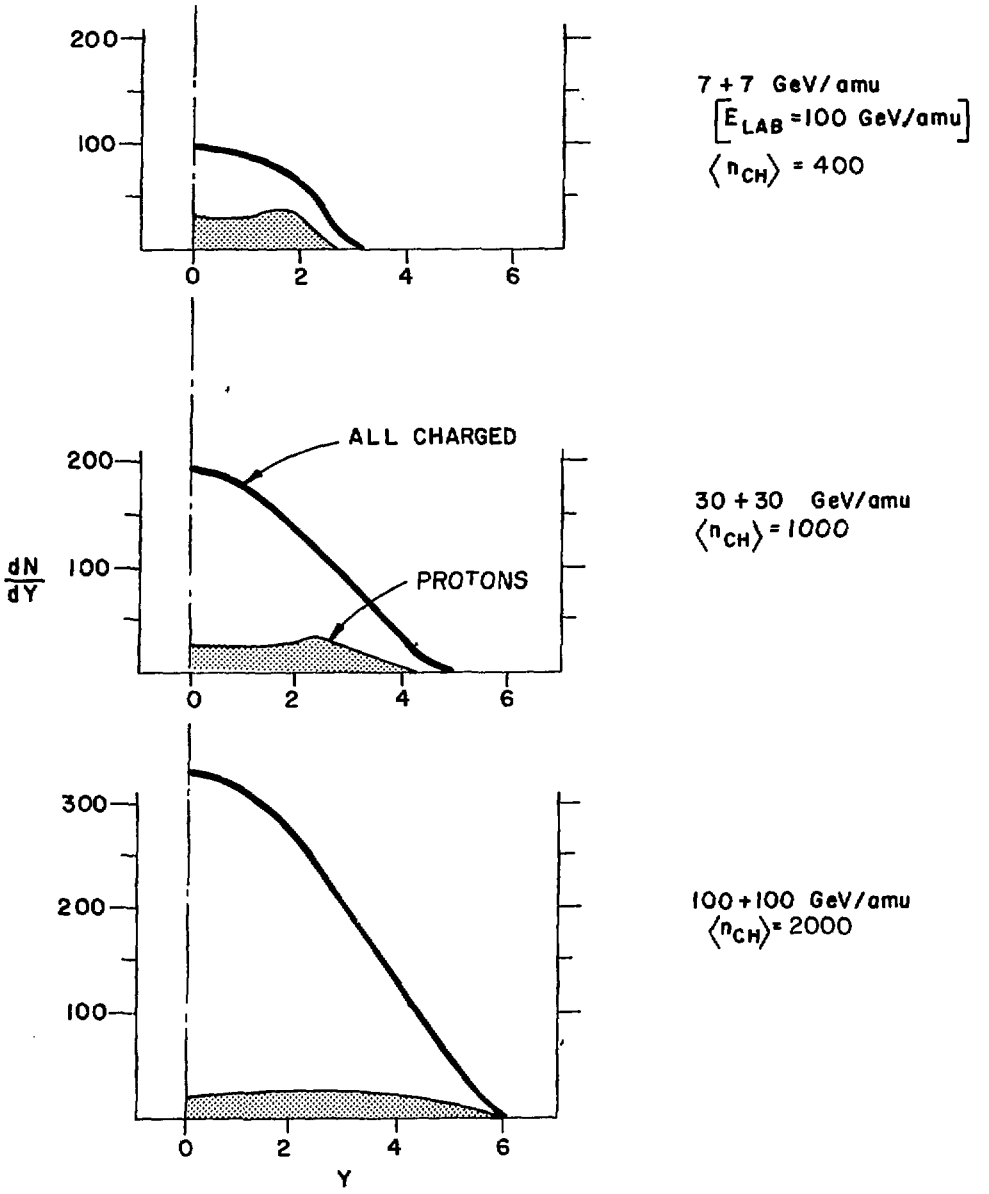

Fig. II.10 Illustrating the expected charged particle spectra for Au + Au collisions at various collider energies. The shaded areas are the net proton densities extrapolated from the stopping power measurments of Ref. 9. $\langle n_{CH} \rangle$ is the mean multiplicity of charged particles.

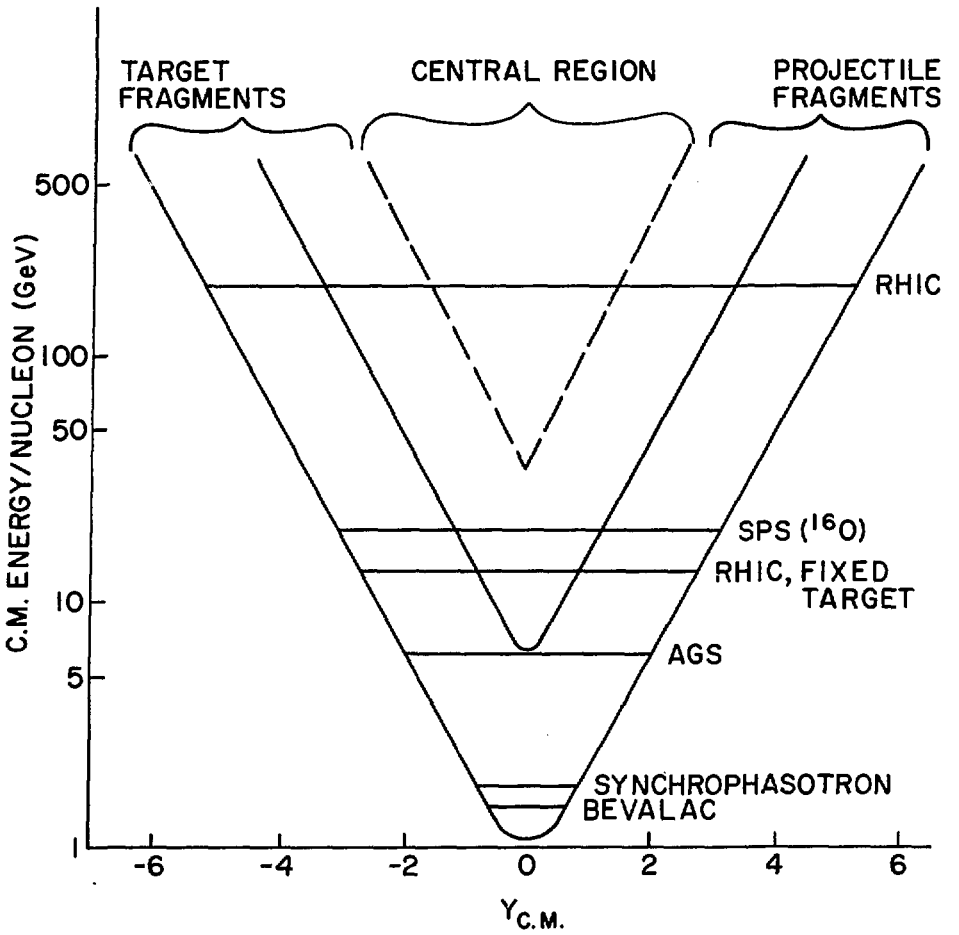

Fig. II.11 The kinematic landscape available to the proposed facility, and some existing machines. The outer "vee" is the phase space limit--the rapiditiy of the incident nucleons. The inner, solid vee delineates fragmentation regions of width $\Delta y = 2$, as observed in proton-proton collisions. The dashed lines indicate the wider ($\Delta y = 4$) fragmentation regions--and hence narrower central region--expected at a given energy for nucleus-nucleus collisions with A $\gtrsim$ 200. The horizontal lines indicate (AGS,RHIC) as well as in the facilities which presently exist (LBL Bevalac, Dubna Synchrophasotron) and the planned oxygen beams in the CERN SPS.

TABLE II.1. EXPERIMENTAL PROBES FOR NEW STATES OF MATTER.

SIGNAL	COMMENTS	
INCLUSIVE PARTICLE SPECTRA PARTICLE INTERFEROMETRY	INDICATORS OF TEMPERATURE, SIZE AND DENSITY	GLOBAL EVENT PARAMETERS
MULTI-PARTICLE CORRELATIONS IN RAPIDITY; ENERGY FLOW	LONG RANGE CORRELATIONS AND MACROSCOPIC FLUCTUATIONS CHARACTERISTIC OF FIRST-ORDER PHASE TRANSITION	
LOCAL CHARGE CORRELATIONS	COLOR SCREENING EFFECTS IN PLASMA DIFFERENT FROM NORMAL PAIR PRODUCTION BY VACUUM POLARIZATION	INDICATORS OF A PHASE TRANSITION
PARTICLE FLAVOR RATIOS	CHEMICAL EQUILIBRIUM IN HOT PLASMA GIVES A LARGE NUMBER OF STRANGE PARTICLES AND ENHANCED $\bar{\Lambda}/\bar{p}$ RATIO	
STABLE MULTIQUARK STATES	6-QUARK AND HIGHER CONFIGURATIONS READILY ASSEMBLED IN THE PLASMA	
DIRECT PHOTON PRODUCTION ($m_T = p_T$) LEPTON PAIR PRODUCTION (VIRTUAL PHOTON: $m_T^2 = m_{PAIR}^2 + p_T^2$)	$m_T \lesssim 50$ MeV: COHERENT EMISSION FROM LOCAL CHARGE FLUCTUATIONS $50 \lesssim m_T \lesssim 500$ MeV: HADRONIC DECAYS; SOME COHERENT EFFECTS $500 \lesssim m_T \lesssim 3$ GeV: DIRECT EMISSION FROM PLASMA $m_T \gtrsim 3$ GeV: APPROACH TO EQUILIBRIUM; STRUCTURE FUNCTIONS OF QUARKS AND GLUONS CHANGE AND ARE COMPUTABLE IN PERTURBATIVE QCD	PENETRATING PROBES: DIRECT INFORMATION FROM THE PLASMA
HIGH-p_T JETS	MEASURES PROPAGATION OF QUARKS AND GLUONS THROUGH NUCLEAR MATTER; HADRONIZATION PROPERTIES REFLECT THE "REAL SEA" OF QUARK-GLUON PLASMA	

II.4. Experiments and Detectors

An experimental program to explore all of the facets of this new physics will involve a systematic study of many reaction properties, and detectors sensitive to different forms of radiation which may be used to probe the nature of matter created in the collision. Theoretical arguments point to certain signals which should be important for observing the deconfinement phase transition and for probing new forms of matter. These are summarized in Table II.1. They include: global characteristics of events, such as fluctuations in rapidity density; new, exotic, or as yet unseen particle states; completely new forms of measurement, such as particle interferometry, which became possible because of the high multiplicity, high charge states, and the large spatial extent of the interesting events. Perhaps the most important probes may be those which interact relatively weakly with nuclear matter and can bring information directly from the interior of a plasma of quarks and gluons. These "penetrating probes" include real photons, virtual photons seen as lepton pairs, and high momentum quarks and gluons which are ultimately observed as jets.

Assuming the interesting events are rare, the measurement strategy will be to employ selective triggers to choose events indicative of a favorable thermodynamic environment. A first-level selection would include a trigger on head-on collisions (small impact parameter) with large energy deposition. Measures of the impact parameter include particle multiplicity and transverse energy in the central rapidity region, the energy carried by fragmentation products at very small angles relative to the beams, and (a recent prediction),[13] photons which are coherently produced when nucleons are accelerated during the collision. One could then be more selective in characterizing the matter thus created in terms of particle multiplicity, energy and momentum flow, and tempera-

ture and volume indicators in various kinematic regions. Triggers yet further refined, as a second level, would then be brought to bear on specific signatures and probes such as are listed in Table II.1.

This approach implies a measurement capability similar to that which we see in spectrometers for high energy elementary particle experiments. The design of instrumentation for experiments with ultra-relativistic nuclear beams has been the subject of extensive workshop activity (see Refs. 1-4), and these discussions have included large, general purpose facilities as well as smaller, more specialized detector systems. Figure II.12a shows very roughly the geometry and kinematics of a large solid angle detector, designed for use with colliding beams and having tracking and calorimetry in the central rapidity region and at forward angles. A real detector system might have more limited solid angle coverage. Note (see Fig. II.10) that the number of particles in each of the indicated rapidity intervals is expected to be many hundreds.

Figure II.12b shows the same detector configuration being used in a fixed target mode, with only one of the collider beams accelerated and striking a thin target, such as a gas jet.[14] Such jets have been employed as internal targets in many accelerator experiments. Operation in the fixed target mode - utilizing, if need be, the same detectors as in the the Collider mode - allows experiments with good luminosity in the range of energies above that of the AGS fixed-target experiments where the Collider luminosities would be unacceptably small. This mode of fixed target operation would not, of course, require the expense of extracted beams, and provides in a natural way (as does collider operation) the extremely thin targets which are crucial for nuclear beams experiments and difficult to realize in conventional fixed target operation with external beams. A detailed evaluation of the design considerations for a gen-

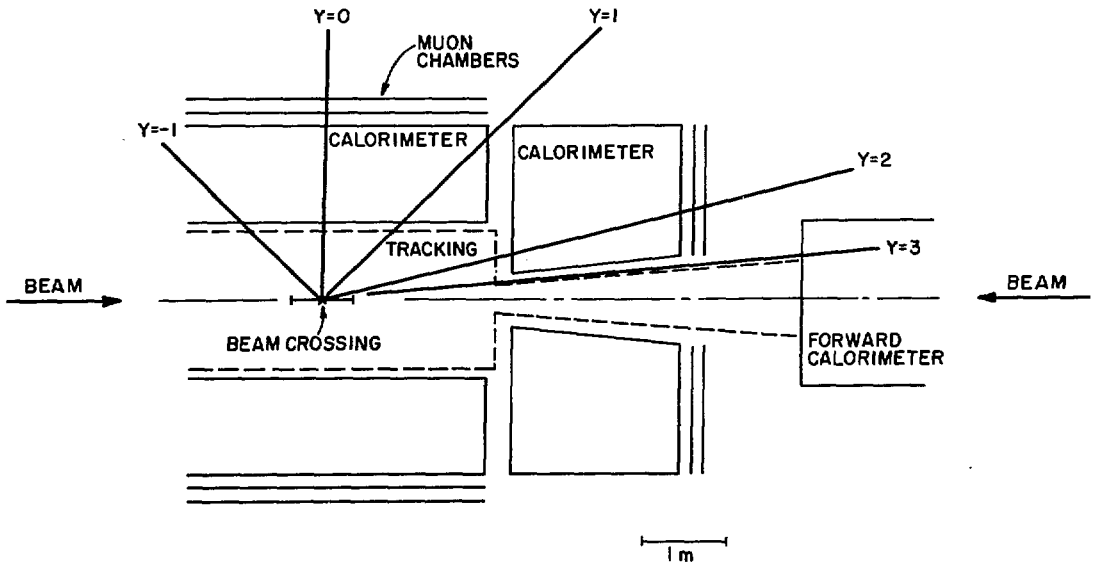

Fig. II.12 (a) Schematic layout showing the geometry and kinematics of a detector system for colliding beams experiments. The angular intervals corresponding to various rapidity (y) values are indicated. A full solid-angle detector would have the same coverage on either side of y = 0; this illustration shows coverage of the central region and one of the fragmentation regions.

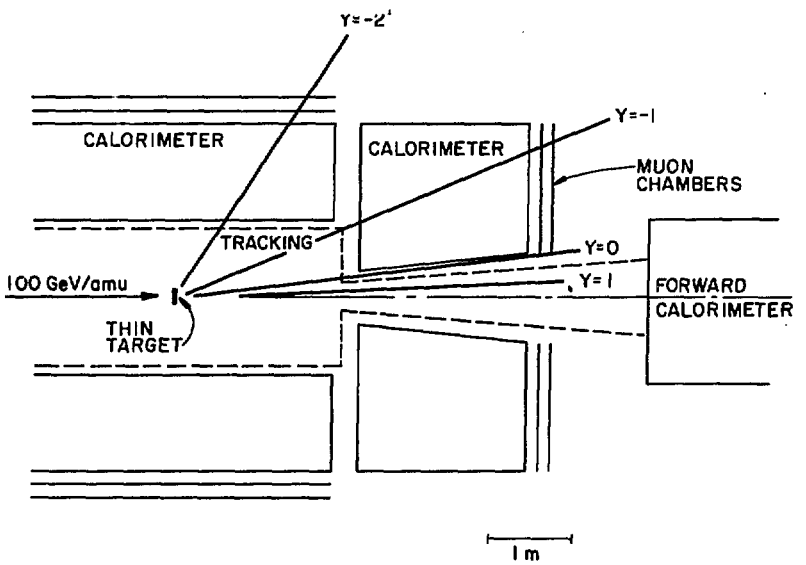

(b) The same detector system, with kinematics of fixed target operation. Here, a single beam at 100 GeV/amu strikes a thin ($\sim 10^{-9}$ gm cm^{-2}) internal target.

eral-purpose fixed target spectrometer such as that shown in Fig. II.12b may be found in Ref. 1.

A schematic rendering of a small aperture, special-purpose spectrometer for colliding beams experiments[15] is shown in Fig. II.13, indicating that not all experiments need huge, multipurpose, detector facilities. Small detector systems would be used in conjunction with a generalized facility to provide triggers, beam monitoring, etc.

The required detector technology for tracking, calorimetry, particle identification and fast trigger decisions has a great deal in common with components of high energy physics experiments, but there are important differences. The most striking is the extraordinary particle multiplicities which experiments must deal with in nucleus-nucleus collisions (see Fig. II.10). Interesting events (central collisions, large energy deposition) will have particle multiplicities larger by at least an order of magnitude than those presently encountered in high energy collisions of elementary particles, and for many of the measurements discussed above it will be desirable to resolve individually a large fraction of the tracks. Tracking detectors capable of resolving high densities of tracks are not unfamiliar. Advanced three dimensional tracking detectors, some examples of which are being prepared for LEP experiments, are designed to deal with track densities $\gtrsim$ 100/steradian as seen in high-P_T jets. The more difficult challenge may not lie in technical limitations of the detectors themselves, but in the data acquisition and processing. Studies of intrinsic limitations of track reconstruction algorithms have found no serious obstacle, in principle, to tracking $\sim 10^3$ tracks per event with presently understood techniques.[16]

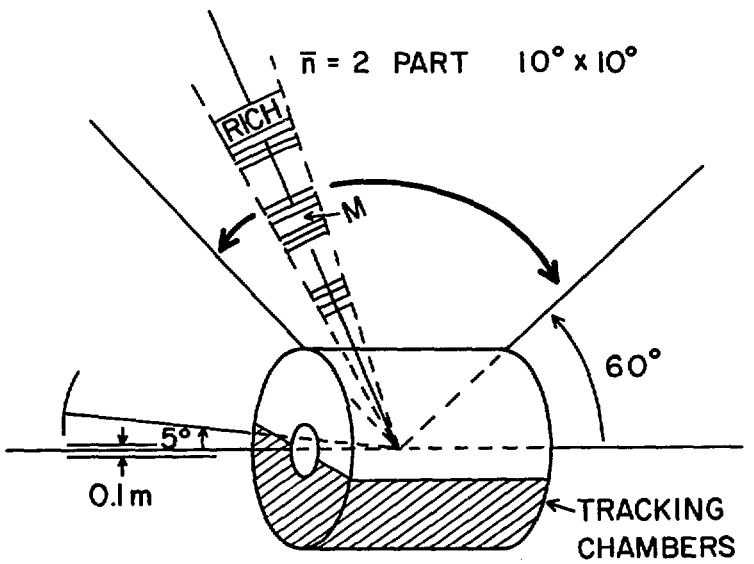

Fig. II.13 A scheme from a recent workshop (ref. 15) for a small spectrometer area sampling the central region in a colliding beams experiment. The mean number of particles seen by the spectrometer is about 2 per event.

Another clear difference between high energy experiments with elementary particle beams and those with ultra-relativistic nuclear beams is that in the latter case most of the essential measurements (Table II.1) involve soft particles, with transverse momenta and pair masses characterisitic of the kinetic energies in a thermalized plasma. These range from near-zero (e.g. coherent photons of a few MeV produced in conjunction with large-scale charge fluctuations) through direct radiation from the plasma in the range 0.5-3 GeV. This is in contrast with the elementary particle case where the focus is largely on very rare processes produced in the tails of momentum distributions ($P_T > 10$ GeV) due to hard scattering events, and thus backgrounds from soft particles characterizing the average properties of events are easily eliminated. For nuclear beam experiments, the signals of interest must generally be extracted from the high multiplicity component of soft particles. This also implies that reasonable samples of useful events can be accumulated without the requirement of extraordinarily high interaction rates.

For the most massive ions ($A \gtrsim 200$) the nuclear interaction cross section is $\sim$10 barns. This means that a machine with luminosity $L = 10^{23}$ $cm^{-2}sec^{-1}$ would provide an interaction rate of 1 event/sec. This is already a vast improvement over the present rate of accumulation for high energy cosmic ray events ($\sim$12 events/year for the JACEE experiment),[12] but would not allow much flexibility of trigger selection. At $L = 10^{24}$ $cm^{-2}sec^{-1}$ we have available one head-on collision per second. With $L \gtrsim 10^{25}$ $cm^{-2}sec^{-1}$ quite sensitive experiments become possible. An upper limit of usable luminosity (again, for the heaviest ions) is probably in the range $L = 10^{29}$ $cm^{-2}sec^{-1}$, where the detectors become exposed to a flux of particles $>10^7$ sec^{-1} $ster^{-1}$. The design luminosity for the proposed facility is $\gtrsim 10^{26}$ $cm^{-2}sec^{-1}$ for Au beams at 100 GeV. The lu-

minosity over the full range of energies is shown in Fig. II.14, which includes the performance for fixed target operation in AGS and RHIC.

At the very highest energies, and at luminosities $\gtrsim 10^{26}\text{cm}^{-2}\text{sec}^{-1}$, a new and potentially very powerful probe of nuclear matter becomes accessible in the form of large transverse momentum jets. Consider a high energy nuclear collision in which a pair of partons suffers a hard scattering event of the sort which produces the hadronic jets observed at large transverse momentum in pp and $\bar{p}p$ collisions. One or both of the observed jets may be the hadronization of a quark or gluon which has propagated through a substantial volume of quark-gluon plasma produced in the collision. The properties of such jets may be substantially different from those of "ordinary" jets. Thus, the hadronization of ordinary jets proceeds as $q\bar{q}$ pairs which are materialized from the "Fermi sea" of the QCD vacuum. It may be that a quark or gluon propagating through the real sea of a deconfined plasma hadronizes with quite different properties, which could signify the presence of a plasma and provide clues to its characteristics. Specifically, if chiral symmetry is restored in the plasma we may expect an enhanced fraction of strangeness and heavier flavors among the fragmentation products of the jet. The correlation within pairs of jets should be examined for evidence of the characteristic energy loss behavior suggested by Bjorken.[17] High energy quarks and gluons traversing the plasma may suffer energy loss comparable to the initial transverse momentum, giving rise to a momentum imbalance in the observed jet pair which is not seen in pp collisions. In the extreme case a hard scatter occurring near the periphery of the plasma results in one jet escaping unattenuated while the other is completely absorbed.

To do these experiments we must detect jets. Unlike most of the possible probes of a quark-gluon plasma, which involve detection of soft particles

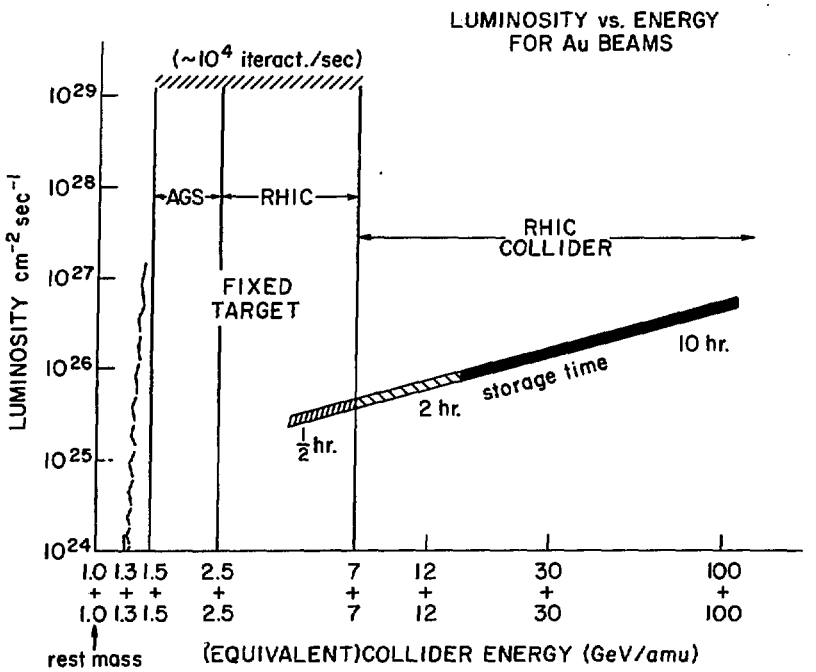

Fig. II.14 The design luminosity for ^{197}Au beams over the full range of energy accessible with AGS and RHIC.

among the very high multiplicity background, these measuremnets allow for very selective calorimetric triggers on local transverse energy deposition. The backgrounds are high, however; referring to Fig. 10, we expect $\sim$800 charged and neutral particles per unit rapidity near y = 0, each carrying $\sim$0.4 GeV of transverse energy. Jets will have to be observed above a soft background corresponding to $\sim$320 GeV of transverse energy per unit rapidity. The amount of this energy in a cone the size of a jet, say $\Delta y = 1$ and $\Delta\phi = 45^\circ$, determines the mimimum p_T of an observable jet:

$$p_{Tjet} > \frac{dE_T}{dy} \Delta y \frac{\Delta\phi}{2\pi} = 40 \text{ GeV} .$$

To estimate the rate for observing jets we take the cross section for p p collisions and assume this scales as A^2. The result[18] for beams of mass A = 200 are shown in Fig. II.15 as a function of the collision energy, for three different p_T thresholds, with a luminosity of 10^{27} cm^{-2}sec^{-1}. It will be seen that the requirement of $p_T > 40$ GeV/c is met for collision energies $\sqrt{s}/A \gtrsim 150$ GeV/amu, and the yields increase very rapidly at higher energies. At $\sqrt{s}/A = 200$ GeV/amu, the RHIC design energy, we expect substantial yields of observable jets up to transverse momenta of $\sim$60 GeV/c.

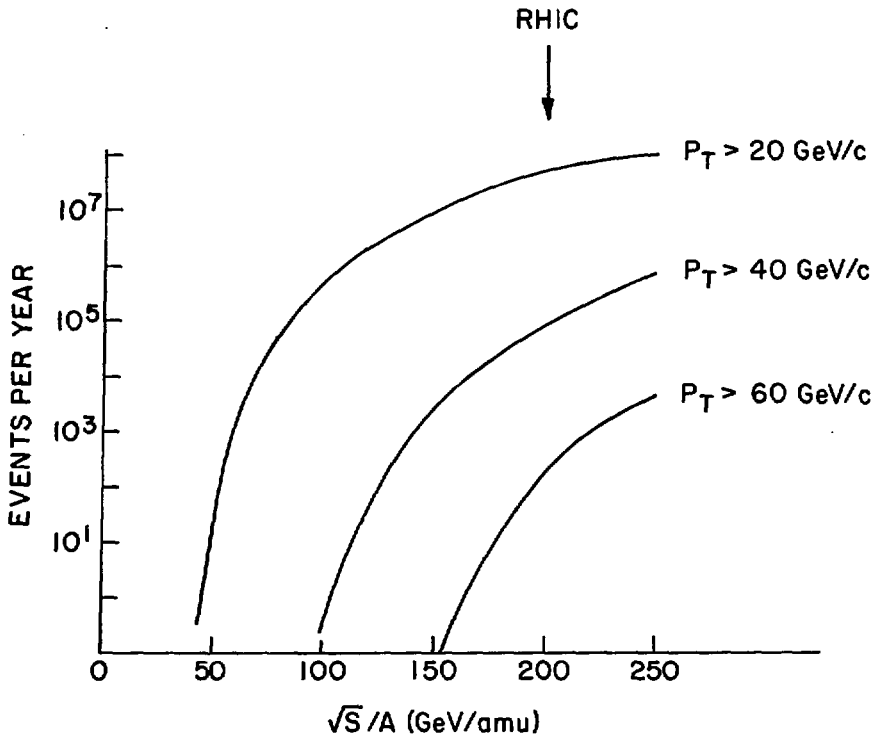

Fig. II.15 The estimated rates for observing jets at large transverse momentum, as a function of the collision energy. The calculation (ref. 18) is for gold ions at a luminosity $L = 10^{27}$ $cm^{-2}sec^{-1}$. The curves for three different threshold values of p_T are shown.

References

1. M. Jacob and H. Satz (eds.) Proc. of the Bielefeld Workshop, "Quark Matter Formation and Heavy Ion Collisions," World Scientific, Singapore, 1982.

2. I. Manelli (ed.) Proc. CERN Workshop of SPS Fixed-Target Physics in the years 1984-1989, CERN 83-02, 1983.

3. T. Ludlam and H. Wegner (eds.), Proc. of the Third International Conference on Ultra-Relativistic Nucleus-Nucleus Collisions, "Quark Matter '83," Nucl. Phys. A418 (1984).

4. L. Schroeder (ed.), Proc. of the LBL Workshop on Detectors for Relativistic Nuclear Collisions, Mar. 1984 (to be Pub.).

5. T. D. Lee in "Statistical Mechanics of Quarks and Hadrons," H. Satz (ed.), North Holland, Amsterdam, 1981.

6. E. V. Shuryak, Phys. Rev. 61, 71 (1980).

7. H. Satz, "New States of Matter," International Conference on Nucleus-Nucleus Collisions, Michigan State University, 1982; see also H. Satz, Ref. 3, p. 447.

8. J. Kogut, Ref. 3, p. 447; J. Polonzi, et al., "Finite Temperature Phase Transition in SU(3) Lattice Gauge Theory with Dynamical, Light Fermions," Univ. of Illinois, Preprint ILL-(TH)-84-22, May, 1984.

9. W. Busza, Ref. 3, p. 381.

10. K. Kajantie, Ref. 1, p. 39.

11. J. D. Bjorken, "Highly Relativistic Nucleus-Nucleus Collisions: The Central Region," Fermilab, Pub. 82-44-THY (1982).

12. W. V. Jones, Ref. 3, p. 139.

13. J.D. Bjorken and L. McLerran, Proc. of the International Workshop on Gross Properties of Nuclei and Nuclear Reaction XII, ed. by H. Feldmeier, Darmstadt, 1984.

14. O. Hagena and W. Obert, J. chem. Phys. 56, 1793 (1972).

15. Summary of the Discussion Group on Few-Particle Correlations, "Quark Matter 1983," Ref. 3, p. 416.

16. W.J. Willis, Ref. 3, P. 425.

17. J.D. Bjorken, Fermilab Pub. 82/59/59-THY (1982).

18. T. Ludlam, L. Madansky, F. Paige, "High Energy Probes of the Quark-Gluon Plasma," Ref. 4.

III. INJECTOR

III.1. The Tandem Van de Graaff

The acceleration of heavy ion beams will be started using two large existing Tandem Van de Graaff accelerators. The construction of a transfer line from the Tandem to the AGS, located in a 2000 ft. long tunnel, is being initiated and will allow these beams to be injected first into the AGS directly, and later into the Booster synchrotron.

A Tandem Van de Graaff accelerator is an attractive choice for injecting heavy ions into a synchrotron. Electrostatic acceleration of the initially very slow heavy ions to kinetic energies of 1 MeV/amu or higher is readily achieved, the ion source is conveniently located close to ground potential, and a wide variety of negative heavy ions is available. Other important advantages are related to the excellent beam quality and stability. The transverse emittance at the exit of the accelerator is better than 1π mm mrad and the energy stability is one part in 10^4.

The usual heavy ion DC beam intensities injected into Tandems are limited to a few μA which would not be sufficient for RHIC injection. The limitation arises mainly from the charging and voltage division systems of the accelerator; but also, until recently the available ion-source outputs were not much larger. The ion source limitation has recently been largely removed through the development by Roy Middleton (University of Pennsylvania) of a new type of sputter source which produces 200 μA of many negative ion species. A pulsed mode of operating this source has been developed at Brookhaven, showing that ten 300 μsec long pulses per second could be injected at maximum intensity without any adverse effects on the performance or stability of the accelerator. The inter-electrode and terminal-to-ground capacitances are large enough to maintain the

voltages essentially constant during the short beam bursts irrespective of charging or voltage distribution systems, as long as the average intensities are low. The duty factor was 3×10^{-3} during these tests and will be much smaller ($\sim 8 \times 10^{-5}$) during RHIC injection.

The Brookhaven Tandem Van de Graaff facility consists of two improved model MP accelerators. One of these machines has been upgraded to operate at a terminal voltage of about 16 MV and improvements which are under way will increase this value by another one or two MV. More importantly, the reliability at lower voltages, which at present is about 90%, will be improved even further. Using the other Tandem Van de Graaff as an alternate injector (see Fig. III.1) will provide an additional degree of operational reliability. This is especially desirable in view of the relatively long turn-around and conditioning times associated with accelerator repairs.

Table III.1. Tandem Operation Parameters

	Q_T	S_T %	Kinetic Energy MeV/amu	β_F	Q_F	S_F %	Current* part-μ-amp
Deuterium	+1	70	15.0	.1768	+1	100	525.**
Carbon	+5	39	7.5	.1262	+6	90	82.
Sulfur	+9	36	4.7	.1002	+14	40	20.
Copper	+11	27	2.9	.0782	+21	27	11.
Iodine	+13	20	1.65	.0595	+29	20	6.
Gold	+13	19	1.0	.0463	+33	17	5.

*75% transmission efficiency.
**Requires source development.

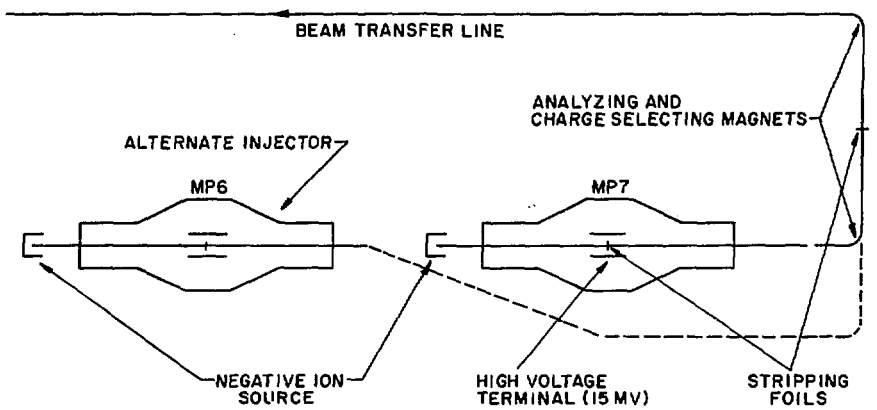

Figure III.1. Arrangement of the two model MP Tandem Van de Graaff accelerators, showing alternative heavy ion beams entering transfer line to the AGS and Booster.

Table III.1 shows the Tandem operation parameters for a high voltage terminal potential of 15 MV. S_T and Q_T are the stripping efficiency and most probable charge state after the negative ions have been accelerated to the high voltage terminal and stripped in a thin carbon foil. The ions leave the accelerator with an energy of 15 MeV x $(1+Q_T)$. A second stripping foil is located at a low beta region following the first 90° analyzing magnet (Fig. III.1) and the second 90° magnet selects the charge state Q_F to be transported to the synchrotron. S_F is the stripping efficiency of this target.

The second stripping target would be a 20 $\mu g/cm^2$ thick carbon foil for gold. The rms scattering angle for gold ions after traversing the foil is expected to be about 1.9 mrad. This will produce an emittance growth of about 1π mm•mrad and the total value should then not exceed 2π mm•mrad for any of the species taken into consideration. Fig. III.2 is a functional diagram of the Tandem area.

In traversing the stripping target there is also an energy loss. The largest loss, again for gold, is about 9.0 keV/amu. An energy spread is also introduced with an rms value typically one-tenth of the energy loss. Although the energy loss is not significant, the spread in energy is rather important. For gold it amounts to a momentum spread (at injection into the Booster) $\Delta p/p = \pm 0.05\%$. The longitudinal area for this debunched beam coasting into the Booster is then 0.065 eV•sec/amu. For lighter ions these values are smaller.

The details of the transfer line between the Tandem and the Booster (through the AGS) are given in Fig. III.3.

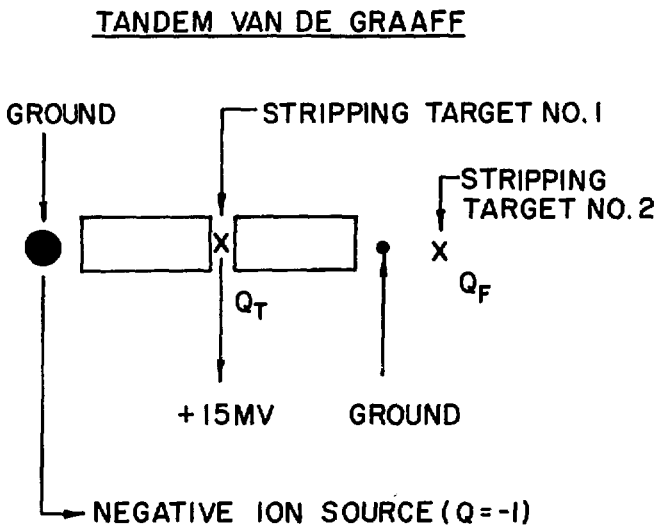

FINAL KINETIC ENERGY (TWO-STAGE MODE)
$= 15\text{MeV} + Q_T \cdot 15\text{MeV}$

Figure III.2. Tandem Van de Graaff with stripping targets.

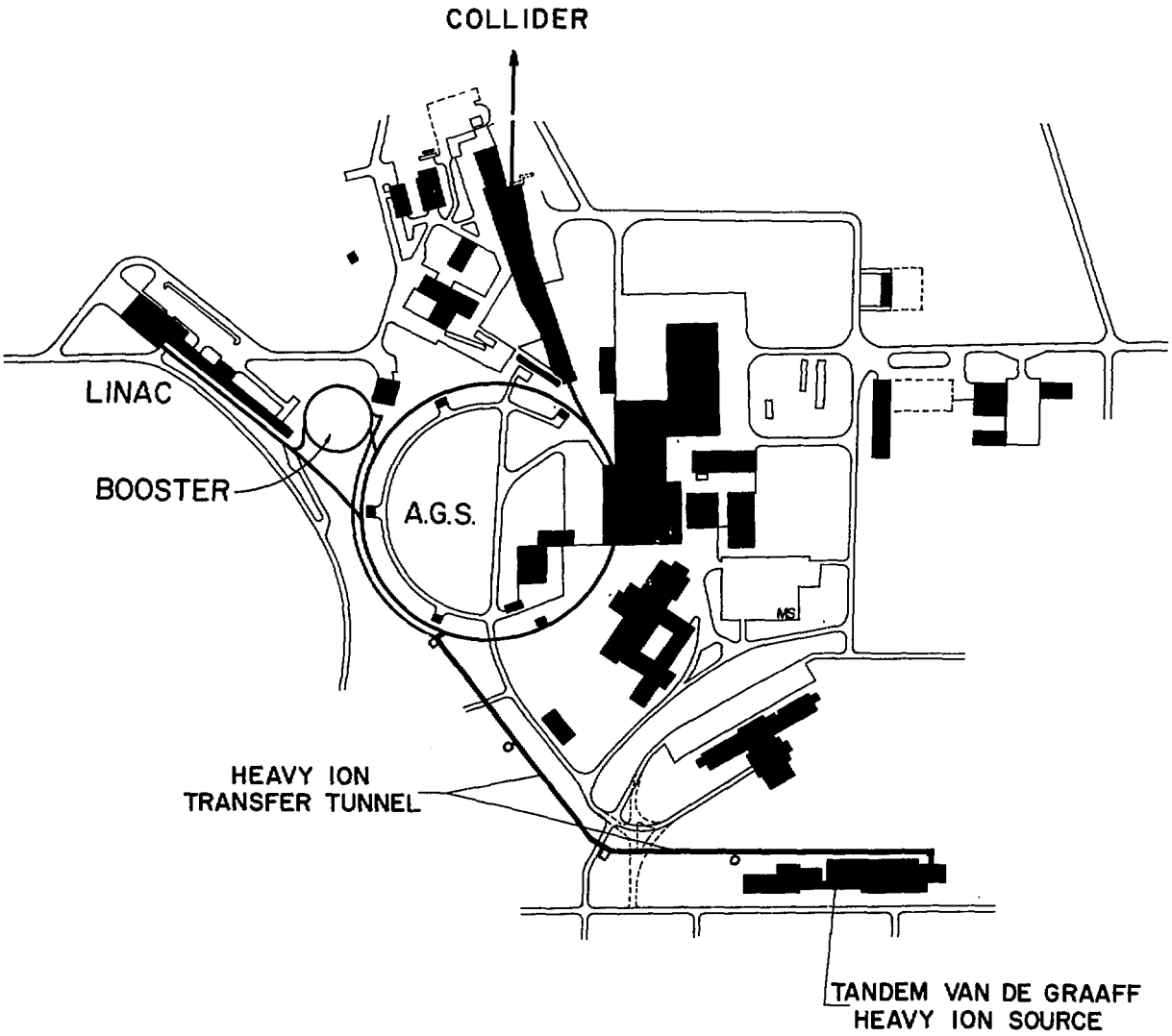

Figure III.3. Injection system for Collider.

III.2. The Booster

The circumference of this ring is one quarter of the AGS circumference. The most important parameters are listed in Table III.2. A plan view of the ring is given in Fig. III.4. A plot of the lattice functions is shown in Fig. III.5.

We assume that the betatron acceptance is 50 πmm·mrad in both planes. It could be larger in the horizontal plane, but very likely the extra amount is not useful because of possible linear and non linear coupling between the two modes of oscillations which cannot be avoided.

Table III.2. Booster Ring Parameters

Circumference		201.75 m
Periodicity		12
Period Structure:	QF/2 O B O QD/2 QD/2 O B O QF/2 QF/2 S QD/2 QD/2 O B O QF/2	
Drifts:	O	0.65 m
	S	3.7 m
Phase Advance/Cell		100.5°
Betatron Tunes, H and V		ν6.7
Transition Energy, γ_T		6.5
β_{max}/β_{min}		16m/2m
η_{max}		1.7 m
Dipole (B):	Length	2.4 m
	Max. Field	12 kG
	Bending Radius	13.89 m
	Aperture, HxV (full)	3.25 x 10 in^2
Quads (QF/2,QD/2):	Half-Length	0.25 m
	Bore Radius	4 in.
	Max. Pole Tip Field	12.7 kG

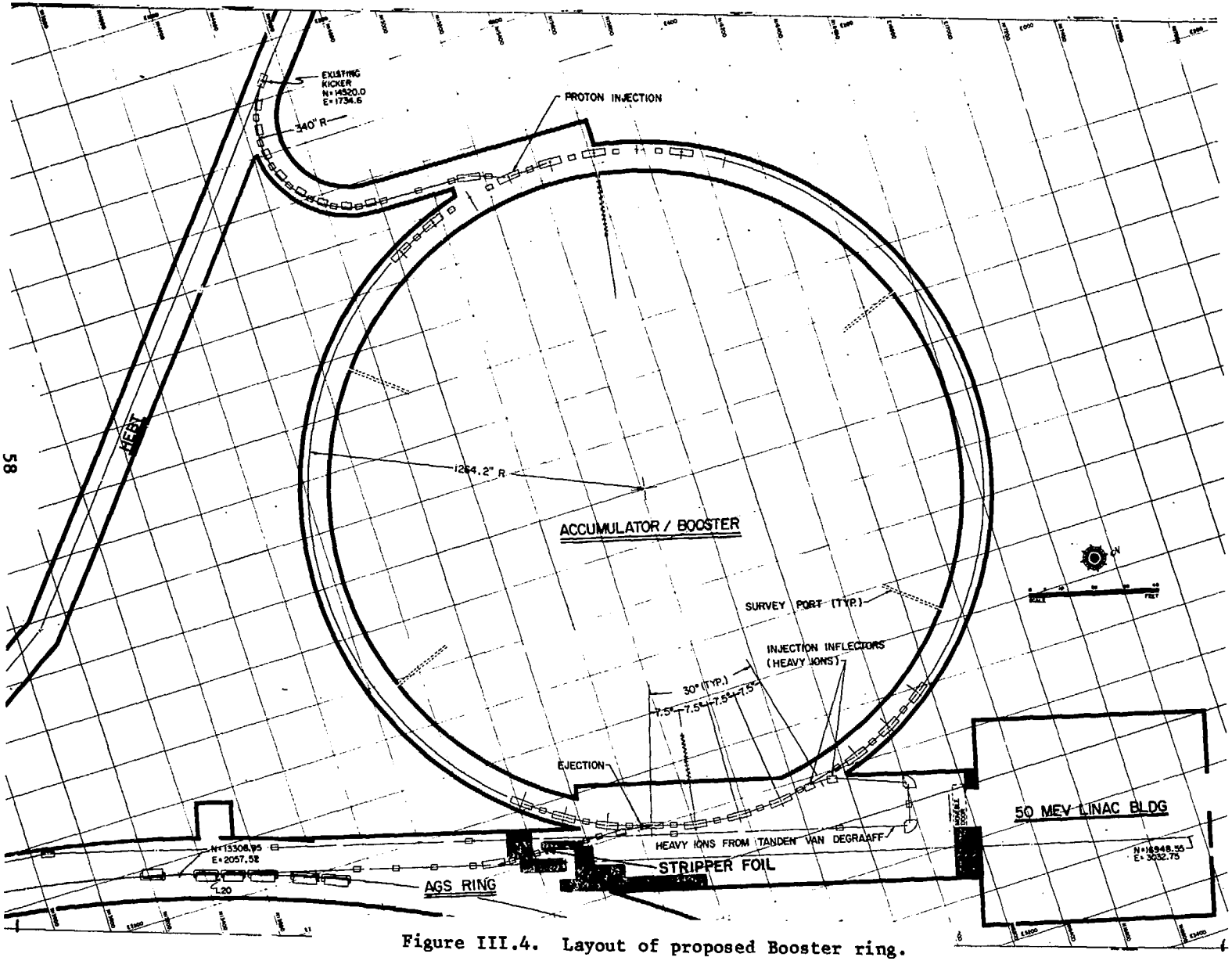

Figure III.4. Layout of proposed Booster ring.

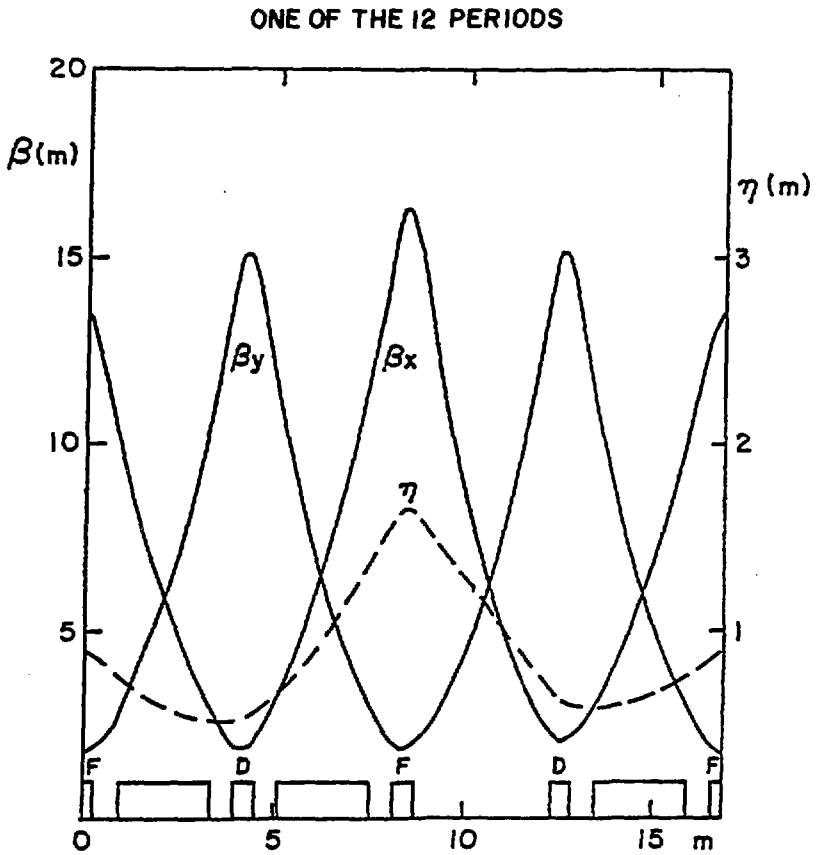

Figure III.5. Lattice functions for Booster.

The beam is injected into the Booster and stacked in the horizontal betatron phase space by filling the machine circumference with the beam pulse for some number, n, of consecutive turns which corresponds to a total number of particles N_B. It is assumed that the beam will quickly fill up the available acceptance in both planes, with the help eventually of other available steering means, until the space charge limit is reached. This corresponds to a maximum number N_{SC} of particles that can be injected according to the formula

$$\frac{N_{SC}}{\varepsilon_N} = (\beta\gamma^2)\,\frac{4\pi B_f \Delta\nu}{3 r_o F}\,\frac{A}{Q_F^2}\,.$$

B_f is the bunching factor, defined as the ratio of the average current to the peak current, $\Delta\nu$ is the maximum allowable tune shift, A the mass number, Q_F the charge state, $r_o = 1.535\times10^{-18}$ m, and F a form factor that for $\beta \ll 1$ is very close to 1. On the left-hand side of the equation, ε_N is the normalized emittance; the actual emittance is given by

$$\varepsilon = \varepsilon_N/(\beta\gamma).$$

Here the emittances are as usual given in πmm·mrad units. It is important that the phase space density, N_B/ε_N, is as large as possible since the luminosity in the collider depends on this quantity, provided that no other effect causes even a stronger limitation than the space charge at injection. The luminosity also depends upon N_B itself. It is therefore essential to get the largest density, N_B/ε_N, and the largest number, N_B, of particles in the Booster. An important side effect is that, by increasing N_B, one also increases the number of particles that can be transferred to the Collider per AGS pulse and this reduces the Collider filling time.

There is some uncertainty in the value to assign to B_f and $\Delta\nu$. We propose here a bunching factor of 0.5 and $\Delta\nu = 0.1$. The bunching factor of 0.5 corresponds to the rf capture process at injection and to the early stage of acceleration in the Booster. As the beam velocity increases during acceleration the bunching factor can be lowered correspondingly.

The different species are injected into the Booster with no further stripping; that is, with the charge state Q_F as shown in Table III.1. Table III.3 gives the maximum number N_{SC} of particles that can be injected with the corresponding normalized emittance ε_N. In Table III.3, we also give the revolution period T_{rev} and the number N_B of particles with n=8 turns injected, assuming the beam current values given in Table III.1. The largest number of turns that can be efficiently injected in one plane is taken here to be equivalent to 8, and this corresponds to a dilution factor as large as 6.25. By inspecting Table III.3 one can see that the beam intensity is limited by the Tandem currents for the lighter ions up to copper. For copper the Tandem current output is about the space charge limit at injection into the Booster. For iodine and gold very clearly there is a space charge limitation by a factor as large as 2. The particle numbers in the dashed squares are those proposed for the estimates in our scheme. For gold only 4 or 5 turns are required to be injected.

The beam is captured at injection by a rf system of harmonic number h = 1, so that only one bunch is used and all the particles given in Table III.3 are in this bunch. Adiabatic capture of the gold beam of momentum spread $\Delta p/p = 0.11\%$ will take a few tens of milli-seconds. We intend to turn on a rf voltage of order 0.5 kV. This will produce the bucket area of $\sqrt{}0.2$ eV·sec/amu in 6 milli-seconds. To avoid further dilution this bucket area is preserved as much

Table III.3. Beam Intensity, Emittance of Injection into the Booster

Element	ε_N π mm·mrad	T_r μsec	N * $\times 10^9$	N ** $\times 10^9$
Deuterium	8.8	3.81	100.0	438.0
Carbon	6.3	5.33	22.0	37.0
Sulphur	6.0	6.72	6.7	11.0
Copper	3.9	8.60	4.7	5.5
Iodine	3.0	11.31	3.4	3.2
Gold	2.3	14.53	3.6	2.2

*With 8-turn injection

**at $\Delta\nu = .1$

as possible during the early stage of the acceleration cycle. The acceleration period is taken to be 0.6 sec for gold and the overall repetition rate 0.8 Hz. In the middle of the cycle a maximum voltage of 30 kV is required. Toward the end of the acceleration, the bunch is made short enough to match the length of the rf buckets in the AGS. The expected rms bunch length at ejection is as small as 20 nsec.

At a top field of 12 kG, we have a maximum kinetic energy of 320 MeV/amu for gold which corresponds to $\beta\gamma = 0.893$. To minimize the amount of rf frequency swing it is sufficient to accelerate the lighter ions to the same value which corresponds to the full acceleration for gold. In this case the required frequency swing covers the range of β-values from 0.046 to 0.7 which corresponds to 60 $\sim$840 kHz. Observe that the ion beam will never have to cross the Booster transition energy during its acceleration.

A vacuum of 10^{-10} mmHg seems to be quite adequate for the survival of practically all the beam against electron capture or loss processes during the acceleration cycle. The beam losses would be about 2%.

After extraction from the Booster and on their way to the AGS the ions pass through one more stripping target. The ions injected into the AGS are then completely stripped. We expect a 50% beam loss for gold, 20% for iodine and 5% for copper and sulfur. Carbon and deuterium do not need further stripping.

The last stripping is accomplished with a foil of copper that, for gold, is 70 mg/cm^2 thick. The rms scattering angle associated with this target is 0.7 mrad for gold. If one does not allow more than 1 πmm·mrad increases in emittance, the stripper foil must be installed in a location where the lattice β function does not exceed 2 meters in both planes. We accomplish this condition using two pairs of quadrupole doublets.

The energy loss associated with this target is 5 MeV/amu and the resulting energy spread (rms) is 0.5 MeV/amu. To minimize the increase of the bunch longitudinal area, it is important that the beam is as tightly bunched as possible when crossing the target. For instance, provided that the beam has preserved its original bunch area of 0.2 eV·sec/amu, an rms bunch length of 20 nsec would give an energy spread in the beam also of 0.5 MeV/amu (rms); which is comparable to the spread introduced by hitting the target. It seems that an appreciable increase in the bunch area cannot be avoided.

III.3. The AGS

The major parameters of the ring are given in Table III.4. Since the injection energy is 367 MeV/amu and the ions are completely stripped, there is no requirement for improvement in either the vacuum or the rf system. The accelerator, as it is, is well suited for the acceleration of the ions to the maximum energy. With the present vacuum of 10^{-7} Torr the beam losses, mostly due to the electron capture process, would be less than 3%.

The scenario that we propose is the transfer of one bunch at a time from the Booster to the AGS; acceleration to the top energy and then transfer to the Collider. The AGS cycle rate is taken to be 0.8 Hz. The transfer line between the booster and the AGS is shown in Fig. III.4.

Table III.4. AGS Parameters

Circumference	807.11 m
Periodicity	12
Betatron Tunes, H and V	$\sim$8.7
Transition Energy, γ_T	8.5
Betatron Acceptance	$\sim$30 πmm·mrad
Injection Energy (proton)	200 MeV
Ejection Energy (proton, γ = 31.4)	28.5 GeV
RF Frequency	2.5-4.457 MHz
Harmonic Number, h	12
Peak RF Voltage	300 kV
Magnetic Rigidity, Bρ at extraction	96.5 kG·m

Taking into account the increase in the beam emittance due to the final stripping, and with $\beta\gamma = 0.893$, at transfer, the emittance values given in Table III.3 are just about those the beam would have when injected into the AGS. These emittances are considerably smaller than the ring betatron acceptance.

There is some uncertainty in the value to assign to the beam longitudinal emittance. The values which correspond to injection into the Booster are small, but we expect some dilution during the capture process and the acceleration cycle. A realistic estimate is 0.3 eV•sec/amu, including the energy spread from the last stripping target, and we use this figure as input to the design of the Collider. On the other hand, the rf buckets in the AGS are the smallest at injection. If we assume a constant voltage of 300 kV, the bucket area is not less than 1.0 eV•sec/amu. At the end of the acceleration in the AGS, the ion bunch is tailored so that it will fit within one of the rf buckets in the Collider. For this purpose we take a final total bunch length of 17 nanosec.

IV. THE COLLIDER

IV.1. General Parameters

The availability of the CBA tunnel and experimental buildings for the collider represents a unique opportunity to construct the new machine at minimal cost. The constraints imposed by existing structures are minimal and in no way limit the performance potential of the collider.

The collider design relies on the existing Tandem Van de Graaff, a proposed Booster synchrotron and the AGS, as discused above. The two transfer lines connecting the AGS to the two magnetic rings are part of the Collider system. Their design is the same as in the latest CBA/ISABELLE proposal. Major parameters of the Collider Rings are given in Table IV.1.

Each ion bunch accelerated in the AGS is extracted and transferred to one of the two Collider Rings. The bunch is captured by a stationary rf bucket. It is essential that the shape of the bunch prior to extraction from the AGS is tailored to match the shape of the buckets in the Collider.

Beam parameters at injection are given in Table IV.2. It is assumed that, because of the required manipulations, the betatron emittances and the longitudinal phase space area are somewhat diluted to the final values shown in Table IV.2. The beam parameters are taken to be the same for all species, except protons, which have a larger emittance since they come from a different source. The number of protons could be increased by an order of magnitude, provided that certain improvements in the rf system and beam dump are introduced. The design number of 10^{11} protons/bunch seems adequate for heavy ion physics. The bunch area, S, is defined for 95% of the beam population by

$$S = 6\pi \sigma_T \sigma_E ,$$

Table IV.1. General Parameters for the Collider

Circumference	3833.8 m
Revolution Frequency ($\beta = 1$)	78.1972 kHZ
Filling Mode	Box-Car
No. of Bunches/Ring	57
Filling Time/Ring	$\sim$ 1 min
Perodicity	6
Magnetic Rigidity, $B\rho$:	
at injection	9.65 T•m
at top energy	839.5 T•m
Transition Energy, γ_T	26.4
Betatron Tunes, $\nu_{H,V}$	34.4
rf Harmonic Number	342
rf Voltage	1.2 MV
Acceleration Time	1 min

where σ_τ is the rms bunch length in unit of time and σ_E the rms energy spread. Correspondingly, the normalized emittance, $\epsilon_N = \beta\gamma E$, is defined by

$$\epsilon_N = 6\pi \frac{\sigma^2_{H,V}}{\beta\gamma\beta_{H,V}},$$

where $\sigma_{H,V}$ is the rms beam width or height and $\beta_{H,V}$ the horizontal or vertical amplitude lattice functions. The bunch dimensions are for 95% of the beam. The bunch length given is the smallest one can obtain from the AGS with the present unmodified rf system.

Table IV.2. General Beam Parameters for the Collider

Element	Proton	Deuterium	Carbon	Sulfur	Copper	Iodine	Gold
Atomic No, Z	1	1	6	16	29	53	79
Mass No, A	1	2	12	32	63	127	197
Rest Energy (GeV/amu)	0.9383	0.9375	0.9310	0.9302	0.9299	0.9302	0.9308
Injection:							
Kinetic Energy, (GeV/amu)	28.5	13.6	13.6	13.6	12.4	11.2	10.7
β	.99947	.99947	.99793	.99794	.99757	.99704	.99680
Norm. Emitt., ϵ_N (πmm•mrad)	20	10	10	10	10	10	10
Bunch Area, S (eV•sec/amu)	0.3	0.3	0.3	0.3	0.3	0.3	0.3
Bunch Length (nsec)	$\pm$ 8.6	$\pm$ 8.6	$\pm$ 8.6	$\pm$ 8.6	$\pm$ 8.6	$\pm$ 8.6	$\pm$ 8.6
Energy Spread, 10^{-4}	$\pm$ 3.8	$\pm$ 7.6	$\pm$ 7.6	$\pm$ 7.6	$\pm$ 8.3	$\pm$ 9.2	$\pm$ 9.6
No. ions/Bunch, x10^9	100	100	22	6.4	4.5	2.6	1.1
Top Energy:							
Kinetic Energy, (GeV/amu)	250.7	124.9	124.9	124.9	114.9	104.1	100.0
$\beta\gamma$	268.2	134.2	135.2	135.3	124.6	112.9	108.4

The number of ions per bunch transferred to the Colldier is also given in Table IV.2. It was derived after adjusting for the losses between the Booster and the AGS. Assuming a maximum rigidity of 839.5 T*m we give, also in Table IV.2, the maximum kinetic energy that can be reached in the Collider rings.

The two rings are filled in box-car fashion. The total number of bunches accepted is 57 per ring; an equivalent number of AGS pulses is required which gives a filling time of a little more than one minute per ring. The situation is different for the proton beam since 12 bunches can be accelerated simultaneously in the AGS; thus only five AGS pulses would be required and the filling time is less than ten seconds.

The choice of 57 bunches is a direct consequence of the fact that the Collider circumference is 4-3/4 times the AGS circumference and that there are 12 bunches (at least for protons), equally spaced, transferred from the AGS to the Collider. In the box-car filling mode the transfer is bunch-to-bucket and therefore the rf frequency must have an harmonic number equal to an integer times 57. The largest integer is 12 since it corresponds to a bucket length which is just about the length of the injected bunches. The harmonic chosen, h = 57 x 6, together with the peak voltage of 1.2 MV provide adequate bucket length and are well matched to the AGS parameters.

The bunch separation is 67 meters and this corresponds to a rise/fall time of 200 nsec for the injection kickers.

IV.2. Lattice

The collider is composed of two identical non-circular concentric rings in a common horizontal plane, oriented to intersect with one another in six crossing points. Its design is reminiscent of various designs for CBA but deviates from them in several respects. Attempting to minimize the overall cost by balancing the cost of aperture with that of focusing strength (numbers and strengths of quadrupoles and dipoles), and taking account of the requirements of intra-beam scattering, we reduced the dispersion from X_p = 2.75 m to 1.38 m and the amplitude function from $\beta_{H,V}$ = 67.5 m to 51.7 m by increasing the number of cells per arc from 9 to 12 and by increasing the betatron phase advance per cell from 90° to 98°. This change had major consequences for the insertion designs, particularly for their dispersion suppressors.

It proved impractical to place the transition energy outside the operating range from 10 - 100 GeV/amu, so that the heavy ion beams will have to pass through it during acceleration. Stored beam operation near the transition energy is not possible; this leaves a gap in the operating range which can, in principle, be bridged by retuning the machine to a transition energy outside the desired operating interval for experiments which require specific beam energies very close to the nominal one.

The longitudinal and transverse emittances are larger than they were in CBA. The momentum spread is large in the vicinity of transition and requires a large momentum acceptance. The net result is that the circulating beams occupy a large fraction of the vacuum-pipe cross section, leaving less space for dumping the beam, for example.

A general lattice layout is given in Fig. IV.1. Each ring consists of a sequence of inner and outer arcs, connected by more or less straight

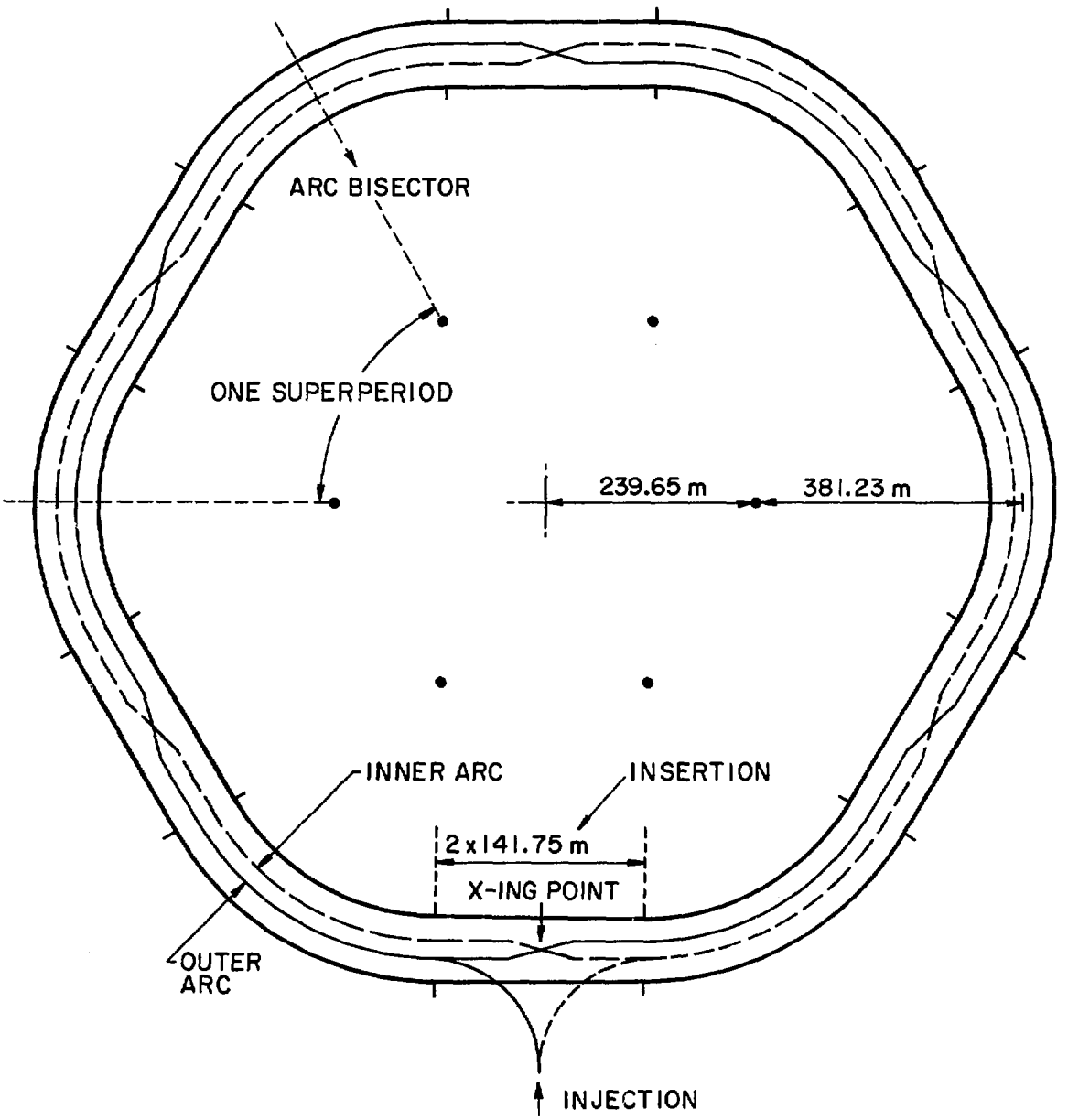

Figure IV.1. Layout of the Collider.

insertions. The ring structure conforms closely to the geometry of the existing tunnel. In the simplest configuration there is reflection symmetry with respect to each crossing point and with respect to each arc bisector. There are then six superperiods, with the half-sextant, consisting of a half-arc and a half-insertion, as the fundamental half period. This superperiodicity is slightly perturbed as a consequence of the fact that outer and inner sextants cannot be perfectly identical because of obvious geometrical constraints. This effect is quite small, since the ring-ring separation (0.30 m) is only a small fraction (8×10^{-4}) of the average radius (381.2332 m). The superperiodicity will be reduced further if the insertions are not all identical, e.g. in order to provide different crossing point conditions (crossing angles, beta values) or to facilitate certain machine functions, such as beam dumping. Probably the collider will initially be operated in its simplest configuration, i.e., one with the highest possible superperiodicity.

i. Arcs

The inner and outer arcs are constructed with the same magnet types and are identical, except for the small difference in average radii, obtained from small adjustments in the drift space lengths. The inner and outer arcs of a pair and the centerline of the tunnel which houses them are concentric. Homologous elements are located on common radii so that they can be housed in common vacuum vessels. There are twelve identical cells in each arc, each with two quadrupoles and two dipoles. The cell configuration and focussing parameters are shown in Figs. IV.2 and IV.3, and the principal characteristics are tabulated in Table IV.3.

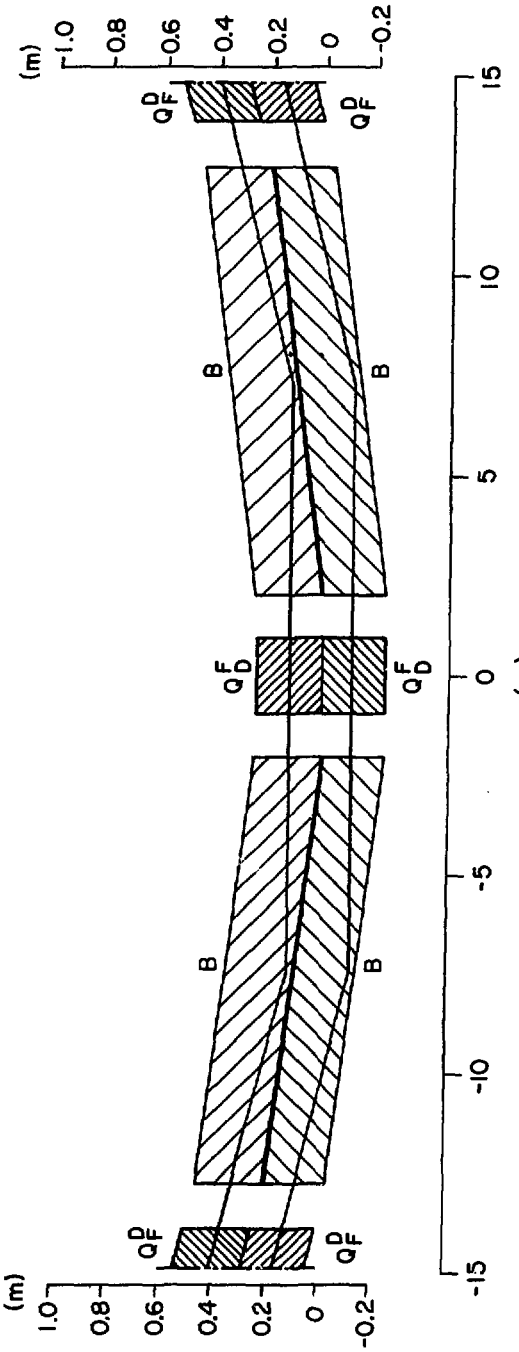

Figure IV.2. RHIC regular cell pair.

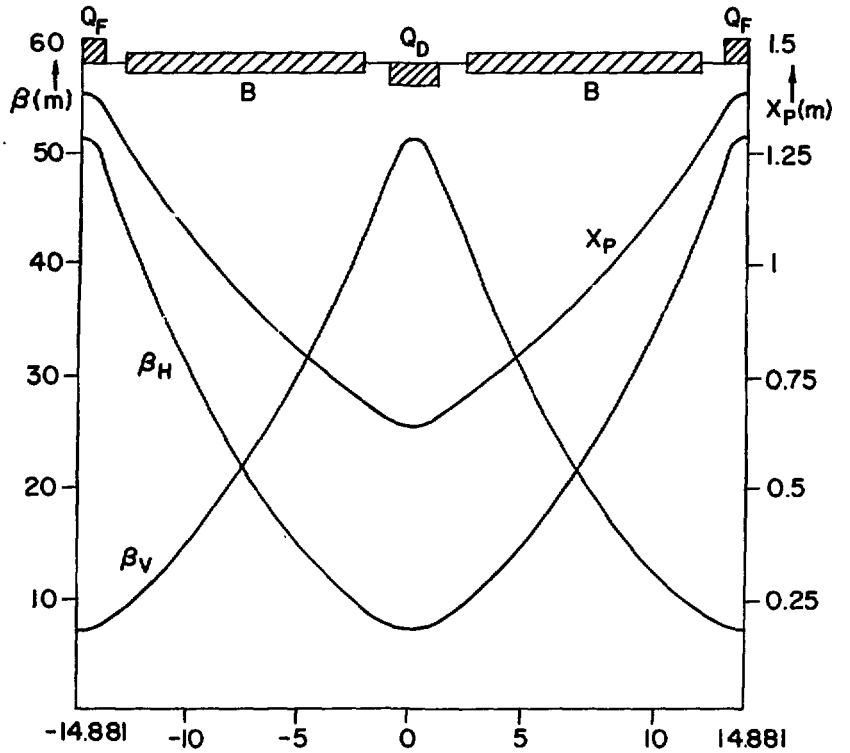

Figure IV.3. RHIC regular arc cell.

Table IV.3. Principal Characteristics of Arc Cells

	Inner Arc	Outer Arc
Length (m)	29.6104	29.6338
Deflection Angle (mrad)	77.7007	
Average Radius of Curvature (m)	381.0831	381.3832
Distance between Centerlines (m)	0.3	
Dipole Strength $\int Bd\ell/B\rho$*	0.038855	
Quadrupole Strength* $\int B'd\ell/B\rho$, (m^{-1}) F/D	0.10686 / -0.10671	
Betatron Phase Advance $\Delta\psi_H/2\pi$, $\Delta\psi_V/2\pi$	0.2730 / 0.2730	0.2730 / 0.2730
$\hat{\beta}_H$ / $\hat{\beta}_H$ in quadrupole midplanes (m)	51.644 / 7.411	51.718 / 7.400
$\hat{\beta}_V$ / $\hat{\beta}_V$ in quadrupole midplanes (m)	51.642 / 7.411	51.719 / 7.400
$\hat{X}_p$ / $\hat{X}_p$ in quadrupole midplanes (m)	1.379 / 0.635	1.379 / 0.635

*Magnet parameters are discussed in Section IV.4.

ii. Insertions

The insertions serve two functions: they transport the beams from arc to arc, and they control the focusing parameters at the crossing points. They should provide some measure of flexibility in the choice of these parameters (crossing angle, β_H^*, β_V^*) so that each insertion may be optimized for a particular experiment or machine function; however, adjustments in one insertion should not affect the others, nor the overall operation of the ring. This is achieved by requiring that each insertion have the same beam transfer matrix between its interfaces with the adjoining arcs, regardless of its internal configuration. It is also desirable to be able to change the betatron tunes in a simple manner, e.g., by adjustment of the phase-advances of the arc cells, without serious repercussions for the machine behavior or crossing point conditions. This is achieved by making each insertion transparent to the beam, i.e., designing it so that arbitrary beam parameters are identical in the entrance and exit faces. This means that the transfer matrix must be diagonal with element values close to one and with betatron phase advances of $\Delta\psi_{H,V} = 2\pi n_{H,V}$ radians. The crossing point conditions are made relatively insensitive to tune variations by choosing the transfer matrix from the crossing point to the entrance and exit planes of the insertion to be diagonal.

Each insertion may be subdivided into an inner and an outer half insertion which are joined at the crossing point. There is near perfect reflection symmetry relative to the crossing point in component location and component strength, with one exception. The small deviations ($\sim 10^{-4}$) stem from the differences in drift space lengths imposed by geometrical constraints. It follows that homologous elements in an inner half insertion of one ring and in the associated outer half insertion of the other may be paired in common vacuum

vessels, as in the arcs. This arrangement, as shown in Fig. IV.4, requires that the inter-beam spacings in the insertions and in the arcs be identical. Differences in these spacings as required by the window frame magnet (Appendix 4) can be accommodated. However, this results in loss of the symmetry between inner and outer half insertions and its attending advantages in physical layout and focusing properties.

Each half insertion is composed of three regions with distinct functions. The first region begins at the crossing point and terminates in quadrupole Q1. The dipoles BC1 and BC2 are used to define the crossing angle α; quadrupole QC reduces the dispersion to zero, which is caused by BC1 and BC2 in Q1 and beyond. Fig. IV.5a shows a layout, with the magnets set for a crossing angle $\alpha = 2$ mrad and with the profiles for gold beams after two hours at $\gamma = 12$ sketched in. Both BC1 magnets have equal strengths and opposite polarities. The same is true for both BC2 magnets. It is this polarity reversal in the QC pairs and in the Q1 pairs that represents the exception to the reflection symmetry mentioned before. It may be seen that BC1, which acts as a separating magnet, is common to both the clockwise and the counter clockwise rotating beams. This makes collinear beam operation (head on collisions) possible, as shown in Fig. IV.5.b. The BC1's are the only magnets which are common to both rings. If the two beams have different magnetic rigidities, i.e., different $B\rho$ values, they will be differently deflected in the BC1's. Operation remains possible, although the machine centerline through the crossing point is rotated, as shown in Figs. IV.5c and d, drawn for $\alpha = 2$ mrad and $\alpha = 0$ respectively and for $(B\rho)_{beam2}/(B\rho)_{beam1} = 2.5$.

The luminosity and the crossing point conditions (β^* values, crossing angle, and $B\rho$ ratio) are interrelated and limited by the magnet apertures, the

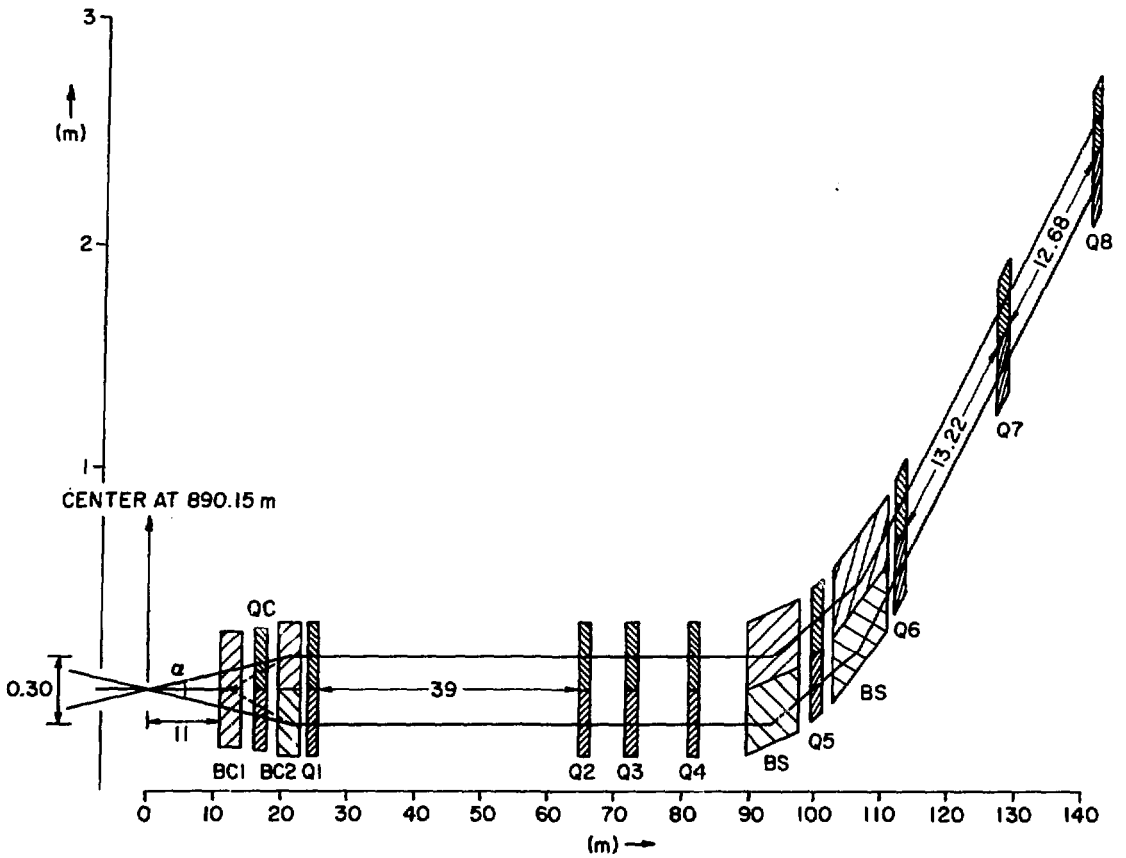

Figure IV.4. RHIC half inserion.

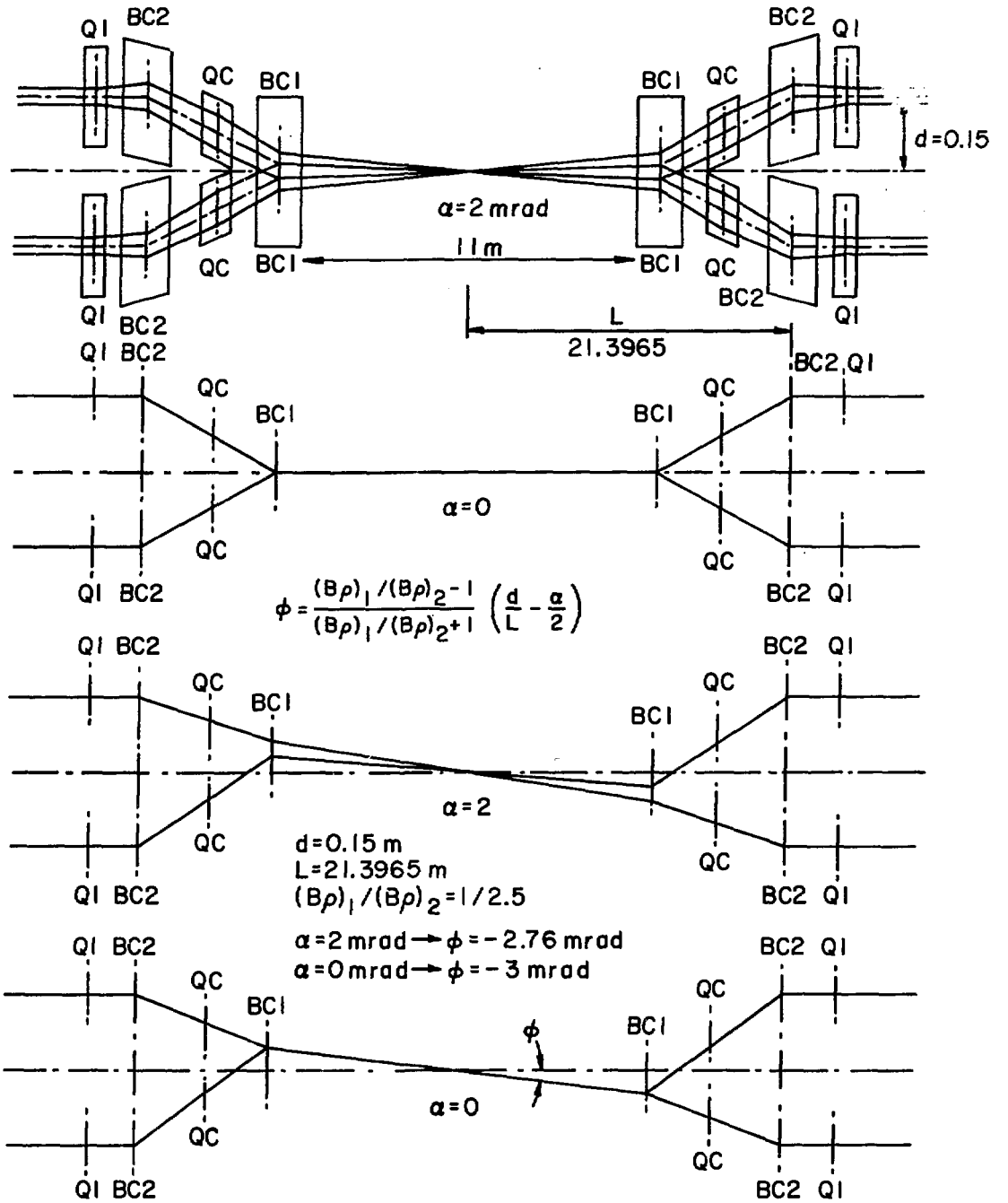

Figure IV.5a-d

beam energy, and the tunability of the insertion. Many of the values quoted in this proposal are calculated for a crossing angle of 2 mrad and a Bρ ratio of 1. Analytic work shows that for fixed β_H^* and β_V^* the maximum values of the amplitude function $\hat{\beta}_H$ and $\hat{\beta}_V$ (the former occurring in QC, the latter in Q1) decrease, yet the aperture available in QC is decreased for zero angle beam crossing. Also $\hat{\beta}_V$, for fixed (α, β_H^*, β_V^*), is minimized by packing BC1, QC, BC2, Q1 as densely as practical and by giving them the highest practical fields and field gradients. Changes in α and/or Bρ ratio require changes in the strengths of BC1, BC2 and QC and consequently retuning of the affected insertion. Since the optimum configuration is a function of energy it may be necessary to retune while the beams are circulating.

The second region incorporates quadrupoles Q1 - Q4 and is free of dispersion. Its quadrupoles are used for controlling the values of β_H^* and β_V^* while preserving the transfer matrix across the insertion.

The last region, which consists of BS, Q5, BS, Q6, Q7, and Q8, is the main dispersion suppressor which reduces the dispersion at the interface with the adjoining arc to zero in the betatron matching middle region. Its design deviates markedly from those made for CBA because the dispersion in the interface with the arc has been reduced from X_p = 2.75 m to 1.38 m, while the tunnel geometry remains unchanged. Another constraint is that adequate space must be reserved for injection equipment.

The basic insertion is defined to range between the midplanes of its terminating quadrupoles QF/Q8, Q8/QF. It proved necessary to redefine it to include one cell of the adjoining arc on each side in order to obtain the diagonal transfer matrix. The only practical implication of this redefinition is that

the number of tunable cells per arc is reduced from 12 to 10. There is no change at all at the nominal betatron frequency.

We tabulate the main insertion characteristics in Tables IV.4 and IV.5 and show the behaviour of the focusing functions in Fig. IV.6, for a crossing angle of 2 mrad. For head-on collisions (α = 0 mrad), the behaviour is similar, but the insertion quadrupoles have to be readjusted in strength and location.

iii. Chromatic Effects

If the insertions are all identical and set up for β_H^* = 0.88 m and β_V^* = 6.3 m, the natural chromaticities (χ = p dν/dp) are: χ_H = -73.5 and χ_V = -63.75; more than half of which is due to the insertions and most of that to the strong quadrupoles QC and Q1 in which β_H and β_V are large ($\hat{\beta} \gtrsim 300$ m). These large negative values of the chromaticities must be reduced to small positive values, e.g. $\chi \lesssim 1$-2 for proper machine operation. This can be done by having sextupoles, in or very near to each quadrupole in which there is significant dispersion. The sextupoles in the arcs are interconnected to form two families and provide adequate means for independent global control of χ_H and χ_V. However, this simple scheme leads to chromaticities which, though correct at the reference momentum, vary with the momentum deviations relative to the reference value and to modulation of the dispersion and amplitude functions in the arcs as a function of the azimuthal position. If the chromaticities are chosen large enough to prevent them from becoming negative inside the required momentum acceptance ($|\Delta p/p| \leq 1.1\%$ at transition) the spread in the betatron tunes in that interval become uncomfortably large; the modulations in χ_p and β tend to increase the aperture requirements. These effects are well known in electron rings and also occurred in the CBA designs. The problem in RHIC is more severe because of much stronger focusing in the insertions as well as in the arcs. They may be

Table IV.4. Principal Characteristics of Insertions (α = 2 mrad)

		Inner Arc	Outer Arc
Quadrupole Q8 F	$\int B'd\ell/B\rho$ (1/m)	0.094657	0.094646
Distance Q8-Q7 (m)		14.0826	14.0826
Quadrupole Q7 D	$\int B'd\ell/B\rho$ (1/m)	0.13066	0.13070
Distance Q7-Q6 (m)		15.0384	15.0384
Quadrupole Q6 F	$\int B'd\ell/B\rho$ (1/m)	0.10991	0.10989
Distance Q6-BS (m)		5.8765	5.88085
Dipole BS	$\int Bd\ell/B\rho$	0.28697	0.028697
Distance BS-Q5 (m)		6.4976	6.5019
Quadrupole Q5 D	$\int B'd\ell/B\rho$ (1/m)	0.11358	0.11353
Distance Q5-BS (m)		6.4976	6.5019
Dipole BS	$\int Bd\ell/B\rho$	0.028697	0.28607
Distance BS-Q4 (m)		11.9893	11.9936
Quadrupole Q4 F	$\int B'd\ell/B\rho$ (1/m)	0.098741	0.098754
Distance Q4-Q3 (m)		9.2437	9.2437
Quadrupole Q3 D	$\int B'd\ell/B\rho$ (1/m)	0.14232	0.14223
Distance Q3-Q2 (m)		6.9591	6.9591
Quadrupole Q2 F	$\int B'd\ell/B\rho$ (1/m)	0.10686	0.10676
Distance Q2-Q1 (m)		40.8208	40.8208
Quadrupole Q1 D	$\int B'd\ell/B\rho$ (1/m)	0.10121	0.10120
Distance Q1-BC2 (m)		3.3652	3.3652
Dipole BC2	$\int Bd\ell/B\rho$	-0.015493	0.015493
Distance BC2-QC (m)		4.4893	4.4893
Quadrupole QC F	$\int B'd\ell/B\rho$ (1/m)	0.1334	0.1334
Distance QC-BC1 (m)		4.3858	4.3858
Dipole BC1	$\int Bd\ell/B\rho$	0.014493	-0.014493
Distance BC1-Crossing Point (m)		12.5	12.5
Distance Q8-Crossing Point (m)		141.7459	141.7631
Free Space Crossing Point-BC2 (m)		10.	10.
Crossing Angle α (mrad)		2.0	
β_H^*/β_V^* (m)		0.8859 / 6.3122	
x_p^* (m)		0.	
α^*		0.	
$\hat{\beta}_H$ in QC (m)		302.61	
$\hat{\beta}_V$ in Q1 (m)		313.75	
$\Delta\psi_H/2\pi$ / $\Delta\psi_V/2\pi$		2.4556 / 2.4556	

Table IV.5. Lengths of Magnets and Driftspaces in the Insertions, (m). (α = 2 mrad, B = 3.5T, B' = 76 T/m at Bρ = 839.632 Tm)

LQ8	1.048
D78	12.838
LQ7	1.4435
D67	13.709
LQ6	1.2143
D562	1.8273 / 1.8316
LBS	6.8843
D561	2.4281 / 2.4323
LQ5	1.2548
D452	2.4281 / 2.4323
LBS	6.8843
D451	8.0017 / 8.0060
LQ4	1.0909
D34	7.9121
LQ3	1.5723
D23	5.5827
LQ2	1.1806
D12	39.4444
LQ1	1.1181

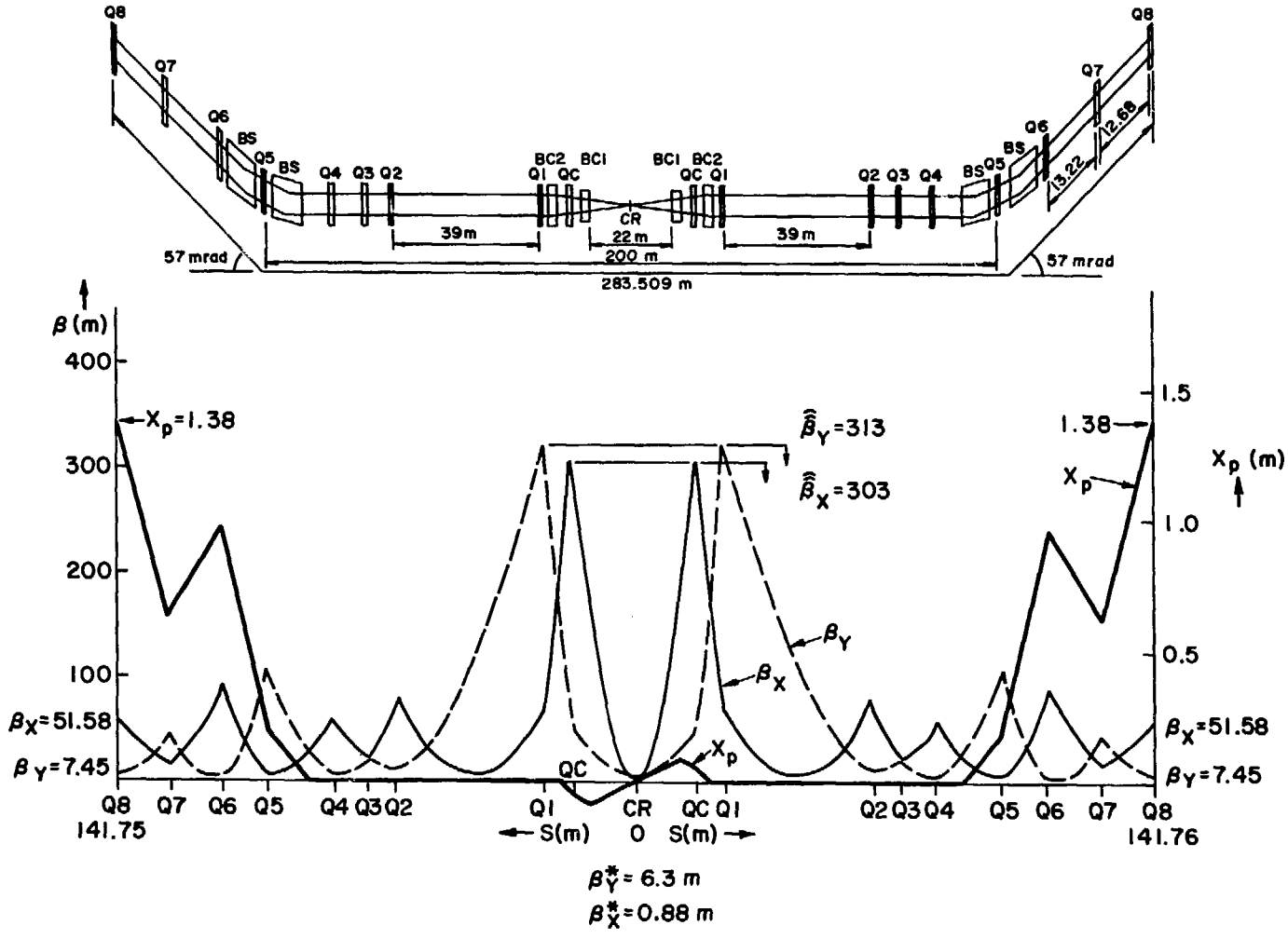
Q8
Q7
Q6
BS
Q5
BS
Q4 Q3 Q2
BC2 BC1
Q1 QC
CR
BC1 BC2
QC Q1
Q2 Q3 Q4
BS Q5
BS
Q6
Q7
Q8
12.68
13.22
39m
22 m
39 m
200 m
57 mrad
57 mrad
283.509 m
β (m)
400
300
200
100
X_p=1.38
$\hat{\beta}_Y$=313
$\hat{\beta}_X$=303
β_Y
β_X
X_p
β_X=51.58
β_Y=7.45
QC
Q8 Q7 Q6 Q5 Q4 Q3 Q2 Q1 CR QC Q1 Q2 Q3 Q4 Q5 Q6 Q7 Q8
141.75
← S(m) 0 S(m) →
141.76
1.5
1.38
1.0
0.5
X_p (m)
β_X=51.58
β_Y=7.45
β_Y^*= 6.3 m
β_X^*=0.88 m

Figure IV.6

interpreted as consequences of mismatches between the insertions and the arcs that increase with the momentum deviation from the reference value. The basic source of the problem is the change with momentum in the focal lengths of the individual quadrupoles. Such changes can be compensated locally, and the momentum dependence of the matches between insertions and arcs negated, by means of local sextupoles, but only if the dispersion is non-negligible in each quadrupole. It is small or zero in a number of the insertion quadrupoles, in particular in QC and Q1. Measures for controlling the mismatch have to be more complex. There is considerable dispersion in quadrupoles Q6, Q7 and Q8, and sextupoles associated with these magnets offer three independent parameters per half insertion for mismatch control. We have used this arrangement in an initial study, The curves in Figs. IV.7-IV.10, which show the behavior of various lattice parameters with relative momentum offset for net values $\chi_H = 2$, $\chi_V = 2$, reflect the results obtained. The sextupole strengths assumed are given in Table IV.6. Further study is needed, in particular if simultaneous operation of different insertion configurations is contemplated.

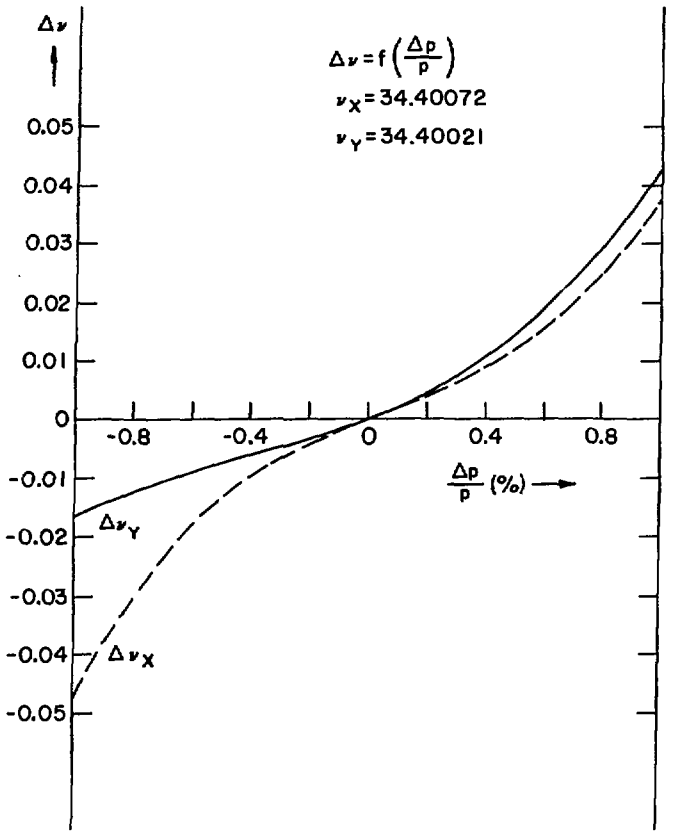

Figure IV.7. Variation of the betatron tunes with momentum offset.

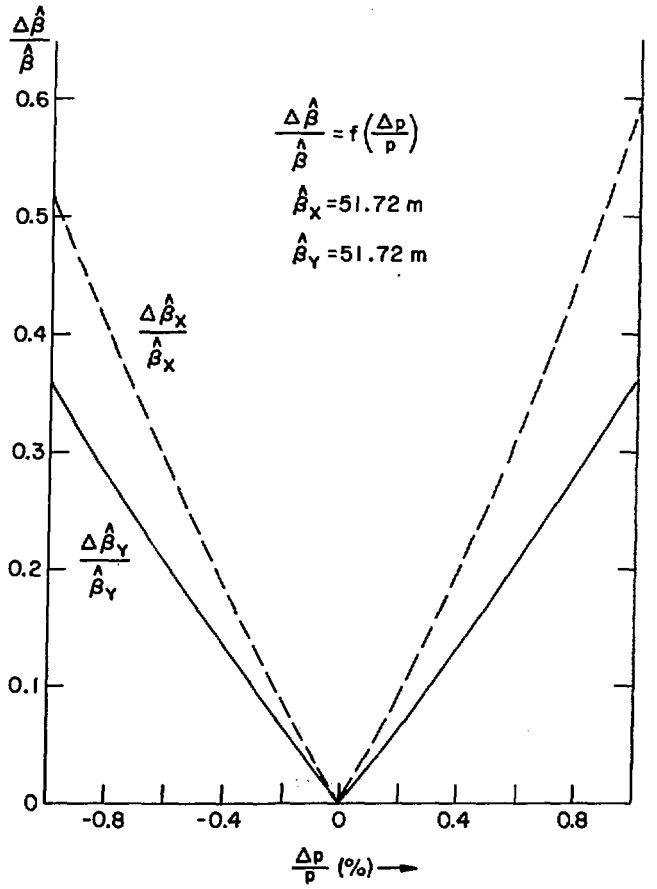

Figure IV.8. Variation of the maximum values of β_x and β_y, in the arcs, with momentum offset.

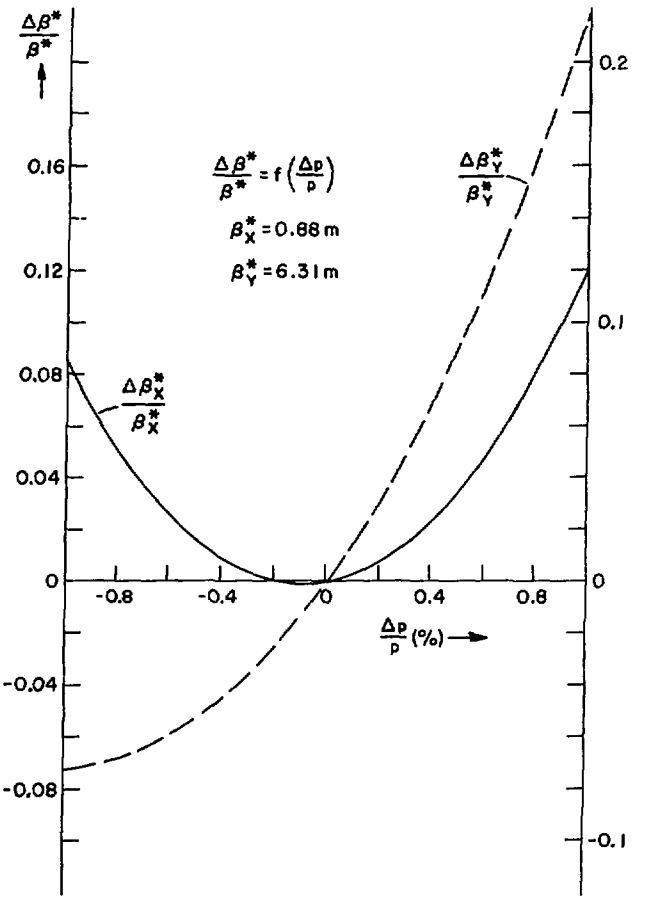

Figure IV.9. Variation of the β-values in the crossing points with momentum offset.

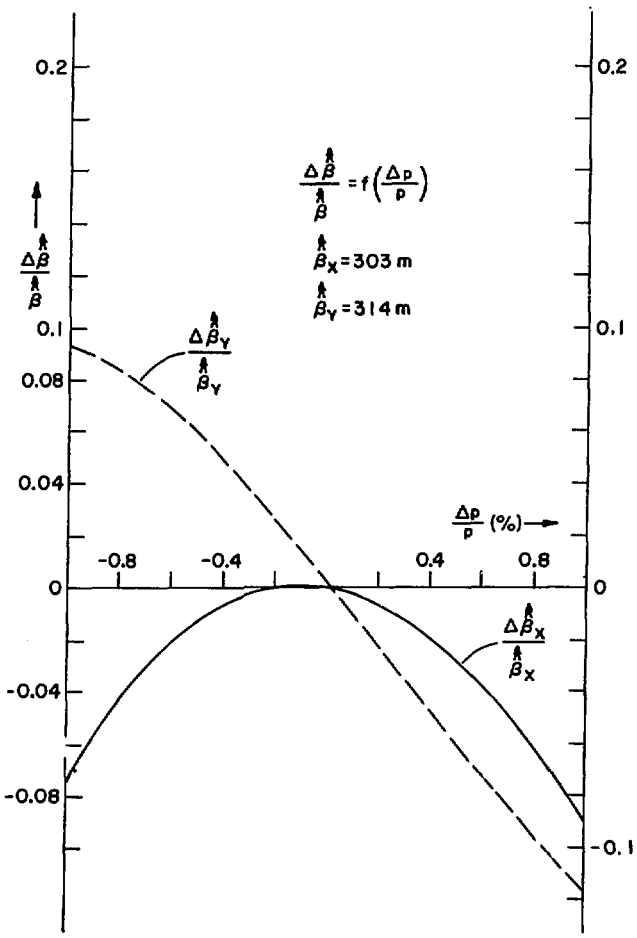

Figure IV.10. Variation of the maximum β-values in the insertions with momentum offset.

Table IV.6 Sextupole Strengths

	$S = (\frac{1}{B\rho} \int B'' d\ell)$ m^{-2}
SSF	0.08771
SSD	-0.1867
SS6	0.1743
SS7	-0.3159
SS8	0.4357

IV.3 Performance

i. Intrabeam Scattering

This is the phenomenon by which particles in the same bunch exchange longitudinal and transverse momenta by Coulomb scattering. This effect depends strongly on the charge Ze and on the mass number A of the ions. The scattering is proportional to

$$Z^4/A^2.$$

For very heavy ions we expect a severe limitation from intrabeam scattering.

The diffusion rates caused by this effect depend linearly on the beam density in the 6-dimensional phase space and on a form factor which is a rather complicated function of the lattice parameters, beta function and dispersion, and on the relative spread in the velocities.

We have made computer estimates of the diffusion rates for the lattice of the Collider specified in Section IV.2 including the insertions. Theories do exist (Piwinski, 1974[1]; Bjorken and Mtingwa[2], 1983) which can be used to estimate the growth rates of the three dimensions of a bunch at a particular location of the lattice, and several computer codes are available for this task. A model has been created to estimate the growth rates averaged over the entire circumference of the lattice. For this purpose magnet and drift lengths have been taken into account. Moreover, actual variations of the lattice functions β_x, and X_p have also been properly handled.

If the two transverse modes of oscillation are taken to be completely decoupled, at the higher energies one finds that the horizontal mode has a positive growth whereas the vertical oscillations are damped, though usually at rather small rates. This fact would convert the initially assumed "roundness"

of the beam to an extreme "flatness." Because both linear and non-linear coupling are inherent in the Collider, and with the assumption that the coupling acts within time periods shorter than the intrabeam scattering diffusion time, we assume that the beam remains round, i.e., that the horizontal and vertical beam emittance are always equal. It was assumed that the horizontal and vertical emittances diffuse at the same rate given by the larger diffusion rate for the two modes of oscillation. At lower energies, $\gamma \lesssim 30$, the horizontal and vertical oscillations grow at about the same rates and the assumption of complete coupling does not change the results by much.

The instantaneous and local diffusion rates are proportional to the peak particle current, given by

$$I_p = \frac{e\beta c}{\sqrt{2\pi}} \frac{N_B}{\sigma_\ell}$$

where N_B is the number of particles per bunch and σ_ℓ the rms bunch length. As the beam diffuses the bunch dimensions increase and the diffusion rates decrease correspondingly. This fact has been taken into account in our estimates.

The results given here are for gold beams since we believe this to be one of the worst cases. This is shown in the following Table IV.7 where the quantity $N_B (Z^2/A)^2$ which is a rough measure of the intra beam scattering is listed for representative elements.

In Fig. IV.11 we give the rms momentum spread of the bunch versus the beam energy at the end of two-hour and ten-hour storage periods. It may be seen that the edge of the momentum range comes close to the height of the RF bucket near $\gamma = 12$ and near $\gamma = 100$, particularly for the 10 hour storage period. This may cause some beam loss over 10 hours, of the order of 15%, which can be reduced by increasing the rf voltage. [In Figs. IV.11, IV.12, and IV.13 the

Table IV.7

Element	N_B	$N_B(\frac{Z^2}{A^2})$
	$\times 10^9$	$\times 10^9$
Proton	100	100
Deuterium	100	25
Carbon	22	198
Sulfur	6.4	410
Copper	4.5	802
Iodine	2.6	1272
Gold	1.1	1104

vertical dashed line at $\gamma = 12$ is injection energy and that at $\gamma = 26.4$ is transition energy.)

In Fig. IV.12 we give similar results for the rms bunch length. Bunches quickly become long at the low energy end.

As initial values, we have taken a bunch area of 0.3 eV•sec/amu for $\gamma < \gamma_T$ and a value of 1.0 eV•sec/amu for $\gamma > \gamma_T$ to take into account the bunch growth from the microwave instability when crossing the transition energy. For the betatron emittance we have always assumed, at any energy, the same initial value of 10 πmm•mrad (normalized emittance, 95% of the beam).

The emittance growth (the same in both planes, because of our assumption of full coupling) is shown in Fig. IV.13. A remarkable result is that the normalized emittance for $\gamma > \gamma_T$ is independent of γ, whereas for $\gamma < \gamma_T$ the growth rate increases quickly as the beam energy decreases.

Finally in Fig. IV.14 we give the overall beam dimensions versus energy at the end of two-hour and ten-hour storage periods. These are the

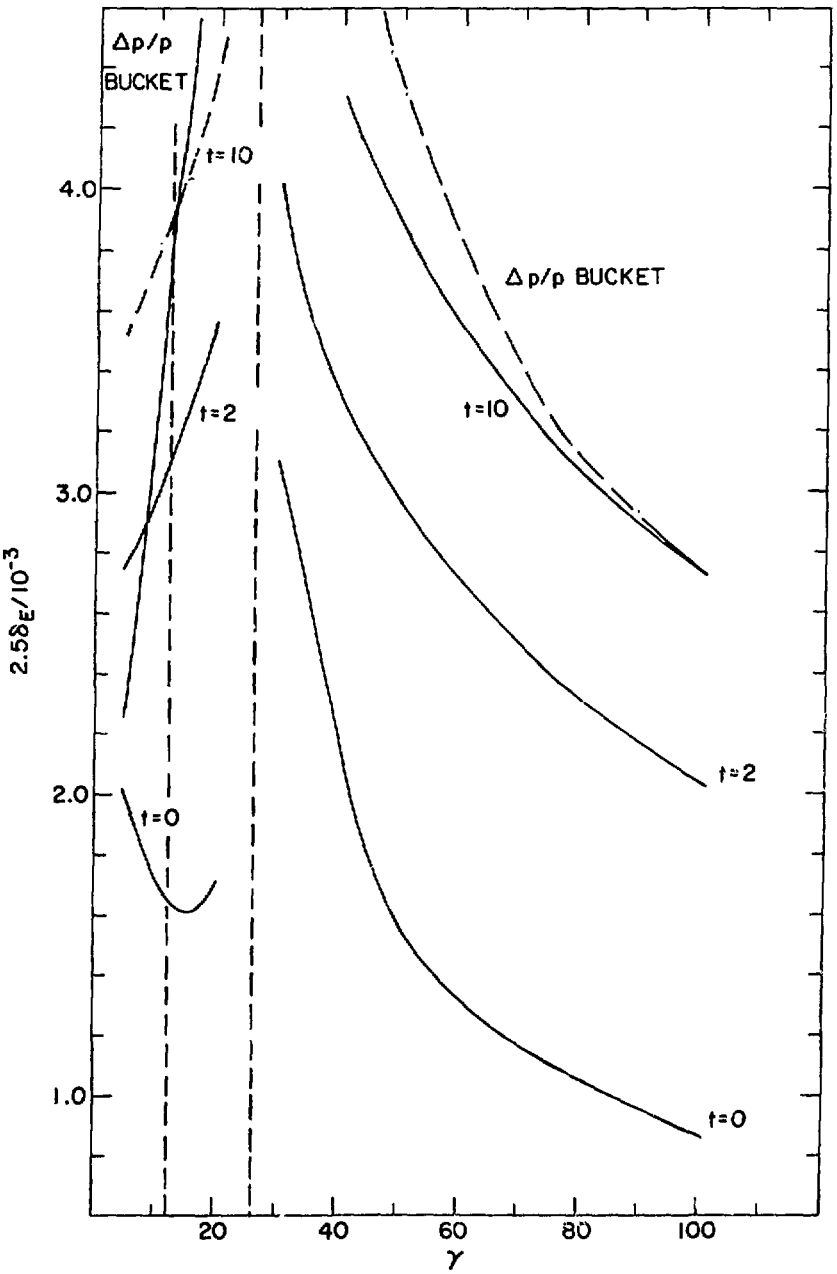

Figure IV.11. Au beam bunch height growth due to intra-beam scattering.

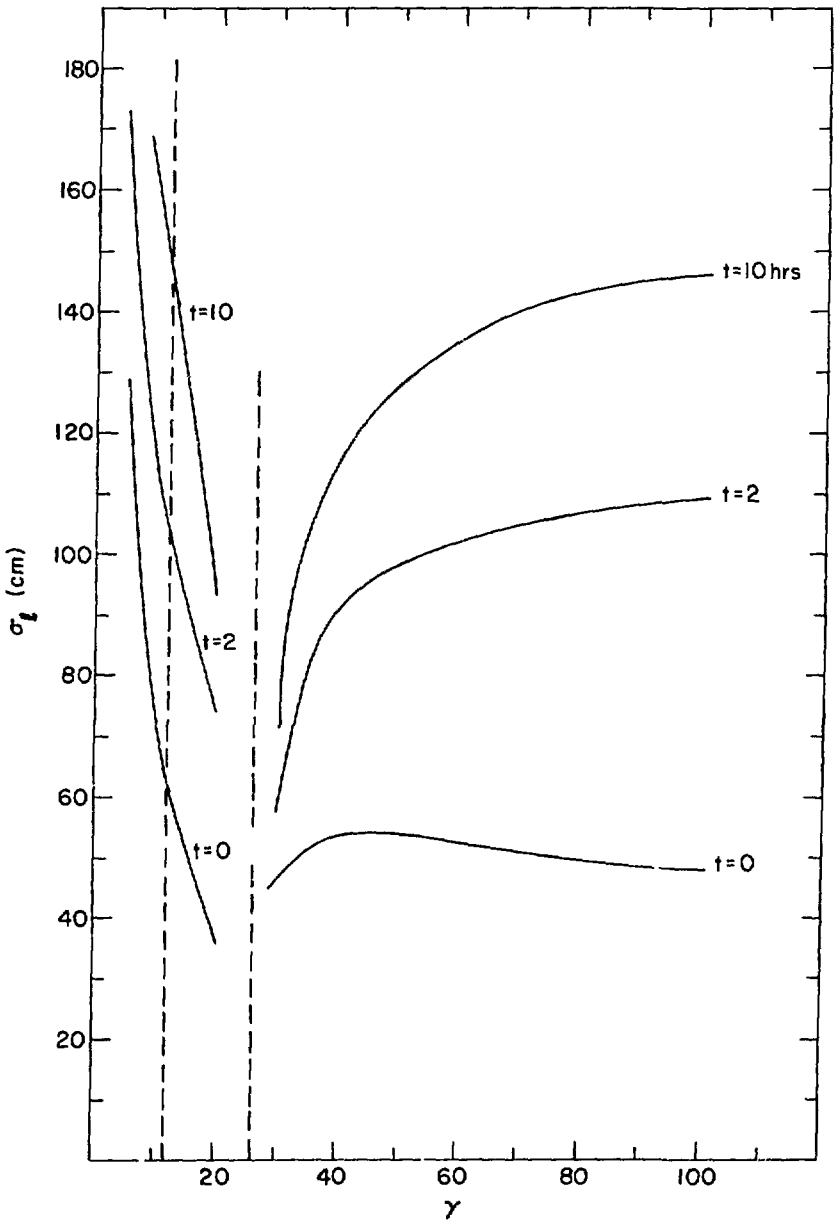

Figure IV.12. Au bunch length growth due to intra-beam scattering.

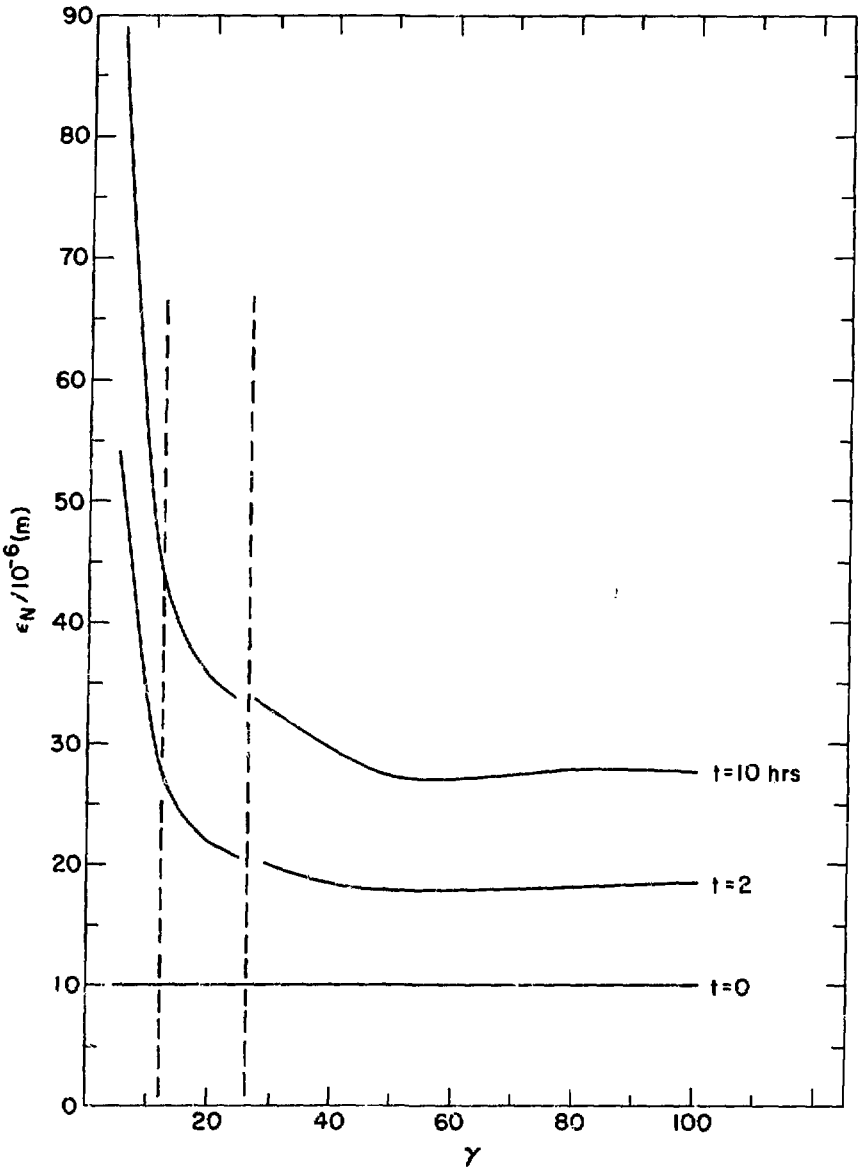

Figure IV.13. Au beam emittance growth due to intra-beam scattering.

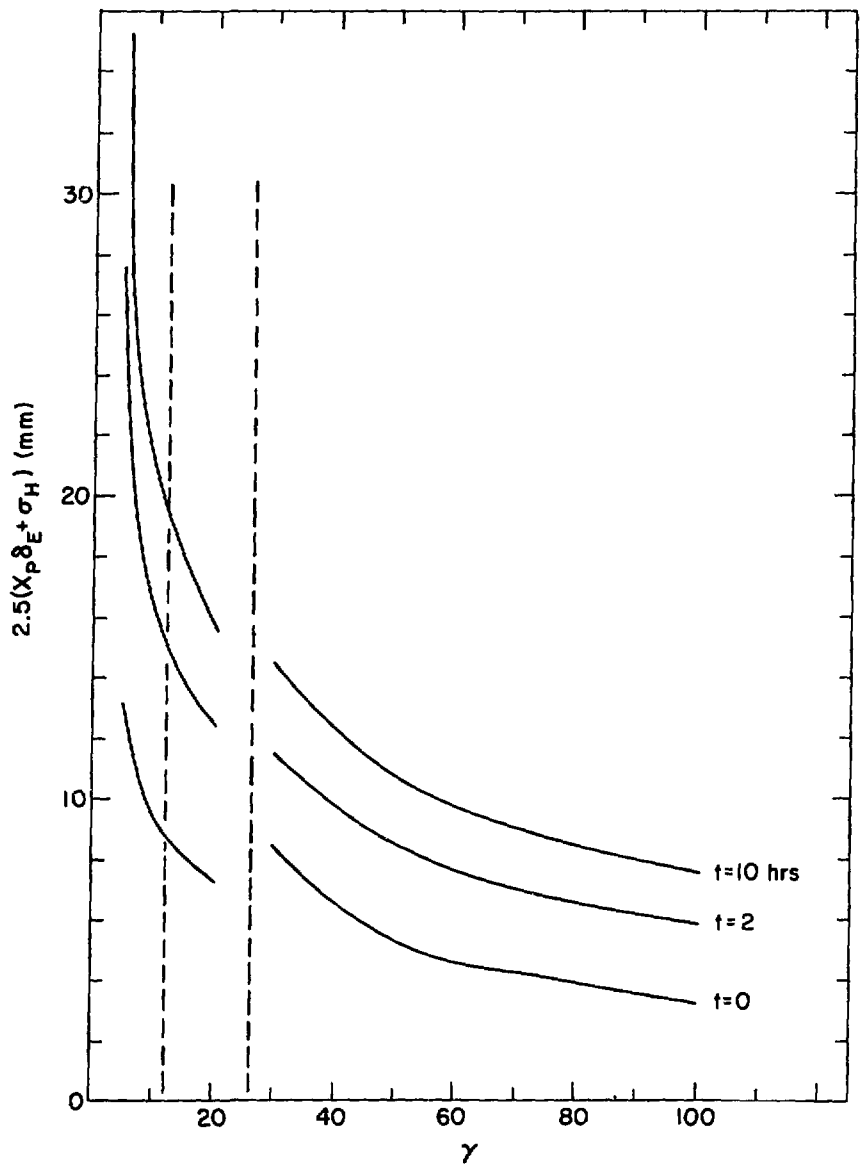

Figure IV.14. Au beam half-width growth due to intra-beam scattering.

maximum values estimated in the center of the focusing quadrupoles in the regular lattice (the arcs) of the Collider. They are half of the full dimensions in the horizontal plane, obtained by the definition

$$\sqrt{6}\ (\sigma_E + \sigma_\beta)$$

where σ_E is the rms contribution from the momentum spread and σ_β is the rms contribution from betatron oscillations. The lattice values used in estimating the beam dimensions are β_{max} = 51.4 m, and X_{pmax} = 1.39 m. Whereas the beam dimension varies at most by a factor two between γ = 20 and γ = 100, it increases rather steeply for smaller energies.

Figure IV.15 shows the beam half-width as a function of time. The beam dimensions are for 95% of the beam computed at the focussing quadrupoles in the arcs from $\sqrt{6}\ (\sigma_\beta + \sigma_E)$ for the beam half width. σ_β and σ_E are rms contributions to the total beam dimensions due to betatron oscillations and energy spread.

ii. Aperture

The criterion adopted for the aperture of the magnet is the following: The "good field" region of either quadrupoles or dipoles should be large enough to contain a beam envelope calculated according to the $6\ \sigma_\beta + \sqrt{6}\ \sigma_E$ rule. This requirement must apply for blown-up beam dimensions after 10 hours of storage for energies above γ = 30.

The good field aperture of the magnets was determined to accommodate the beam growth due to intra beam scattering. Fig. IV.16 shows the half aperature requirement as a function of γ after t = 2 hours and t = 10 hours. As expected, the magnet aperture is set at γ = 30. By also including a possible

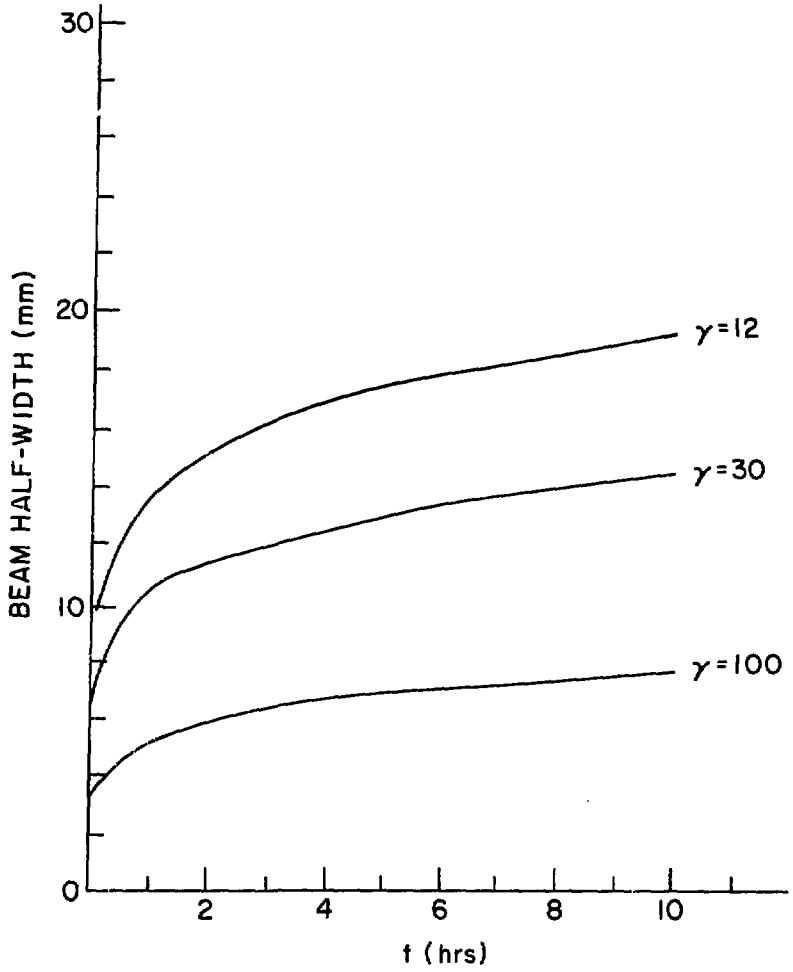

Figure IV.15. Beam Half-width versus time.

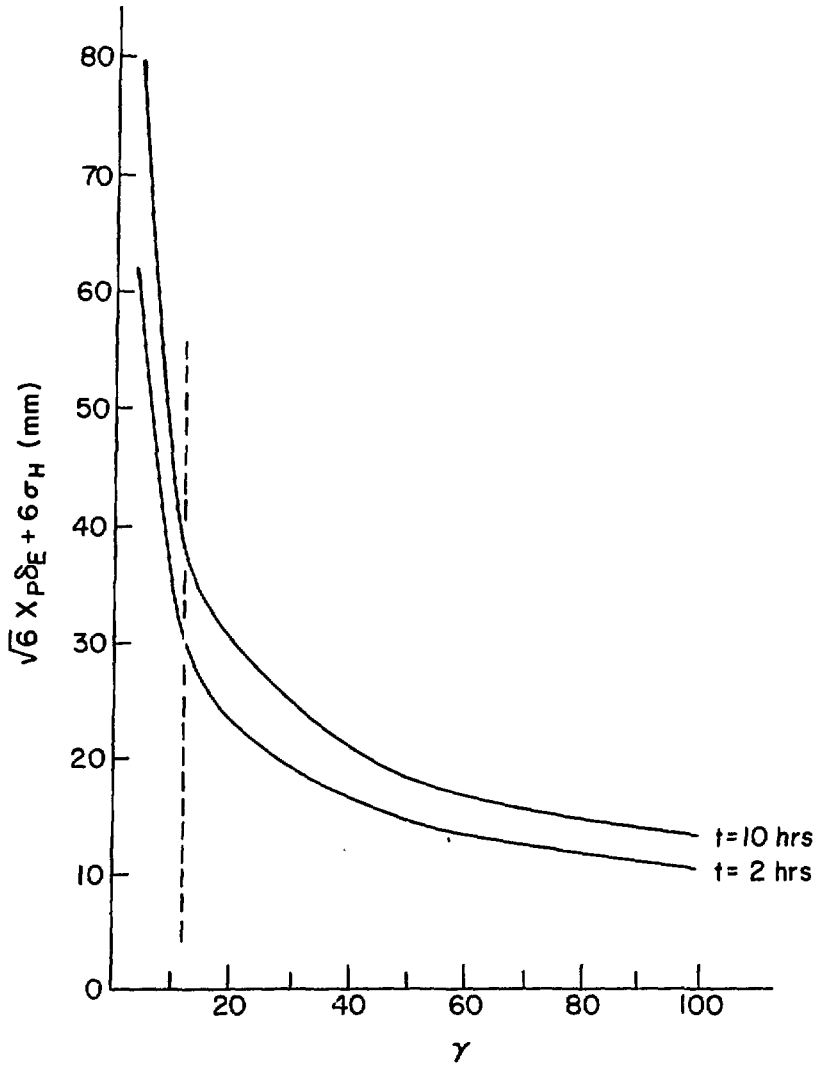

Figure IV.16. Half-aperture versus energy.

closed orbit distortion of ±1 mm (after correction), the "good field" region requirement for the magnets becomes ±26 mm.

For the magnet considered in this proposal it is expected that the ratio between the "good field" region and the coil i.d. would be 2/3 or even better. Therefore, a coil i.d. of 7.5 cm with a vacuum chamber i.d. of 6.6 cm was adopted for the arc magnets.

The above good field aperture of ±26 mm was chosen to allow operation over 10 hours above $\gamma = 30$. The situation for energies below $\gamma = 30$ is indicated in Table IV.8 for a gold beam. Operation of the collider is still possible, however, with reduced performance. The operational time interval is, in fact, limited by the available rf bucket size, i.e. $\sqrt{6}\ \delta_E = \Delta_{Bucket}$. Beam losses at energies below $\gamma = 30$ result from the rf bucket size as well as the magnet aperture limitation. At the lowest energies, the loss contribution from either effect is about equal whereas at energies above $\gamma = 30$ the losses are dominated by rf bucket limitations. An estimate of these losses combined is listed in the same table. The impact on the luminosity is considered to be insignificant when compared to the luminosity reduction due to emittance growth from intra beam scattering.

Table IV.8. Aperture Requirements in Arc OF for Au Beam

γ	5	7	12	30	100
Time interval (h)	.65	2	10	10	10
σ_β (mm)	8	7.1	5.61	3.08	1.54
Beam Half-width (mm)	23	21.2	19.1	14.3	7.52
Available space for - betratron osc.	2.73 σ_β	3.0 σ_β	3.5 σ_β	6 σ_β	14 σ_β
- synchrotron osc.	2.45 δ_E	2.39 δ_E	2.44 δ_E	5 δ_E	2.44 δ_E
Combined losses	4.5%	6%	12%	<0.1%	14%

In the insertions, there are two quadrupoles, Q1 and QC, with either high β_y or high β_x, that need to have larger good field apertures than the ±26 mm specified for the arcs. A good field aperture of about ±50 mm has been adopted for these quadrupoles as well as for the crossing point dipole BC2. Dipole BC1, common to both beams, must have an horizontal aperture of at least ±75 mm for a crossing angle of 2 mrad. Table IV.9 shows the situation at Q1. Comparing Table IV.9 for Q1 with the previous table for QF in the arcs, one sees that the choice of ±50 mm good field aperture in Q1 and QC is a good match for the ±26 mm chosen in QF.

Table IV.9. Aperture Requirements in Q1

γ	5	7	12	30	100
Time interval (h)	.65	2	10	10	10
σ_β (mm)	19.8	17.6	13.9	7.61	3.80
Beam Half-width (mm)	48.5	43.1	34.1	18.64	9.31
Space for betatron osc.	2.52 σ_β	2.84 σ_β	3.60 σ_β	6.54 σ_β	13.1 σ_β

At the transition energy, $\gamma_t = 26.4$, the energy spread in the beam increases to $\Delta p/p = \pm 0.012$. The 95% width of the beam at QF is ±21 mm and the room for betatron oscillations is 5 σ_β (not including chromatic effects). Figures IV.17 through IV.20 illustrate the behavior of the beam envelope in the mid-planes of the quadrupoles around the rings for various conditions. Its width is defined as the distance between the curves for $6\,\sigma_{H+} + x_{co+}$ and $-6\,\sigma_{H-} + x_{co-}$ where $x_{co\pm}$ represent the closed orbit shifts for the specified momentum deviations $\pm\,\Delta p/p$ and where

$$\sigma^2_{H\pm} = \frac{\varepsilon}{6\pi}\,\beta_{H\pm},$$

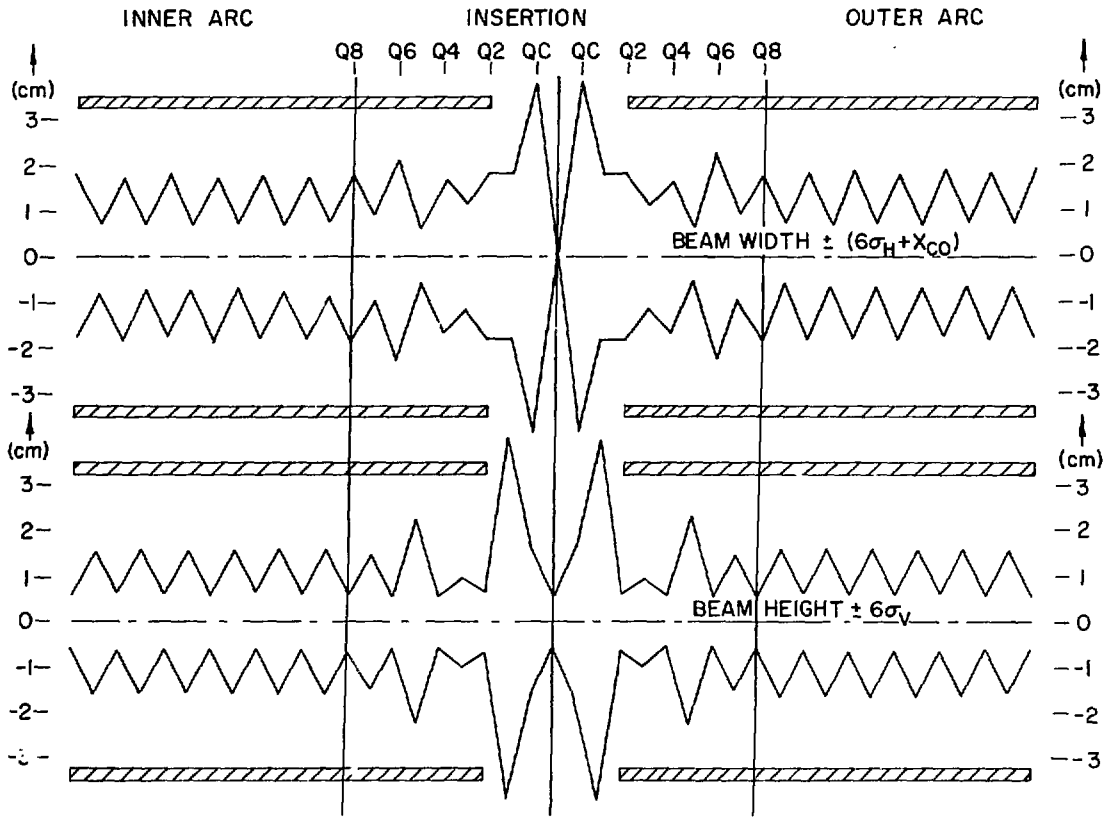

Figure IV.17. Width and height of the Au beam at injection. (γ = 12, ε_N = 10 x 10^{-6} π rad-m, $\Delta p/p$ ± 1.7 x 10^{-3})

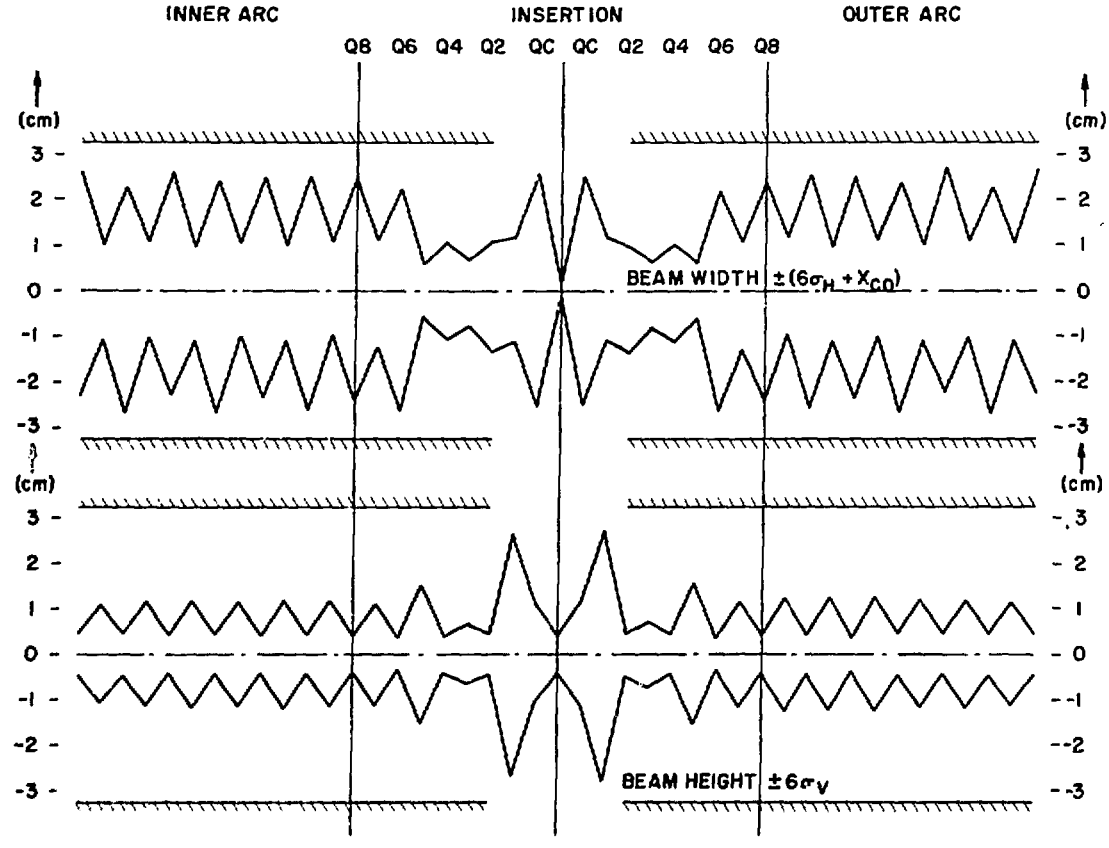

Figure IV.18. Width and height of the Au beam when passing through transition. (γ = 26.4, ε_N = 10 x 10^{-6} π rad-m, $\Delta p/p = \pm 0.01$)

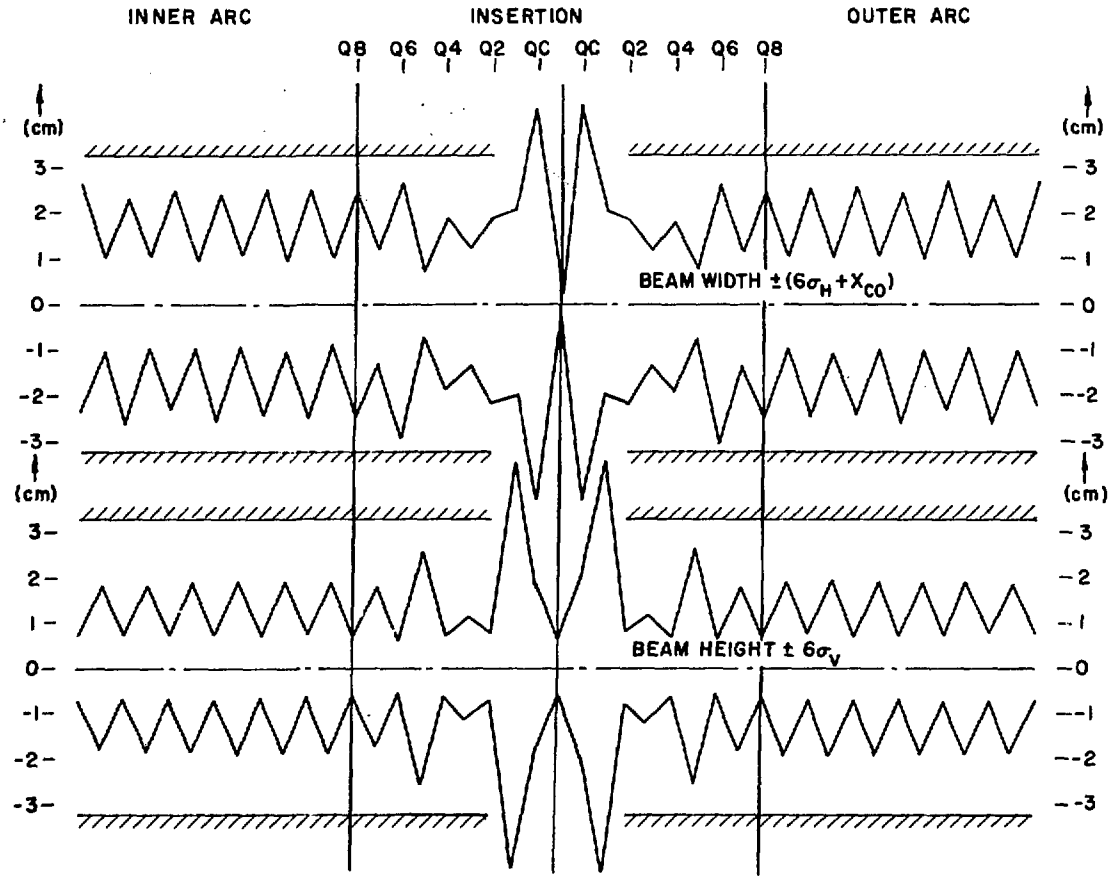

Figure IV.19. Width and height of the Au beam after 10 hours at $\gamma = 30$. ($\varepsilon_N = 33.2 \times 10^{-6}$ π rad-m, $\Delta p/p = \pm 5.0 \times 10^{-3}$)

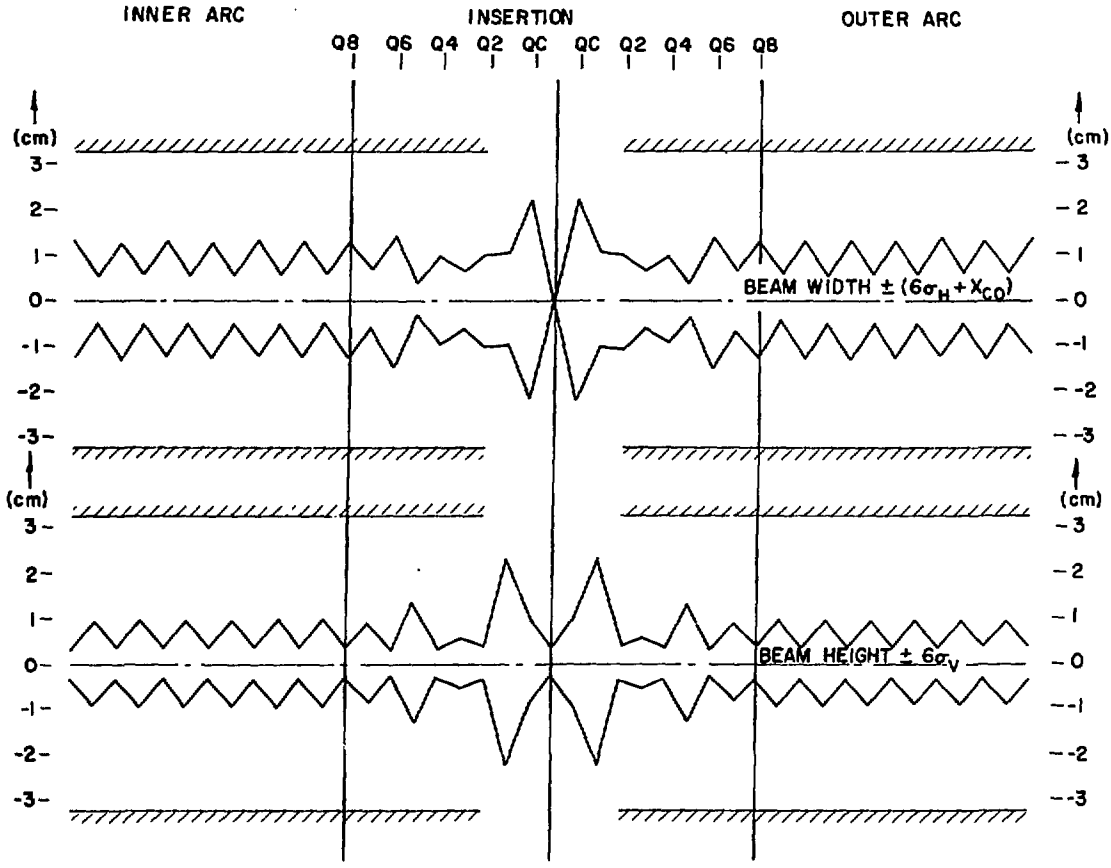

Figure IV.20. Width and height of the Au beam after 10 hours at $\gamma = 100$ ($\varepsilon_N = 27.8 \times 10^{-6}$ π rad-m, $\Delta p/p = \pm 2.7 \times 10^{-3}$)

with β_{H+} and β_{H-} the local values of the horizontal amplitude function, taking into account the chromatic effects of the momentum deviations. The height of the beam envelope is shown in similar fashion by the distance between the curves for $+6\ \sigma_V$ and $-6\sigma_V$ where σ_V is the maximum of $\sqrt{\varepsilon/6\pi}\ \beta_{V+}$ and $\sqrt{\varepsilon/6\pi}\beta_{V-}$. The boundaries indicated represent the physically available aperture of 65 mm with holes left in the insertion regions where a larger aperture has been adopted.

iii. Acceleration through Transition

With the exception of protons all ions are injected below transition energy, $\gamma_T = 26.4$, and have to be accelerated through transition for operation at top energy. Consequently, it became necessary to analyze the momentum aperture requirements as well as the negative mass instability at transition. Both problems are minimized by fast acceleration through transition. Cost considerations established 1 min as the time in which to accelerate the beam from injection to the top energy.

Table IV.10 shows the longitudinal beam acceleration and rf bucket parameters. A peak rf voltage of 1.2 MV is necessary for the acceleration of the beam and to provide sufficiently large rf buckets in the storage mode. We take a period of 60 sec in which to accelerate the beam from injection to the top energy. The energy gain per turn for the different ion species is given in Table IV.10. The synchronous angle is given by $\sin \theta_s = 0.04$, assuming a linear ramp at constant rf voltage. For a moving bucket during acceleration the area is obtained by multiplying the value in Table IV.10 by $\alpha = 0.90$, and bucket height by $Y/\sqrt{2} = 0.96$. At injection the bunch area is 0.3 eV•sec/amu for all species, thus one can see that the buckets have enough area and height.

In Table IV.10 we also give the 95% bunch half length and half height of the beam at the transition energy crossing, assuming a full voltage of 1.2 MV

Table IV.10. Beam Acceleration and RF bucket Parameters*

	Proton	Deuterium	Carbon	Sulfur	Copper	Iodine	Gold
Energy Gain/Turn (keV/amu)	47.5	23.7	23.7	23.7	21.9	19.8	19.1
Stationary bucket area: (eV•sec/amu)							
Injection	21.7	3.3	3.4	3.4	2.7	2.2	2.0
Top energy	29.9	15.2	15.2	15.2	13.9	12.8	12.2
Bucket half-height: $\Delta p/p$(%)							
Injection	1.58	0.481	0.487	0.489	0.431	0.376	0.356
Top energy	0.250	0.254	0.254	0.254	0.255	0.256	0.256
Bunch height @ transition $\Delta p/p$ (%)		±1.26	±1.27	±1.27	±1.25	±1.23	±1.22
Bunch length @ transition $\sqrt{6}\ \sigma_L/c$ (nsec)		±1.18	±1.18	±1.18	±1.20	±1.22	±1.23
Characteristic time of transition energy crossing (msec)		24.5	24.3	24.3	25.7	27.4	28.2
$N_B\ Q^2/A$ (x 10^9)	100	50	66	51	60	58	35

*Transition energy γ_T = 26.4
harmonic number = 6 x 57 = 342
RF Frequency (β =1) = 26.743 MHz
Total RF voltage = 1.2 MV
Acceleration period = 60 seconds
RF Phase Angle, θ_s = 2.3°

and unchanged acceleration rate. These quantities have been calculated for a blown-up bunch area of 1.0 eV•sec/amu, because it has been found that the beam bunches suffer a coherent microwave instability when crossing the transition energy; this results from the vanishing of the parameter $\eta = (\gamma^{-2} - \gamma_T^{-2})$ at transition. Eta measures the Landau damping which is required for stability.

A simple phenomenological model has been proposed and the analysis of the instability has been worked out numerically. In this model the beam bunch is assumed to take the shape as required by the external rf voltage and remains otherwise unmodified as it goes through the transition energy. The growth rate of the instability is then calculated locally for a given impedance, Z/n (complex), and integrated over the entire crossing. The growth rate is estimated by numerically solving the dispersion relation for the instability assuming a gaussian for the energy distribution. The growth rate depends on the choice of the harmonic number, n, which, considering the short length of the bunches, has been taken in proximity of the beam pipe cut-off frequency ($\sim 2 \times 10^4$).

According to this model the maximum bunch growth factor depends crucially on the parameter

$$N_B \, |Z/n| \, Q^2/A$$

where N_B is the number of particles per bunch, Q the charge state and A the atomic mass.

The results are shown in Figs. IV.21 and IV.22 for gold, which give the upper-limit estimate of the local growth rate and of the total bunch area growth respectively. Note the strong dependence on the initial values of the

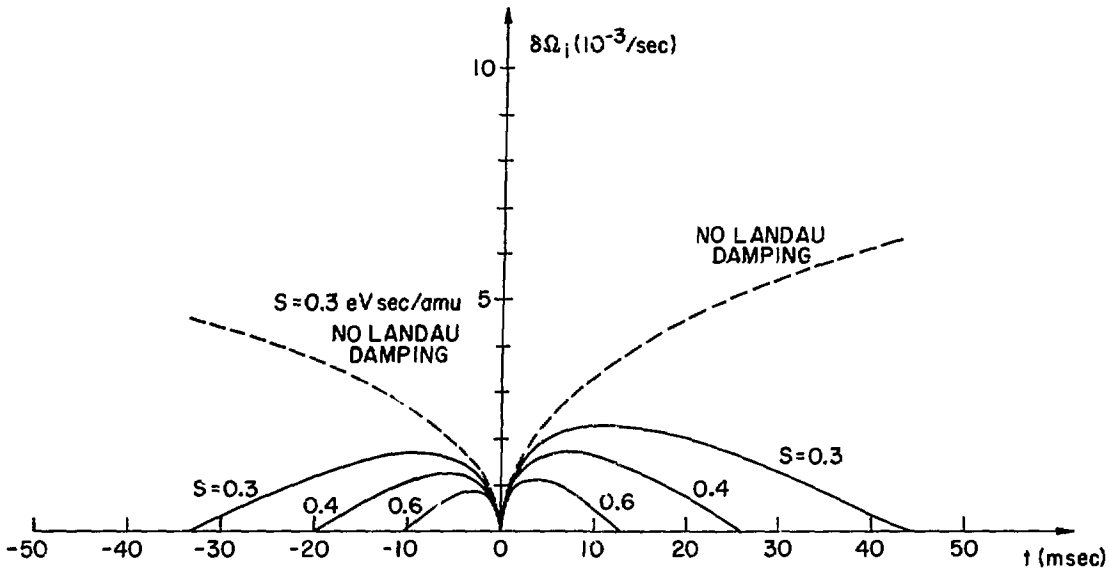

Figure IV.21. The imaginary part of the microwave frequency, $\delta\Omega_i$, representing the growth rate of the instability, is plotted as function of time during crossing of the transition energy. The curves are calculated with the initial phase space as parameter. The dashed curve represent the growth rate without Landau dumping.

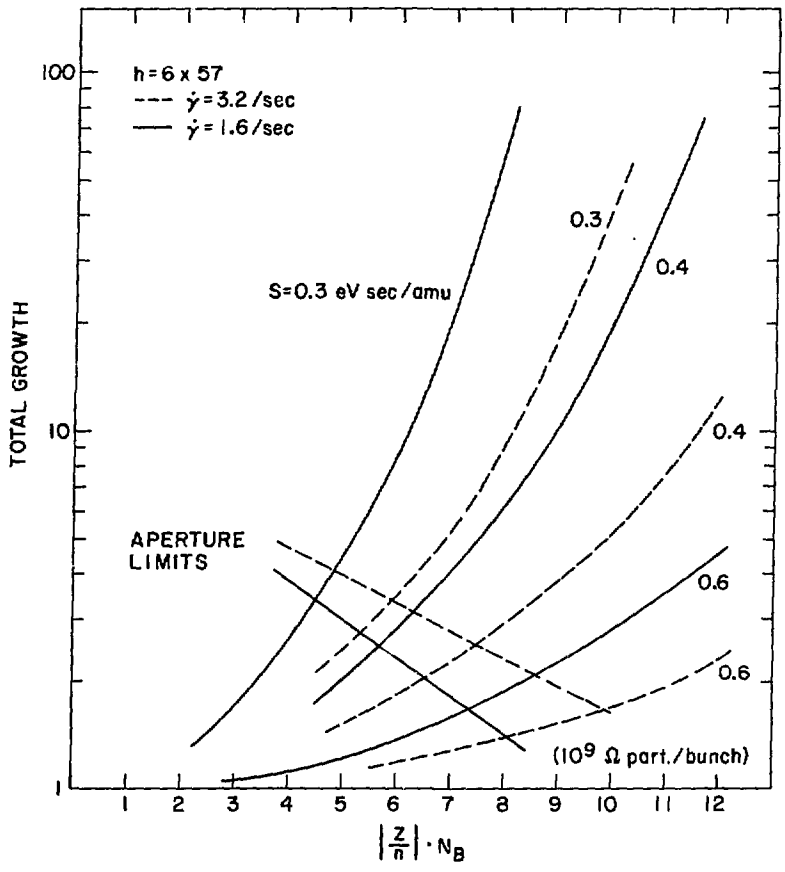

Figure IV.22. Total growth of longitudinal phase space as function of $N_B \cdot |Z/n|$ with the initial phase space area as parameter.

bunch area. Assuming $|Z/n| \lesssim 5\ \Omega$, with 1.1×10^9 particles per bunch, we expect the bunch area to increase to no more than 1.0 eV•sec/amu for gold.

A comparison in Table IV.10 of the scaling factor $N_B\ Q^2/A$ for different species suggests that the crossing of transition results in roughly equal blow up in all cases, except for protons which do not go through transition.

One important parameter, which determines the bunch shape when crossing the transition energy, is a characteristic time, also given in Table IV.10, during which the motion is "non-adiabatic." There is another related effect that has been investigated. This is the mismatch of the longitudinal space charge forces with the external rf forces. This effect has been found to be negligible.

iv. Collective Effects

Beam-Beam Tune-Shift. The largest beam-beam tune-shift for a given number, N_B, of particles per bunch occurs for head-on collisions. For a "round" beam in which the emittances are the same in both planes and $\beta_V^* = \beta_H^*$, the tune-shift does not depend on the beam energy and is given by:

$$\Delta\nu_o = \frac{3N_B r_o Z^2}{2\pi\epsilon_N A}$$

where $r_o = 1.535 \times 10^{-18}$ m and ϵ_N is the normalized emittance for 95% of the beam. But for unequal β^*-values, the tune-shift is

$$\Delta\nu_{H,V} = \frac{2\Delta\nu_o}{1 + \sigma^*_{V,H}/\sigma^*_{H,V}}$$

where $\sigma^*_{H,V}$ are the rms beam dimensions at the crossing point. In the case in which the two beam have different ion species, the tune-shift in beam number "1" due to beam number "2" is

$$\Delta\nu_{H,V(1)} = \frac{3N_{B2}r_o Z_1 Z_2}{2\pi\epsilon_{N2} A_1} \frac{2}{(1+\sigma^*_{V,H2}/\sigma^*_{H,V2})} .$$

Assuming a horizontal crossing, since $\beta^*_H < \beta^*_V$, the larger tune-shift occurs in the vertical plane. The numerical results are given in Table IV.11 for the case $\beta^*_H = 0.9$ m, $\beta^*_V = 6.3$ m and for colliding beams of the same species. The values shown are the initial ones, that is, for a normalized emittance of 10 πmm·mrad. With the exception of gold, all the numbers in Table IV.11 are larger than the accepted canonical value of 0.005. We show in the same Table N_{BB}, the number of acceptable particles per bunch. The situation is, nevertheless, of no concern since a slight increase of the original emittance as, for instance, caused by intrabeam scattering, will easily reduce the other values below 0.005.

For crossing at an angle, the initial tune-shifts are smaller than those given by the above equations. Assuming an initial rms bunch length of 50 cm and a total crossing angle of 2 mrad, the tune-shift is always well below 0.005 for the design number of particles per bunch as given in Table IV.11.

Table IV.11. Beam-Beam Tune-Shift for Head-On Collision (Initial Values)

Element	$\Delta\nu_V$	N_{BB}
Proton	0.0052	96×10^9
Deuterium	0.0052	96
Carbon	0.0068	16
Sulfur	0.0053	6.0
Copper	0.0062	3.6
Iodine	0.0060	2.2
Gold	0.0036	(1.53)

Microwave-Instability. The following tolerance applies for the longitudinal coupling impedance in order to limit microwave instability within a bunch:

$$|Z/n| \lesssim 2\pi \frac{E|\eta|}{I_p} \left(\frac{\sigma_E}{E}\right)^2 \frac{A}{Z^2}$$

where the peak particle current is given by

$$I_p = \frac{e\beta c}{\sqrt{2\pi}} \frac{N_B}{\sigma_\ell}$$

We have already seen the relevance of this relation at the transition energy where

$$\eta = \frac{1}{\gamma_T^2} - \frac{1}{\gamma^2}$$

vanishes and imposed a limit on the tolerable coupling impedance of about $Z/n < 5\Omega$. We now calculate this limit at the top energy where $\eta \gtrsim \gamma_T^{-2}$ for all elements. The tolerable coupling impedance is shown in Table IV.12, calculated for an initial rms bunch length σ_ℓ = 50 cm. The rms energy spread σ_E/E corresponds to an initial bunch area of 1.0 eV°sec/amu. At top energy the worst case is for the proton beam. For other elements the impedance tolerance was established by the transition blow-up, which is the more severe criteria.

Table IV.12. Longitudinal Coupling Impedance Limit at Top Energy

Element	E (GeV/amu)	I_p (particle A)	σ_E/E	$\lvert Z/n \rvert$ (Ω)
Proton	252	4.8	0.16×10^{-3}	12
Deuterium	126	4.8	0.32	46
Carbon	126	1.1	0.32	34
Sulfur	126	0.31	0.32	44
Copper	116	0.215	0.34	40
Iodine	105	0.124	0.38	48
Gold	101	0.053	0.40	82

The threshold condition for the transverse microwave instability reads

$$Z_T < 10 \frac{E|\eta|}{I_p} \frac{\sigma_E}{E} \frac{\sqrt{\omega_c}}{c} \frac{A}{Q^2}$$

where $\omega_c \sim c/b$ with b the chamber radius. If we use the approximate expression,

$$Z_T \simeq \frac{2R}{b^2} \frac{Z}{n} ,$$

and compare the two threshold conditions above, we find that the transverse instability is more lenient by a factor of $\sqrt{10}$.

Summary of the dependence on the Ion Species. Table IV.13 summarizes the information on collective effects. Assuming the number N_B of particles per bunch on which the design is based as shown in Table IV.13, we give the average electric current $i_{electric}$. There is less than a factor of two between iodine and gold, which is very important for estimating beam loading of the rf system.

Even for iodine, the beam induced voltage is around 1 MV, and this should be an acceptable situation.

In Table IV.13 we have also listed the quantity $N_B (Z^2/A)$. This parameter is a measure of the beam-beam tune-shift and of the microwave instability (as well as of all other coherent and incoherent space charge effects). The value for protons is largest; on the other hand, all the other species from deuterium up to gold have about a comparable factor.

Last, we list the quantity $N_B (Z^2/A)^2$, which is a measure of the intrabeam scattering. The effect is very strong for gold and iodine and reduces considerably for lighter ions down to protons.

Table IV.13. Performance Limitations Scaling with Ion Species

Element	N_B	$i_{electric}$ (mA)	$N_B \frac{Z^2}{A}$	$N_B (\frac{Z^2}{A})^2$
	$\times 10^9$		$\times 10^9$	$\times 10^9$
Proton	100	75	100	100
Deuterium	100	75	50	25
Carbon	22	99	66	198
Sulfur	6.4	77	51	410
Copper	4.5	98	60	802
Iodine	2.6	103	58	1272
Gold	1.1	65	35	1104

V

v. Luminosity

For head-on collisions the luminosity is given by

$$L_o = \frac{N_B^2 \, B \, f_{rev}}{4\pi \sigma_H^* \sigma_V^*}.$$

N_B is the number of particles per bunch, B the number of bunches per beam, f_{rev} the revolution frequency, and σ_H^*, σ_V^* are respectively the horizontal and vertical rms beam dimensions at the crossing point. This equation applies to the case of two identical beams. For crossing at a total angle α, assuming the crossing is in the horizontal plane, the luminosity becomes

$$L = \frac{L_o}{\sqrt{1+p^2}}$$

where $p = \alpha\sigma_\ell / 2\sigma_H^*$ and σ_ℓ is the rms bunch length.

The lattice parameters at the crossing point are

$$X_p = 0 \text{ m}, \; \beta_H^* = 0.9 \text{ m} \quad \text{and} \quad \beta_V^* = 6.3 \text{ m}.$$

For this crossing point geometry, the initial luminosity, that is the luminosity at the beginning of the storage period and prior to blow-up from intrabeam scattering, has been estimated and listed in Table IV.14. The results correspond to the top energy and to an initial rms bunch length of 0.5 m. The initial luminosity is reduced only by a factor of about 4 for crossing at an angle of 2 mrad. At lower energies, down to 10 GeV/amu, the initial luminosity will decrease linearly with γ for head-on collision and with $\sqrt{\gamma}$ for crossings at an angle.

Over a period of storage, because the beam dimensions are increasing from intrabeam scattering, the instantaneous luminosity will decrease. The average luminosity normalized to the initial luminosity L_{ave}/L_o is plotted in Fig. IV.23 vs. beam energy (γ) for the case of gold on gold and head-on collisions.

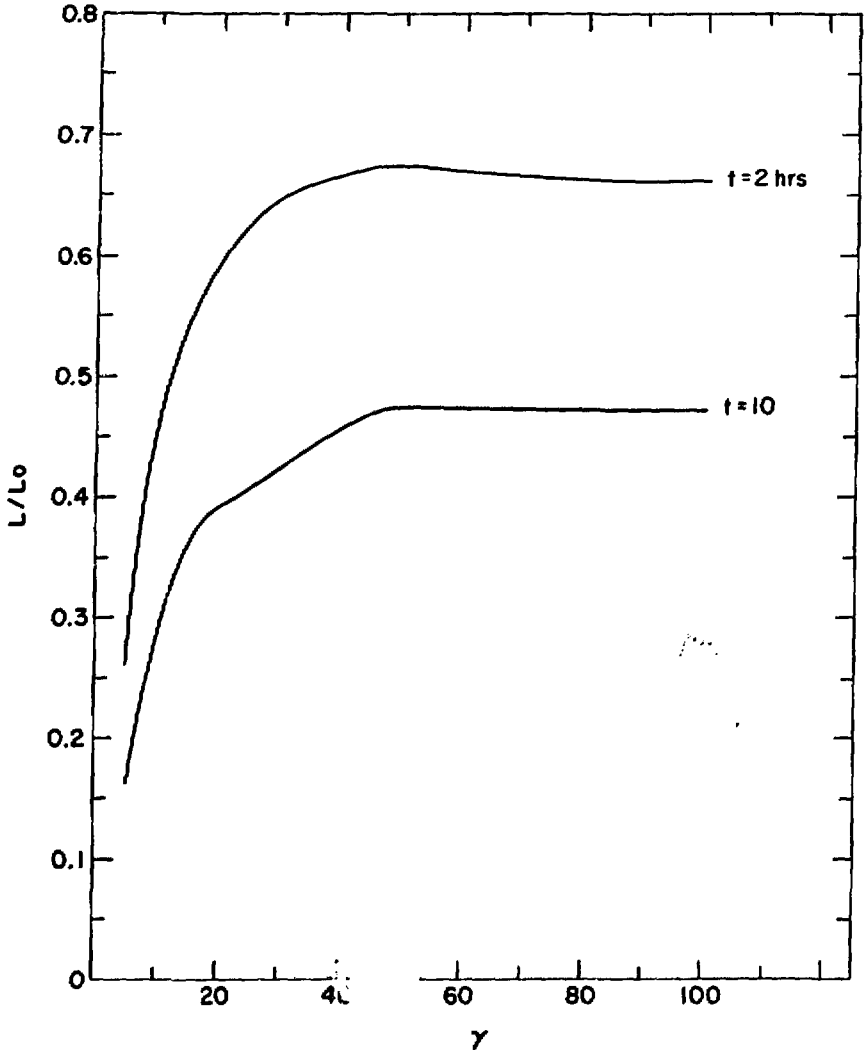

Figure IV.23. Average luminosity (normalized to its initial value) versus energy for the case of Au on Au and head-on collisions.

Table IV.14. Initial Luminosity at Top Energy

	N_B	E/A (GeV/amu)	Luminosity ($cm^{-2}sec^{-1}$) Crossing Angle (mrad) 0.0	2.0
	$x10^9$			
Proton	100	250.7	1.2	0.28×10^{31}
Deuterium	100	124.9	11.9	$2.8 \quad 10^{30}$
Carbon	22	124.9	5.8	$1.4 \quad 10^{29}$
Sulfur	6.4	124.9	4.9	$1.2 \quad 10^{28}$
Copper	4.5	114.9	22.6	$5.7 \quad 10^{27}$
Iodine	2.6	104.1	6.7	$1.7 \quad 10^{27}$
Gold	1.1	100	1.2	$0.30 \quad 10^{27}$

For energies larger than 30 GeV/amu the average luminosity over a period of 10 hours is about one-half of the peak luminosity, but it drops to about 30% at the injection energy ($\gamma = 12$). At $\gamma = 7$ the average is down to 35% for a running period of two hours. A similar behaviour, if not better, can be expected for the finite crossing angle cases. Figure IV.24 shows the average luminosity that can be obtained for gold on gold as a function of beam energy. At $\gamma = 100$, the average luminosity over 10 hours is 5.8×10^{26} $cm^{-2}sec^{-1}$ for head on collisions, and 8×10^{25} $cm^{-2}sec^{-1}$ for $\alpha = 2$ mrad beam crossing. Ten hours is possible down to $\gamma = 12$. At $\gamma = 7$, a running time of about 2 hours is possible with a luminosity of about 10^{25} $cm^{-2}sec^{-1}$.

The luminosity for different species colliding can be obtained simply by taking the geometric average of the luminosity figures in Table IV.14 for the corresponding ions. Head-on collisions between protons and gold would have a luminosity of $\sim 10^{29}$ $cm^{-2}sec^{-1}$ at 100 GeV/amu for both beams.

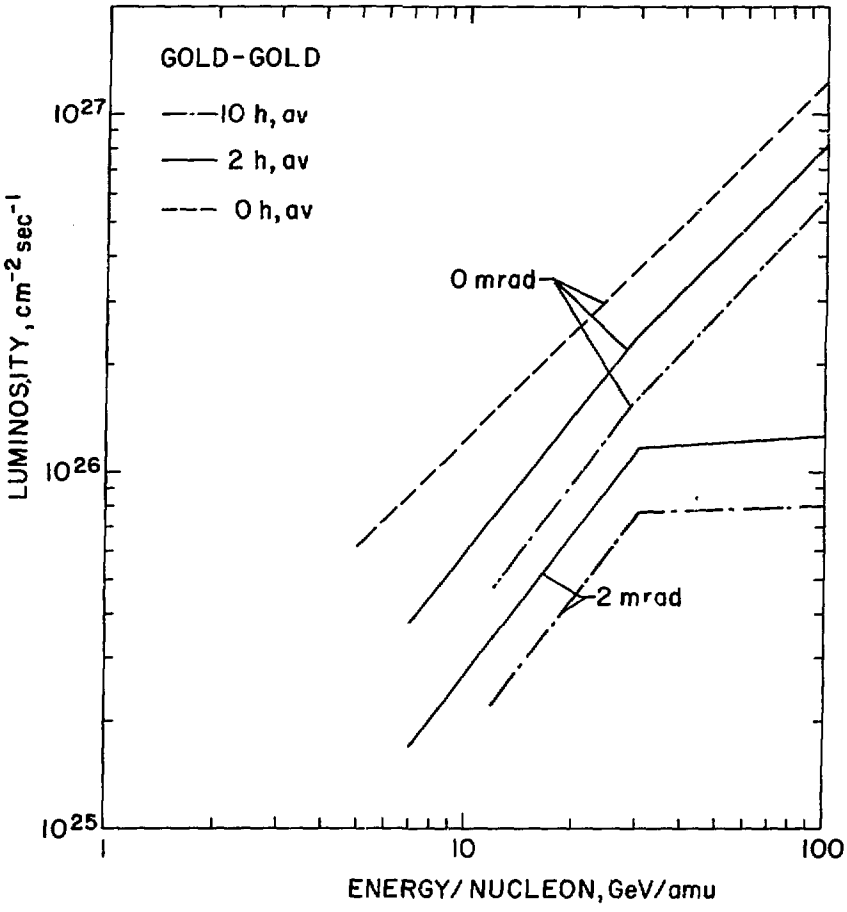

Figure IV.24. Dependence of average luminosity on energy for the case of Au on Au.

An important parameter required for the design of the detectors is the length σ_I of the interaction region. Its rms value is approximately given by

$$\sigma_I \approx \frac{\sigma_\ell}{\sqrt{2}\ \sqrt{1+p^2}}$$

with p as defined above. For head-on collisions p = 0 and σ_I is $1/\sqrt{2}$ of the rms bunch length which is given in Fig. IV.12. For gold σ_I varies from 35 to 106 cm over a period of 10 hours at 100 GeV/amu. It is almost constant, around 35 - 50 cm at 30 GeV/amu, but grows from 42 to 113 cm at the low energy end (10 GeV/amu).

The interaction region is considerably shorter for crossing at an angle. For the top energy case the rms value is about 14 cm for 2 mrad crossing angle. This value does not change significantly over a period of 10 hours and is about the same for all species involved.

vi. Lifetime Limitations

The performance of any heavy ion collider is largely determined by the intrabeam scattering process. Intrabeam scattering and its implications on the design have been discussed in the previous sections. Other scattering processes will cause beam loss and emittance blow up and have to be considered. Nuclear scattering between the ion beam and the residual gas establishes the vacuum specifications. Beam-Beam interactions due to nuclear scattering, Coulomb dissociation, and capture of electrons from pair production will result in beam loss and luminosity reductions. Estimates of reaction rates and resulting total beam half life is summarized in Table IV.15 where the initial luminosity at 2 mrad crossing angle (Table IV.14) is used. The actual beam half life will be longer because the average luminosity is smaller (Fig. IV.24).

Table IV.15. Initial Reaction Rate $\lambda = -1/I\ dI/dt$ and total half life of particle beams.

	Beam-gas nuclear reaction λ_1	Beam-beam nuclear reaction λ_2		Beam-beam Coulomb dissociation λ_3	Beam-beam Bremsstrahlung electron pair production λ_4	Half Life
Beam	$p = 10^{-10}$ Torr	A on A	p on A	A on A	A on A	A on A
	10^{-3}/h	10^{-3}/h	10^{-3}/h	10^{-3}/h	10^{-3}/h	h
p	.15	.46	.46	--	--	1100
d	.19	6.0	2.2	--	--	110
C	.36	2.5	3.8	--	--	240
S	.55	1.4	7.0	--	--	360
Cu	.76	1.3	10.7	.17	.04	305
I	1.08	1.2	16.8	4.3	1.5	86
Au	1.37	.69	21.5	5.2	10.3	40

Beam-residual gas nuclear scattering.[3,4] Nuclear reactions between the beam ion and the residual gas will result in beam loss. The loss rate can be expressed as

$$\lambda_1 = -\frac{1}{I}\frac{dI}{dt} = \quad (\beta c\ \Sigma_g n_g\ \sigma_{bg})/BN_B,$$

where n_g is the density of the residual gas, σ_{bg} is the total cross section for the reaction between the beam and the gas nuclei. At relativistic energies, σ_{bg} is equal to the geometrical cross section,

$$\sigma_{bg} = \pi(1.25\ (A_b^{1/3} + A_g^{1/3}))^2 \times 10^{-26}\ cm^2\ .$$

In terms of the gas pressure P at 300K , the residual gas density is

$$n_g = k\ P$$

where $k = 3.22 \times 10^{16}$ molecules/cm^3 Torr.

Assuming the gas composition to be 45% H_2, 45% He, 5% N_2 and 5% CO, the loss rate λ_1 is listed in Table IV.15 for a total pressure $P = 10^{-10}$ Torr. The corresponding pressure in cold sections (at 4.2°K) is 1.4×10^{-12} Torr. Indeed, it is preferable to have the vacuum pressure at 10^{-10} Torr or lower in the warm sections around the crossing point to minimize background. The vacuum does not pose a serious limitation to the beam life time.

The emittance will grow through elastic scattering with the residual gases. Assuming pure Coulomb scattering, the small angle Rutherford scattering cross-section is

$$\left(\frac{d\sigma}{d\theta}\right)_{bg} = 8\pi \left(\frac{Z_b Z_g e^2}{A_b \gamma \beta^2 E_o}\right)^2 \frac{1}{\theta^3}$$

where we disregard the spin, and laboratory reference frame to center of mass frame transformation. The mean square angular dispersion of a scattering process becomes

$$\langle \theta_{bg}^2 \rangle = 2\, \theta_{min}^2 \ln \frac{\theta_{max}}{\theta_{min}}$$

where θ_{min} and θ_{max} are the minimum cut off angle due to atomic screening and the maximum cut-off angle due to the finite size of charge distribution respectively. At high energy, θ_{min} and θ_{max} are given by $\theta_{max} = \hbar/pR$; $\theta_{min} = \hbar/pa$ respectively, where p is the momentum, R is the nuclear radius and $a = 1.4\, \alpha^{-1} Z_g^{-1/3} \hbar/m_e c$ is the atomic screening radius in the Thomas-Fermi model and α is the fine structure constant. The mean squared angular dispersion per unit time is therefore given by

$$\frac{d\langle \theta^2 \rangle}{dt} = \sum_g n_g \sigma_{bg} \beta c \langle \theta_{bg}^2 \rangle$$

where n_g is the number of residual gas molecules per unit volume. Assuming the gas composition as above, we obtain

$$\frac{d\langle\theta^2\rangle}{dt} = \frac{5.9}{\gamma^2} \times 10^{-9} \text{ rad}^2/\text{h}$$
$$= 5.1 \times 10^{-13} \text{ rad}^2/\text{h}$$

for a gold beam at 100 GeV/amu. The rms betatron amplitude increment is 0.08 mm after 10 hours of operation. Also note that the blow up rate is insensitive to the beam species.

Beam-beam nuclear scattering. The interbeam nuclear reaction is the central theme of the heavy ion collider. Yet this process contributes also to the beam loss. The loss rate is given by

$$\lambda_2 = -\frac{I'}{I}\frac{dI}{dt} = (6\ L\ \sigma_{bb})/B\ N_B$$

where we have 6 intersecting regions with luminosity L and a beam-beam nuclear reaction cross-section σ_{bb} between particles. Using the luminosity of Table IV.14 for 2 mrad crossing angle, we find the collision rate λ_2 listed in Table IV.15 for A-A collision modes (e.g., Au on Au, I on I, etc.) or for p-A collision modes (eg., p on Au, p on I, etc.) respectively.

In Table IV.15, we note especially that d-d has a high collision rate because of its high luminosity and large radius (the deuteron has a mean square radius of $\langle r^2\rangle^{\frac{1}{2}} = 2.1 \times 10^{-13}$ cm). We note also that p-A storage collision modes pose an important limitation on the life-time of the heavy ion beam because of the high intensity proton beam. By comparing λ_1 and λ_2 in Table IV.15, the pressure at $P = 10^{-11}$ Torr is useful to reach a clean background in the intersecting experimental area.

Coulomb-dissociation of high Z nuclei.[5] Recent experiments from the Bevalac show that the cross-sections for single nucleon breakup reactions are large at relativistic heavy ion energies. The phenomenon is interpreted as due to the Coulomb excitation into giant dipole states and leads to single nucleon breakup reactions. Extrapolation of the experimental results indicate that the Coulomb-dissociation cross section for Au on Au is of the order of 30 ∿ 50 barn at energies 10 - 100 GeV/amu. These extrapolated cross sections will be verified experimentally in the RHIC collider.

Using the extrapolated cross section (50 barns), we calculate the beam intensity decay rate to be

$$\lambda_3 = -\frac{1}{I}\frac{dI}{dt} = (6\ L\ \sigma^{CD})/B\ N_B = 5.2 \times 10^{-3}/h\ .$$

Using the dipole sum rule, the Coulomb dissociation cross-section can be shown to be proportional to $Z_1^2 Z_2^{2/3}$. We list the extrapolated Coulomb-dissociation reaction rate in column λ_3 of Table IV.15 for A-A collision modes.

Bremsstrahlung pair production and subsequent electron capture.[6] An interesting process which can appear in RHIC is the reaction

$$Au^{79+} + Au^{79+} \rightarrow Au^{79+} + e^+ + (e^- + Au^{79+})\ ,$$

where the electron from the Bremsstrahlung pair production is recaptured into the electron orbit of the colliding nuclei. Using the Weizsäcker-Williams (W.W.) formalism, the cross-section for pair production leading to a bound K electron is estimated to be 160 barns for Au on Au at 100 GeV/amu collider energy (80 barns for each of the intersecting beams). Alowing 25% increase in cross-section for L, M, shell bound electron processes, we assign a total 200 barns (with 20% uncertainty) cross section to this process. Since only 100 barns (the

cross section for one of the beams) is directly related to the beam loss, we thus obtain the reaction rate to be $\lambda_4 = 0.010/hr$, which is shown in Table IV.14.

Because of the Bremsstrahlung of virtual photons in the atomic collision process, the energy loss can be estimated by integrating the inclusive W.W. spectrum, i.e.

$$\Delta E = \int I(\omega)d\omega = \frac{2}{\pi} Z_b^2 \alpha \frac{0.6811\ \gamma\hbar c}{b_{min}}$$

where $b_{min} \simeq a_{Bohr} = Z_b^{-1} \alpha^{-1} \hbar/m_e c$.
Thus the relative energy loss is given by

$$\frac{\Delta E}{E} = \frac{2}{\pi} Z_b^3 \alpha^2 \frac{0.6811\ m_e}{m_N A_b}$$

where $m_N = 931\ MeV/c^2$ is the atomic mass unit. For ^{197}Au ion, we obtain $\Delta E/E \simeq 3\times10^{-5}$, which is small compared to the bucket size ($\simeq 2.7\times10^{-3}$ at $\gamma=100$; see Fig. IV.11). We conclude that the energy loss due to Bremsstrahlung is not an important factor in the design of the heavy ion collider.

vii. Beam Set-Up Procedure

The beam set-up procedure, from switch-on until accceptable data-taking conditions for the experiments have been achieved, will take some time and influence the long-term average luminosity. Both the ISR and the SPS collider require set-up procedures which take about 12 hours on the average. Such a set-up time would reduce luminosity for the high-energy operation of RHIC (30-100 GeV/amu) and would be unacceptable at lower energies. However, there

are good reasons to expect shorter set-up times for RHIC, in particular for regular refills. In the following we give an outline of a RHIC procedure with some comparison with the ISR which in this respect has the best documentation. For this purpose we shall examine set-up procedures for four different operational conditions:

- Switch-on - after a scheduled or unscheduled shut-down of the facility.
- Refill for 30-100 GeV/amu operation - repetitive refill after >10h runs
- Refill for 12-30 GeV/amu operations - repetitive refill after 2-10h runs.
- Refill for 5-12 GeV/amu operation - repetitive refill after very short runs (<2h).

Recycling of magnets. For switch-on a careful recycling will be needed for both transfer lines and for the rings. This averaged about 1 hour on the ISR. There is no reason to believe that the procedure will be simpler on RHIC, but, with experience, it should be possible to make the operation more automatic. We therefore assume ½h for this operation on RHIC.

For carefully planned refills it should be possible to cycle the transfer line while the beams are still circulating. For short-lifetime runs the transfer lines may even be kept active all of the time. In either case it should require no operational time. For the main rings it should be possible to establish an accurately reproducible cycle similar to a synchrotron (e.g. Tevatron), and with this assumption the cycling of magnets should require negligible time for all planned refill modes.

Injection adjustments. The transfer lines from AGS can be set up with beam, using a beam dump close to RHIC. This will follow the cycling of the magnets in the switch-on mode. In the refill modes we assume that this operation will be done while the beams are still circulating in the rings, prior to dumping. Precise beam-observation equipment must be provided. Thus for injection adjustments no time need be allocated for beam refills. When the main rings have been reset to the injection field, injection tests can start with fine-trimming of septum magnets, kickers, feed-back, and rf parameters. The tune of the machine will have to be checked, adjusted, and the whole good-field aperture may have to be sampled and trimmed. It may be necessary to go through a few accelerating cycles with trim corrections, etc. for the switch-on mode or high-energy refill mode since >10 hours will have passed since the last time that the equipment had been operated. The corresponding procedure averaged ~1.5h per ring on the ISR. On RHIC the procedure is somewhat simpler. In addition, the incentive to shorten the procedure is high in RHIC with its shorter beam life-time, and one might plan to set-up the two rings in parallel. In the light of this we assume 1½ hours for both rings for the switch-on mode. For the high-energy refill mode, both planned preparation, while the beams are still on, and some reliance on memory should allow a shorter time say 1 hour. For medium nergy runs (12-30 GeV/amu) again one can rely more on the memory and reproducibility of the components and reduce these beam adjustments to ½ hour. For the very low energies (5-12 GeV/amu) no acceleration is needed and we assume no change of components from refill to refill, apart from those normally observed and adjusted during runs. In this case, therefore, no time is allocated for this operation.

Stacking and acceleration. These two operations are much shorter than in the ISR: about one min/ring for a box-car stacking and one minute acceleration. With some safety factor we assume ¼ hour.

Beam optimization. These procedures averaged 2 hours on the ISR. There are reasons why we ought to do better on RHIC. The intensity of the beams is much lower, and the beams are further from the walls at the beginning of the run (for ≈100 GeV/amu). The beam scraping operation will therefore be quicker. Steering would be about the same, but with existing experience we will be able to make full use of computer controlled procedures. We, therefore, assume 1 hour for this optimization for the switch-on mode and for long refill runs (30-100 GeV/amu). For shorter runs (12-30 GeV/amu) we again rely more on memory from refill to refill and assume ½ hour, and for the low-energy runs without acceleration only small adjustments should be needed and for this we reserve ¼ hour. It should be emphasized that successful fine-adjustments of the beam conditions may be crucial for experimental data taking. It is clear that considerable thought and ingenuity must be given to these procedures in order to minimize the time involved.

Beam cleaning. Experimental conditions may deteriorate during a run, requiring cleaning up beam halo. This reduces the average useful luminosity, as it requires that experimental equipment be either switched off or otherwise protected, scraping, testing of conditions, and switch-on of equipment. With extensive use of automation and careful planning we assume this will take on the average ¼ hour for all runs except the very short runs, for which we assume no cleaning during actual data-taking time.

Summary. In the following table the time needed for the various operations is summarized. There is uncertainty in these numbers, and the cases listed are examples only of a continuous spectrum of operating conditions.

Table IV.16. Set-Up Times (in hours)

	Switch-on	Refill		
		30-100 GeV/amu	12-30 GeV/amu	5-12 Gev/amu
Cycling of magnets	0.5	0	0	0
Injection adjust.	1.5	1	0.5	0
Stacking and acc.	0.25	0.25	0.25	0.25
Beam optimization	1	1	0.5	0.25
Beam cleaning	n.a.	0.25	0.25	0
Total	3.25	2.5	1.5	0.5

We see that set-up procedures could reduce average luminosities by 25-50% according to the energy chosen for the run. This is acceptable, but it illustrates how important it will be to arrive at an efficient procedure. The above estimates assume that we can do considerably better than at the ISR. This will need careful planning and effort.

References

1. A. Piwinski, Proc. 9th Int. Conf. on High Energy Accelerators, 1974, p. 405.
2. J.D. Bjorken and S.K. Mtingwa, Particle-Accelerators, 13, 115, (1983).
3. G. Young, 'Collider Vacuum Requirement', RHIC-PG-11.
4. T.S. Chou and H. Halama, private communication.
5. M.T. Mercier, J.C. Hill, F.K. Wohn and A.R. Smith, 'Electromagnetic Dissociation of ^{1} Au by Relativistic Heavy Ions'; Phys. Rev. Lett. 52, 898, (1984).
6. S.Y. Lee and J. Weneser, to be published.

IV.4. Magnet System

i. Dipoles and Quadrupoles

There are several requirements for the design of RHIC magnets: 1) the ring of magnets must be accommodated in the existing tunnel; 2) the maximum operating energy of the collider will be 100 GeV/amu, with good operating performance down to 7 GeV/amu; 3) operation with beams of unequal rigidity must be possible; 4) the design of the collider assumes a short cell-"strong" focussing lattice; 5) magnet cost must be minimized. Various basic magnet parameters follow from these requirements: a central dipole field in the range of 2.4 to 4.0 Tesla (depending on magnet length), a "good field" aperture of approximately 50 mm diameter, and a cell configuration with one dipole per half cell. The latter requirement, in turn, dictates a magnet length of 8 to 13 meters. These lengths, and the relatively small radius of curvature (about 250 m) result in sagittae of 40-50 mm. Increasing the aperture to this extent would be more expensive than bending the magnets. With the properties of the magnet iron and superconductor determined by the above constraints, the cost of materials is almost independent of the detailed design. The principal remaining variables, in an effort to reduce cost are, consequently, the labor and auxiliary components. Clearly, the ends of magnets and their dewars are expensive--thus the goal of only one dipole per half cell. It is believed that savings can also be realized if the magnets for the two rings share a common dewar and support system. A cost-effective design may be one with maximum mechanical commonality between adjacent magnets, yet with minimum magnetic coupling.

After examining closely a number of promising magnet designs for the collider, two candidate magnets appear about equally viable for this application. Both designs are based on magnetically decoupled magnets mounted side-

by-side in a common vacuum chamber. One, known as the dual RHIC magnet, utilizes a single layer dipole design based on experience with the CBA magnets,[1] as well as dipoles under consideration by Brown-Boveri Corporation for the HERA Project at DESY, and dipoles under study for the Superconducting Super Collider (SSC).[2] The other magnet, also designed specifically for the present application, draws on BNL's experience with dipoles designed and constructed according to the "window frame" concept.[3] In this section, a magnet system based on the dual magnet design is described; an alternative option based on the Window Frame design is summarized in Appendix 4.

General Description. The RHIC will require a total of 144 dual dipoles in the regular arcs, operating at fields up to 3.5 Tesla, and 138 dual quadrupoles with maximum gradients of 75 T/m. In addition, 108 additional dual quadrupoles, 36 dual dipoles and 12 single dipoles are needed in the various experimental insertions. Finally, 144 dual correction magnets ("spool pieces") will be needed, one each located adiacent to every quadrupole in a half cell, as well as approximately the same number of correction elements associated with the insertion magnets.

The dipoles and quadrupoles are "cold bore, cold iron" magnets; i.e., both the beam high vacuum chamber and iron return yoke are maintained at cryogenic temperatures. An overall cross section of a pair of dipole magnets is depicted in Fig. IV.25. The center-to-center separation between beam apertures is 0.3 m. The dipoles have a magnetic length of 9.3 m, and are curved to a radius of 240 m (representing a sagitta of 46 mm). The quadrupoles have a magnetic length of 1.2 m. The physical aperture (inner diameter of the high vacuum beam tube) is 65.8 mm. The annular space between the stainless steel beam vacuum chamber and the main coil i.d. (75 mm) contains, in the case of the dipole,

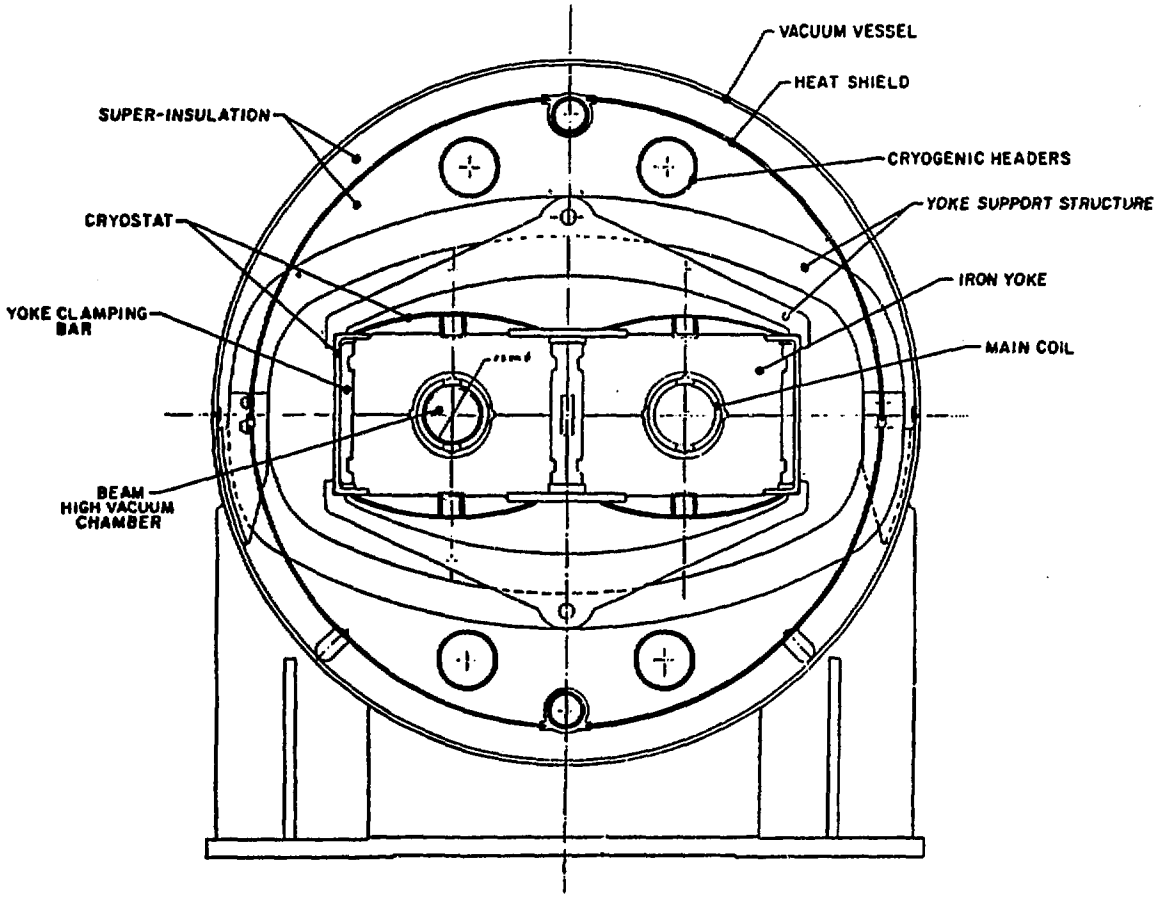

Figure IV.25. Overall cross section of a dual dipole. The separation between centers of adjacent dipoles is 0.3 m.

a superconducting winding to provide correction for systematic sextupole field harmonics. The trim coil assembly carries longitudinal spacers whose radial thickness is adjusted to furnish mechanical support for the trim coil package; supercritical helium flows in the gaps thus provided. The single-layer main dipole (or quadrupole) coil is wound from a slightly modified version of the superconducting cable developed at the Rutherford Laboratory and used in the Tevatron magnets at Fermilab.

The main coils are insulated from the iron return yoke by high strength glass-phenolic spacers. The laminated yoke is rectangular in cross section. The diameter of each iron aperture is 101 mm, and the overall cross sectional dimensions of the yoke are 260 mm in width by 260 mm in height. The coils are clamped between the two yoke halves and prestressed in a press by means of longitudinal steel clamping bars, pre-bent to the required sagitta, utilizing an assembly technique developed at Brown-Boveri Corporation and described in a later section. After coil-in-yoke assembly, the two separately bent yokes are mechanically joined together as a unit with a key and by a welding operation. Side pieces and top and bottom shells are welded to the yoke sections to provide leak-tight helium containment vessels (not curved). The entire assembly is suspended in a fiberglass ring girder support structure (devised by General Dynamics Corporation) in a common vacuum vessel of 0.94 m o.d., wrapped with blankets of superinsulation interrupted by a cylindrical metal heat shield, (cooled by helium gas). Cryogenic helium headers are located inside this heat shield for returning gas to the refrigerator from the recoolers located around the ring.

The maximum design operating dipole field, corresponding to 100 GeV/amu, is 3.5 T (32.7 T•m for a magnetic length of 9.3 m), and the operating

temperature will be approximately 4.5 K. The quadrupoles, connected in series with the dipoles, will operate at 76 T/m (90 (T/m).m for a magnetic length of 1.2 m). The conductor current at full field is 4.68 kA. Each half of a dual dipole has an inductance of 32 mH and a stored energy of 0.36 MJ. In addition to allowing operation over a field range between 0.25 T (7 GeV/amu) and full field, the design allows for operation with a maximum current imbalance at full field, or a corresponding momentum imbalance, of 2.5:1 between the two rings. The ramping time from injection to maximum operating field is 60 sec ($\sim$0.05 T/sec).

Main Coil. The conductor chosen is a Rutherford-type flat cable, quite similar to that used in the magnets for the Fermilab Tevatron and those for the CBA project, but containing a larger fraction of stabilizing copper. The cable will consist of 23 strands of 0.68 mm diameter, each containing 1800 twisted niobium-titanium filaments of 10 μm diameter embedded in a high purity copper matrix. The Cu/NbTi ratio is 2.1. The conductor, initially fabricated as a cable of rectangular cross section, is pulled through a Turk's head die to provide the necessary keystoning, approximately 2°. The cable is spiral wrapped with 0.0254 mm of Kapton, fully overlapped to provide 0.0508 mm of insulation, and with 0.0762 mm of B-stage epoxy-impregnated fiberglass tape providing some further insulation. The epoxy serves to bond the conductor turns together after the coil has been wound. The insulated cable has a width of 8.26 mm and a (mean) thickness of 1.40 mm.

With the modest peak field requirement, a single-layer coil is feasible, offering obvious simplifications in construction and insulation. Experience with this type of coil construction has shown that it is practical to achieve a field quality of $\Delta B/B = 10^{-4}$ over 2/3 the inner radius of the coil.

For a good field aperture of 2.5 cm radius, this implies an inner coil radius of 3.75 cm.

Figure IV.26 shows a quadrant of the main dipole coil cross section meeting these constraints, and Fig. IV.27 an octant of the quadrupole coil cross section. The dipole design is based on a four-block coil configuration, with a total of 30 turns per quadrant and wedges appropriately distributed to achieve the necessary field quality. The harmonics calculated for an ideal coil of the dimensions given in Fig. IV.26 and iron of infinite permeability are listed in Table IV.17. The table also lists the design value for the dipole transfer function. The quadrupole design is based on a two-block coil configuration, with a total of 15 turns per octant. The infinite permeability harmonics for this design, as well as the transfer function, are listed in Table IV.18.

Coil winding will utilize automated production techniques developed for the CBA magnets. The dipole coils, i.e., the upper and lower saddle-shaped coil halves, will be wound horizontally under tension on a stationary circular mandrel around which the cable supply spool travels in a horizontal path. For the shorter quadrupoles, consisting of four quarter coils, a horizontally oriented mandrel will rotate around a vertical axis with the cable supply spool stationary. Complete coils, still attached to the mandrel, are transferred from the winding machine to a molding fixture where they are cured at a temperature of approximately 135°C. After cooling, the azimuthal size of the coil is measured and, if necessary, the coil is re-cured to the proper size. Its length and final azimuthal dimensions, as well as its elastic and insulating properties under compression, are measured at various longitudinal locations. If an electrical short between turns is discovered, repair is attempted or the coil is rejected.

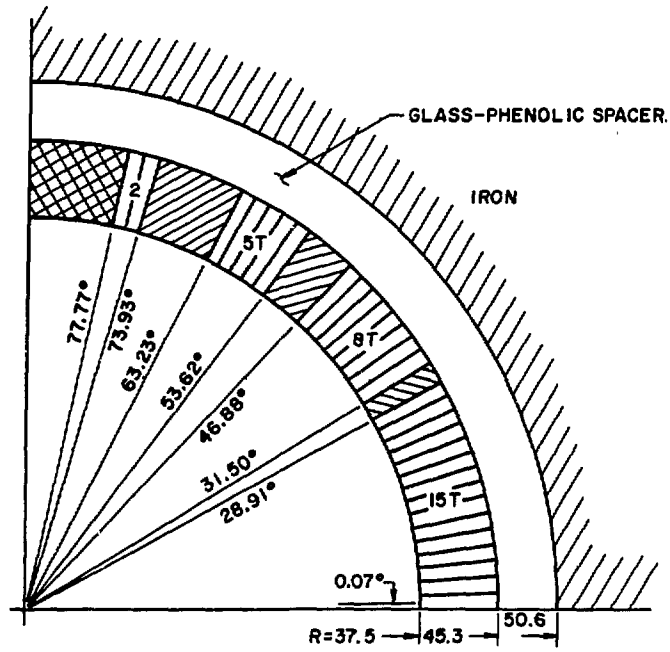

NOTE: ALL LINEAR DIMENSIONS GIVEN IN mm.

Figure IV.26. Quadrant of dipole coil cross section.

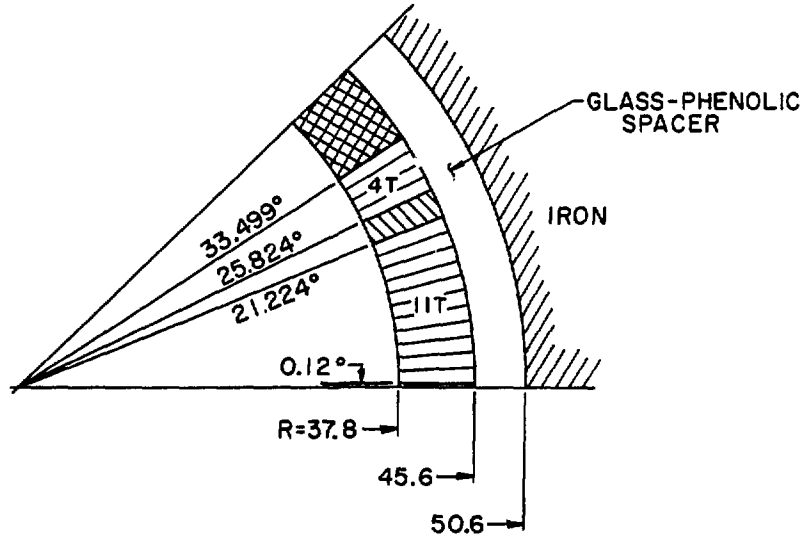

Figure IV.27. Octant of quadrupole coil cross section.

Table IV.17. Dipole Multipoles

b_n @ r = 25 mm	
	$x10^{-4}$
b_2	0.0
b_4	0.0
b_6	0.0
b_8	0.0
b_{10}	0.1
TF(T/kA)	0.764

Table IV.18. Quadrupole Multipoles*

b_n @ r = 25 mm	
	$x10^{-4}$
b_5	0.3
b_9	0.1
b_{13}	0.0
b_{17}	-0.6
TF[(T/m)/kA]	16.32

*Relative to quadrupole field. Multiply by 0.07 to normalize to dipole field.

Internal Trim Coils. The trim coil system for the RHIC must perform three main functions: correction for systematic variations in the main magnet fields (due to superconductor magnetization and iron saturation effects), correction for closed orbit dipole errors, and chromaticity correction. The last two functions are best performed with lumped correction elements near the quadrupole locations in the lattice. These are described later in this section. The first function usually is performed by an internal trim coil distributed along the length of each dipole.

The distributed trim coils correct the sextupole (b_2) multipole generated in the dipole magnets. A schematic drawing of such a trim coil is shown in Fig. IV.28. The maximum excitation current necessary to correct for the saturation is 13 A, or a small fraction of the short sample limit (70 A) of the conductor to be utilized at these fields. The forces generated by the operation of such coils are approximately 30 times lower than those which were encountered in successful trim coils for the CBA magnets.

The trim coil conductor will consist of a single superconducting wire of 0.3 mm diameter, again made of NbTi filaments twisted and embedded in a copper matrix. This wire will be insulated with Kapton tape and a braided fiberglass sleeve. The coils will be wound flat around a racetrack-shaped mandrel, by a procedure similar to that described for the main coils, with the aid of a programmable controller and cured in situ. They will then be formed to a curved shape on a cold bore stainless steel tube previously wrapped with fiberglass-epoxy and Kapton. The trim coils will be epoxy bonded to the bore tube, and layers of Kevlar thread wound "wet" over them under tension, and cured. The bonded unit will finally be wrapped with Kapton for further insulation. Longitudinal RX630 phenolic support strips will be epoxy bonded to the

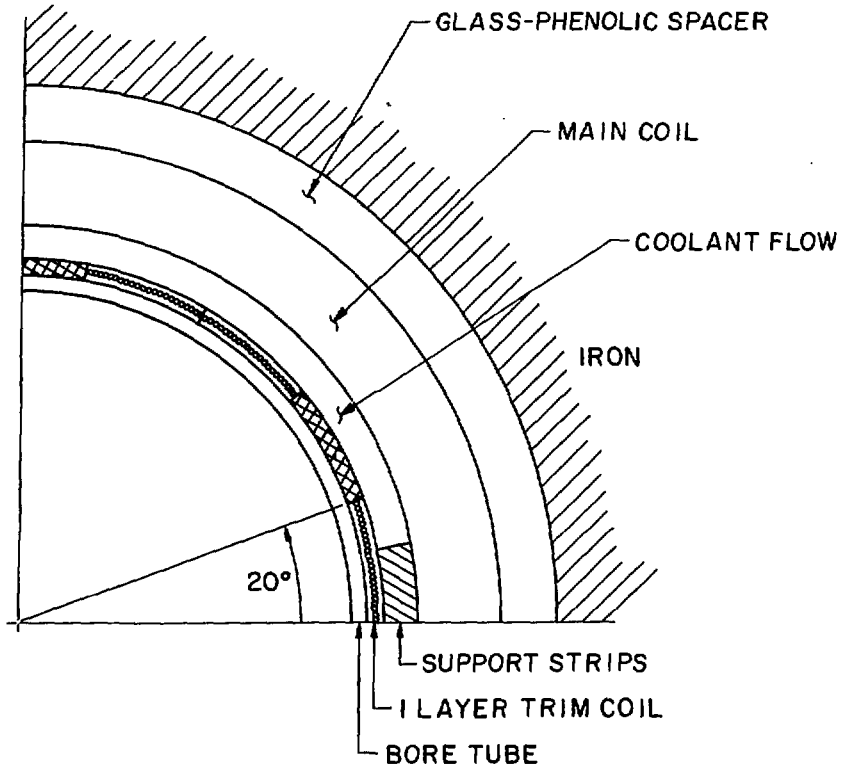

Figure IV.28. Schematic drawing of sextupole trim coil inside main dipole coil.

surface, to ensure the necessary support and helium passages between the trim coil assembly and the main coil.

Iron Yoke. The yoke assemblies, split on the mid-plane, will be produced from purchased fine-blanked, die-cut iron laminations of 5 mm thickness. The low carbon iron will have the required uniformly high permeability, low coercive force and saturation properties necessary for precision magnets. The laminations will be ground smooth after stamping and thoroughly cleaned prior to assembly.

Yoke Assembly. The method of yoke assembly and coil clamping outlined below follows, in general, the procedure developed by Brown-Boveri Corporation (BBC) for the manufacture of a prototype dipole for the HERA project at DESY in Hamburg.

After cleaning, laminations comprising an upper or lower yoke half will be stacked in a full length fixture. The stack of laminations will be held in place with the aid of stainless steel pressure plates at each end; these will be secured to each other by means of four longitudinal steel tie rods in each yoke half assembly. Special 0.7 mm-thick baffle plates will have been inserted between the standard 5 mm-thick laminations at approximately 0.3 m intervals. Their function will be to divert the coolant flow appropriately through the magnet structure. Either end of a yoke will consist of approximately 0.2 m of stainless steel laminations; these will serve to reduce the peak magnetic field in the magnet ends. In addition to providing proper alignment and clamping during assembly, the stacking fixture and longitudinal tie rods will also maintain the proper magnet bend radius.

Coil-in-Yoke Assembly. The coils will be assembled in the yoke halves with a hard mandrel, and partially compressed between the upper and lower yoke

halves. The mandrel will then be removed and replaced with a cold bore tube assembly including trim coils.

Next, the magnet sub-assembly will be placed in a lateral press provided with longitudinal stainless steel side clamping bars. The clamping bars will incorporate a beveled surface with an angle matching that of a mating surface on the yoke laminations, and will be pressed laterally against the sides of the yokes. This lateral load from the press will cause closure of the mid-plane gap between the yoke halves, resulting in a compressive stress of approximately 10,000 psi in the coil. The clamping bars will also provide the required longitudinal rigidity and thermal contraction coefficient of the structure. During the press operation multiple independent welding heads will be used for automatically welding them to the yoke assembly.

Cryostat and Vacuum Vessel. The initial cryostat assembly step will consist of welding channel-type stainless steel rails to one side of each of two iron yokes placed side-by-side and separated by their non-magnetic clamping bars; these will serve the dual function of holding the longitudinal yoke clamping bars firmly in place and of acting as the side walls of the helium containment vessel. After keying the two yokes, a central stainless steel strip will be welded directly to the top and to the bottom of the yoke laminations, thereby joining the two adjacent yokes. The cryostat cross section will be completed by welding arch-shaped stainless steel sheets between the central strips and the side rails. Flat plates welded to either end, with circular tube extensions, will complete the cryostat. It will be suspended within the vacuum vessel by means of bow-shaped fiberglass support pieces, utilizing a method similar to one developed by General Dynamics Corporation in collaboration with the

Lawrence Berkeley Laboratory. This design allows no mechanical adjustment once the assembly is completed, and will necessitate positioning by means of very accurate tooling.

During the cryostat welding operation, the yoke assembly will be held to the proper bend radius by lateral cylinders. Since the top and bottom cryostat shells will be straight, the sagitta of approximately 46 mm will be taken up by the relatively wide top and bottom surfaces of the stainless steel side rails.

Thermal insulation will have to be installed in the form of previously prepared sections of insulating blankets (aluminized Mylar and Dacron netting). The heat shield will be assembled from sections, with cooling tube extrusions attached to the inner surface of the shield at top and bottom on its vertical center line.

The bottom half of the vacuum vessel will be fabricated from 6.35 mm thick steel plate rolled into a semi-circular cross section, with four support weldments attached. The vessel half will be placed on four pads in a common plane, and holes drilled relative to that plane to receive the bow-shaped cryostat support pieces. The upper and lower heat shield halves will be prefabricated by welding cylindrical aluminum quarter shells to aluminum extrusions that provide the coolant flow channel. Next, the lower half of the heat shield will be placed in the vessel with insulating blankets already attached on the outside. The cryostat with its insulating blankets can now be inserted and pinned to the support bows.

The next step in assembly will be to fit the top half of the cylindrical heat shield into the extruded grooves extending along the edges of the bottom half of the shield. The top half of the shield will also include pre-

attached insulating blankets; these will be interleaved with the bottom set of blankets. Finally, the top half cylinder of the vacuum vessel can be lowered in place and a longitudinal weld made on each side, thus sealing the vessel. The interconnection between vacuum vessels can be a large-diameter tube and bellows assembly that will be slid back over the vessel end before assembly. This design minimizes the longitudinal space between magnet ends. Cryogenic supply and return headers will be located inside the heat shield, attached to the cryostat support bows; their particular functions are described later in the Cryogenics section.

Electrical System. The overall electrical system for the magnets, including power supplies, electrical bus and quench protection system, is described in Section IV.10. The quench-protection diodes, which divert current around a quenched magnet, will be mounted after assembly of the magnet cryostat. Superconducting main and trim coil leads, insulated with rectangular plastic poltrusions, will be inserted through rectangular channels inside the cryostat wall on top and bottom of the iron yoke, all connected and supported against the forces resulting from the interaction between currents and stray magnetic fields. Thermal expansion loops must also be installed with the leads. Instrumentation wiring leading to voltage taps across the coils, to the thermistors, pressure transducers, and other test equipment will also be installed.

ii. Magnet Testing

Magnet testing will rely heavily on the equipment and techniques developed for the CBA and currently under development for the SSC. Electrical tests will include DC resistance, AC impedance, voltage hold-off and current-leakage measurements. Magnetic measurements are described in the following paragraphs.

Symmetries and Expected Errors. The values of the multipole coefficients reflect, to a large extent, the basic symmetries in magnets. Thus, if there were ideal symmetry about the horizontal median plane (top-bottom symmetry), it follows necessarily that all the skew coefficients must vanish ($a_n \equiv 0$). If there were perfect current antisymmetry about the vertical plane (left-right antisymmetry), then the odd normal coefficients must vanish ($b_1 = 0$, $b_3 = 0$, ...), as well as the even skew coefficients ($a_o = 0$, $a_2 = 0$, ...). These two symmetries are typical of dipole magnets. In contrast, although a quadrupole magnet exhibits top-bottom symmetry, it also has a current distribution symmetric about the vertical plane (left-right symmetry). This symmetry, if perfect, would require that the even normal coefficients as well as the odd skew coefficients vanish; that is, $b_o = b_2 = .. = 0$, and $a_1 = a_3 = .. = 0$.

RHIC magnets will be constructed by compressing the coils into an iron yoke, with precision keyways providing alignment of the coils relative to the iron. This assembly technique guarantees reproducible magnetic field quality and allows the iron surface to serve as the reference point for survey and alignment.

It will be prudent to check that the magnetic center corresponds to the center of the physical aperture and that the dipole field direction in the iron corresponds to that expected from the keyed alignment. The dipole magnetic center can be calculated from observations of the non-linear sextupole contribution to the (otherwise linear) quadrupole field as a function of magnet current. The misalignment between the measuring coil and the observed magnetic axis is proportional to this non-linear contribution. In warm measurements, powering of the sextupole trim coil provides a workable method for alignment. For

quadrupole magnet measurements, the relationship between the quadrupole and dipole terms can be used to calculate the magnetic center.

The field direction in either a dipole or a quadrupole magnet is determined with a probe that has previously been calibrated with room temperature calibration magnets that have a magnetic field precisely referenced to gravity (±0.1 mrad). These techniques are routinely employed at BNL and will work well for measuring RHIC magnets.

Apparatus. Measurements of quality of the magnetic field will be made with rotating "tangential coils." Two versions of these coils are being developed in the SSC program. One type is quite similar to existing coils where the rotating wires are driven from one end by an electric motor. The other type is a short, traveling probe driven by a self-contained gas motor; the probe will be pulled through the magnet under computer control, stopping to make measurements at regular intervals. A drawing of the first traveling probe, currently under construction, is shown in Fig. IV.29. The time required for this probe to map the field over the full magnet length (at a fixed current) will be on the order of 10 minutes. It is expected that this type of development will continue over the next few years and will be generally applicable to any proposed RHIC magnet design.

Analysis. The tangential-coil measuring system and corresponding method of analysis are shown schematically in Fig. IV.30. This system is able to measure multipole-field components at the level of several parts in 10^5 through its use of precision digital voltmeters. Thus it can be (and has been) used either for room-temperature measurements while the magnet is being assembled or for "cold" measurements when the magnet has been cooled to cryogenic temperatures. For warm measurements only a few amperes can be used

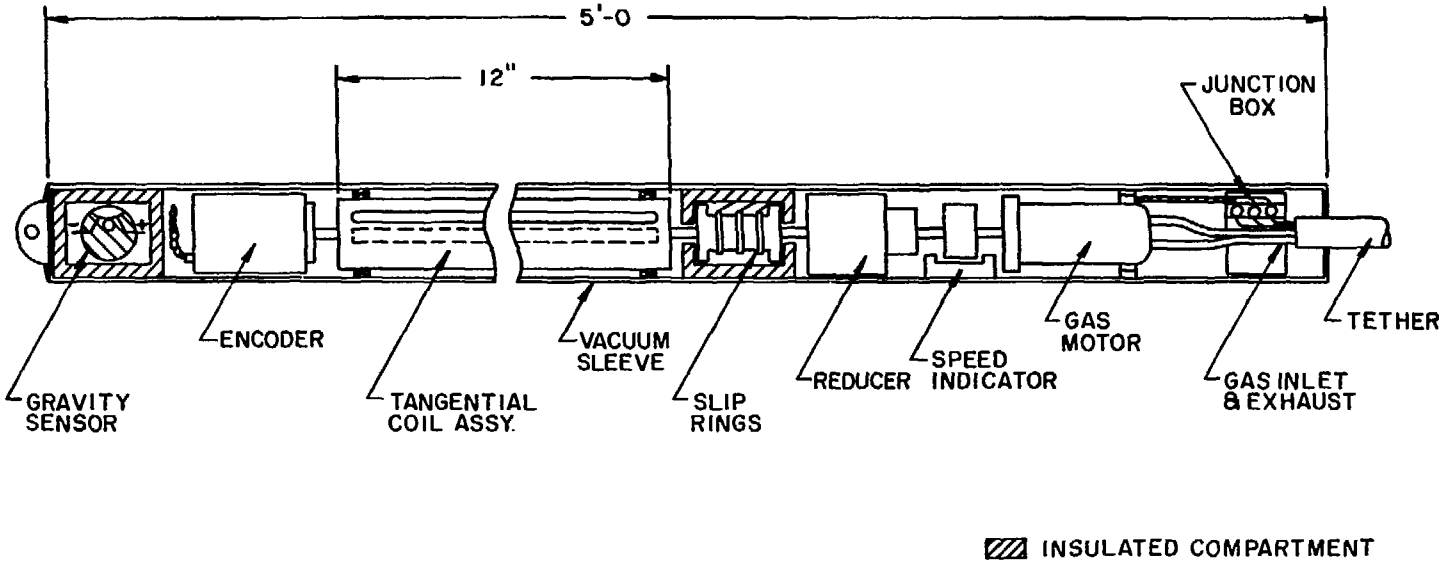

Figure IV.29. Field measurement probe.

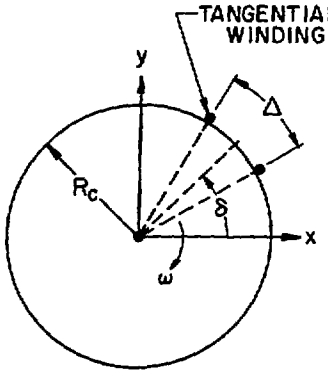

2-D FIELD REPRESENTATION IN APERTURE

$$\vec{B}(r,\theta)=\sum_{n=1} C(n)(r/R)^{n-1}\left[\vec{i}_r \sin n(\theta-\alpha_n)+\vec{i}_\theta \cos n(\theta-\alpha_n)\right]$$

VOLTAGE INDUCED IN TANGENTIAL WINDING

$$V(t)=-\sum_{n=1} C(n)(R_c/R)^{n-1} 2\ell R_c N\omega \sin(n\Delta/2) \cdot \cos n(\omega t-\delta+\alpha_n)$$

FLOW CHART–DIGITAL HARMONIC ANALYSIS

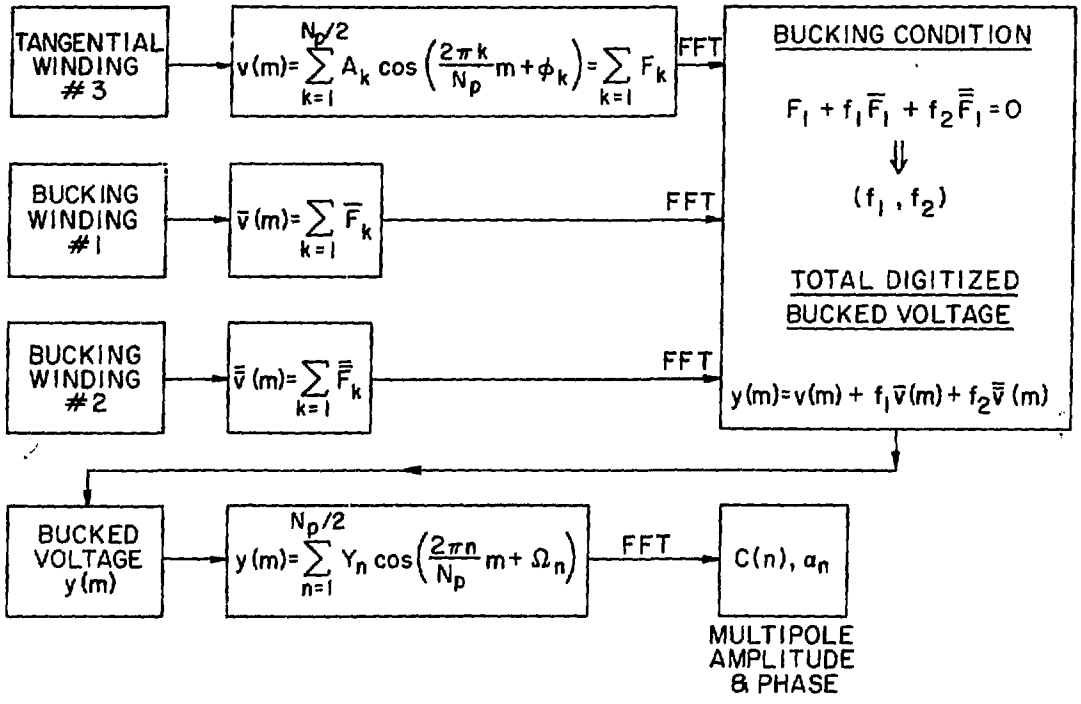

Figure IV.30. Formalism for digital harmonic analysis.

to power the magnet, so sensitivity is limited to multipoles through the 14-pole. For cold measurements, multipoles through the 26-pole are obtainable. Through the use of "digital bucking" to reduce the effect of the relatively large fundamental field, the system is completely automatic and under computer control, lending itself well to the production testing of magnets.

Extensive cross calibrations between warm and cold measurements of magnets built for the CBA program have verified that measurements of the magnetic field made on the warm magnet are in close agreement with those made on the magnet at cryogenic temperature. Thus, the warm-measurement technique can be used to reliably measure a magnet just after assembly of the coil into the yoke. In this way, manufacturing and assembly errors can be detected at an early stage and corrected before additional effort is invested in the magnet. Furthermore, systematic deviations in coil construction tolerances can be detected and corrected before too many "bad" coils are built.

Cryogenic Testing. Magnets to be tested cryogenically would be installed into the MAGCOOL system at Brookhaven. This system cools and (after testing) warms a magnet completely under computer control. MAGCOOL was designed for a throughput of 2 magnets per day; with minor modifications, it can easily handle the RHIC production rate.

Data Analysis. Rapid on-line analysis of data is essential for timely monitoring of the performance of newly built magnets. Additional off-line analysis is necesary to carry out more complex calculations (including final calibrations and corrections) and to permit statistical analysis and plotting of magnet performance. An extensive investment in software is necesary to carry out these analyses; such software has been developed at BNL for the CBA program and could easily be adapted to the RHIC program.

In summary, we believe that the testing of RHIC production magnets can be carried out with confidence and at a reasonable cost by relying on the proven efficacy of thorough room-temperature testing as well as the complete cryogenic testing of the magnets.

iii. Expected Performance

Operating and Quench Performance. Since the magnet design is, basically, very similar to that for the CBA magnets (in some respects considerably simplified), and magnet fabrication will also utilize demonstrated procedures, the magnet performance should not be significantly different from experience to date, both with respect to training as well as field quality. The CBA magnets exhibited very little training, and all exhibited a non-allowed multipole content low enough to be acceptable for accelerator use. The expected performance is summarized in Table IV.19. Note that because the magnet under discussion

Table IV.19. Operating and Quench Parameters

Operation	
Operating Current	4.68 kA
Operating Field	3.5 T
Operating Current/Copper Area	0.83 kA/mm^2
Stored Energy per Aperture	360 kJ
Inductance per Aperture	32 mH
Quench	
Quench Current	5.31 kA
Quench Field	3.96 T
Quench Current/Superconductor Area	1.97 kA/mm^2

has a lower field at the conductor than in the CBA magnets, the critical current is higher and, thus, the operating current is 25% higher than that for the former magnets. This has necessitated increasing the copper to superconductor ratio in the conductor, thus maintaining the current density in the copper and avoiding too high a temperature rise during a quench. The second part of the table shows that the margin between normal operation and quench is 13% of the operating field.

Table IV.20 gives calculated, normalized field harmonics at two different field levels: low field ($\mu=\infty$) and at maximum operating filed (3.5T). The only term of significance is the sextupole (b_2) term at high field due to iron saturation. A sextupole term of similar magnitude will occur at low field due to magnetization effects in the superconductor. As discussed earlier, the dipoles will incorporate an internal trim coil to correct for these effects.

Table IV.20. Calculated Systematic Harmonics for Dual Dipole

	Low Field Values	Maximum Field (3.5T) Values
T.F.	0.764 T/kA	0.756 T/kA
b_2	0.0×10^{-4}*	20.0×10^{-4}
b_4	0.0×10^{-4}	2.4×10^{-4}
b_6	0.0×10^{-4}	0.1×10^{-4}
b_8	0.0×10^{-4}	0.0×10^{-4}
b_{10}	0.1×10^{-4}	0.1×10^{-4}
b_{12}	-0.2×10^{-4}	-0.2×10^{-4}
b_{14}	-0.8×10^{-4}	-0.8×10^{-4}
b_{16}	0.2×10^{-4}	0.2×10^{-4}
b_{18}	0.3×10^{-4}	0.3×10^{-4}

* magnetization omitted

Figure IV.31 also shows the calculated variation of the dipole field, $\Delta B/B$, as a function of distance along the midplane (y=0) in the magnet aperture at low field and at high field. The high field curve has been plotted with the calculated sextupole term subtracted out. As can be seen from the figure, the good field requirement of $\Delta B/B \leq 2 \times 10^{-4}$ is satisfied over an aperture of ±32 mm at low field and ±26mm at high field.

Random Field Errors. The expected random field errors for the RHIC magnets may be estimated using a model in which the position of the current blocks have a random error of 0.05 mm rms. The results of the calculation are given in the following Table IV.21.

In Table IV.21, where different results are computed for b_n and a_n, the larger of the two are listed. The measured results for the Fermilab superconducting dipoles are also listed in the table. The coefficients are given at x = 25 mm in units of 10^{-4}.

The lower random multipoles, b_0, a_0, b_1, a_1, b_2, and a_2, produce well known orbit effects which can be computed.

The multipoles b_0 and a_0 produce closed orbit effects which are corrected by the closed orbit correction system.

The multipoles b_1 and a_1 produce random dispersion and coupling effects which may be corrected by a skew quadrupole correction system. In addition, these multipoles produce a half-integer stop band with a half-width of $\Delta\nu$ = 0.029 rms.

The random multipoles b_2 and a_2 produce a one-third integer stop band with a half-width of $\Delta\nu$ = 0.005 rms.

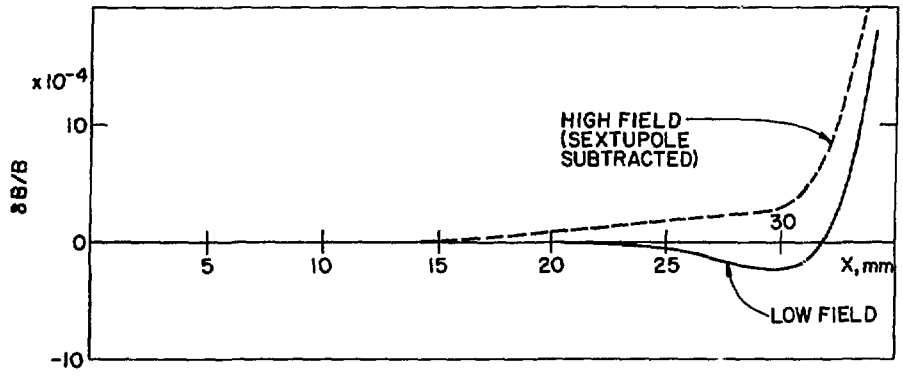

Figure IV.31. Calculated variation of dipole field as a function of distance in magnet aperture, for two different field levels.

Table IV.21. Random Field Errors for RHIC Magnets

n	RHIC expected b_n, a_n (dipoles)	RHIC expected b_n, a_n (quads)	Fermilab measured b_n, a_n (dipoles)
	$\times 10^{-4}$	$\times 10^{-4}$	$\times 10^{-4}$
0	5.0	.54	-
1	5.2	3.0	1.1
2	3.12	2.8	4.1
3	2.41	1.8	1.7
4	1.84	1.4	1.5
5	1.28	1.0	.8
6	.79	.71	1.0
7	.509	.50	.5
8	.300	.34	2.0
9	.19	.23	.6

The effects of the higher order random multipoles will be studied through tracking studies in which all the random multipoles are present.

iv. Surveying and Installation

The surveying system envisioned for RHIC is essentially an extension of the procedures developed for the CBA. Survey monuments have been accurately positioned around the ring relative to a global coordinate system. Magnet stands will be anchored in approximate locations and grouted level. Magnets will be installed relative to the survey markers in positions appropriate to the desired lattice.

The system used to support and align the magnets was originally developed by General Dynamics Corporation for the SSC program, and adopted for RHIC. The quadrupole or dipole magnet cold mass will be accurately assembled

into a dewar and the bore center lines accurately located with respect to fiduciary marks external to the vacuum vessel. The precisely aligned magnet assemblies will be placed on the stands, already in place, and aligned with respect to the survey markers. The external fiduciary marks will be used to align the magnets with respect to roll, pitch, and yaw. Quadrupoles must be aligned to within 0.25 mm, while dipoles have a larger tolerance of 0.5 mm. One of the more critical parameters, alignment of the adjoining dipole bores, will be determined by the keyed side rails. Survey of the dual magnets is estimated to require approximately 50 man hours per magnet. Installation also will require connection of the electrical leads between magnets and closure of the helium containment bellows and bore tubes. Bellows are provided at each interconnection to match the thermal contraction of the magnets. The total number of man hours required for interconnections of each dual magnet is estimated to be 120.

v. Special Magnets

Magnets for the Insertion Sections. The optical design of the insertions is considerably more complex than that of the regular cells; at this time it is still preliminary. In addition, the magnets nearest the crossing points must be special purpose, high performance designs. For these two reasons, the details of the magnets in the insertions are not yet finalized. The information presented in this section represents a plausible design, and the overall properties such as the number and type of magnets, are not expected to change. The details, such as quadrupole gradients, lengths and apertures, will most probably differ in the final version.

In the proposed collider the two rings are required to run with unequal beam rigidities. This means that the inner and outer apertures in each magnet must be powered by separate supplies. The insertion regions must also be

independently tuneable. A plausible powering system would be main power supplies for the inner and outer arcs of each insertion, with detailed tuning provided by several auxilary power supplies of approximately 10% of the capacity of the main supplies. These auxilary supplies could be used either to trim the main quadrupoles directly or through a separate trim coil. It is practical to use this independent adjustment capability to provide the required gradients for all eight quadrupoles with only 5 physically different magnet types. Table IV.22 lists the various insertion quadrupoles (and dipoles) in this insertion example, and Table IV.23 lists the main parameters of the quadrupoles. Inspection of Table IV.23 reveals that seven (of 9) are standard quadrupoles with various lengths. The necessary gradients for QC and Q1 can be achieved with small modifications of the CBA two-layer coil design. The only anticipated complexity is the comparatively close spacing of the bores in QC; the significantly different operating current for a two-layer quadrupole will require a separate power supply system for these magnets.

The equivalent parameters for the dipoles are presented in Table IV.24. BC1 is a much larger dipole than any of the others in this machine; however its parameters are easily achievable with standard superconducting technology. There will only be 12 of these magnets in the entire machine and they will require a special design. BC2 is approximately a reduced (4T) field version of a CBA dipole. BS1 and BS2 are simply shortened RHIC dipoles.

Lumped Correction Elements. The corrections necessay for beam dynamics--particularly the chromaticity sextupoles--will be generated by lumped elements which will be part of the quadrupole assembly. This device will have a magnetic length of 1 meter and will be mechanically split into two sections which will be assembled on either end of the quadrupole as shown in Fig. IV.32.

Table IV.22. Representative Parameters for Insertion Magnets*

Dual Quadrupoles (9 per Half-Insertion)

7-with lengths from 0.5 to 2.0 times the standard length (1.2m), but otherwise identical to the standard dual quadrupoles.

1-(Q1i/O) large aperture dual quadrupole (a modification of the CBA two-layer coil design).

1-(QCi/O) is a large aperture dual quadrupole of maximum strength and non-standard bore spacing.

Dual Dipoles (3 per Half-Insertion)

2-(BS1,BS2) standard dual dipoles, but only 6.883 m long.

1-(BC2) large aperture 4 Tesla dual dipole (modified CBA two-layer coil design).

Special Dipole (Single Aperture)

1-Large aperture dipole (BC1), magnetic length $\sqrt{3}$ m, maximum field $\sqrt{4}$ tesla.

Total Number of Insertion Magnets

Dual Quadrupoles	108
Dual Dipoles	36
Special Dipoles	12

*Preliminary parameters. Both the optical and mechanical details of the design are incomplete. These parameters define a plausible insertion, but will be modified as the design progresses. The nomenclature for designating the various magnets is more fully defined in Tables IV.23 and IV.24.

Table IV.23. Insertion Quadrupoles - Example Parameters

Name	QxL (Tesla)	Q (Tesla/m)	Length (m)	Layers	Beam Size x(mm)	Beam Size y(mm)	Coil ID (mm)
Q8i/o <1>	79.47	67.35	1.18	1	...	...<2>	75
Q7i/o	109.72	75.67	1.45	1	...	...	75
Q6i/o	92.27	73.82	1.25	1	30	7	75
Q5i/o	95.34	76.27	1.25	1	9	26	75
Q4i/o	82.90	70.25	1.18	1	...	...	75
Q3i/o	119.46	74.66	1.60	1	...	...	75
Q2i/o	89.68	71.24	1.25	1	...	...	75
Q1i/o	84.98	65.37	1.30	2	22	46	138
QCi/o <3>	112.01	67.88	1.65	2	45	20	138

Note 1: Q8i/o are "half" in the insertions and "half" part of the regular cells. They are counted as part of the insertions. Thus for the insertions 12 x 1 = 12 dual quadrupoles will be required, which will be designated Q8i/o. For the other eight types 12 of each will also be needed. The inner and outer apertures of a dual quadrupole are designated Qni and Qno; thus there is one dual unit which may be referred to as Qn or Qni/o. The fields are different in the two apertures - but this does not affect the construction or unit count. For this example insertion design the fields in the inner and outer apertures differ by less 1%. For this table the average values are used.

Note 2: The beam half sizes given are the maximum at 30 GeV/amu operation. Where they are not significantly larger than the maximum values (25 mm) in the regular cells they are ommitted.

Note 3: QC will be a special design with apertures close together than standard and not parallel. Probably a 2-layer quadrupole similar to CBA.

Table IV.24. Insertion Dipoles

Name	BxL (Tesla•m)	B (Tesla)	Length (m)	Beam Half-Size x(mm)	Beam Half-Size y(mm)	Coil ID mm
BC1 single aperture	12.17	4.0	3.040	75	13	225x40
BC2	13.01	4.0	3.252	45	45	135
BS1	24.091	3.5	6.883	8	25	75
BS2	24.091	3.5	6.883	29	7	75

The correction windings will be mounted on the common bore tube with the quadrupole and the entire assembly of quadrupole and correction windings compressed inside standard iron laminations as shown in Fig. IV.33. This yoke is excessive for the correction windings, but there are mechanical advantages in using the same laminations and assembly techniques. In addition, the iron will provide mechanical alignment between the correction coils and the quadrupoles. Because many of the correction windings will be individually powered there will be numerous feed-throughs and copious bus work. To minimize the cost of these parts of the system it is desirable to use a relatively modest current. This encourages a design with a comparatively large number of turns of moderate size conductor. The magnetic parameters of the design developed with these constraints are given in Table IV.25. The functions and details of the individual correction terms are discussed below.

The strongest field component which must be generated by these elements is the sextupole (b_2). Two independent sets of sextupole windings are required to correct the chromaticity in the quadrupoles. Studies are in progress to determine whether it will be necessary to further subdivide these into

additional sets, for the correction of the shape of the working line and the dependence of the ν-values on the amplitude of the betatron oscillation.

Table IV.25. Parameters for Lumped Correction Elements

Overall Description

Type: Multi-layer with $a_o/b_o, b_1, b_2$ windings

Magnetic Length	2 x 0.5 m
Iron I.D.	140 mm
Iron Height	260 mm
Iron Width	260 mm

Conductor

Type: Solid round NbTi conductor

Short Sample Limit (at 1 Tesla)	~825 A
Diameter (bare)	1.0 mm
Diameter (Insulated)	1.25 mm

Winding Parameters

	Multipoles			
	b_2	b_1	a_o/b_o	Misc.
Number of Layers	3	2	2	2
Turns per Layer-Pole	11	20	46	(40)
Coil radius (mm-mean)	40	47	55	60
Operating Current (Amperes)	750	160	230	--
Coil Field (Tesla)	1.0	0.14	0.32	--
Multipole Strength	600 T/m	3 T	0.2 T•m	--

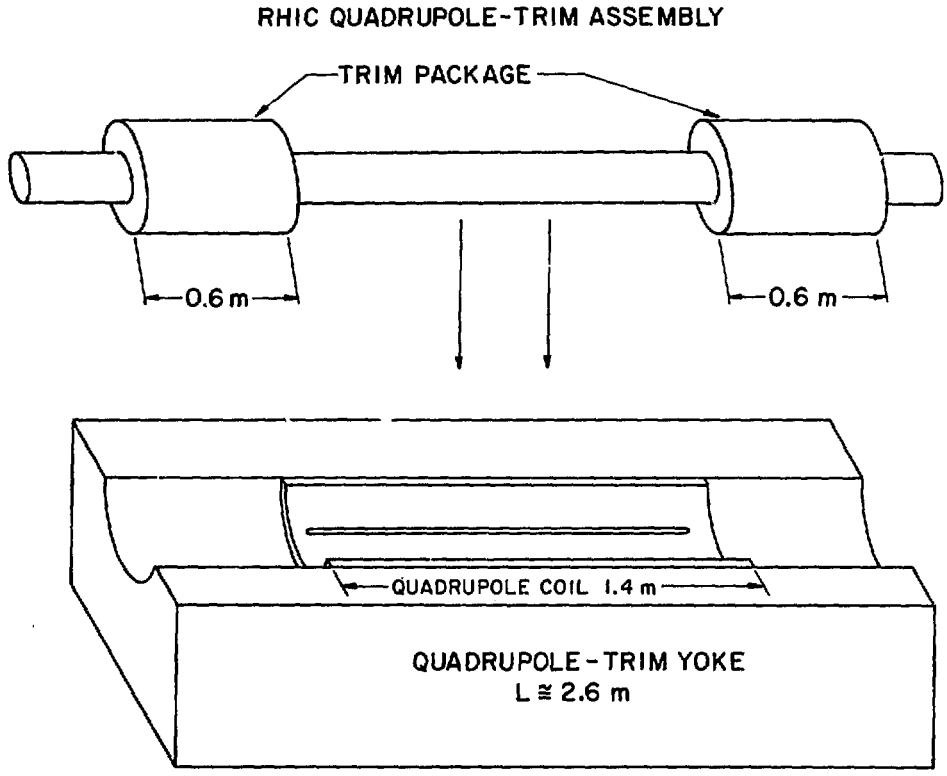

Figure IV.32. Quadrupole-trim coil assembly.

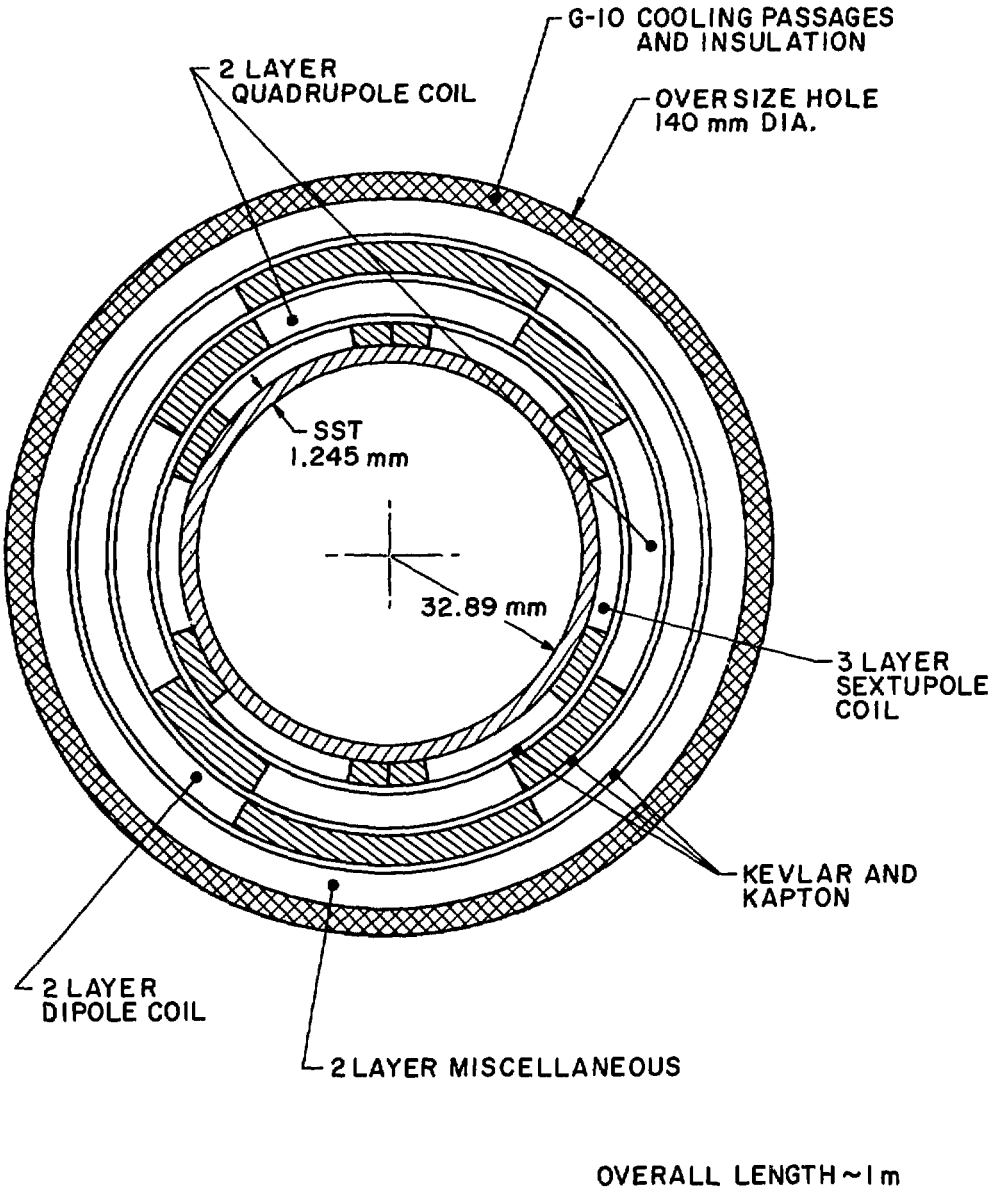

Figure IV.33. Trim coil cross section.

The next set of windings in the correction element are the quadrupole (b_1). These are wired to provide adjustment of the tune (ν) perpendicular to the diagonal. The capacity is sufficient to provide $\Delta\nu = \pm 0.5$ at full energy and $\pm$ 1.5 at transition. Tune adjustments along the diagonal will be provided by the quadrupole bypass with capacity $\Delta\nu = \pm 1.5$ at full energy and ± 4.0 at transition.

A third set of windings will be needed to provide closed orbit corrections. The design strength of these dipoles has been chosen to be equivalent to a quadrupole displacement of ±2 mm (0.2 T•m). Since they are intended to correct local errors they must be individually powered.

The present design provides for an additional two layers for corrections which are not yet specified. At the start of actual construction these layers will be specified (or possibly omitted).

Correction Elements in the Insertions. The optical design of the insertions is still being refined and hence the exact requirements for correction elements in these portions of the accelerator are not yet determined. It is known that the following will be required:

1) quadrupole corrections to facilitate tuning the insertions;

2) dipole corrections for steering;

3) sextupole corrections for chromaticity adjustment.

4) skew quadrupoles for coupling and dispersion correction.

It is possible that there will also be a need for octupoles. Within the insertions quadrupoles Q6-Q8 will have the standard correction assembly described above. The special quadrupole QC will require a special correction assembly because of the space constraints. The remaining quadrupoles in the insertion are

at present intended to have a scaled down version of the standard correction elements.

vi. Production Scenario

Figure IV.34 shows a schedule for magnet production. This schedule spans five years with two and a half years for research and development preceding and partially overlapping three years for magnet fabrication and installation. The rate of magnet production increases in a series of steps until peak rates of 27 dual dipoles per quarter (2.2 per week), 16 dual quadrupoles per quarter (1.3 per week), and 32 "spool pieces" containing lumped correction elements per quarter (2.6 per week) are achieved in FY 1989. These rates continue for a full year until a total of 192 dipoles, 144 quadrupoles for the regular arcs, 102 insertion quadrupoles, and 246 spool pieces are completed

During the R&D phase, six short dipoles of 4.5 m length will be constructed, and then, immediately prior to commencement of production, 3 full-length (9.3 m) dipoles will be fabricated. In addition, six quadrupoles and six spool pieces will be fabricated and tested during the first two years. Insertion quadrupoles and dipoles will be developed after start of production to allow time to finalize the ring lattice and define the detailed insertion requirements. Ten R&D insertion quadrupoles and two insertion dipoles will be constructed prior to the start of production of these magnets in FY 1988.

Magnet Production Facilities. In order to achieve the peak rates in the schedule, most of the facilities originally developed for the CBA will be required.

The factory plan, from subassembly to completion of a magnet, must necessarily include provision for movement of parts and subassembly components between plants. Thousands of interchangeable machined parts will be fabricated by

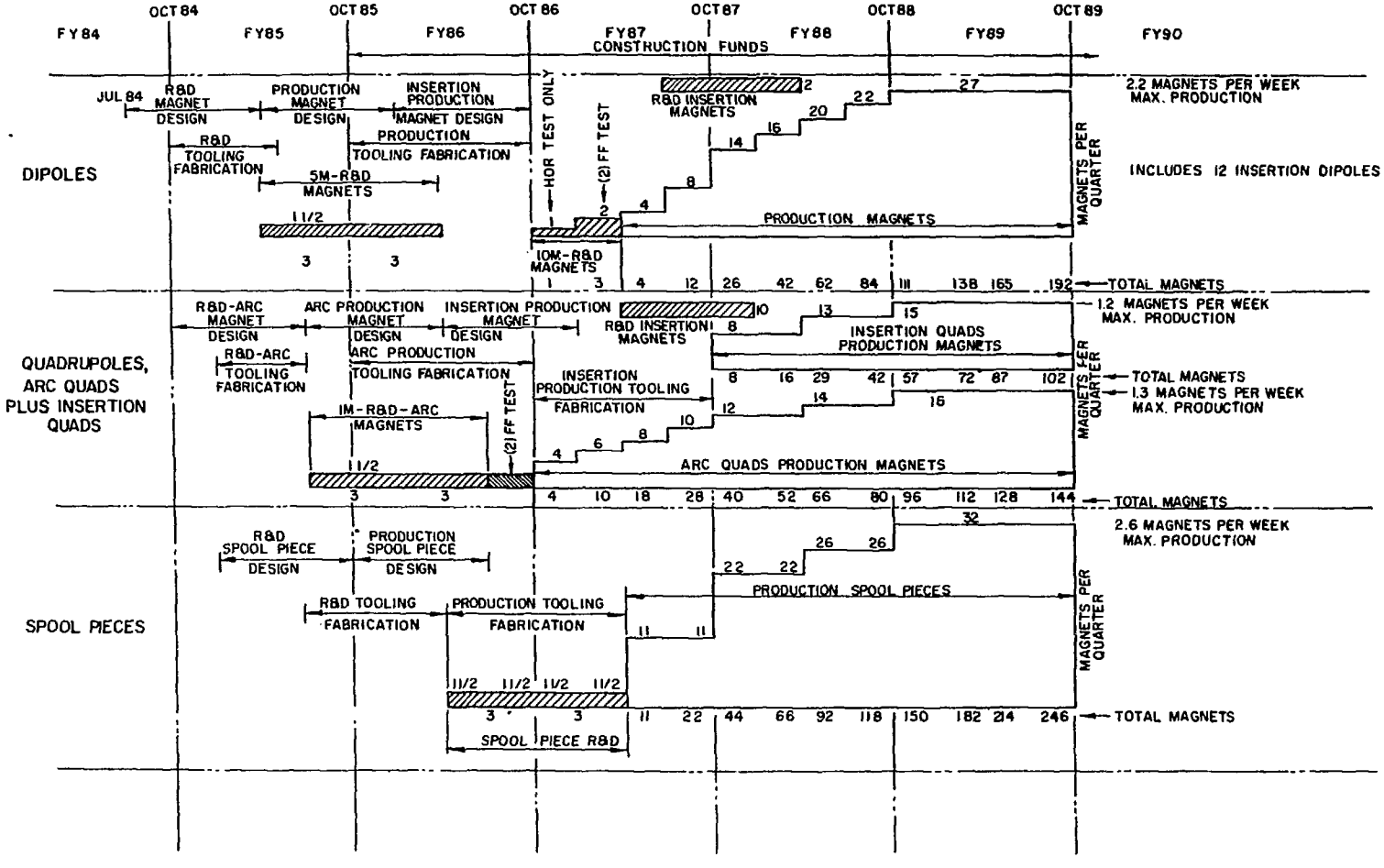

Figure IV.34. Magnet production schedule.

vendors. Upon arrival at any factory building, they will be quality inspected, warehoused, and will enter the production line in a timely and organized manner. A "Production and Material Control" system will be developed to handle the tasks of maintaining an orderly flow of materials, parts and subassemblies to the magnet assembly complex. Inventory control will be accomplished using data processing techniques.

The quality assurance plan that is envisioned will be integrated into every aspect of the factory complex from incoming receipt inspection to the installation of magnets in the tunnel. "Travelers" or specifications, which follow each magnet in production, will also be incorporated. This, coupled with a uniform inspection procedure, will maintain a record on each magnet. All procurements will be subject to incoming inspection as well as specification review. Age or environmentally sensitive materials will be subject to strict controls to ensure life and reliability.

Subassembly. During the construction of the CBA, three major factories totalling approximately 50,000 square feet were in use, and are presently used for SSC R&D. Various subcomponents of the RHIC magnets will have to be assembled prior to being installed in the magnet coil or yoke. Overall efficiency of production will be increased by designating separate areas for completing specific subassembly work. Plants would also house stock rooms, parts cleaning facilities and receiving inspection. The components in subassembly form would be placed in storerooms as kits, distributed to the major assembly areas as needed.

Main Coil Assembly (Bldg. 924). The components for the quadrupole and dipole coils will consist of spools of pre-insulated NbTi cable (stored in an adjacent refrigerator to stabilize the epoxy in the pre-coated insulation), spacer

wedges, coil end spacers and inserts (stored in stockrooms awaiting assembly into kits). As described earlier, the coils will be wound by an automated method developed for the CBA project. The wound coils will be secured to the winding mandrel with a wrap of Tedlar film, which also will act as a mold release agent during the curing operation. The mandrel with coil will be transferred to a fixture which applies the prescribed amount of heat and pressure to cure the coil. After curing, the coil will be inspected, tested electrically and placed in special storage containers, ready to be forwarded to the yoke assembly area. Prototype (4.5-m long) dipole coils will be wound and cured with existing fixtures, but the longer production dipole coils will require new, longer fixtures and tooling. Production quadrupole coils can be wound with existing fixtures, but will also require tooling for a new curing fixture.

Trim Coil Fabrication Facility (Bldg. 924). The procedure for winding the internal (b_2) dipole trim coils, mounting them on the electrically insulated cold bore beam tube, and completing the trim coil package, have been described in an earlier section. The trim coil winder is presently located in Bldg. 924, and it remains to be determined whether the curing and grinding equipment necessary will be located in this area or elsewhere. The present winder, although adequate for 4.5-m long prototype coils, will require an extension to provide sextupole trim coils for full-length production dipoles.

Yoke, Coil-in-Yoke, and Cryostat Assembly (Bldg. 905). In this facility iron laminations, pole spacer subassemblies and various component kits will be received from stock rooms and the subassembly area, and main and trim coils from Bldg. 924. The yoke assembly, as it passes through the factory, will increase in weight rapidly. Components will be handled with conveyors supplemented by overhead cranes.

The present coil-to-yoke assembly facility in Bldg. 905 will require modification to handle the longer RHIC dipoles. The existing quadrupole fixtures are adequate in length, but will require modification to facilitate handling. Existing yoke module block facilities will continue to be used for fabrication of R&D magnets. It is anticipated, however, that loose laminations will be used for production magnets--a development from the SSC program. This method will avoid yoke block handling and curing, thus reducing costs and facilitating production.

The yoke laminations will be inserted into temporary support tube halves, one half the length of a magnet in the case of a dipole. The two lengths will be butted together to form one complete half yoke assembly. The steps of assembly of main and trim coils into the yoke halves, joining of yoke halves into a complete split yoke assembly, clamping in a hydraulic press, installation of side rails, bending and welding, have been outlined earlier. Building. 905 also contains the magnet warm measurement facility.

Although the existing yoke press in Bldg. 905 is adequate for R&D magnets, a new press must be constructed to handle the assembly and bending of production dipoles. Provisions for automatic welding will be incorporated in the press to hold the laminations and side rails after the magnets are bent to the required sagitta. Additional welding and handling equipment will be incorporated for joining the two individual magnets together and final closure of the helium containment vessel.

Final Assembly and Testing (Bldg. 902). The final assembly steps, including electrical bus work, vacuum vessel with heat shield, thermal insulation and cryogenic headers, have been described previously. After all internal assembly steps have been completed, final electrical checks and leak testing

will be performed, all closures and surfaces protected, and temporary supports installed for transport of the magnet. The last operation, before installing a magnet in the tunnel, will be its testing in the MAGCOOL test facility utilizing instrumentation and procedures outlined earlier.

References

1. R.B. Palmer et al., "Superconducting Magnets for the CBA Project," Submitted to Nuclear Instruments and Methods; also BNL Formal Report No. 34863.

2. SSC: Reference Designs Study Group, Draft II (May 8, 1984), unpublished.

3. J. Allinger, A. Carroll, G. Danby, B. DeVito, J. Jackson, W. Leonhardt, A. Prodell and J. Smarita, IEEE Trans. Magnetics MAG-19 (1983) 1348.

IV.5. Refrigeration System

The main feature of the proposed RHIC cryogenic system (shown in Figure IV.35) is the helium refrigerator, whose installation is now nearly complete. The refrigerator was designed to match the load of the CBA Project (allowing a capacity to load margin of 1.5) with a primary capacity of 24.8 kW at about 4 degrees Kelvin, and secondary capacity of 55 kW at about 55 K. Both these capacities are three times the estimated heat loads for RHIC. The refrigeration is transmitted to the load by heat exchange with single-phase, supercritical pressure helium circulated in a loop. The helium enters the loop at a low temperature (4.3 K), which is produced by heat exchange in two subcooler pots containing liquid helium pumped on by two cold turbo-compressors used as vacuum pumps. Work is removed from the helium in the refrigerator proper, by expanding it against five large, low speed, oil bearing turbines. High reliability is provided by incorporating redundant partners for all components which are subject to fouling by contaminants.

The compressor station consists of 25 identical screw compressors, arranged into ranks of first and second stages, and including an oil removal system. Despite the great reliability of this type of compressor, redundancy is provided here also. This station is being constructed by the same company as is building the refrigerator, and to the same required date.

Single-phase helium coolant from the refrigerator flows once around the ring through each magnet in series. The temperature of helium entering each sextant is 4.3 K and it leaves at 4.6 K. The coolant helium is recooled between sextants to its original temperature in a recooler heat exchanger which has boiling liquid helium on its low pressure side. Four pipes extending around the ring carry the helium to and from the recoolers and are used, as required, for

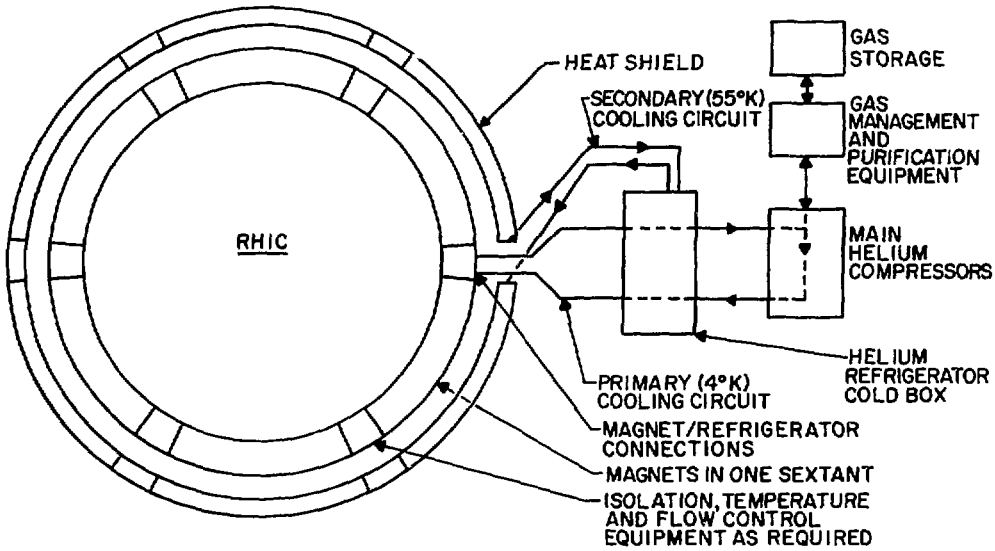

Figure IV.35 Simplified Drawing of RHIC Cryogenic System.

cooldown and warm-up operations. These four pipes are located in the vacuum spaces of the magnets except at straight sections, e.g., insertion regions, where there are no magnets and there the cryogenic piping proceeds in its own vacuum jacket across these regions. All the pipes share a common jacket and heat shield.

Control will be provided by a "standard" industrial process control system of well-proven and flexible design. It will involve a hierarchy of microprocessors for sensor interpretation and device control, supervised by small distributed computers for compressor station, refrigerator and ring, and a host computer overseeing all and providing a central control point with operators' consoles in the Cryogenic Wing. A link will also be installed to the main machine control room so that the system required for operation of the refrigerator, its compressor station, and all tunnel components are on hand.

i. Design Load and Refrigerator Size

As designed, the machine will consist of 180 superconducting dual dipoles and 246 superconducting dual quadrupoles, and 12 common dipoles, arranged in six sextants and connected within each sextant by cryogenic transfer lines carrying the interconnecting (superconducting) leads. At each end of each sextant gas cooled power leads are provided to carry the main leads out to room temperature, cooling them with a small flow of helium "stolen" from the main cooling circuit. The lower current leads for correction and steering are brought to room temperature at the spool pieces in groups or "bunches". Allowance can also be made for helium to be withdrawn from the main circuit to cool experimenters' equipment. Finally, a portion of the total load is imposed by the piping needed to distribute the refrigerant to the load.

The load is composed of three parts: 1) the "primary" load, defined as that portion maintained at temperatures below 4.6 K; 2) the "secondary" load, imposed on the 55 K heat shields surrounding all primary loads, and 3) the "liquefaction" load, consisting of the gas flows "stolen" from the primary refrigerant for cooling leads and experimental equipment, and returned to the cryogenic system at room temperature. The liquefaction load (nominally in units of g/sec) is converted to equivalent watts and lumped together with the primary load.

The expected load has been estimated for all components. Table IV.26 shows the load calculated for individual magnets, and Table IV.27 summarizes the sources of heat for the entire machine.

Given the magnitude of the expected load, it is usually necessary to choose a design refrigerator capacity to "match it." In the case of RHIC, the capacity is already fixed. The ratio of capacity to load has extremely important effects. A large ratio is desirable for faster cooldown and for ability to maintain operations in the face of increased heat load, (e.g., due to vacuum

Table IV.26. Individual Magnet Heat Load Allowance

	Allowed Load - Watts					
	Dipole (9m)		Quad (1.3m)		Spool (2m)	
	4K	55K	4K	55K	4K	55K
Insulation - radiation and conduction @ 10^{-4} Torr	4.0	20.0	1.4	4.0	1.5	5.0
Supports	0.3	2.0	0.3	1.0	0.3	1.0
Connecting Piping	1.0	3.0	1.0	3.0	1.0	3.0
Other	0.5	----	0.5	---	0.2	2.0
Total	5.8	25.0	3.2	8.0	3.0	11.0

Table IV.27. RHIC Heat Load Allowance

	Primary Load Watts @ 4.6K	Secondary Load Watts @ 55K	
Magnet System			
192 Dipoles	1100	4800	
246 Quadrupoles	790	2000	Includes Insertions
246 Spool Pieces	740	2700	
Insertion Magnet Connecting Pipe	300	1200	
Total	2940	10700	
Magnet Power Leads			
Main Coils	750	---	Includes conduction
Correction Coils	2150	---	& liquefaction load
Lead Pots (included in spool pieces)	---	---	
Total	2900	0	
Distribution System			
Piping	150	1800	
Valves	500	2500	
Total	650	4300	
Experimental Area Detectors			
(1000 liter/hr. Equiv.)	1800	---	
Total Expected Load	8290	15000	
Refrigerator Capacity	24800	55000	

leaks) or decreased refrigeration capacity (e.g., due to contamination). A ratio of 2 or more is typical for small existing systems. A ratio of 1.5 had been chosen for the CBA system. The ratio of capacity to load for RHIC is 3.

ii. System Design

A detailed review of the capital cost and operating economics of distributed vs centralized systems and of the expected differences in reliabil-

ity (assuming certain redundancies in a centralized refrigerator), resulted in the choice of centralization as the preferred system for the CBA. A conceptual design for the entire system was then produced, and the compressor and refrigerator portions of it were contracted to Koch Process Systems, Inc. Both are well along in construction, with no further room for design change without additional cost.

A block diagram of the system is shown in Figure IV.35. Figure IV.36 shows the helium flow circuit during steady-state operation. As shown there, the helium from the refrigerator passes alternately through a sextant of magnets (in series) and then through one of the five recoolers. The heat which is picked up from the magnets in each sextant is removed by heat exchange with boiling liquid helium in the recooler. See Figure IV.37 and Table IV.28.

After the helium has passed through all of the sextants a fraction of the flow is sent through the Recooler Supply Header (one of the pipes in the magnet vacuum space), to a control valve at each recooler which meters the required amount of helium to maintain a constant level in its recooler. The helium which is not required by recoolers is sent to the "High Pot" in the refrigerator where it is used to cool helium on its way to the magnets.

The helium vapor from the recoolers is returned to the refrigerator in two parallel pipes located in the magnet vacuum space, Return Header No. 1 and Return Header No. 2. The flow from these two headers goes to the suction of a two-stage cold turbocompressor located in the cold box. This compressor maintains the low pressure in the return line so that the temperature in the recoolers is at the desired low level.

A flow through the heat shield piping is also maintained during steady-state operation. This flow is from the Secondary (40 K to 70 K) Section

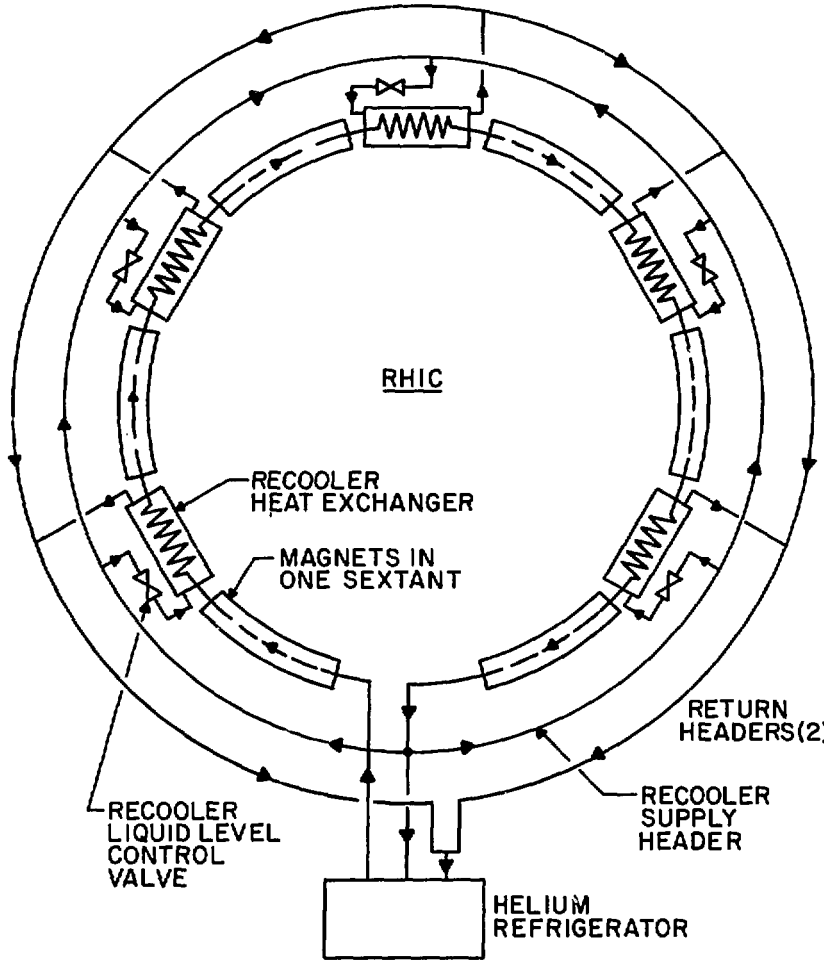

Figure IV.36. Helium primary flow circuit for steady-state operation.

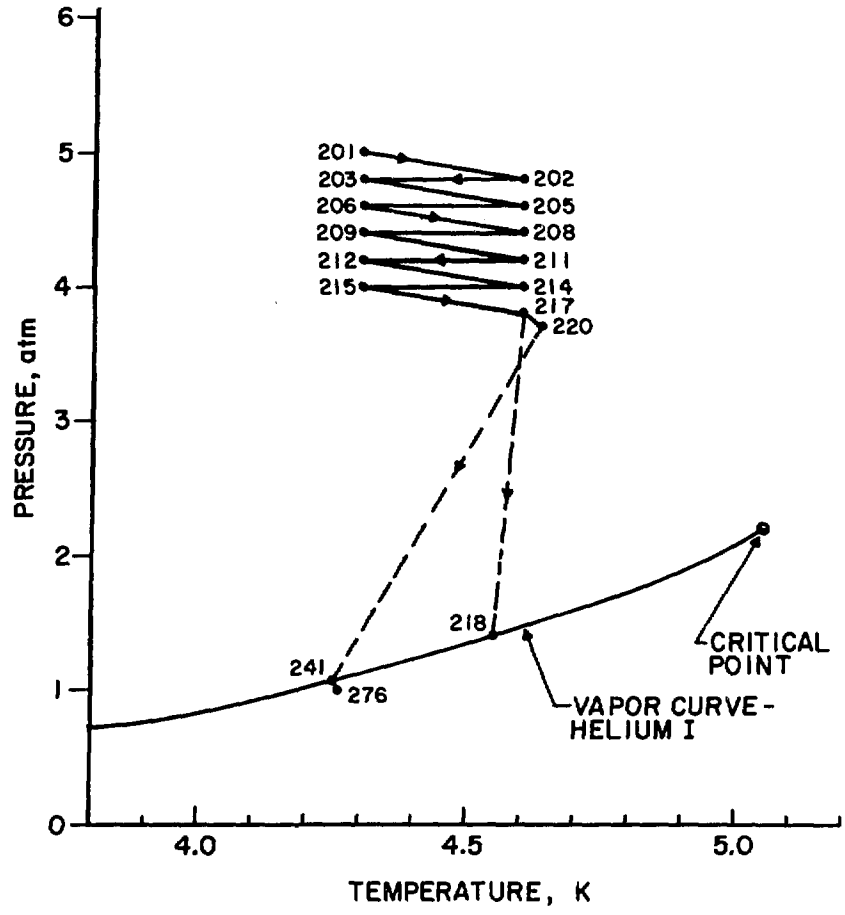

Figure IV.37. Load process diagram on helium pressure-temperature plot.

Table IV.28. Process Point Description for Figure IV.37

Process Points	Description
201	Conditions at Inlet to Magnets (6 O'Clock)
201-202	Heat Input from Sextant 7
202-203	Heat Removed in Recooler (8 O'Clock)
203-205	Heat Input from Sextant 9
205-206	Heat Removed in Recooler (10 O'Clock)
206-208	Heat Input from Sextant 11
208-209	Heat Removed in Recooler (12 O'Clock)
209-211	Heat Input from Sextant 1
211-212	Heat Removed in Recooler (2 O'Clock)
212-214	Heat Input from Sextant 3
214-215	Heat Removed in Recooler (4 O'Clock)
215-217	Heat Input from Sextant 5
217-218	Portion of Flow Sent to High Pot
217-220	Flow in Recooler Supply Header
220-241	Expansion Across Recooler Level Control Valve (Typical)
241	Boiling Liquid/Vapor in Recooler
241-276	Flow in Return Headers (2)
276	Conditions at Return to Refrigerator
276-201 218-201	Net Effect of Refrigerator

of the refrigerator and is not shown in Figure IV.36 to simplify the drawing. The flow in this circuit is once around the ring in two parallel pipes, passing through all heat shields in series. One other header, the Cooldown/Warm-up

Header, is also not shown in Figure IV.36. It is shown, along with all the other piping mentioned above and the valves required to effect the magnet/refrigerator connections in Figure IV.38. The piping in the "typical" half of Figure IV.38 occurs five places around the ring (2, 4, 8, 10 and 12 O'Clock).

The Cooldown/Repair/Warm-up Header is used in conjunction with other piping to permit warm-up/cooldown cycles of any one sextant without requiring that any other sextant be cycled with the ailing one. It is estimated that the warm-up/repair/cooldown cycle can be accomplished in 5 to 6 days. When it becomes necessary to repair a cold section, the sextant containing that section will be isolated by closing the valves between that sextant and the two adjacent sextants. A warm helium gas flow would then be sent through the Cooldown/Warm-up Header, through the ailing sextant and back through one of the Return pipes. When warm-up is complete the ailing sextant is isolated and repairs can be effected. During this warm-up and repair period, the other sextants can be maintained near their normal temperature. When the repairs and leak check have been completed, the repaired sextant is purged and then cooled using the same piping path as during warm-up.

iii. Refrigerator Design

A simplified schematic of the refrigerator, together with its load, is shown in Figure IV.39 (Brown, Schlafke, Wu and Moore, 1981). The system proposed for RHIC is a simplification of the original CBA cycle. A cold compressor which was used to circulate helium through the magnets in the CBA design has been eliminated because the high flow rate produced by that compressor is not required for RHIC.

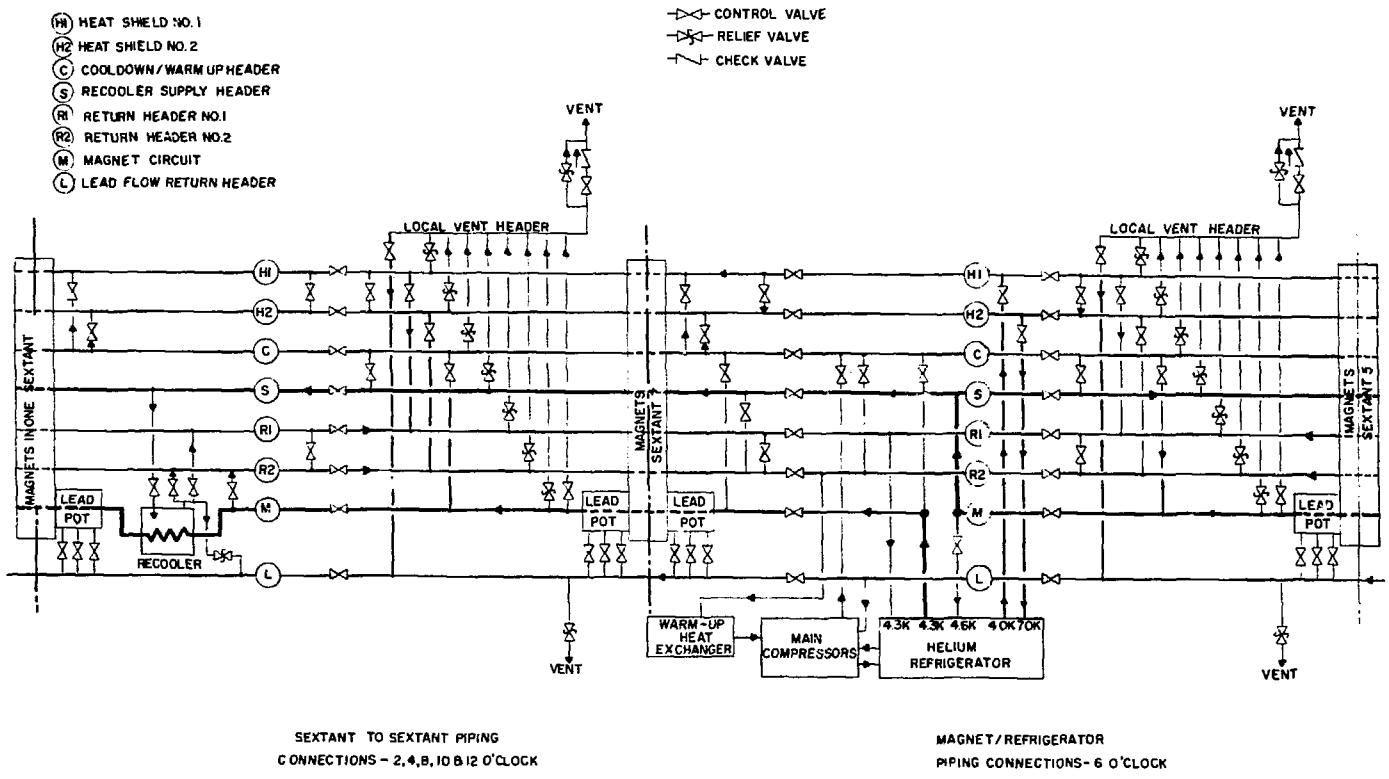

Figure IV.38. RHIC Helium Distribution System Piping Diagram.

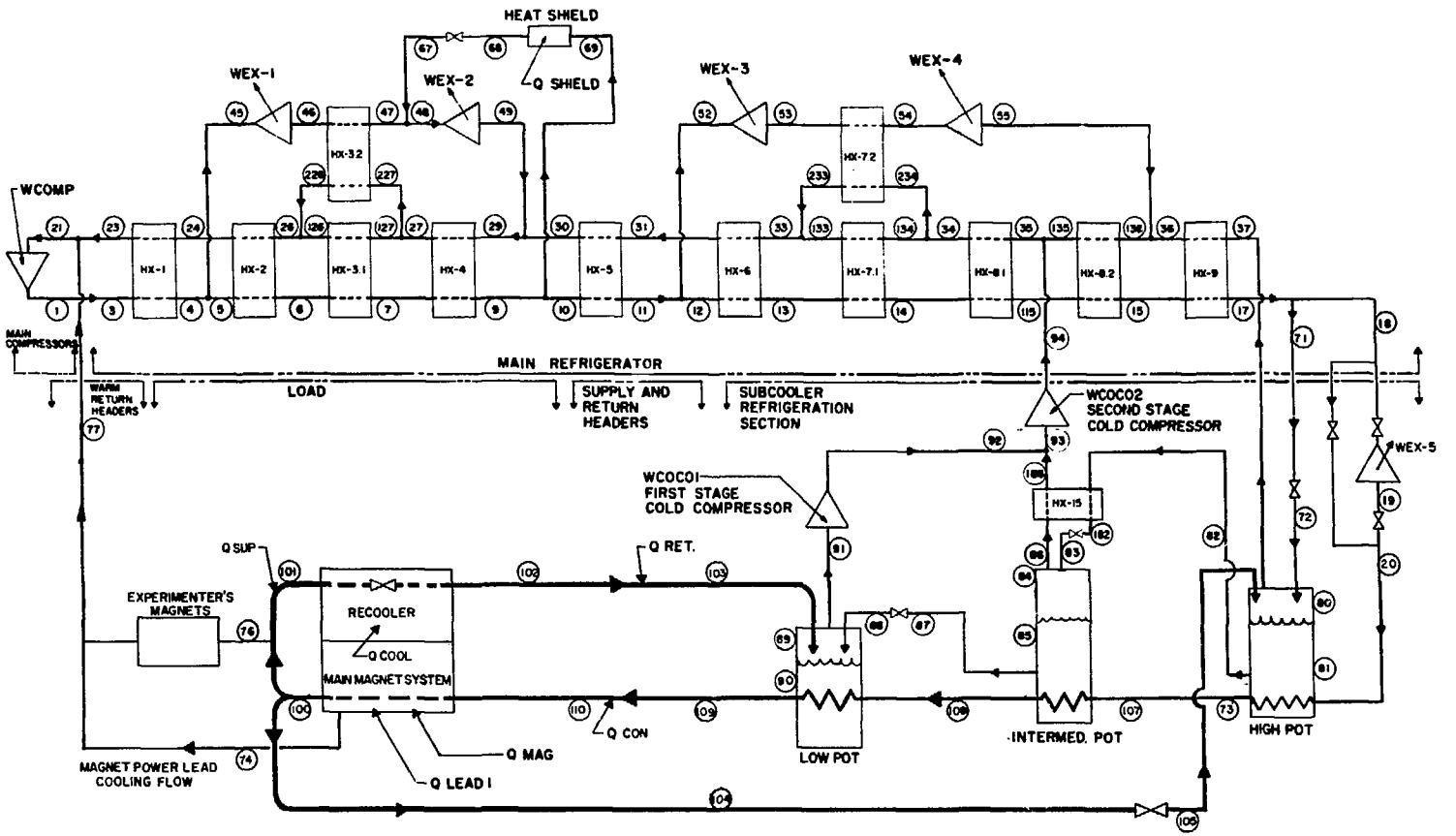

Figure IV.39. Refrigeration system schematic.

In Figure IV.39, the flow from the main refrigerator heat exchangers (point 17) will, in steady-state operation, pass through a final expander (WEX-5) and then pass through heat exchangers located in three "pots." The pots contain boiling liquid at progressively lower pressure (and temperature). The main helium flow will exit from these heat exchangers (point 109) at a pressure of 5 atm and temperature of 4.3 K. The helium returns from the load in two streams. One stream (point 104) returns at 3.8 atm and 4.6 K and is then expanded through a J-T valve (between points 104 and 105) and partially liquefies. The liquid is accumulated in the high pot and the vapor is directed to the bottom of the main refrigerator heat exchanger train (low pressure side). The liquid from the high pot is distributed to the intermediate pot and from there to the low pot as required to maintain their levels. These two pots are pumped to their required low pressures by the two stages of a cold compressor (labelled WCOCO1 and WCOCO2).

The second stream from the load is the vapor which returns from the recoolers. It returns at a pressure of 1 atm and temperature of 4.25 K. This flow enters the low pot as shown in Figure IV.39.

In order to give the refrigerator higher capacity at higher ouput temperatures to speed cooldown, and to make its operation reliable in the face of possible contaminants in the gas stream, it has been provided with a number of redundancies not shown on Fig. IV.39. The low temperature end of HX-2 is at 154 K, so any water and oil which might remain in trace amounts should freeze out on the surfaces of the first two exchangers. These are provided as redundant pairs so that they can be valved on and off line, allowing the contaminated ones to be warmed and cleaned without stopping the refrigerator. Similarly, turboexpanders 1, 2, 3, and 4 have redundant partners. Expander 5 operates below 7 K; all

contaminants will have been frozen out above that temperature. In addition, a pair of redundant activated-charcoal cryogenic adsorbers is provided between HX-3.1 and HX-4 (at 70 K) to remove any traces of O_2 or N_2 which may enter the system. All of the rotating machinery is large, uses oil lubricated room-temperature bearings, and runs at speeds below all shaft resonances. Such machinery in other installations displays mean times between failure of several tens of thousands of hours. It can be expected to run for many years of RHIC operation without mechanical breakdown.

The main compressors consist of 19 parallel first stages and 5 parallel second stages with a pressure ratio of about 4 across each stage to achieve the 16 atm pressure and approximately 4000 gm/sec flow required at the refrigerator inlet. They are all identical oil-injected screw compressors, chosen primarily for high reliability and low cost. There is considerable experience with such compressors, here and elsewhere, showing mean times between failure of more than 30,000 hours, or about five years of RHIC operation. In order to avoid any chance of significant running time loss due to compressor failure there is an installed redundant compressor for either first or second stage. The contractor (Koch) has purchased the compressors from Howden in Glasgow, in order to get the highest quality available. In addition, the compressors have been selected for high isothermal efficiency on the basis of test runs in the factory. Those used as first stages are driven by 600 HP motors, and second stages by 2250 HP motors. Four stages of coalescers for oil removal are provided in each of six parallel paths. A maximum of five paths are required, allowing on-line replacement of elements in the sixth. These are followed by a single stage of charcoal adsorption in each of three parallel paths, where two are required.

iv. Cooldown and Operation

At normal operating temperatures, the main compressor flow is matched to the flow capacity of the five turboexpanders. However, at higher temperatures the gas has lower density, and the redundant expanders can be used simultaneously with their mates. By using appropriate ones at various temperature levels, the cooldown capacity of the refrigerator can be increased greatly over its steady-state capacity. The cooldown presents three sequential but overlapping loads: 1) removal of heat from the magnet structure; 2) cooling of a large quantity of helium to fill the headers and magnets, and 3) cooling of both to final operating temperature with the refrigerator in its normal configuration. While the time required for the first two is greatly reduced by the use of the redundant expanders, the time for the third depends entirely on the ratio of capacity to load and the second depends partly on this ratio. Cooldown of the entire machine should be accomplished in ~10 days.

The management of the large quantity of helium in this system during cooldown and operation is an important factor in attaining stability. Most cryogenic systems are designed for constant pressure, and therefore require venting or adding gas to the system to control pressure whenever there are temperature or other fluctuations in the load. The RHIC system, on the other hand, is designed to maintain a constant mass of helium in the load. The intended operating line is shown in Fig. IV.40. Cooldown proceeds with the helium pressure in the load at 14 atm. When an average temperature of about 6.5 K is reached, the helium density will be 0.136 gm/cc, which is the final desired density at the nominal average operating point (5 atm, 4.4 K). No more helium will be added to the system after that time. The cooldown, therefore, will phase smoothly into operation.

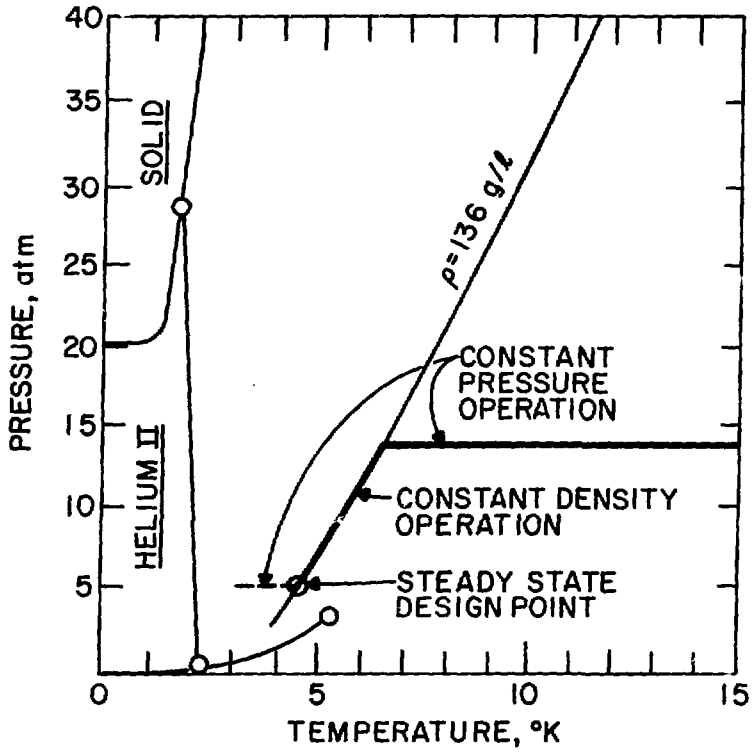

Figure IV.40. Shows constant pressure operation during cooldown at about 14 atm. When the average temperature is 6.5 K, the final system density will have been reached and the system will be operated in a constant density mode thereafter.

During operation, no venting will be required unless the average temperature rises to 6.5 K, in which case the pressure will again be 14 atm. The magnets and cryogenic system are designed for a working pressure of 20 atm. The temperature is measured after each half-cell of magnets and at many other points throughout the system. The process control computer will monitor these temperatures and compute the desired pressure to hold constant density in the system. Thus, if there is any leakage from the system, the loss will be detected and gas added as required.

It is anticipated that the entire machine will not be warmed to room temperature frequently. Very likely this would be confined to yearly machine maintenance shutdowns. It is of somewhat more interest to examine the time required for repair, e.g. replacement of a magnet. For this, only one sextant will be warmed, while the rest of the machine remains at low temperature. Such a warmup, including end effects, is estimated to require two days, and recooling, two additional days. To this thermal cycle time must be added the warm repair time, and for magnet replacement this is estimated at two days also, after some initial practice. Thus a complete magnet replacement should take $\sim$6 days.

v. Instrumentation and Controls

Through a process of selection and calibration of semi-conducting diodes and the use of inexpensive PROMs to contain individual calibration curves, BNL produces for its own use temperature measuring devices good to 0.05 K through the entire range 300 K $\rightarrow$ 2.5 K (Sondericker, 1981). These, together with thermistors good below $\sim$7 K, are being used throughout the cryogenic system including the refrigerator. An ultrasonic time-of-flight helium flow measuring device, usable also over the entire temperature range, has been developed at BNL,

and will be used at several places in the system. Pressure measurement will be done using commercially available sensors.

For control of the cryogenic system, a "standard" industrial process control computer system will be used. The requirements in this regard are so similar to those of the petrochemical industry, that it is possible to choose from a large number of such systems, all well tested and unusually user-friendly. Such a system was purchased in 1981 to be used for control of MAGCOOL, the production magnet testing facility. It has proven to be extremely easy to interface with complicated systems, and has been used by several technicians, both electronic and mechanical, with minimal training.

At the top of the cryogenic control system for the RHIC is a host processor located in a local cryogenic operations area. Peripherals include alarm and logging typewriters, a program development CRT and color graphics operator interface displays. The host provides the drive capability for the operator's color consoles and performs communications, polling and data storage and retrieval duties. Compressor room, refrigerator and ring distributed processors will be similar, each handling its own data acquisition and control tasks. Initially, these satellites are down loaded from the host with an operating system, control logic and communications programs so they can act as stand alone process control modules. Distributed microprocessors periodically send important data to the host computer for real time display and trending purposes. Data transmissions can also be event (process upset) or operator initiated. An interface to the main machine control room computer network will be provided so that the cryogenic control system can be operated from main control when the RHIC begins operation.

vi. Current Status

Koch Process Systems, Inc. (KPS) is under contract to provide both the refrigerator and the compressor system. All major components have been delivered to BNL and are in place. Piping and other installation work as required by the KPS Contract was started in September, 1983. They are progressing at a satisfactory rate. The critical path for initiation of acceptance testing is the cooling water distribution system which must be completed before the compressors can be tested. It is expected that the test will begin by December, 1984.

BNL is providing the Cryogenic Control System. All required components are on hand and installation has begun. Software development is well advanced and appears to be on schedule.

References

D.P. Brown, et al.; "Design of 24.8 kW, 3.8 K Cryogenic System for Isabelle", Advances in Cryogenic Engineering, 27, 509 (1981).

D.P. Brown, A.P. Schlafke, K.C. Wu, and R.W. Moore, "Cycle Design for the Isabelle Helium Refrigerator", Advances in Cryogenic Engineering, 27, 501 (1981).

K.C. Wu and D.P. Brown, "Analysis of Cooldown Performance for Isabelle Helium Refrigerator", Advances in Cryogenic Engineering, 27, 525 (1981).

A.P. Werner, D.P. Brown, and W.J. Schneider, "Heat Load Measurement of Prototype Cryogenic Magnets and Leads for the Isabelle Project", Advances in Cryogenic Engineering, 27, 517 (1981).

J.H. Sondericker, "Production and Use of High Grade Silicon Diode Temperature Sensors", Advances in Cryogenic Engineering, 27, 1163 (1981).

D.P. Brown, Update of Cryogenic Refrigeration Requirements for Isabelle, ISA Tech. Note 243 (1980).

W.J. Schneider and J.H. Sondericker, Heat Load Measurements of Prototype Transfer Lines, ISA Tech. Note 358 (1982).

D.P Brown and K.C. Wu, Choice of Design Pressure for Helium Coolant of Isabelle Magnet System, ISA Tech. Note 88 (1979).

IV.6. Vacuum System

In RHIC, there will be two completely independent vacuum systems. One, which operates in the 10^{-10} Torr region, provides the required environment for the circulating proton beam. The other system maintains an insulating vacuum of less than 10^{-5} Torr in the superconducting magnet vessels. At this pressure the heat loss by convection becomes negligible.

i. Beam Vacuum

The major portion of the beam tube will operate at liquid helium temperature which will result in an immeasurably low pressure if helium leaks are avoided. The experimental straight sections as well as some longer sections without magnets, which accommodate rf cavities, injection, ejection and scraping equipment, will operate at room temperature with H_2 pressure of $\sim 1 \times 10^{-10}$ Torr. At this pressure the beam loss due to nuclear scattering will be 1.6×10^{-4} per hour for protons, giving a beam life time of 6000 hrs. Beam life time for gold will be 460 hours. Emittance growth of 1 mm due to multiple Coulomb scattering would require 400 hrs for protons at $\gamma = 30$. Since the scattering cross sections vary as $(Z/A)^2$ the growth rate for heavier ions will be proportionately smaller.

Beam neutralization for bunched beams will be accomplished by self clearing due to the large spacing between bunches of $\sim 2 \times 10^{-7}$ sec.

The pressure bump instability in the cold bore is not anticipated, based on the experience at FNAL. In warm sections, $\eta I_{critical}$ will have a sufficient safety margin for the design current.

The warm sections in the beam vacuum are separated from those which are cold by cold-to-warm transistions and polyimide gate valves. Warm sections will have a provision for a bake-out at $\sim 250°C$, with the exception of the

polyimide-sealed gate valves, which can be baked up to 200°C, the highest temperature the polyimide seals can take. If later experience demonstrates this not to be satisfactory, the valves can easily be replaced with more expensive all-metal valves. The intersections will be isolated by metal gate valves and will be baked to 300°C.

In the 6 bending arcs, which have cold bore, a pumping port will be provided at every second quadrupole and will be equipped with a 20ℓ/s ion pump to be used as a high vacuum gauge during operation, a convectron gauge to read higher pressures during pump down, and an all-metal hand valve for roughing. The convectron gauge with a set point will also act as a hard wired interlock. The beam tube will be evacuated by portable turbomolecular stations that will connect to the all-metal hand valves. A pick-up electrode will be placed at every quadrupole. Its coaxial cables will be brought out of the dewar through the insulating vacuum. In this way ceramic feed-thrus operating at cryogenic temperature will not see liquid helium and small leaks will not disturb the beam vacuum. To minimize vacuum leaks in the high vacuum beam tube, it is imperative that no feed-thru and a minimum of welds and bellows be in contact with cryogenic helium.

Warm sections, including the crossing points, will use conventional all metal UHV components such as ion pumps, titanium sublimators and BA gauges.

ii. Insulating Vacuum

The insulating vacuum will be divided into ∿60 m long sections by vacuum barriers installed in the magnet dewars. On either side of the barrier there will be a pump-out port containing a cold cathode gauge, a thermocouple gauge and a hand valve. There will be no permanent pumps installed since none are required if helium leaks are avoided or kept very small. Instead, pumping

carts similar to the UHV roughing station, but simpler, will be used to evacuate the insulating vacuum through the ports at vacuum barriers. After cool-down these carts will be valved off. If a gauge indicates an increase in pressure, one of these pumping carts will be used to pump on the leak. There will be 25 of these cart units. The UHV roughing station can also be used here.

IV.7. Beam Transfer and Injection

The AGS will serve as the injector for the heavy ion Collider. Beam will be ejected from the AGS in a single revolution, making use of the existing fast extraction system in the North Area, and it will be transferred to the Collider through the already existing beam transfer tunnel. The geometry of the beam transfer and injection magnet system will be identical to that described for the CBA Project (see Figure IV.41).

The beam current will be accumulated in the Collider rings by the "box-car" stacking technique. The AGS will be accelerating a single ion bunch at a time, and initially each of the rings will accept up to 57 equally spaced bunches into the 342 waiting rf buckets. This limitation is the consequence of the initial specification for the kicker rise time of about 150 nsec. In the case of protons, the AGS will deliver pulses containing 11 bunches at a time, filling 55 waiting buckets in a similar manner.

Before an AGS pulse is transferred to the Collider, the two rf systems will be synchronized in frequency and phase so that the AGS bunches arrive well centered in the waiting buckets. In addition to arriving at the proper time (phase), the bunches must also have the proper momentum. At the given frequency this is accomplished by ejecting at a certain magnetic field in the AGS (or equivalently at a certain radial position) which is in a proper and reproducible relation to the Collider injection field. Thus, while the rf systems are locked in frequency and phase and the Collider field is held constant, an integrating flux probe in the AGS (or a high sensitivity radial pickup electrode) will enable the extraction trigger at the appropriate field value during a slow AGS field ramp. With a flux probe a field reproducibility of $\sim 2 \times 10^{-5}$ (rms short

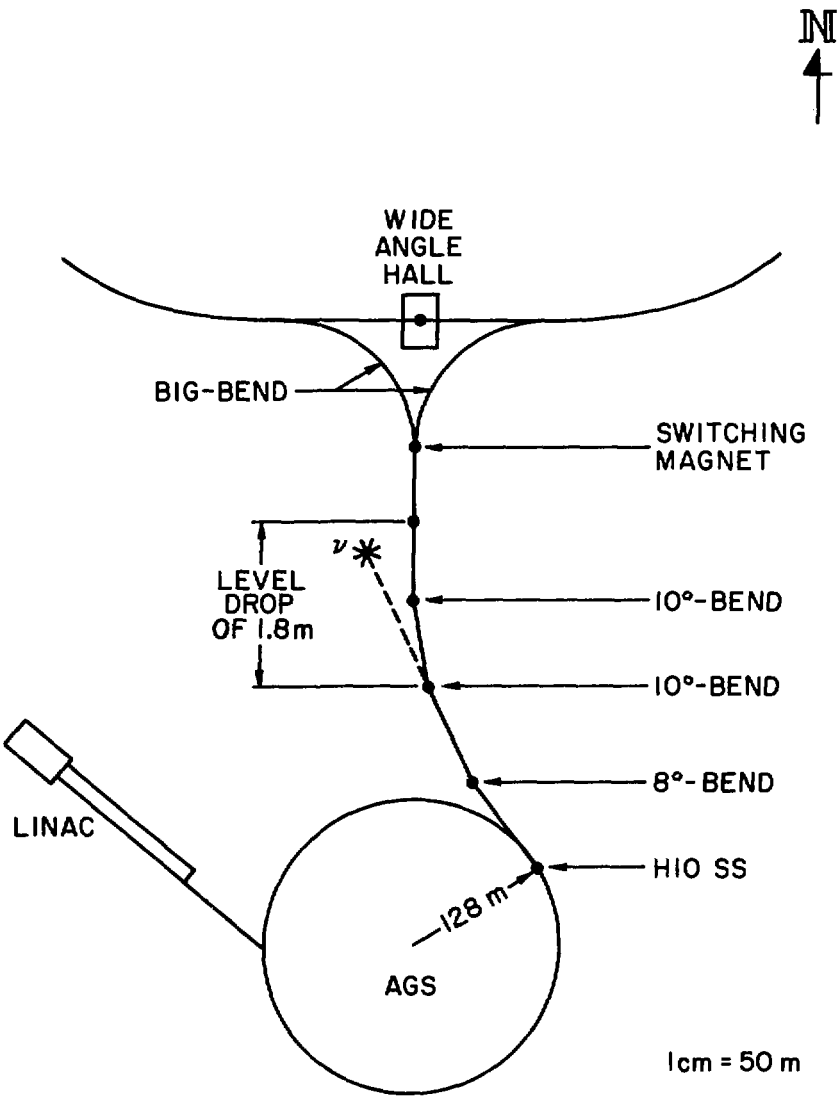

Figure IV.41. Schematic layout of the beam transfer line from the AGS to RHIC.

term) has been achieved in the AGS and the Collider injection field is to be held constant with similar precision throughout the beam transfer process. Deliberate energy or phase mismatches may be introduced to shape the longitudinal beam distributions.

The beam transfer magnets are conventional and the major bending sections employ a combined function magnet design. Near the Collider tunnel, distinct, separately excited quadrupoles and dipoles provide tuneability for steering and matching flexibility. Beam diagnostic equipment (current transformers, pickup electrodes, secondary emission beam profile wire arrays, beam loss monitors) will be located in appropriate places to facilitate efficient analysis of beam properties. Adjustable collimators will be placed near the entrance of the big bend and near the injection areas to provide a sharp re-definition of the transverse emittance limits prior to beam insertion into the Collider.

The beam is injected onto the central orbit of the Colliders' outer arcs. The injection components take up the free spaces in the outer dispersion suppression regions of the 6 o'clock insertions. Injection occurs in the horizontal plane. The beam approaches the rings, on the horizontal mid-plane, upstream of the horizontally defocussing lattice quadrupoles, Q70. A series of thin current septum magnets will take the beam close to the equilibrium orbit so that it will pass through the Q70 beam aperture. The beam will then meet the equilibrium orbit at the location of the fast kicker (upstream of Q80) which will provide the necessary deflection to deposit the beam in the proper circulating beam trajectory of the Collider. The current septum magnets will be pulsed with millisecond pulse duration and they will be designed to have negligible magnetic fringe fields in the region of the circulating beam close to the

septum conductor. The fast kicker will cover the full aperture of the Collider beam. It will have a rise time to full field of about 150 nsec in order to permit the successive insertion of bunches from the AGS with bunch spacing of about 220 nsec without disturbing the already circulating bunches. In the future, a faster kicker rise time would make it possible to accept more bunches, thus increasing the luminosity.

In general, error tolerances for various beam component specifications are such that undue dilution of transverse and longitudinal phase space is avoided.

The beam transfer line magnets will be identical to those designed and already partially manufactured for the CBA Project.

IV.8. RF System and Acceleration

i. General Considerations

The rf system must capture, accelerate, and store for many hours 57 bunches of particles. Particle species vary from protons to gold ions. Each function places certain requirements on the rf design. The choice of frequency, 26.74 MHz or h = 342, and peak voltage 1.2 MV, were dictated by the need to provide sufficient longitudinal phase space area to accommodate the bunch area dilution due to intrabeam scattering that will occur during the time the beams are stored for experimental data taking. A frequency change of about 1% must be allowed in order to decelerate as well as accelerate the heavier ions (4×10^{-3} for acceleration of Au ions alone). Since it is planned to use six high voltage (200 kV) high-Q cavities some provision for the small amount of tuning must be made.

The acceleration period of 60 sec for all species will result in a stable phase angle given by $\sin \theta_s = 0.04$, assuming a linear rise in the field and a constant voltage of 1.2 MV peak. This will provide more than adequate bucket area for the bunches, which will have a longitudinal emittance of 0.3 eVsec/amu at injection and perhaps as much as 1 eVsec/amu after passing the transition energy.

When the bunches are accelerated, the gap voltage V_{gap} = 200 kV and the power per cavity delivered to the beam will be $V_{gap}\, i_b \sin \theta_s/2$, where i_b is the component of beam current at the rf frequency. For $\sin \theta_s = 0.04$ and $i_b \lesssim$ 0.12 A (corresponding to 1.1×10^9 Au ions/bunch) this is less than 0.5 kW, which is a small fraction of the 20-25 kW of rf power dissipated in the cavity and its driver. During the injection process, when 57 bunches will be sequentially stacked box car fashion into every sixth rf bucket (h = 342), it

will be necessary to reduce the voltage per gap to ≲32 kV in order to match these bunches to the phase space trajectories in the chosen buckets. Because of the reduced voltage and the stationary buckets, the reactive beam loading will be a maximum at this time. However, the cavity detuning necessary to compensate for this effect is very small and in the same direction as needed for acceleration of the heavier ions. Hence, no additional tuning range will be required. In order to damp injection errors and to provide control of coupled-bunch instabilities, a separate low voltage, wide bandwidth, i.e. several rotation harmonics, cavity and power amplifier will also be required in each ring.

One additional requirement on the rf system in the storage mode is that of very low noise at multiples of the synchrotron frequency (f_s = 47–64 Hz at 100 GeV/amu) and of the rotation frequency, f_o, namely $(f_{rf} \pm nf_s)$ and $(f_{rf} \pm (f_o \pm nf_s))$ by which the rf signal can be modulated. A single bunch phase lock loop and low noise voltage controlled oscillator, along with a low noise frequency control loop as used at the CERN SPS collider, will be employed to reduce the effects of noise on all of the bunches. An additional lower gain phase correction loop acting on all the other bunches to correct for noise at $f_{rf} \pm f_o$ will be closed through the wideband auxillary cavity mentioned above. The goal of this system will be to assure that only the longitudinal dilution due to intrabeam scattering will limit the useful luminosity lifetime.

ii. The RF Cavities

Because of the constraint on radial separation between the two rings these will be capacitively loaded coaxial resonators. A sketch of the proposed design is given in Figure IV.42. Also shown is one possible method of tuning the structure by varying the position of a diaphragm opposite the cavity disc. Due to the high gap voltage (200 kV) the cavity is operated in vacuum with a nom-

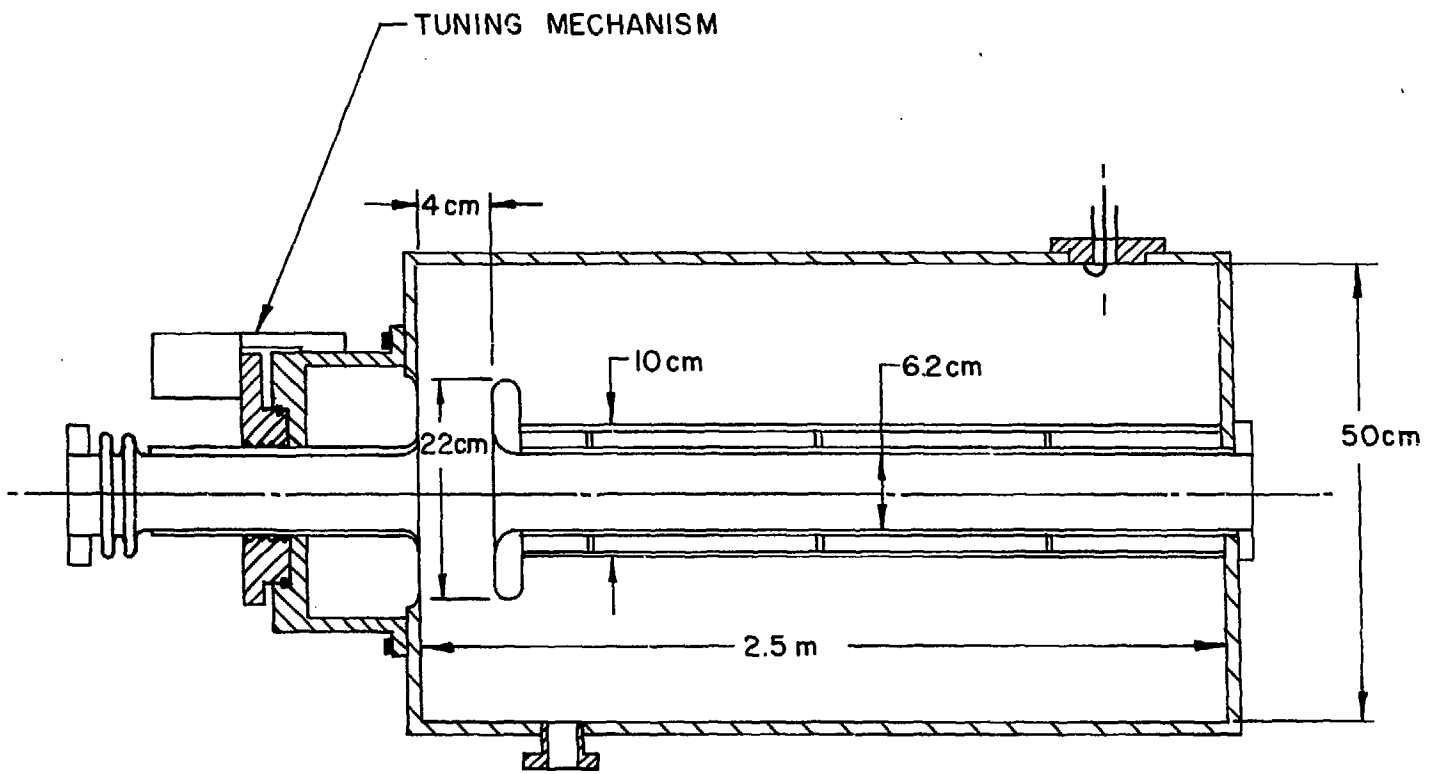

Figure IV.42. RF cavity for RHIC, including possible tuning mechanism.

inal gap spacing of 4 cm. Each cavity has its own vacuum system, not shown in the figure. For the dimensions shown, the tuning capacity provided by the disc is about 16 μ pf. Computer calculations for an ideal copper structure give $Q \approx 10^4$, $R_{SH} \approx 0.9$ MΩ, and about 22 kW of excitation power required at $V_{gap} = 200$ kV. It is planned to drive the cavity from a tetrode with a 20:1 voltage step-up ratio. More detailed design studies, as well as modeling, will be required in order to assure that all higher modes of the structure, including the coupling network, are damped.

The auxiliary cavity will necessarily be of the same general design. However, because the voltage requirement will be much less, the gap can be in air. It will be driven by a low impedance source more tightly coupled to the gap.

IV.9. Beam Dump System

The energy contained in the heavy ion beams is of the order of 300 kJ, which may cause damage to accelerator components if lost in an uncontrolled manner. Moreover, a small fraction of this energy, if dissipated in a superconducting magnet winding, may quench the magnet string. Therefore, whenever deviations from normal operations are detected which may permit the beams to stray beyond a safe region within the vacuum chamber, the beam dump system will be activated. The response time to such deviation will be about 50 μsec to maintain control over events in all conceivable cases of accidents or beam instabilities. The beam dump system will not only serve in emergencies but also serve for routine beam disposal prior to a refill of the rings.

Beam dump systems which employ internal absorber blocks and which do not resort to extraction from the machine have been in routine use at the CERN ISR, where the stored beam energy exceeded 3 MJ. For the superconducting magnet lattice of HERA an internal beam dump has been proposed as well, for a beam with 8 MJ stored energy. On the other hand, for the CBA beam (40 MJ) an external disposal system had been judged necessary, because within the machine it was not possible to spread the beam over a large enough volume to prevent absorber damage, and because it was not possible to prevent quenching of magnets downstream of an absorber, from secondary particle spray.

The stored energy of the heavy ion beam is low enough to be safely disposable on an internal dump without magnet quenching. The layout of the beam dump system in one of the straight sections not used by experimenters is shown in Figure IV.43. A fast kicker near the matching section quadrupole Q4I will be triggered to deliver a deflection to produce a transverse displacement of about 20 mm in the absorber block located near insertion quadrupole Q2I. The

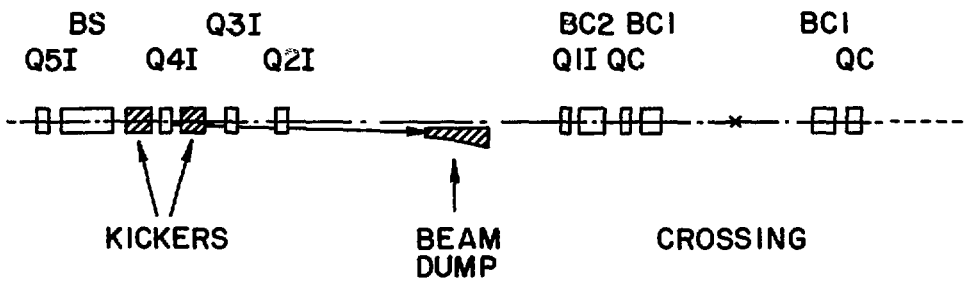

Figure IV.43. Internal beam dump (one ring).

beam will always be bunched but some of the buckets will be left empty to create a gap of about 0.7 μsec. The kicker will rise to full amplitude in a time of about 3.0 μsec in synchronism with the passage of the "empty" beam buckets. Most of the bunches will be disposed of well inside the absorber block, while a few of them will scrape on its exposed surface during the slow kicker rise. The particles which fail to reach the absorber on the first pass during the kicker rise will either reach the dump on the next turn or will be intercepted ed by protection collimators around the ring. Leaving some of the beam buckets empty alleviates some of the surface scraping. As proposed here the kicker magnet specifications are about the same as those of the CBA proposal. The pulsed power supply has a slower risetime, but it could be upgraded for a fast risetime as part of a future improvement program.

The internal beam dump system will be adequate for the conservative beam intensity scenario which is the basis of this proposal.* If, at a later date, the intensity rises far beyond the level assumed here, then one may need to add a full-fledged beam extraction system. In that case, septum magnets would take the place of the internal absorber, and would deflect the beam outside the Collider toward an external beam dump. A reconfiguration of one of the standard crossing regions to create more room for these extraction components may then prove to be advantageous. Initially it may be prudent to reserve a complete insertion for beam dumping, beam scraping, and eventual beam extraction.

*It is assumed, in particular, that when protons are used the intensity will not exceed 10^{11} protons/bunch.

IV.10. Power Supplies and Quench Protection System

i. Power Supply

The electric power supply system required to operate the superconducting magnets for RHIC fall into three categories: 1) the main or ramp supplies required to provide enough voltage for ramping the magnets from injection field to full field in 60 seconds, 2) the flat-top supplies required to hold the main magnet current to a precise pre-selected value during beam storage, and 3) the correction/trim coil and by-pass supplies.

The main and flat-top power supplies are similar in design. They consist of a 12 phase rectifier power unit whose output voltage is phase controlled, a passive filter section, and a control and regulating system. A voltage rating of about 650 volts for ramping and 120 volts for the flat-topping voltage are required. The flat-top power supply is a single unit operating symmetrically about ground. The passive filter consists of critically damped L-C sections, if necessary an active section can be added. The low frequency component of the ripple voltage will be controlled by electronics operating on the rectifier firing. The control and regulating system will be interfaced with the main control computer and will consist of 16-bit digital to analog converters to produce the required accuracies.

Most correction/trim and by-pass power supplies are built following the common design philosophy of modularity. The building blocks can be assembled in various ways to construct all the various sizes of supplies with minimal duplication of engineering and development effort. A typical power supply requires the following components:

a) A digital controller which receives information from the central computer and develops the necessary control information;

b) A phase control rectifier or amplifier module which generates the required current in response to regulating information;

c) A precision current measuring device;

d) A regulator amplifier which uses the output current and reference information to drive the supply in a standard feedback sense.

ii. Magnet Bus

The power supplies for the Collider magnets are distributed in the support buildings, equipment alcoves off the tunnel and in the Service Building. The physical location is determined by the position of the associated lead pots to minimize cable runs. The diagram in Fig. IV.44 shows schematically how typical coils are powered. The superconducting leads within each sextant of a ring are carried through each magnet in two bus packages, one containing the main current and quadrupole by-pass leads, and the second package contains the correction circuits.

iii. Quench Protection System

To prevent magnet damage in the event of a quench, the current in the quenching magnet must be reduced to zero before overheating occurs. This is accomplished by one of the two passive protection systems shown in Fig. IV.45. In both of these circuits the current is forced out of the magnet and into the shunting diode by the natural action of the quench developed resistance. The IR voltage generated across this resistance opposes the current flow and with time will force the current out of the magnet inductance. This current commutation is faster in the double diode circuit which will be used, if it is required. The Collider magnet must be able to absorb its own energy, which is accomplished by providing enough copper in the magnet conductor so that it will not overheat during the current commutation process described. Energy from the

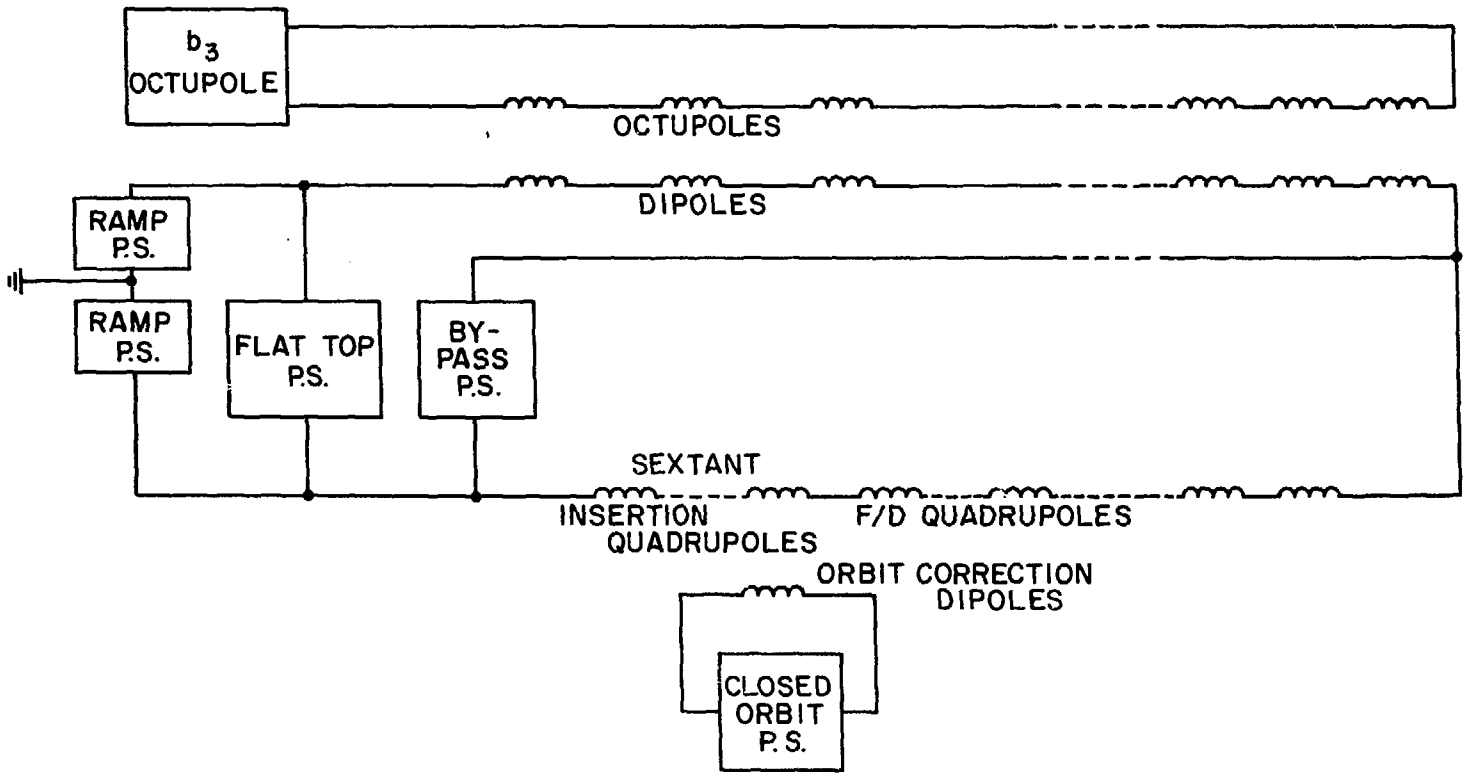

Fig. IV.44. Simplified diagram of magnet power supply bus wiring for one ring. For clarity only the octupole trim coils are shown, and one closed orbit power supply circuit.

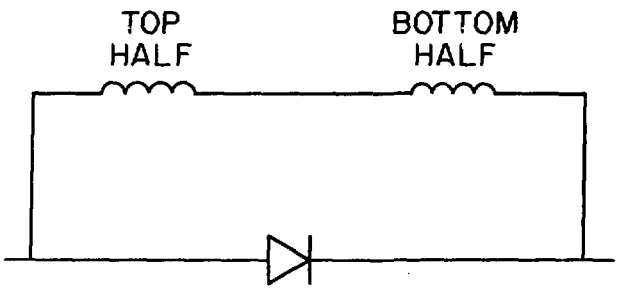

SINGLE DIODE PROTECTION CIRCUIT

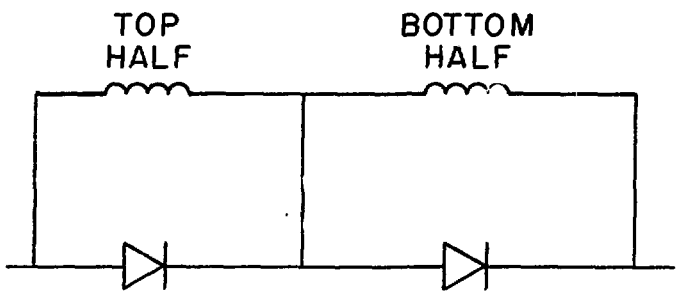

DOUBLE DIODE PROTECTION CIRCUIT

Fig. IV.45. Two alternative quench protection circuits.

non-quenching magnets will not heat the quenching magnet because of the shunting action of the diodes.

Even though the individual magnet in which the quench initiated is protected, it is necessary to remove the stored energy from the entire string as rapidly as possible to avoid quenching an excessive number of other magnets and to protect the bus work and diodes from overheating. These thermal time constants are long enough to permit a simple solution.

Figure IV.46 is a simplified schematic of the energy extraction system. Current is diverted from the non-quenching magnets by a redundant set of switches. The primary switches are solid state silicon controlled rectifiers (SCR). Redundancy is provided by commercially designed dc interrupters commonly used to protect large power systems. When these switches open, the current is diverted into dump resistors which dissipate the stored energy and exponentially reduce the current to zero. The bus and the diodes together with their heat sink have been tested to withstand the rated current for 45 seconds. This time is longer than the decay time for the magnet current in the circuit shown. Should an even more pessimistic "worst case" scenario arise, a shorter decay time can be achieved by adding additional dc interrupters at appropriate locations in the circuit.

The quench detection system is also made redundant by using two completely independent quench detection methods. The primary method involves comparing total sextant voltages and triggering the switches when one sextant differs from the others by more than a preset limit. The detection backup is accomplished by using differential pressure switches sensing the helium pressure in the magnets. These pressure switches are hard wired to the dc interrupters to minimize failure modes.

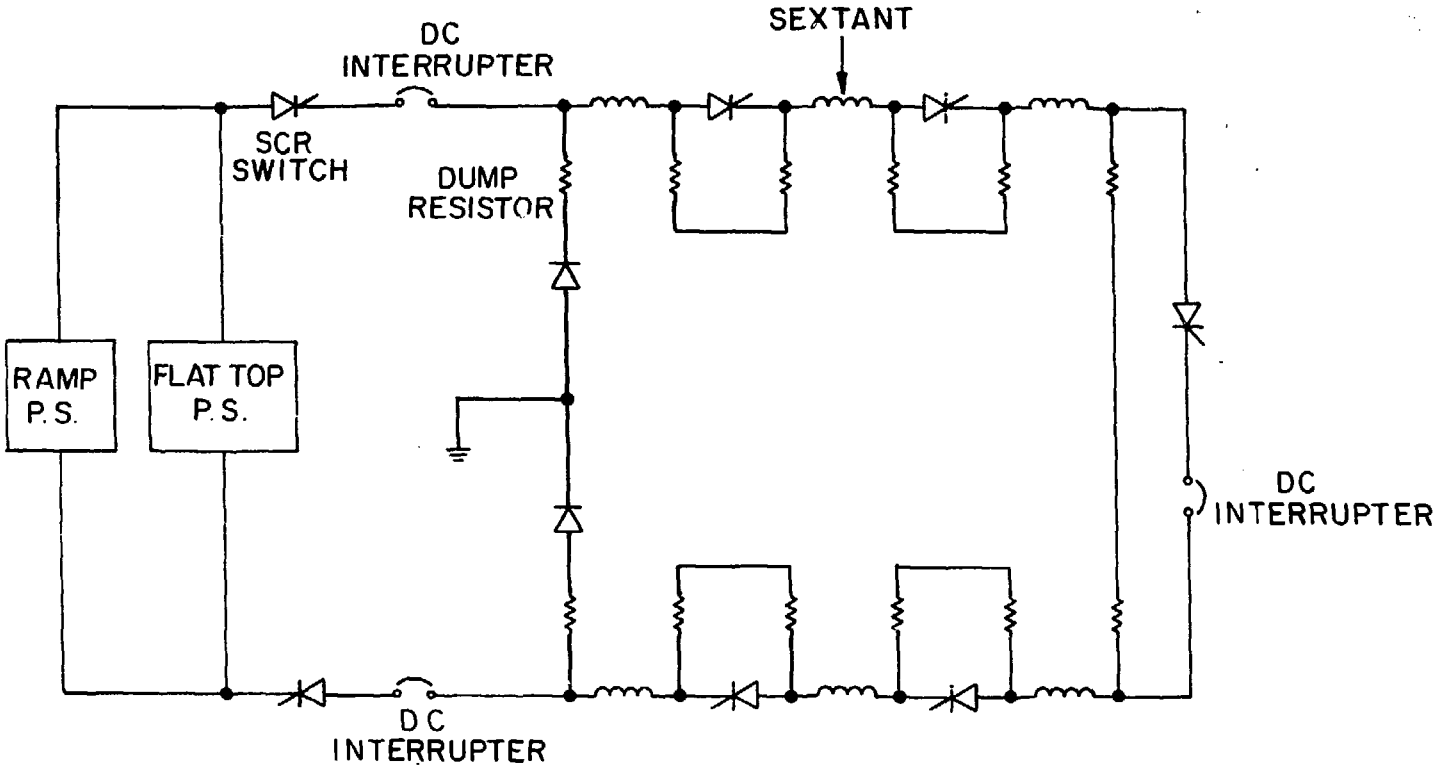

Fig. IV.46. Simplified diagram of the magnet quench protection circuit for one ring. Silicon controlled rectifiers (SCRs) are used as "normally on" switches. When a quench is detected the SCRs are commutated "off" and the current is diverted through the dump resistors where the stored energy is dissipated.

IV.11. Beam Instrumentation

Operation of the accelerator and achievement of full luminosity will require continuous monitoring of the beams. Initial instrumentation will include pickup electrodes at each quadrupole, as well as one wide-band pickup electrode, and a current measuring device in each ring. Beam transfer and machine start-up will require single-pass position monitors in the transfer lines and adjoining ring sextants. Feedback systems will be provided to suppress longitudinal and transverse instabilities. Radiation monitors will be used in conjunction with the beam scraper system to control and minimize beam loss. Luminosity monitors required at each intersection region will be part of the experimental equipment. A summary of beam instrumentation is presented in Table IV.29, and more detailed information is given below on the most important items.

i. Beam Orbit Position Measurements

The properties of the circulating beam will themselves be a very sensitive monitor of the performance of the superconducting magnets in each ring. It is planned to record conventional closed orbit information, that is, the center of the beam vertically and horizontally, at 250 locations in each ring, spaced at intervals of about one quarter betatron wavelength where vertical and horizontal β functions are maximum. The beam will be sensed by pick-up electrodes (PUE) with an effective sampling time of about 0.3 msec. Such information can be exploited rapidly enough to be used in lattice control and feedback procedures in a real time sense without prolonging the expected acceleration time.

Identical PUE's working with single pass electronics are also used to measure beam position in the transfer lines.

Table IV.29. Beam Instrumentation

Instrument System	Basic Elements	Function	Total Number
Beam current monitor	Transformer/ magnet modulator	Circulating proton beam intensity	2
Luminosity[1] monitor	Scintillation counter tele-scopes/beam displacement coil	Measure beam collision rate	6
Radiation and loss monitor	Solid state detectors	Measure radiation loss background	50
Orbit position monitor	Split capacitive pick-up electrodes	Equilibrium orbit bunched beam	500
		Single pass measurements	200
Wide band PUE		Beam structure	2

[1]Experimental equipment in crossing regions

ii. Beam Current Monitors

These monitors will be very sensitive dc-wide band transformers having a large dynamic range with a resolution of 10 μA and with calibration windings similar to those used at the ISR. They will be used to measure both beam current and beam current loss rate to a high accuracy. Output from these devices will be used in many control programs and will also be a source for a hard-wired beam dump trigger.

iii. Radiation Monitor System

A Radiation Monitor (Beam Loss Monitor) will employ solid state detectors. About 50 units will be mounted on chambers at selected locations of horizontal β maximum around the rings and used in conjunction with beam scrapers

and aperture defining fingers. They can also provide a trigger for the protective fast beam dump.

Prototype horizontal and vertical pick-up electrodes have been designed, constructed, and tested. They consist of a simple stainless steel split cylinder and glass guard rings coated with nichrome, in order to suppress microwave mode excitation. Two types of associated electronics have been designed. A closed orbit digitizing system which measures the position of the equilibrium orbit of the circulating beam to 0.1 mm was tested at the AGS. The results agreed with measurements done with existing AGS electronics.

The single pass electronics, for measuring beam position on a single fly-by, to be used in the injection line, has been tested with simulated signals. Initial tests of this system in the AGS U-line were also carried out.

IV.12. Control System

The function of the central control system is to provide the control and communication necessary to provide stable, well defined beams in the RHIC storage rings. It must translate basic physics requirements such as beam energies, intensities, and more special characteristics into instructions which govern thousands of individual activities within the storage rings. As in other modern accelerators, the RHIC control system must support the needs of typical subsystems and utilities which provide beams, power, RF, and other services. Moreover, computer aided control procedures now include simulation techniques which review the expected behavior of changes upon accelerator models before committing them to the accelerator itself.

The Collider is to provide stable beams with usable lifetimes ranging from less than 2 hrs. at injection energy to more than 10 hrs. at full energy (100 GeV/amu). A simultaneous need therefore exists for both continuous reliability and the ability to bring up beams in a relatively short time.

There are no intrinsic reasons for long delays in producing beams because the Collider employs simple box car stacking and accelerates relatively low currents rapidly. In this regard it is encouraging to note that Fermilab, after only 9 months operation of the Energy Saver, is able to restore beam in less than 15 minutes following routine run termination. This is made possible by excellent monitoring software and increasing reliance on computer calculations for beam tuning.

To meet the reliability requirement a controls design goal has been established which stresses 10 day system availability and protection against control and data loss.

The essential features of the distributed computer control system designed for the CBA project will be adapted for the Collider. The conceptual design is remarkably similar to systems developed independently by both LEP at CERN and the Linear Collider at SLAC, and those evolving in the commercial controls industry in the United States.

The structure of the system is that of a three-level hierarchy shown schematically in Figure IV.47.

The CONSOLE MODULE is at the highest level of the hierarchy. This module includes operator consoles, transaction processors which handle subsystem activities and administration, and a major analytic computer which performs beam analysis and probes working line and lattice adjustments. Normal analogue and waveform analysis facilities are also present. The transaction processors are closely networked so that the group as a whole can recover from the failure of any single member. The analytic computer will help guide beam management procedures to prevent beam loss. It will be a powerful, specialized processor of over 50 million instructions per second effective capacity. Sample tracking programs already tested have guided this specification.

The second hierarchical level is the communications network which links the Console Module to the process control elements. This network consists of a high speed data highway called RELWAY, and communication modules called STATIONS.

RELWAY is a broad band data highway employing CATV technology to distribute information over the more than 4 km extent of the Collider. A prototype version of RELWAY has been installed at the AGS for control of the Polarized Proton project and is currently transmitting data at a maximum rate of 1 Mbit/sec over 1 channel. For the Collider up to 12 channels will be available, each wi

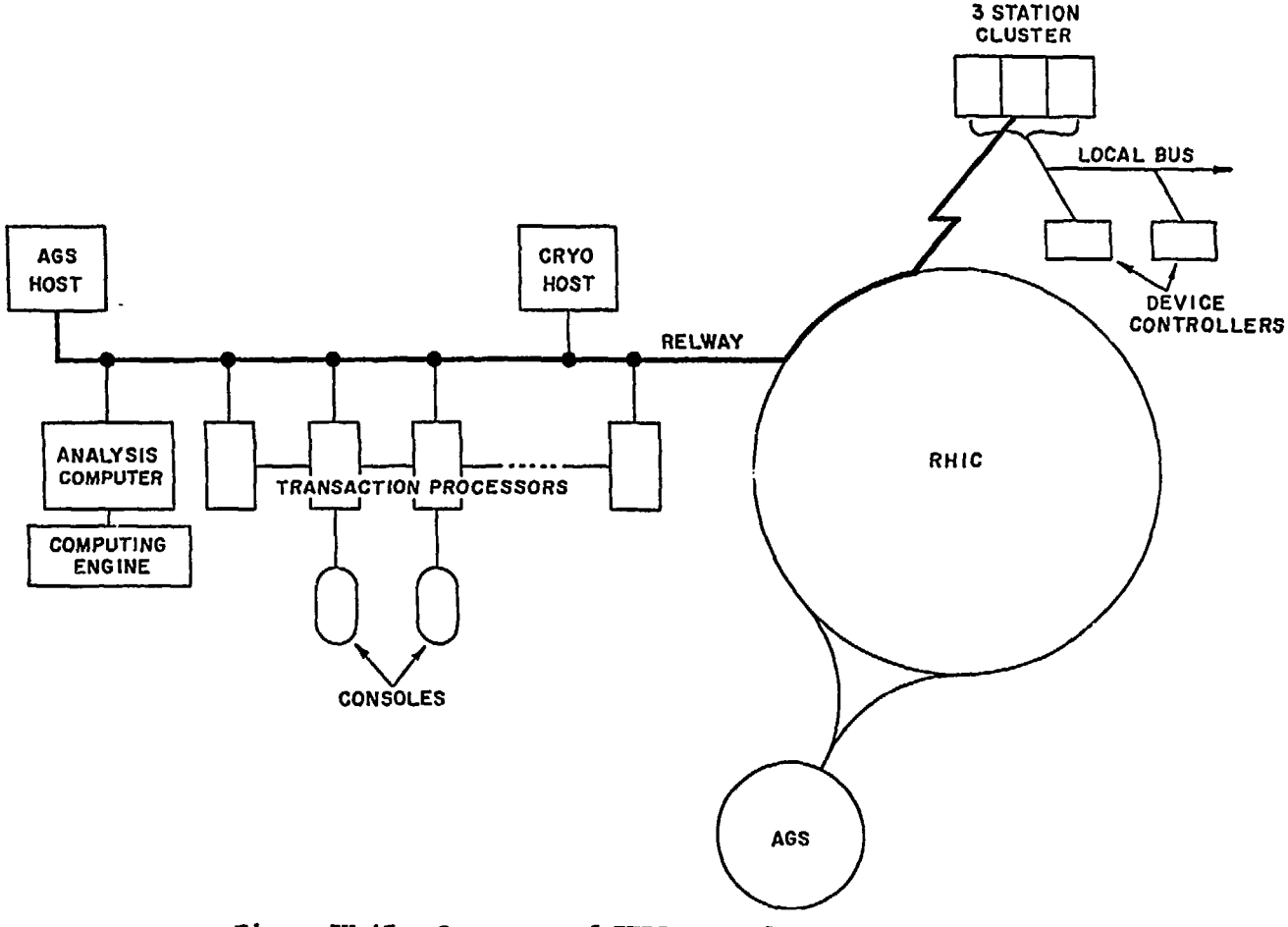

Figure IV.47. Structure of RHIC control system.

a maximum data rate of 10 Mbit/sec per channel. Following industry practice, RELWAY will be duplicated for reliability. A second utility, the Message Transfer system, will carry voice, computer terminal, video, and similar communications throughout the Collider. It is based on the economical channel multiplexing features of standard telephone transmission modules.

RELWAY STATIONS, located uniformly around the ring and in the principal utility centers, connect and monitor the process control elements belonging to one geographical area. Because some stations are inaccessible during a beam storage cycle, stations are grouped together in such a way that communications can continue to function even if individual stations may fail. A cluster of 3 microprocessor based stations has the following functionality. The first unit is dedicated to intrinsically fast devices (e.g. beam instrumentation). It communicates via a high data rate channel of RELWAY. A second unit is used for the remaining devices. The third unit helps with peak message traffic, and in addition monitors the other two and provides the ability to take over the work of another unit if it should fail. Such a system is currently being developed by BNL in collaboration with August Systems, a firm which has pioneered fault tolerant control elements.

At the lowest hierarchical level are the DEVICE CONTROLLERS which perform process I/O. These are constructed using microprocessors and/or logic components and act as intelligent instruments to control and monitor physical devices (power supplies, pumps, etc.). Although some of these controllers require special timing links, the principal communication to the outside world is via local buses connected to the stations.

V. RING TUNNEL, EXPERIMENTAL HALLS AND CONVENTIONAL FACILITIES

The availability of the CBA conventional facilities for use in the RHIC represents an unprecedented opportunity to build the Collider at minimal cost. The existing tunnel configuration provides for six experimental areas where the ring beams will cross. Four areas have been provided with the major structures necessary for an operating experimental area. The RHIC lattice will use these existing areas which are at the 2, 4, 6 and 8 o'clock locations (see Fig. I.1). The 4 o'clock facility is an "open area" and is suitable for the proposed internal fixed target mode. The proposal calls for closing the ring gaps at each of the two undeveloped areas - 10 and 12 o'clock - using the standard tunnel cross section and adding support buildings, thus making the ring operational. These areas will be available for development as experimental facilities at a later date thus maintaining the option of adding experimental halls for future experimental needs.

The experimental halls at 2, 6 and 8 o'clock are fully enclosed structures complete with support buildings. The area and height of the facilities vary and each is equipped with overhead cranes, air conditioning, and sprinkler protection and has direct access from grade. Table V.1 gives the dimensions, crane capacities and beam heights in each of these facilities as well as the 4 o'clock open area. This area has a concrete deck capable of supporting portable shielding blocks in varying configurations. All conventional services including a support building are in place.

The Collider Center (approximately 50,000 square feet), consisting of a Cryogenic Wing, a Compressor Structure and a four level Main Building is complete. The air conditioned main building contains technical shops, an RF/Power Supply wing, office and conference room space and space for the Collider control

Table V.1. Summary of Hall Dimensions (m)

		Length	Width	Beam Height	Hook Height and Capacity (tons)
2.	Small Angle Central Hall	28	12	1.7	6.1/20
	Forward Experimental Building	68	7.9	1.7	5.3**
	"Stub"	91	2.4	1.0	2.0*
4.	Open Area.4	57**	37**	2.2	---*
6.	Wide Angle	16	32	4.3	10/2×20
8.	Major Facility Central Hall	19	15	5.2	11/40
	Forward Experimental Buildings (2)	16	9	3.3	6.6*
	Assembly Building	19	19	5.2	11/40+14/7.5

*No crane - ceiling height given
**Pad dimensions given

center. The RHIC cost estimate includes funding to complete such items as a power sub-station for the accelerator RF and Power Supplies Wing, site improvements such as paved access roads, hardstands, parking areas, yard lighting and general restoration of drainage and grounds.

Construction of the utility services, roadways, drainage and other site improvements for the CBA have been underway since 1979. All have been complete except for some paving and site work. The extension of the 69 kV substation was completed in May 1982. The underground ductbank for electrical power and communication distribution was completed in 1981. Installation of conventional power feeder cables to the Collider Center was finished in 1982. Installation of the balance of the power cables around the Ring Road ductbank and the unit substations at areas 2, 4, 6 and 8 o'clock location was completed in the

Spring of 1983. The Main Ring from the midpoint of Sextant 9 to the midpoint of Sextant 1, approximately one-third of the enclosure, is without permanent power, lights, fire alarm, HVAC and dehumidification. The completion of the Main Ring and construction of the two support buildings at areas 10 and 12 o'clock is required to supply the utility services to these areas to make the ring operational. These costs are included in this proposal.

VI. COST AND SCHEDULE

VI.1. Construction - Cost

The RHIC cost estimate was completed by developing costs utilizing the "bottom-up" approach by each system manager.

Each manager prepared cost elements broken down into purchased material, labor, and other miscellaneous costs both for the hardware and Engineering, Design, Inspection, Administration (EDIA) work breakdown structure elements.

Technical and cost reviews were held by the Task Force management and then were presented to BNL management.

The BNL RHIC Task Force developed the present cost estimate using the Dual magnet design as described earlier. The estimate assumes completion of the Tandem AGS Transfer Line Project now under construction, and the Booster Project planned to start in FY 86. All costs are shown in FY 84 dollars.

Figure VI.1, the RHIC Work Breakdown Structure, represents the framework of the technical, cost, and schedule effort. All system managers have prepared estimates for labor, purchased parts, and other expenses. The WBS shows detailed breakdowns for the following Level 2 construction elements.

Accelerator Systems

Conventional Facilities

Systems Engineering (EDIA)

Project Management (EDIA)

All summary costs are shown in Table VI.1.

Table VI.2 has the RHIC manpower, in man-years, for each WBS element.

RHIC WORK BREAKDOWN STRUCTURE

RHIC 1.0

ACCELERATOR SYSTEM	1.1	CONVENTIONAL FACILITIES	1.2			R&D	1.3	SYSTEMS ENGINEERING	1.4	PROJECT MANAGEMENT	1.5
INJECTION SYSTEM	1.1.1	CONSTRUCTION	1.2.1	A/E	1.2.2	INJECTION	1.3.1	INJECTION	1.4.1	MANAGEMENT SYSTEMS	1.5.1
MAIN MAGNET SYSTEM	1.1.2					MAGNET	1.3.2	MAGNET	1.4 2	QUALITY ASSURANCE	1.5.2
MAGNET POWER SUPPLIES	1.1.3	LAND IMPROVEMENTS	1.2.1.1			POWER SUPPLY	1.3.3	POWER SUPPLY	1.4.3	PROJ.MGMT.ADM.	1.5.3
VACUUM SYSTEM	1.1.4	MAGNET ENCLOSURE	1.2.1.2			VACUUM	1.3.4	VACUUM	1.4.4	SAFETY	1.5.4
RF SYSTEM	1.1.5	SERVICE BUILDING	1.2.1.3			RF	1.3.5	RF	1.4.5		
BEAM INTSTRUMENTATION	1.1.6	GAS STORAGE AREA	1.2.1.4			BEAM INSTR.	1.3.6	BEAM INSTR.	1.4.6		
REFRIGERATION SYSTEM	1.1.7	RESEARCH AREAS	1.2.1.5			REFRIGERATION	1.3.7	REFRIGERATION	1.4.7		
CENTRAL CONTROLS	1.1.8	SUPPORT BUILDINGS	1.2.1.6			CONTROLS	1.3.8	CONTROLS	1.4.8		
BEAM DUMP SYSTEM	1.1.9	UTILITIES	1.2.1.7			BEAM DUMP	1.3.9	BEAM DUMP	1.4.9	START-UP	1.6
		COLLIDER CENTER	1.2.1.8			ACC.PHYSICS	1.3.10	ACC.PHYSICS	1.4.10		
						ADMIN.	1.3.11	DES.&DRFTG	1.4.11		
						CONSTRUCTION	1.3.12	CONSTRUCTION	1.4.12		

START-UP	1.6
INJECTION	1.6.1
MAGNET	1.6.2
POWER SUPPLY	1.6.3
VACUUM	1.6.4
RF	1.6.5
BEAM INSTR.	1.6.6
REFRIGERATION	1.6.7
CONTROLS	1.6.8
BEAM DUMP	1.6.9
ACC.PHYSICS	1.6.10
ADMIN.	1.6.11
CONSTRUCTION	1.6.12

TYPICAL LEVEL 4

INJECTION SYSTEM	1.1.1
TEST & ASSY.	1.1.1.1
MATERIAL	1.1.1.2

Figure VI.1

Table VI.1. RHIC Cost Estimate Summary (M$)

WBS		MSTC	LABOR	TOTAL
1.1	Accelerator Systems			
1.1.1	Injection	5.7	2.1	7.8
1.1.2	Magnets	34.2	12.6	46.8
1.1.3	Power Supplies	6.3	1.9	8.2
1.1.4	Vacuum	2.3	1.5	3.8
1.1.5	RF	3.4	0.9	4.3
1.1.6	Beam Instrumentation	0.9	0.6	1.5
1.1.7	Refrigeration	4.9	2.1	7.0
1.1.8	Central Controls	5.1	1.1	6.2
1.1.9	Beam Dump	2.0	0.7	2.7
	Sub-total			88.3
1.2	Conventional Facilities			
1.2.1	Construction			
	Site Improvements	0.6		0.6
	Tunnel & Buildings	2.4		2.4
	Utilities	0.7		0.7
	Sub-total			3.7
1.2.2	AEM	0.5		0.5
	EDIA			
1.4	Systems Engineering	1.2	13.7	14.9
1.5	Project Management	1.7	3.7	5.4
	Incremental Overhead			4.7
	Sub-total			25.0
	Total			117.5
	Contingency			16.9
	Project Total (FY 84 M$)			134.4

Table VI.2. RHIC Manpower Estimates in Man-Years

	WBS	TEST & ASSEMBLY	WBS	EDIA	PROJECT TOTAL
Injection	1.1.1	49.2	1.4.1	31.7	80.9
Magnets	1.1.2	325.0	1.4.2	101.1	426.1
Power Supplies	1.1.3	46.0	1.4.3	16.0	62.0
Vacuum	1.1.4	36.0	1.4.4	15.5	51.5
RF	1.1.5	19.0	1.4.5	16.0	35.0
Beam Instrumentation	1.1.6	14.0	1.4.6	11.0	25.0
Refrigeration	1.1.7	57.8	1.4.7	24.5	82.3
Controls	1.1.8	28.0	1.4.8	61.0	89.0
Beam Dump	1.1.9	15.7	1.4.9	10.0	25.7
Construction			1.4.12	2.8	2.8
Sub Total		590.7		289.6	880.3
Project Management					
Management Systems			1.5.1	28.0	28.0
Quality Assurance			1.5.2	16.5	16.5
PM Administration			1.5.3	36.0	36.0
Sub Total				80.5	80.5
Total		591		370	961

VI.2. Construction - Schedules

Figures VI.2 and VI.3 are the RHIC Major Milestones Timeline and a logic network for all integrated systems with the completion of the Project in July 1990.

Figure VI.4, the Magnet R&D and Production Schedule, shows Construction starting in FY 86, with the build up of the magnet production rates from FY 87 through FY 89.

The 4 year magnet production schedule, and 5 year total project schedule, is predicated on a conservative approach using the funding profile shown in the RHIC Funding Plan (Table VI.3). Advanced funding in FY 85 and an aggressive FY 86 funding profile could give a substantially earlier completion date.

PROJECT RHIC
TIMELINE

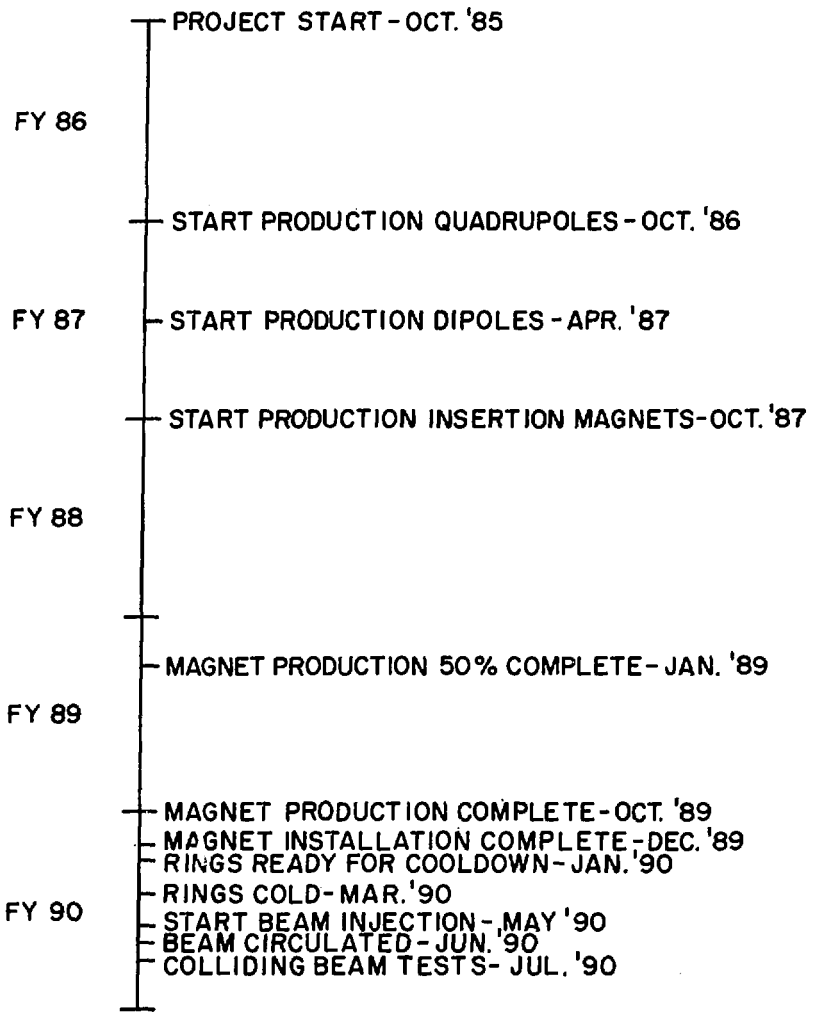

Figure VI.2

RHIC
Accelerator System Network

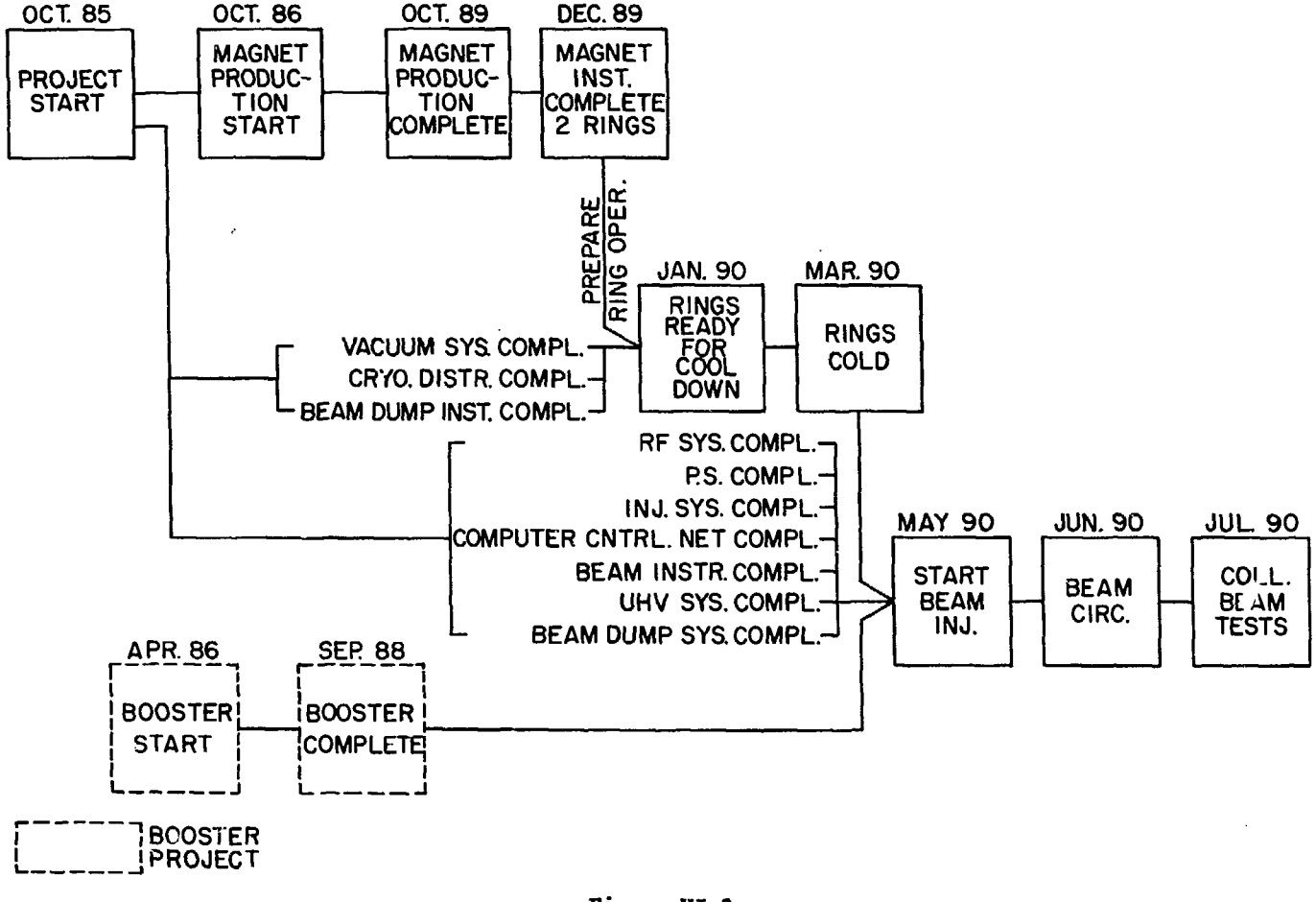

Figure VI.3

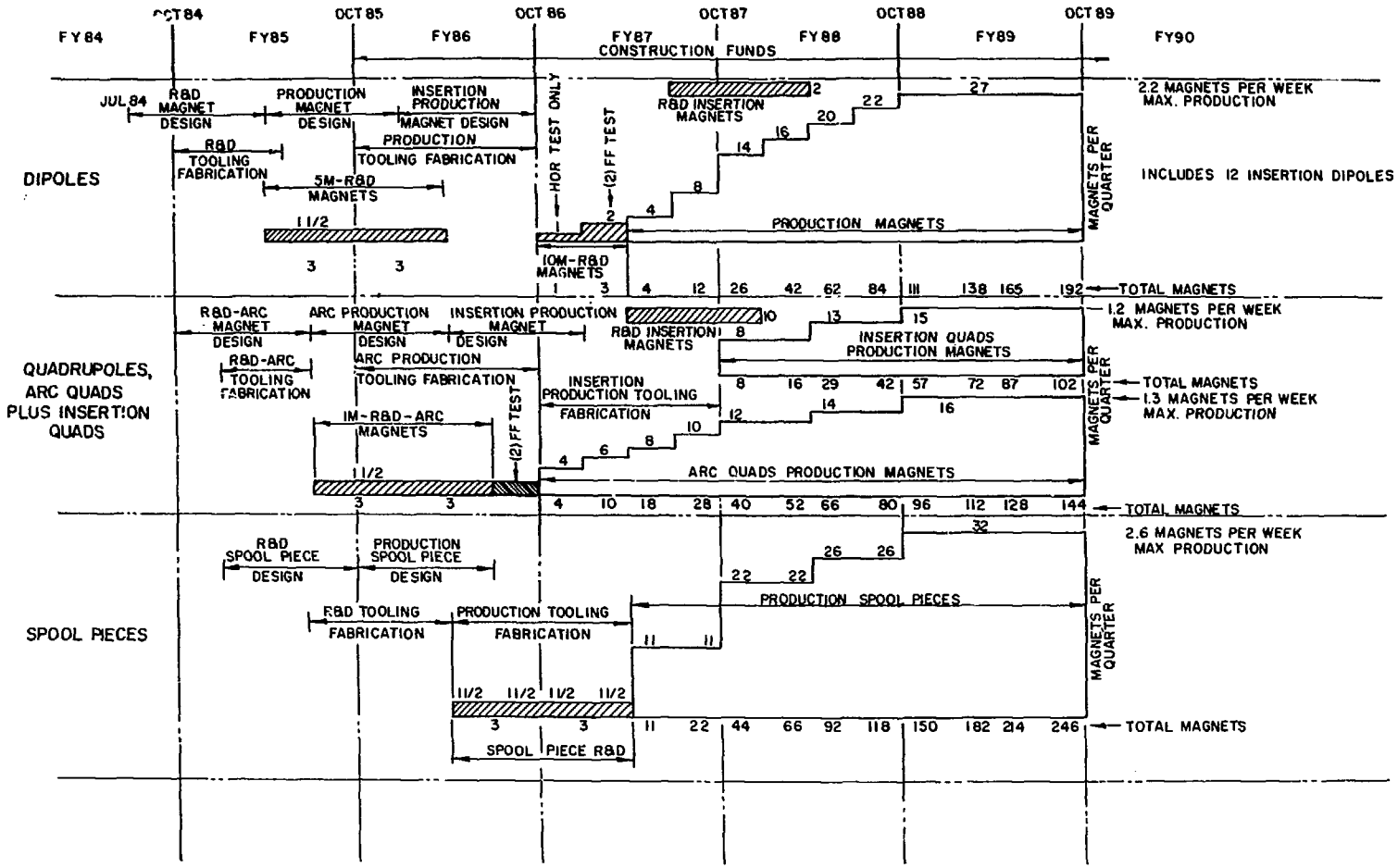

Figure VI.4 Magnet production schedule.

VI.3. RHIC Funding Plan

The annual funding needs based on the schedules and manpower requirements of the previous section are presented in Table VI.3.

Table VI.3. RHIC Funding Plan (FY 84 M$)

	FY 85	86	87	88	89	90	Total
Construction (Materials, Labor, EDIA & Contingency)							
Magnets	-	4.2	15.8	23.3	17.5	1.2	62.0
Other Systems	-	4.2	19.5	23.7	14.5	5.8	67.7
Conventional Systems	-	-	4.7	-	-	-	4.7
Total		8.4	40.0	47.0	32.0	7.0	134.4
R&D							
Magnets	3.2	4.2	1.4	.7	-	-	9.5
Other Systems	1.1	2.6	2.6	2.1	1.3	.8	10.5
Sub-Total	4.3	6.8	4.0	2.8	1.3	.8	20.0
G&A	1.7	2.8	1.5	1.0	0.5	.2	7.7
Total	6.0	9.6	5.5	3.8	1.8	1.0	27.7
Start-Up (including G&A)	-	-	-	-	4.6	10.0	14.6
Man-Years							
Construction	-	61	284	300	241	77	961
R&D	59	90	46	30	22	12	259
Start-Up	-	-	-	-	46	86	132

VI.4. RHIC R&D Requirements

The design concepts proposed for the Relativistic Heavy Ion Collider resulted on one hand in a significant reduction in construction cost when compared to a simple reduced-energy CBA adaptation but on the other hand demanded new technical solutions. The R&D funds listed in Table VI.3 cover work required to complete the preliminary design prior to submission of the final RHIC proposal as well as supporting R&D work on critical accelerator components before and during the construction phase.

A preliminary R&D plan for RHIC magnets has been developed to substantiate the magnet production schedule (Fig. VI.4). The R&D funds listed cover the development of;

- six 5 m and three full length (10 m) arc dipoles
- six quadrupoles
- approximately 12 insertion magnets
- six trim/correction spool pieces.

Tooling to build R&D arc dipole magnets will be fabricated beginning on October 1, 1984. The first 5 m dipoles will be ready in mid-FY 85, with a total of six by mid-FY 86. Production tooling fabrication will be underway during FY 86 and will allow the fabrication of three full length (10 m) R&D dipole magnets in early FY 87. R&D arc quadrupole magnets will follow the same time scale as the 5 m R&D dipole magnets, but three months later. Six R&D quadrupoles will be produced. This will allow the start of production of final arc quadrupole magnets at the beginning of FY 86. Upon completion of the R&D program for arc dipoles and quadrupoles, a similar program for insertion dipoles and quadrupoles will get underway and extend into FY 88. Approximately 12 mag-

nets will be built. Spool piece R&D will be carried out beginning mid-FY 85 and continue through mid-FY 87. A total of six R&D spool pieces are planned.

R&D work for the cryogenic system is closely tied to the magnet development program. The cryogenic group will provide support by operating refrigerators required for magnet and short sample testing and by making heat load measurements on test and production magnets. Special helium transfer lines as required for RHIC will be developed here using technology proven out on CBA. Further preliminary design work on modifications to the existing CBA refrigerator as required by the new superconducting magnet system remains to be done. System tests of a magnet string is desirable but not absolutely necessary.

Accelerator systems other than superconducting magnets and their cryogenic system involve conventional technology. More preliminary design work as needed for a final proposal remains to be done. Accelerator physics studies will continue throughout the construction program. Beam lifetime limitations due to intrabeam scattering or the recently suggested Bremsstrahlung pair production will require further theoretical and perhaps experimental work. In later years, the accelerator physics group will collaborate with the controls group to develop theoretical models of the collider and applications software. The choice of an internal beam dump was technically feasible and included at substantially lower cost. A careful study of the associated beam scraper system is necessary to prevent magnet quenching and to minimize background at the crossing points. Alternatives to the presently proposed high-impedance rf cavities will be studied in view of operation with higher beam currents and cost reduction of the rf system.

VI.5. Operating Costs

We have estimated operating costs for RHIC after the initial start-up period. We have assumed that this facility will be unique and that experimenter's demands for experimental time will exceed the facilities capability even with very efficient operations. In short, there will be a large backlog of proposals. We therefore plan on 38 weeks of operation (for example, 34 for physics and 4 for machine studies). It should be noted that in addition, perhaps up to six additional weeks will be needed for cooldown and warmup of the magnet system.

As at PETRA and other world class colliders, experimenters will have the responsibility to operate their detectors and their local experimental areas. Manpower is thus not included for these functions.

We assume for this estimate that four experimental areas are in use (2, 4, 6 and 8 o'clock). Major installation costs for detectors are also assumed to be included in the detectors costs. Table VI.4 summarizes the annual operating costs and Table VI.5 the associated manpower. These are the incremental costs for operating the collider, and thus do not include the costs of operating the injection system (AGS, Booster, and Tandem Van de Graaff).

We point out that the startup costs, shown in Table VI.3, for FY 90, 10.0 M$, include pre-operation funds plus funds for actual operation of the Collider for the last quarter of the year. FY 91 would be a year having one half of a full operating program. By FY 92, the program should be fully underway.

In addition to these operating costs for RHIC, there are operating costs associated with the injector systems: Tandem, Booster, and AGS. The estimate of cost for operation of the injector systems is shown in Table VI.6.

Table VI.4. Operating Cost (FY 84 k$)

Labor	8,530
Purchases	2,800
Electric*	10,670
G&A	4,500
Total	26,500

*Rate (58 $/MW•h) is 1984 BNL average.

Table VI.5. Operating Manpower (MY)

Operations (shift)	51
Support & Maintenance	103
Shops & Administration	29
DDL	20
Total	203

Table VI.6. Injectors Operating Costs (FY 84 k$)

AGS	11,500
Booster	1,000
Tandem	1,500
Total	14,000

Furthermore, programmatic operating expenses directly related to the facility have been estimated at 4.4 M$ per year of full operation. This estimate is for the on-going accelerator research and development tasks associated with the new machine.

The assumption made in this estimate is that the injector system is not being used for any function other than as a RHIC injector. (Of course the AGS could, and perhaps will, be used to provide fixed target capability for experimental programs in both particle and heavy ion physics in the early 1990's. If so, the cost of running as an injector system to RHIC would be somewhat reduced from the 14 M$ estimate given above.)

The total operating budget estimate for RHIC including injectors and on-going accelerator R&D is thus 44.9 M$ (26.5 + 14.0 + 4.4). We estimate that prior to operation of RHIC, there wil be Heavy Ion beams for fixed target physics at the AGS involving about 6 M$ per year for accelerator operation. Thus the change from AGS to RHIC collider physics would require an incremental budget of approximately 39 M$ for facility operations for Relativistic Heavy Ion Physics in 1992.

VI.6. Detector Plans and Costs

In Section II, we have described the phenomena, the signals and the profiles which will be of foremost importance in the early experiments at RHIC. These call for an experimental program which involves systematic study of many different reaction properties, some of which require fairly complete and detailed information about each of the selected events. The early configuration of experimental detectors should include at least one large solid angle, general purpose spectrometer capable of a broad search with sensitivity to many of the expected signatures of new phenomena. There should also be specialized apparatus whose performance is optimized for particular signals (e.g. leptons, strange particles, jets, etc.). The program of early experiments should also have some degree of flexibility to respond to new theoretical and experimental developments which may arise during the years when the collider is under construction and the designs of large detectors effectively frozen by long construction schedules. This flexibility might be achieved by planning for a few relatively small experiments to be approved later in the proposal cycle, and by phased implementation of the various components of large detection systems.

The design of instrumentation for such a program is, at this time, not known at the same level of detail as is that of the machine. The design of experiments must evolve through the process of proposal and review by the community of experimenters. Nonetheless, planning for development and construction of instrumentation for experiments must begin at an early stage in order to ensure full use of RHIC as soon as possible. Capital expenditures for detector equipment should begin four years before turn-on, with most of the cost incurred before the start of the physics program. Some of the equipment money for first-round experiments could be expended during the first year of operation.

On the basis of these considerations we plan that the first round of experiments will use the four completed experimental areas. Our planning assumes an active user pool of more than 300 physicists. Our model for a balanced, flexible program of experiments as the collider comes into operation is as follows:

- One full solid angle, multipurpose, detection facility designed specifically for a broad range of measurements at RHIC. This would be similar in size and scope to first-rank detector systems at present colliders. Using the costs of current collider detectors as the basis for our estimates, we conclude that 35 M$ (FY 84 $) would provide a superb experimental facility.
- One large detector system constructed largely of existing components, refurbished and modified for the heavy ion requirements. A presently existing collider detector, or high energy fixed target detector system might be used. Based on studies done for some candidate detectors for the CBA program we estimate the cost at ~10 M$.
- Two of the experimental areas would be left as "open areas", each to be configured with one or more relatively small, specialized experiments. These could include small aperture, high resolution spectrometers as well as genuinely small experiments with a short time scale for design and execution. An initial equipment budget of 10 M$ would assure an excellent beginning for these modest experiments.

APPENDIXES

A.1. FUTURE IMPROVEMENTS

The design of RHIC which is described in this proposal is conservative in the sense that a decision was made to attempt neither to maximize the luminosity, nor minimize the interaction length. We firmly believe that the RHIC design will allow improvements in the future, not all of which are now recognized. A period of operation, during which basic experimental information about the machine parameters is acquired, should clarify how to improve the integrated luminosity, for example. However, even now there are some ideas which show, in a general way, how improvements might be made.

Our design is based on a current of 200 μA from the Tandem, which matches the optimum injection energy into the Booster of ≈1 MeV/amu. Ion source experts feel that it may be possible to produce as much as 400 μA of heavy ions. With this current an added acceleration section, a Linac for example, would be needed to inject ions into the Booster at ≈ 1.7 MeV/amu, the new optimum value. Naturally with higher current, space charge effects may complicate the process of reaching higher luminosity, especially for the heaviest ions.

Another way to improve luminosity for all species would be to increase the number of bunches in the Collider. Our design has 57 bunches which are separated by about 200 nsec in order to minimize the cost of the injection kickers. Kickers with rise times of less than 200 n sec would make it possible to fill more buckets and would yield a higher average luminosity without changing its peak value. However, to avoid multiple collisions in the straight section, especially for zero angle collisions, the minimum bunch seperation, S_B, is about 27m limiting the total number of bunches, B. Table A.1.1 gives the maximum 0-99% kicker rise time allowable for filling every n^{th} bucket(n) and the luminosity multiplier M_L. These numbers are only nominal since a

gap of ≈450 nsec must be left for beam disposal as well for the injection kicker fall time.

Table A.1.1. Future Luminosity Gain

B	n	τ(nsec)	M_L	S_B(m)
55	6	205	1	67.3
114	3	90	2.0	33.6
171	2	50	3.0	22.4*

*Incompatable with zero angle crossing

Note that intrabeam scattering is unaffected by this procedure. The average beam current would be increased and so would the total energy stored in the beam. The filling time would also increase linearily with the total number of bunches.

Increasing the rf voltage could also be advantageous, since it would shorten the bunch length and hence the interaction length for head-on collisions. Higher rf voltage would also improve the average luminosity by increasing the bucket height, thus reducing ion losses.

Protons are a special case. For example, at the level of 10^{11} protons per bunch, intra-beam scattering has little effect. We have limited the number of protons to 10^{11} per bunch in order to keep the beam-beam tune shift at a reasonable value, although 10^{12} protons per bunch are currently available at the AGS. In this proposal the peak luminosity for proton-proton collisions is $\approx 10^{31}$ cm^{-2} sec^{-1}. It should be possible to increase this to $\approx 10^{32}$ $cm^{-2} sec^{-1}$ by using more bunches per beam and by increasing the number of protons per bunch while adjusting the beam parameters so as not to increase the beam-beam tune shift. A low impedance rf cavity system is under investigation which would minimize the beam loading problem of the present design.

A.2. MANAGEMENT PLAN

1. Introduction

The RHIC Management Plan will be developed to establish guidelines for management, technical, and administrative responsibilities throughout the life of the Project.

The Management Control System (IMPACT) developed and implemented on the CBA project encompasses the major DOE guidelines used for Major System Acquisitions. Reporting requirements will be met using the Uniform Contractor Reporting System Guidelines (DOE/CR-0001/2) and Cost and Schedule Control Systems Criteria (DOE/CR-0015) as outlined by the DOE.

The IMPACT (Integrated Management Planning and Control Tracking) System Manual has been reviewed by DOE Consultants and preliminary acceptance for implementation was received. The IMPACT System will be used, with further improvement as required, on the RHIC Project.

As prepared for a previous Major System Acquisition (CBA), the Management Plan will be a two section document. Section I will be an overview of technical goals, and Section II will cover project management descriptions for administrative functions. Table A.2.1, describes the Table of Contents of the proposed plan.

Table A.2.1. Table of Contents of Proposed Management Plan

I. Technical

1. Introduction
2. Overview of Goals
3. Organization
4. Work Breakdown Structure
5. Work Statements

Table A.2.1. Table of Contents of Proposed Management Plan (Cont.)

II.	Management
	1. Management Control System
	2. Schedules
	3. Manpower and Cost
	4. Quality Assurance
	5. Configuration Management
	6. Safety
	7. Laboratory-wide Directives
	8. Reporting Requirements

2. Work Breakdown Structure

i. WBS Elements

Figure VI.1 shows the preliminary RHIC Work Breakdown Structure which will be used as the basis for all technical objectives and required management systems.

It is extended to Level 3 elements where cost and schedule performance data is collected, analyzed with respect to plans, and reported on in accordance with internal (IMPACT) BNL and DOE requirements.

All subsystems such as CPM/PERT and Accounting will have complete traceability to the WBS names and numbering system.

ii. Organization Responsibility

A WBS/Organization Responsibility Matrix shall be completed showing the integration of the Organization chart with the Work Breakdown Structure.

Identified managers are responsible for all aspects of technical and administrative planning to complete the objectives of the assigned RHIC tasks.

Responsibility of maintaining the WBS planning and reporting format is assigned to the Management Systems Group.

iii. Reporting Requirements

All required DOE documentation shall be traceable to the Work Breakdown Structure, and in accordance with DOE reporting requirements checklist DOE-CR-537. BNL has fulfilled its reporting commitments over the past few years and is very familiar with the Major System Acquisition reporting requirements.

iv. WBS Dictionary

The Work Breakdown Structure Dictionary and Index as developed for the Project shall continue to be updated and maintained as a formal set of documents in the IMPACT System. All Level 1, 2, and 3 Dictionaries shall be updated to the technical, cost, and schedule objectives of the Work Breakdown Structure.

3. Management Control System

i. General

The Management Control System (IMPACT-Integrated Management Planning and Control Tracking System), will be used on the RHIC Project.

The IMPACT Manual has been reviewed by two different DOE Consultants and the present revision reflects all agreements and changes as a result of these reviews. BNL has received preliminary acceptance of the System. Improved modifications are expected during its implementation.

BNL completed the implementation of IMPACT on the CBA Project and reporting requirements were achieved on the Construction Work Breakdown Structure.

Direct responsbility for control and maintenance of the system is assigned to the Management Systems Group.

ii. Subsystems

The Management Control System is organized by subsystems which prov uniform guidelines for all managers responsible for technical as well as admi trative goals, working within the framework of the Work Breakdown Structure.

The IMPACT Manual summarizes all guidelines under the following subsystems.

1) Organization
2) Planning and Budgeting
3) Accounting
4) Analysis
5) Revisions
6) Reporting

Figure A.2.1 shows the Overall System Flow of functional responsibilities across the management control subsystems.

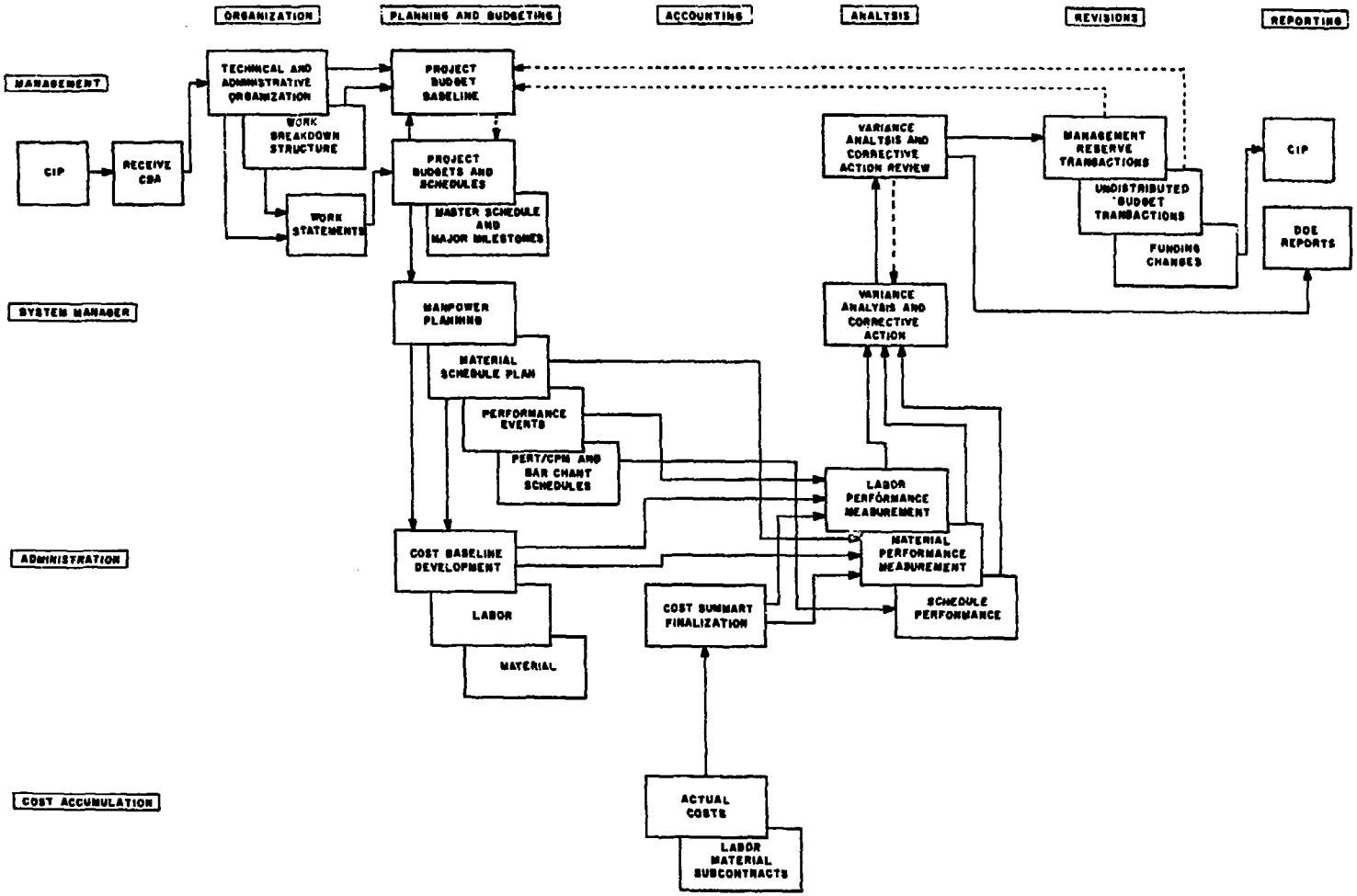

IMPACT-S OVERALL SYSTEM FLOW

FIGURE A.2.1

A.3. RHIC PARAMETER LIST

Performance ($^{197}_{79}Au$)

Design energy per beam	100	GeV/amu
Injection energy	11	GeV/amu
Luminosity @ 100 GeV/amu, 10h av & 0 mrad	5.8×10^{26}	cm^{-2} sec
Luminosity @ 100 GeV/amu, 10h av & 2 mrad	8.0×10^{25}	cm^{-2} sec^{-1}
Luminosity @ 30 GeV/amu, 10h av & 0 mrad	2.4×10^{26}	cm^{-2} sec^{-1}
Luminosity @ 7 GeV/amu, 2h av & 2 mrad	1.7×10^{25}	cm^{-} sec
Number of ions per bunch	1.1×10^{9}	
Number of bunches per ring	57	
Beam current, average	65	mA
Bunch separation	67	m
Beam-beam tune shift, initial, 0 mrad	3.6×10^{-3}	
Normalized emittance @ 100 GeV & 10h	28	π mm•mrad
Bunch phase space area @ 100 GeV & 10h	12	eV•sec/amu
Beam height @ X-ing, 100 GeV/amu	2.6	mm
Beam width @ X-ing, 100 GeV/amu	1.0	mm
Diamond length rms @ 100 GeV/amu, 0 mrad	±106	cm
Diamond length rms @ 100 GeV/amu, 2 mrad	±14	cm

Experimental Insertions

Number of insertions	6	
Beta vert @ X-ing	6.3	m
Beta horiz @ X-ing	0.88	m
Dispersion @ X-ing	0	m
Beta max. (horiz/vert)	303/313	m
Crossing angle	0-2	mrad
Free space @ X-ing	±10	m
Insertion length	±141.75	m
Phase shift per insertion	3x360°	

Lattice

Circumference, 4 3/4 C_{AG}	3833.85	m
Radius of arcs	381.23	m
Beam separation in arcs	30	cm
Betatron tune (horiz/vert)	34.4/34.4	
Transition energy, γ	26.4	
Natural chromaticity (horiz/vert)	-73.5/-64.8	
Operating chromaticity (horiz/vert)	+2/+2	
Number of cells per arc	12	
Half cell length	14.81	m
Beta max in arc (horiz/vert)	51.6/51.6	
Dispersion max in arc	1.39	m
Phase shift per cell (horiz/vert)	98°/98°	

Magnets

Number of dipoles (180 dual + 12 common)	192	
Number of quadrupoles (dual)	246	
Magnetic rigidity, Bρ: at injection	96.5	T.m
at top energy	839.5	T.m
$\int$ Bdl, Half cell	32.61	T.m
$\int$ B'dl	89.48	T
Field at 100 GeV/amu	3.5	T
Quench field	4	T
Current at 100 GeV	4.68	kA
Dipole magnetic length	9.32	m
Bending radius	239.9	m
Sagitta	4.6	cm
Quadrupole magnetic length	1.2	m
Gradient	76.3	T/m
Coil i.d. arc magnets	7.5	cm
Good field aperture, arc	±2.6	cm
Good field aperture, insertion	±5	cm
Field nonuniformity $\Delta B/B$ in dipole @ 2.6 cm	2.0×10^{-4}	
Gradient nonuniformity $\Delta G/G$ in quad @ 2.6 cm	$2.5 \times 10^{-}$	
Yoke aperture	10	cm
Yoke cross section	26x26	cm^2
Vacuum vessel o.d.	94	cm
Stored energy per dipole aperture	360	kJ
Stored energy, per quad aperture	19	kJ
Dipole correctors	0.2	T.m

Trim quadrupole strength	3	T
Chromaticity sextupole strength	600	T/m

Refrigeration System

Maximum operating temperature	4.6	K
Temperature refrigerator output	4.3	K
Temperature heat shield, av.	55	K
Mass flow in magnets	800	g/sec
Heat load, dipole vessel primary	5.8	W
Heat load, dipole vessel secondary	25	W
Heat load, magnet system primary	2.94	kW
Heat load, distribution system primary	0.65	kW
Heat load, lead system	2.9	kW
Heat load, experimental magnets	1.8	kW
Heat load, total primary	8.3	kW
Heat load, total secondary	15.0	kW
System capacity, primary	15.4	kW
System capacity, secondary	26.0	kW
Number of compressors, first stage	20	
Number of compressors, second stage	5	
Compressor power requirements	8	MW
Helium pressure in magnets, operation	5	atm
Helium pressure in magnets, cooldown	15	atm
Cooldown time, entire system	10	days
Magnet replacement time	6	days

Injection System

AGS energy, kinetic	10.7	GeV/amu
Au Ions/AGS pulse	1.1×10^{9}	
Invariant emittance	10×10^{-6}	π rad•m
Longitudinal phase space	0.3	eV•sec/amu
Bunch length	17	nsec
Momentum spread	$\pm 9.6 \times 10^{-4}$	
AGS pulses stacked/ring	57	
Ions/collider ring	6.3×10^{10}	
Total filling time, per ring	$\sim$1	min

Rf System

Harmonic numbers	342	
rf frequency	26.743	MHz
Total rf voltage	1.2	MV
Number of cavities per ring	6	
Shunt impedance per cavity	0.9	MΩ
Acceleration period	1	min
Frequency charge	1%	
rf phase angle	2.3°	
Maximum $\dot{B}$	500	G/sec
Bunch area @ transition	1	eV•sec/amu
Momentum spread @ transition	±1.2%	
Bucket length	11.2	m
Bunch-to-bunch separation	67.3	m

Vacuum Systems

Vacuum chamber, aperture	6.58	cm
Pressure, H_2 in warm section	10^{-10}	Torr
Bake out temperature	250°	C
Cold bore molecular density, H_2 and He	3×10^{6}	cm^{-3}
Cold bore pressure, room temperature equivalent	10^{-10}	Torr
Insulating vacuum	1×10^{-5}	Torr

Power Supplies

Main supply current capability	5	kA
Main supply voltage maximum	650	V
Main supply voltage, flat top	120	V
Main supply accuracy, pulse to pulse	10×10^{-6}	
Number closed orbit correction supplies	492	
Number trim supplies	246	

Internal Beam Dump

Stored energy per beam	300	kJ
System response time	50	μsec
Kicker rise time	3	μsec
Kicker strength	14	kG•m

Conventional Facilities

Main tunnel width	5.0	m
Main tunnel height	3.4	m
Injection tunnel width	3.0	m

Size, narrow angle hall	27.7x12.2x8.4	m^3
Size, wide angle hall	16.1x32.0x12.2	m^3
Size, major facility	50.9x17.4x14.3	m^3
Open area	57.3x29.3	m^2
Beam height, narrow angle hall	1.7	m
Beam height, wide angle hall	4.3	m
Beam height, major facility	5.2	m
Beam height, open area	2.2	m
Floor area, collider center	42200	ft^2
Floor area, compressor structure	10000	ft^2
Floor area, inj/ejec. PS building total	12000	ft^2
Floor area, support building total	14300	ft^2
Floor area, rf tunnel structure	1800	ft^2

A.4 RHIC WINDOW FRAME MAGNET SYSTEM

1. Introduction

To achieve conciseness, only special aspects of the window frame design are described herein. These aspects were selected from a detailed study which included all features of the magnetic concept, engineering design, contruction methods and testing. A comprehensive BNL Report is being prepared.

The Window Frame Magnet design has a number of unique features:

- Parallel plane, single layer, dry-wound current sheets all of monolithic, rectangular conductor (non-impregnated construction).
- Field quality is determined by the iron boundaries below saturation, up to 80 GeV/amu (Au), thus: the conductor location is not critical.
- There are no saturation effects up to $B \leq 2.2$ T, equivalent to 80 GeV/amu for Au beams.
- Magnetization problems do not exist at low fields.
- Outward forces ($\sim$ 500 psi) are low and no prestressing is required.
- Rapid quench propagation and excellent thermal stability is assured by a pure aluminum backing sheet.
- The stored energy is low ($\leq$ 240kJ in dipoles).
- The curvature is only two dimensional, which simplifies providing slip planes.

This design for the RHIC was based on previous experience with window frame magnets. Two 2 meter long window frame magnets connected in series were operated at 4 Tesla in an AGS 30 GeV/c extracted beam of over 10^{13} protons per pulse for ten years. Radiation heating experiments showed that these magnets could absorb energy approaching 1kJ per pulse before quenching and required no quench protection. Measurements of the relative difference in $\int Bds$ for the two

4 T magnets are plotted in Fig. A.4.1. This figure demonstrates the construction accuracy achieved for window frame magnets without a modeling program. In addition the measured values are in excellent agreement with the design values.

Another widow frame magnet, a R&D prototype for the CBA, with a 6 layer main dipole coil, eventually reached a peak field of 6.8T (short sample). Its coil i.d. (80 mm) is comparable to the RHIC design (75 mm). With no quench protection, the maximum temperature reached, during a quench, was $\sim$ 90° K. Thus, very little mechanical stress from thermal expansion could occur. The current carried by the copper at quench ($\sim$ 104 kA/cm^2) was substantially the same as the quench curent in this design ($\sim$106 kA/cm^2). In addition, the field in the 6.8T magnet was about double that of this magnet at quench (3.6T). This leads to the conclusion that a diode quench protection system may not be necessary.

Table A.4.1 shows the normalized error terms of the field of the 6.8T magnet measured at a radius of full beam aperture (70% ρ_{sc}). The measurements, with no iron saturation, were integrated over the length of the magnet using a long coil. The allowed terms were in agreement with the values computed for the design.

The straightforward nature of the window frame design, coupled with previous successful construction experience, means that R&D can be limited to the new engineering features (long, curved dipole, etc.) needed for the RHIC.

Table A.4.1. CBA Prototype Magnet
Integral Field: Normalized Error Terms Only
Measured at Full Beam Aperture (70% ρ_{sc})

Multipole	Amplitude	Multipole	Amplitude
	$\times 10^{-4}$		$\times 10^{-4}$
a_1	-1.49	a_7	-0.14
b_1	-0.36	b_7	+0.21
a_2	+1.45	a_8	+0.14
b_2	----	b_8	----
a_3	+0.77	a_9	+0.14
b_3	-0.71	b_9	+0.21
a_4	+0.63	a_{10}	+0.21
b_4	----	b_{10}	----
a_5	-0.36	a_{11}	0
b_5	-0.57	b_{11}	+0.36
a_6	+0.07	a_{12}	-0.07
b_6	----	b_{12}	----
		a_{13}	+0.07
		b_{13}	0

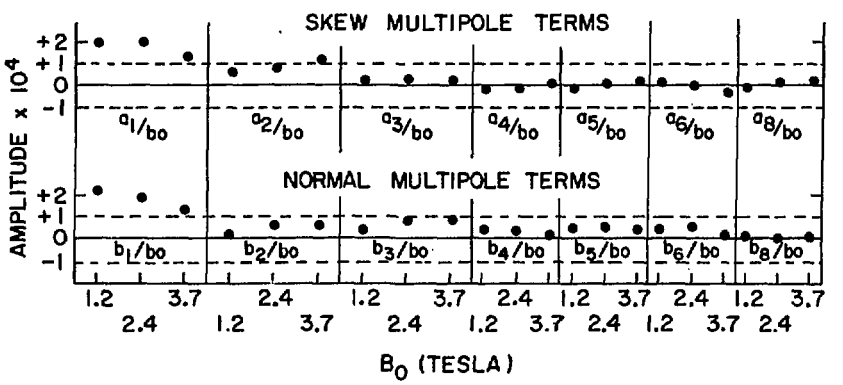

Figure A.4.1 Relative difference of ∫Bds for the two 4T AGS extracted beam magnets. The measurements were made at full beam aperture (70% ρ_{sc}).

2. The Unicell Concept

The overall magnetic design uses a novel "unicell" concept. Each half cell is packed so that the maximum length is occupied by magnetic fields. The dipole is long, resulting in a reduced magnetic field and less stored energy. The unicell incorporates, for each beam, a dipole, an orbit correcting coil, a sextupole, a quadrupole and another sextupole in an approximately 15 m long single cryostat (Fig. A.4.2). The center to center beam spacing is 0.22 m.

The unicell reduces the number of dewar ends, the waste space associated with them, and obviously reduces the costs associated with these ends. All magnets are designed so that their magnetic length essentially equals their physical length. The sextupoles are powered in series to produce an "achromatic quadrupole." All magnets and the pick-up electrodes share the common central bore tube to which they are keyed. The magnets are surrounded by a tightly fitting cryostat. The unicell elements are thus accurately and automatically internally aligned to provide the correct optics.

This design meets and, in some cases, exceeds the desired RHIC specifications: bore tube i.d. of 70 mm, "good field" aperture of 50 mm at injection and 25 mm at 100 GeV/amu, a dynamic range of 100/1, unlimited momentum imbalance between the colliding beams, and ramping time less than 30 seconds (<0.09T/sec). Short sample field is at $\sim$130 GeV/amu. Correction elements and electrical interconnections are adequate for $\sim$125 GeV/amu. The operating and quench parameters are given in Table A.4.2. The margin between normal operation and quench is 33% of the operating field. Although it may later prove to be unnecessary, quench protecting diodes have been included in the present design.

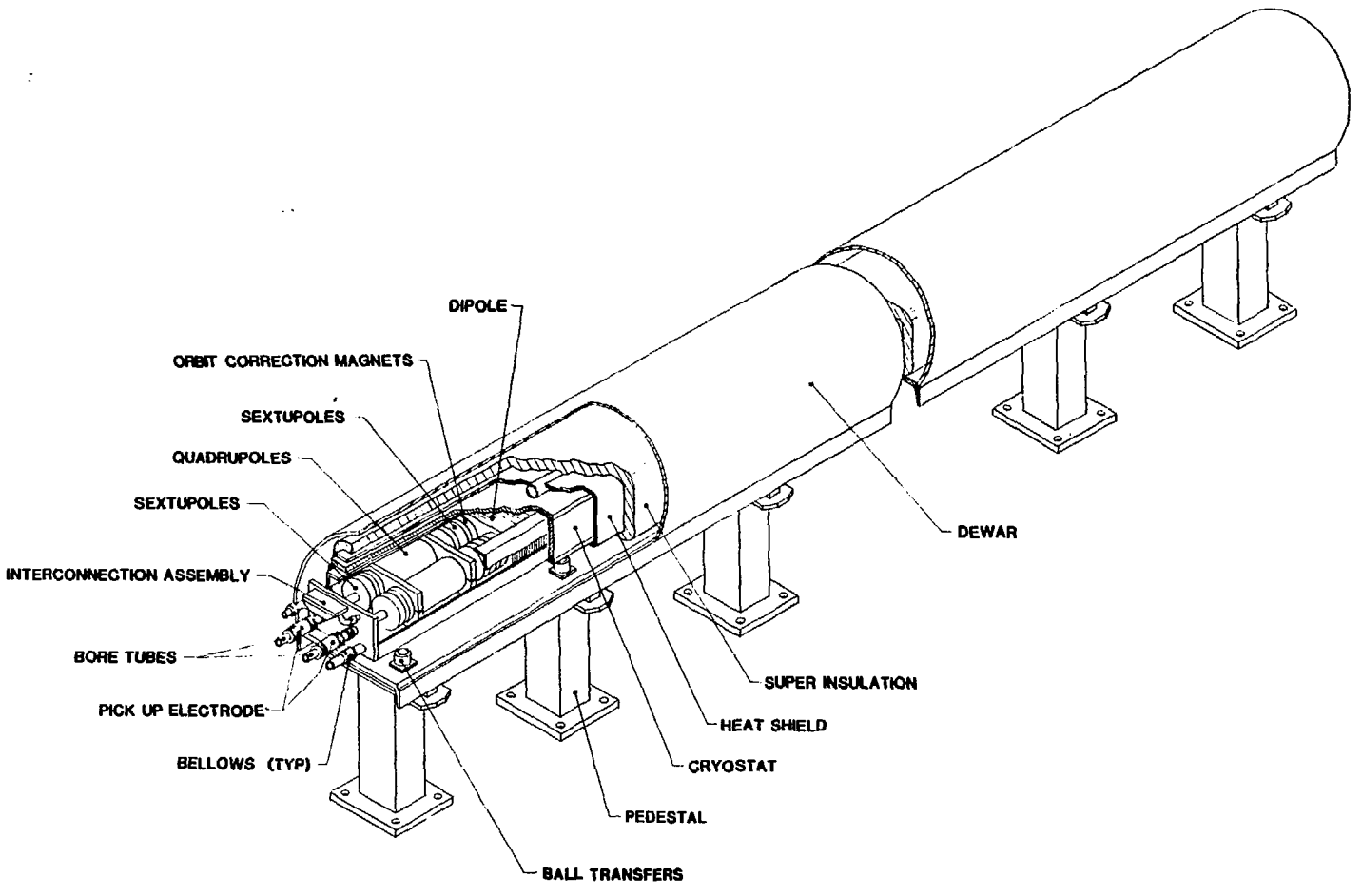

Figure A.4.2. Unice11 Assembly.

Table A.4.2. Dipole Operating and Quench Parameters

Operation	
Operating Current	3.86 kA
Operating Field	2.7 T
Operating Current/Copper Area	0.82 kA/mm^2
Stored Energy per Aperture	240 kJ
Inductance per Aperture	32 mH
Quench	
Quench Current	>5 kA
Quench Field	3.6 T
Quench Current/Superconductor Area	2.40 kA/mm^2

3. Magnets

i. Dipoles

The window frame dipole utilizes dipolar parallel current sheets. These terminate at parallel iron pole faces perpendicular to the current sheets (Fig. A.4.3). Below saturation image currents in the iron effectively extend the dipolar current sheets to infinity, resulting in very pure dipole fields.

The superconducting magnetization currents are similarily imaged to infinity. Thus no magnetization fields occur in the aperture. They are contained within the superconducting current sheets and the surrounding iron.

The 12 m dipole magnet is designed with monolithic rectangular conductor (1.69 mm x 4.06 mm), having a copper to superconductor ratio of 1.7. Operation at 100 GeV/amu would be at less than 60% of short sample (J_c x B_c) current capacity. The sextupole correcting pole-face windings are independently excited above 2.2 T. Iron saturation effects produce no other harmonics. The simple design of the pole-face windings produces higher multipoles, but these do not significantly affect the "good field" region (r ≃ 12.5 mm above 80 GeV/amu). Cross coupling of fields between beam apertures is negligible. The absence of magnetization problems at low fields means that the magnets are less sensitive to temperature variations and have a large dynamic range.

Table A.4.3 shows the calculated systematic normalized multipoles produced by the dipole. All magnetic field calculations were performed using the two dimensional magnetostatic program POISSON. The permeability table used in the computations was for low carbon steel. Above 2.2 T, 80 GeV/amu (Au), the pole-face windings are excited to cancel the sextupole harmonic. At this energy the required "good field" aperture is less than one third of the radial distance to the superconductor. The field variation on the mid-plane as a function of ra -

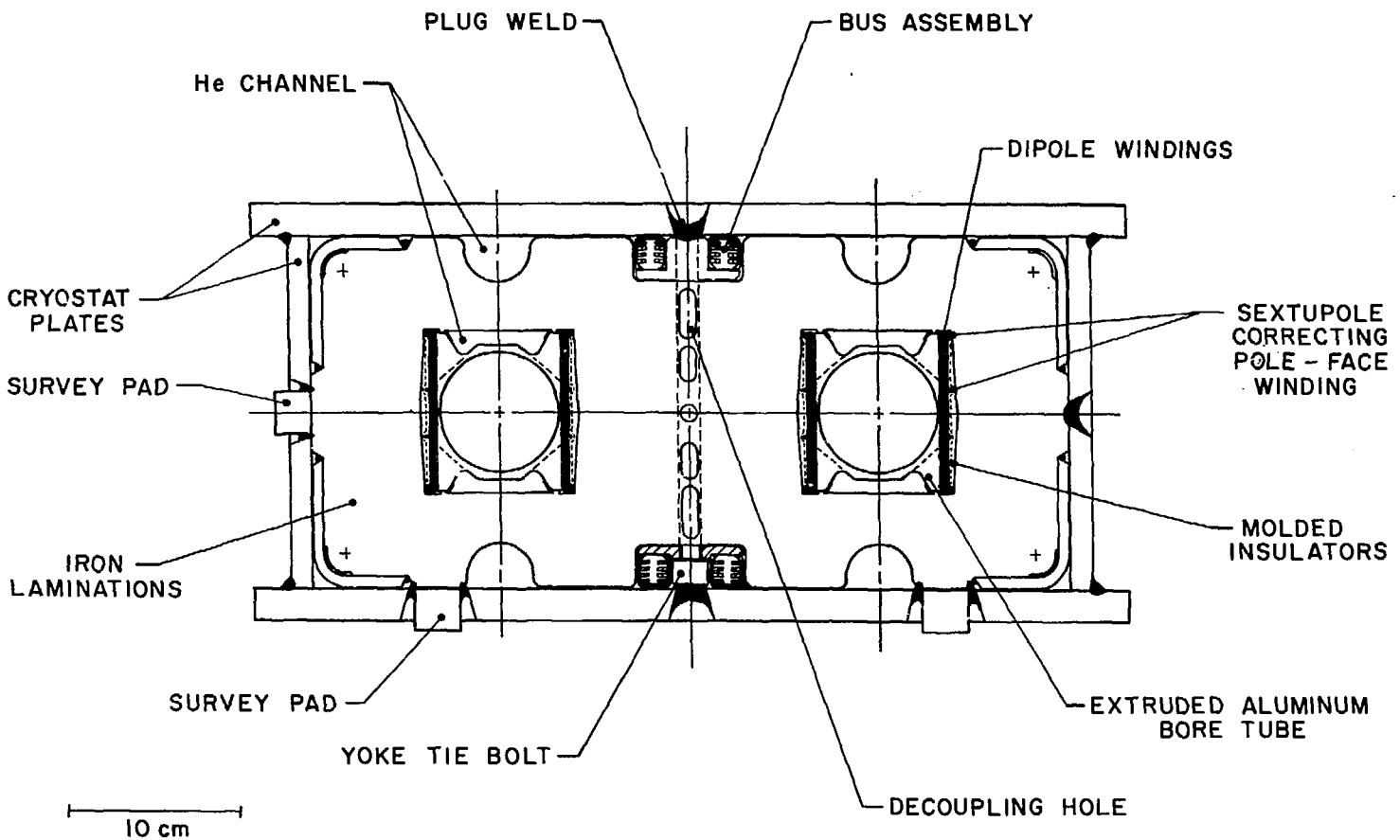

Figure A.4.3. RHIC window frame dipole cross section. Center to center beam spacing is 22 cm.

Table A.4.3. Calculated Systematic Normalized Harmonics for the Window Frame Dipole

	$b_n \times 10^4$			
GeV/amu (Au)	<70	80	100	100
B_o (T)	< 1.9	2.18	2.72	2.72
x (cm)	25.4	25.4	25.4	12.7*
b_2**	0	0	0	0
b_4	-0.08	-0.68	-6.08	-0.38
b_6	0.08	0.38	3.84	0.06
b_8	0.02	0.08	0.84	0.003
b_{10}	0	-0.01	-0.09	0
b_{12}	0	0	-0.05	0
b_{14}	0	-0.01	-0.02	0
b_{16}	0	0.01	0.02	0
b_{18}	0.01	0.02	0.03	0
b_{20}	-0.01	-0.02	-0.03	0
b_{22}	0	0.01	0.01	0

*Required "Good Field" radius.
**Sextupole cancelled by pole face winding.

dial position in the aperture is tabulated in Table A.4.4 and plotted in Figure A.4.4. The excellent field quality achieved by the window frame design is evident. The radial variation on the mid-plane of the normalized first and second field derivatives, at 2.72 T, is shown in Fig. A.4.5.

This magnet was designed with separately tunable magnetic circuits with magnetic coupling $<1 \times 10^{-4}$ of the quadrupole component. Higher multipole components are much smaller and, therefore, negligible. Calculations show that sufficient iron has been used to achieve this result up to 100 GeV/amu (Au). In addition, steel is removed on the vertical centerline between the two apertures (see Fig. A.4.3). This would allow operation at still higher energies without significant coupling.

The dipole is curved with a radius of 275 m and a sagitta of 60 mm. Uniquely high level heat exchange from the coil package to a large volume of helium is made possible by the high purity aluminum backing sheets and a profusion of helium cooling channels. As a result, much more energy is required to initiate a quench than with other comparably high current density designs. When a quench is produced it propagates so rapidly throughout the coil that it is self-protecting.

ii. Quadrupoles

The 1.56 m long quadrupole is very compact. The outer diameter is 0.17 m. Its field gradient is 59 T/m, with a pole tip field of 2.22 T. The continuous single layer coil is dry wound directly on the bore tube using rectangular monolithic conductor (Fig. A.4.6). Windings are continuous across the midplanes between the poles, as in the dipole. As a result, the field shape is precisely determined by the accurately located iron boundaries.

Table A.4.4. Window Frame Dipole Field Variation in x

GeV/amu (Au)	<70	80	100
B_o (T)	<1.9	2.18	2.72
	$\Delta B/B_o$	$\Delta B/B_o$	$\Delta B/B_o$
x (cm)	$x10^6$	$x10^5$	$x10^4$
0	0	0	0
0.313	0	0	0
0.625	-0.03	-0.03	-0.02
0.838	-0.14	-0.1	-0.11
1.25	-0.37	-0.40	-0.32
1.563	-0.70	-0.8	-0.68
1.875	-0.91	-1.4	-1.16
2.188	-0.41	-2.0	-1.59
2.5	-2.00	-2.3	-1.54

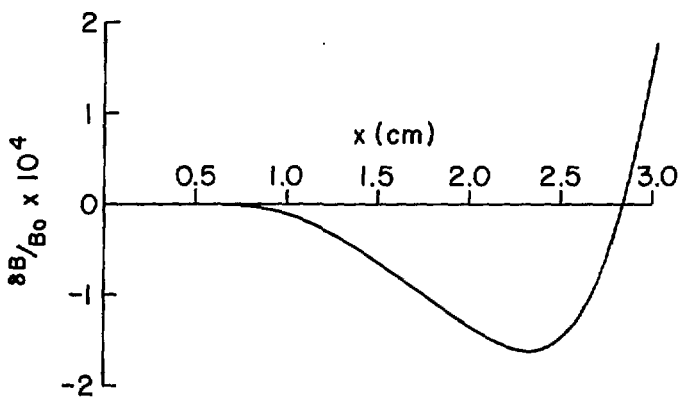

Figure A.4.4. Window frame dipole field variation with x at 2.72 T, 100 GeV/amu (Au). Sextupole harmonic cancelled by pole-face winding.

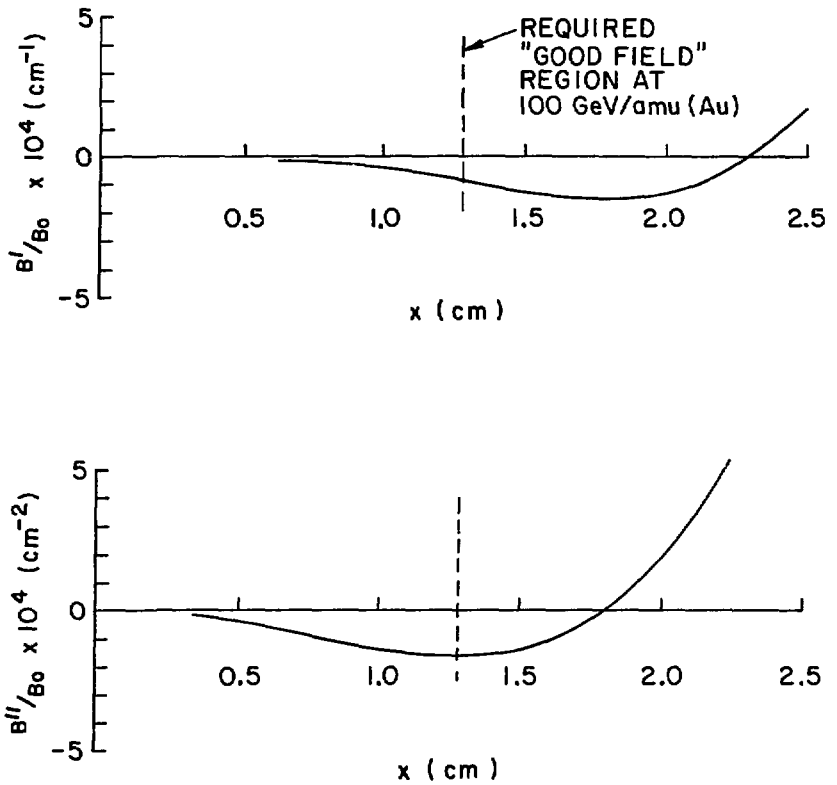

Figure A.4.5. Window frame dipole normalized field derivatives variation with x at 2.72 T, 100 GeV/amu (Au).

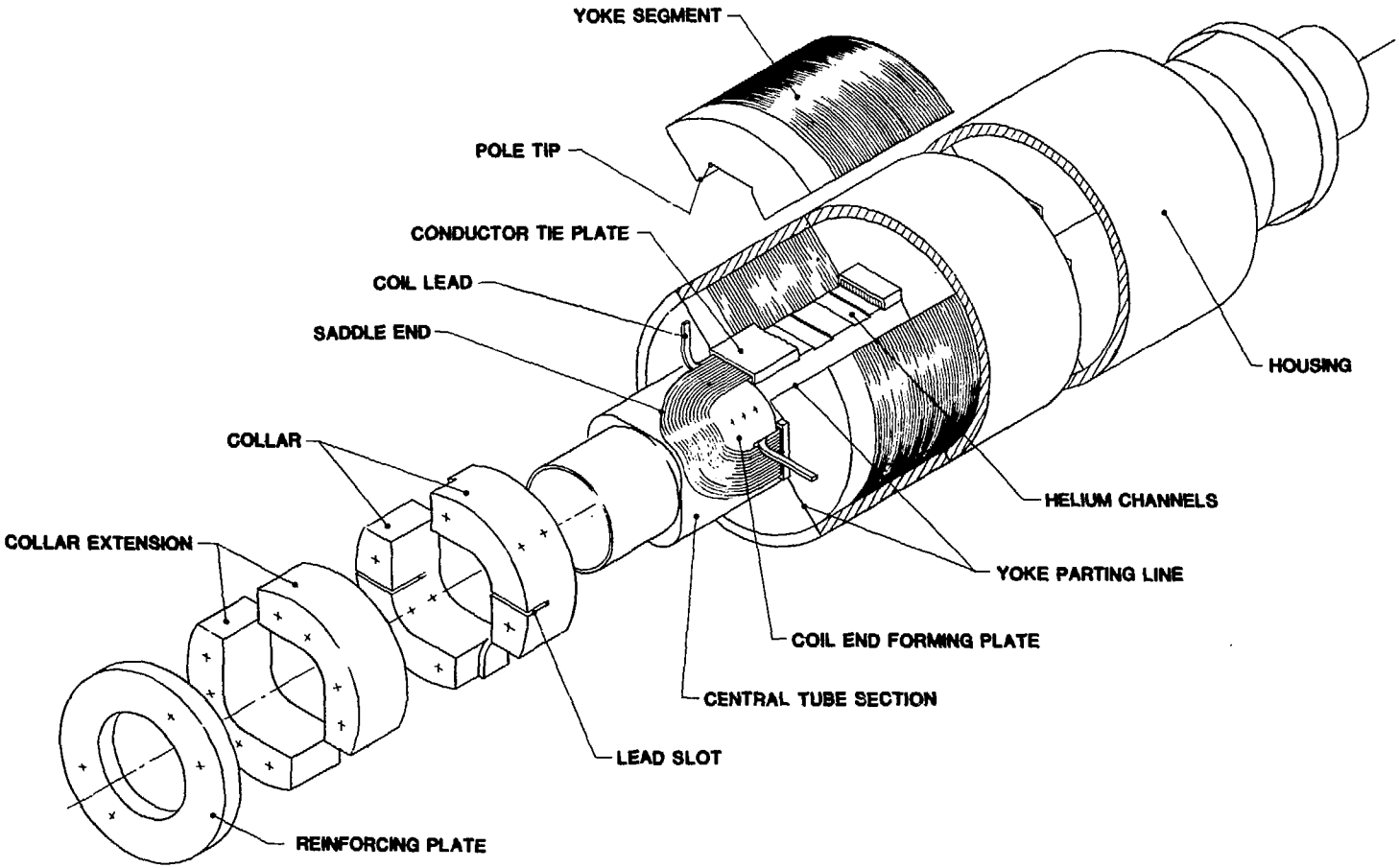

Figure A.4.6. RHIC window frame 2-coil quadrupole.

Table A.4.5 shows the calculated systematic multipoles produced by the quadrupole. The window frame quadrupole field quality comfortably exceeds RHIC requirements.

The subdivision of the quadrupole into two, rather than four, unit windings is a unique feature of the design. This greatly simplifies the winding and assembly procedures (fewer terminations). A completed winding on a pole does not obstruct the next winding.

The quadrupole yoke is subdivided into four segments. The parting line lies along the pole tip centerlines. A precision honed cylinder is shrunk fit around the yoke segments and the conductor blocks. This design assures accurate location of the iron and conductors. The quadrupole bore tube extremities are machined to a prescribed radius to support and center the chromatic sextupoles, the orbit correcting coil and a precisely located pick-up electrode.

Table A.4.5. Calculated Systematic Normalized Harmonics for the Window Frame Quadrupole

GeV/amu (Au)	<18	100	100
Pole Tip Field (T)	<80	22.2	22.2
x (mm)	25.4	25.4	12.7*
	$b_n/b_1 \times 10^4$		2 -2
b_5/b_1	-0.59	19.58	1.22
b_9/b_1	-0.10	0.29	0.001
b_{13}/b_1	-0.04	-0.23	0

*Required "Good Field" radius

iii. Correction Coils

The two 0.15 m long sextupoles have an outer diameter of 0.15 m. The sextupoles also have single layer windings, containing only three hand wound turns of a rectangular monolithic conductor. Their basic, iron dominated, compact design is similar to that of the quadrupole (Fig. A.4.7), and they have a very pure sextupole field. The field strength is more than double that required for the chromaticity correction alone.

The orbit correcting coil (wound to correct a_o, b_o and a_1, b_1) has low current, (60A), locally powered feedback capability. Combined with the pick-up electrode, this capability results in a "cybernetic" accelerator. Observation of beam position coupled with on-line computer orbit analysis and feedback capability keeps the beam at the center of the aperture with high precision. It also permits elimination of horizontal and vertical coupling. This concept means that internal self-alignment of magnets in the unicell to an accuracy of ± 1/4 mm is more than adequate. Even with "perfect" magnets such feedback control is highly desirable to cope with possible beam induced effects. It has the additional advantage that possible long term alignment changes as large as 2 mm could be tolerated. The main requirement on the magnets is that their position be stable. Location and orientation errors can be compensated. The refined "survey" can be done with the beam.

iv. Magnet Construction

The dipole coil is wound directly on the bore tube using a simple race track fixture. The conductor spool is mounted on a moving carriage which travels about a stationary mandrel. The quadrupole coil is wound using the same type of fixture modified for the shorter coils.

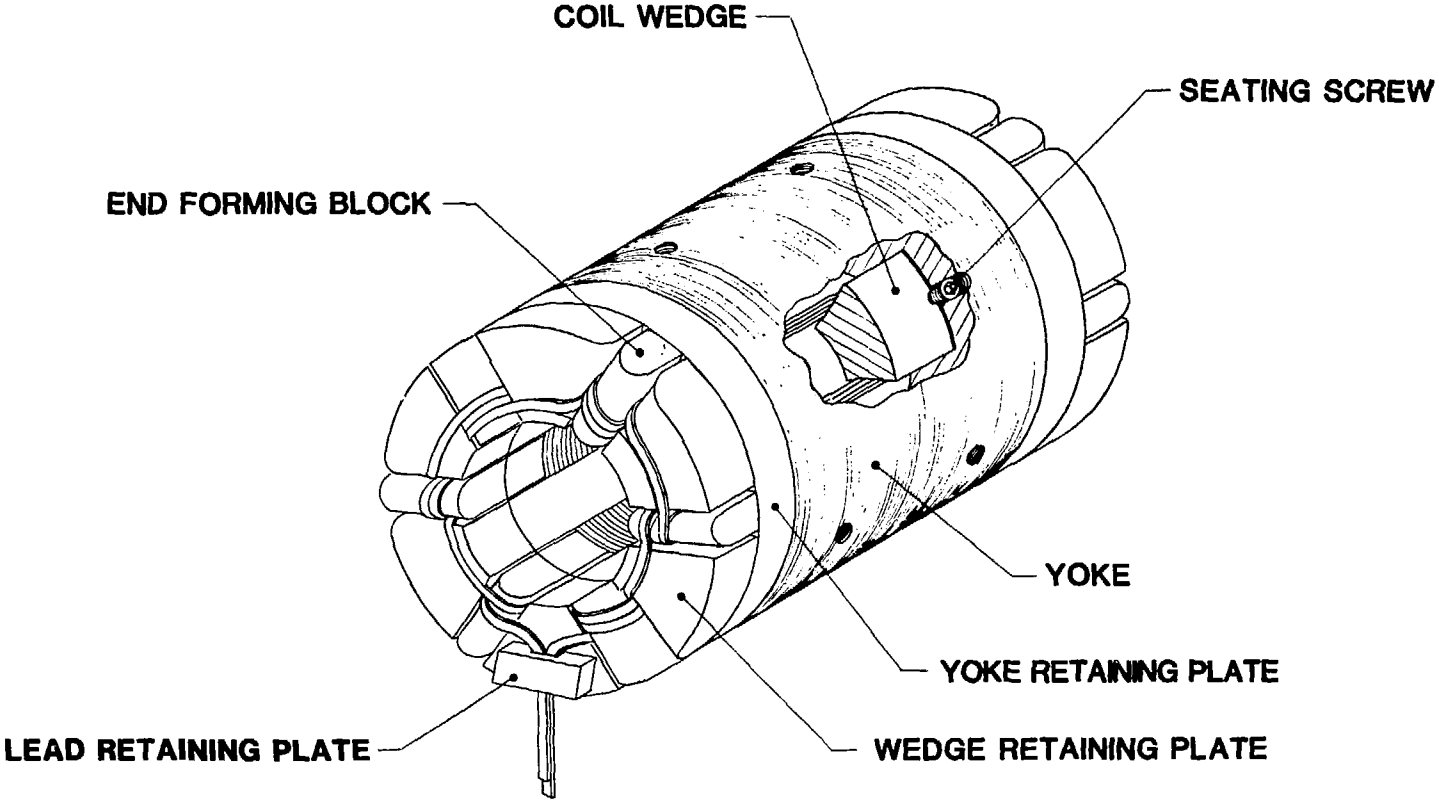

Figure A.4.7. RHIC window frame sextupole assembly.

The coils are not prestressed and require no impregnation or curing. These features, combined with the inherently low magnetic forces, simplify the yoke, cryostat, and coil design. They require relatively simple tooling and are thus cost effective. Both features minimize coil stress relaxation. The coil is free to take a set, but it only moves outward as a single, coherent current block. The effect of this motion on field quality is negligible.

The dipole yoke consists of two laminated half cores which envelop the bore tube and coil assembly of both magnets. The parting line is the horizontal centerline of the magnets. The thin laminations (1.5 mm thick), which can be accurately contoured, are light and easily handled. They can be readily shuffled to achieve cores with uniform magnetic characteristics. The difference in gap between inner and outer contour edges after the dipole is curved is less that 0.002 mm. They are stacked in 4 m long straight units joined together in a stainless steel box which, when welded, becomes the cryostat. BNL experience in the stacking procedure assures that the centerline parting gap will not exceed 0.1 mm.

v. Assembly

The major assembly of the unicell would take place in one of the large experimental halls. A novel transporter (Fig. A.4.8) has been designed to transfer the unicell to its location in the tunnel. There the thermal shield and the superinsulation would be installed and the dewar vacuum envelope welded in place.

The unique design of the unicell assembly packing press, (Fig. A.4.9) and the unicell transporter, provides efficient assembly and installation procedures. Transporting many components in one unicell reduces installation time and minimizes cost.

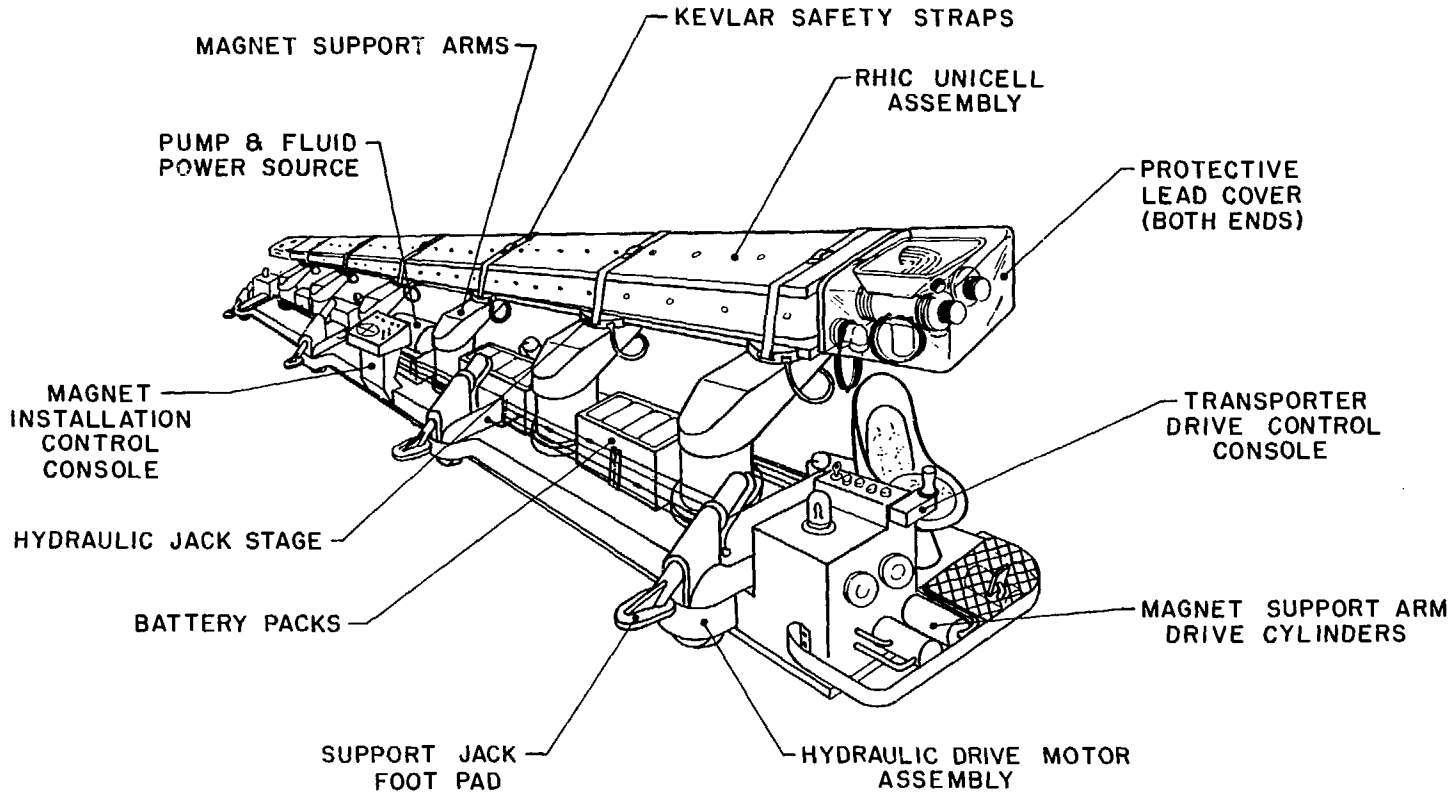

Figure A.4.8. Unicell transporter.

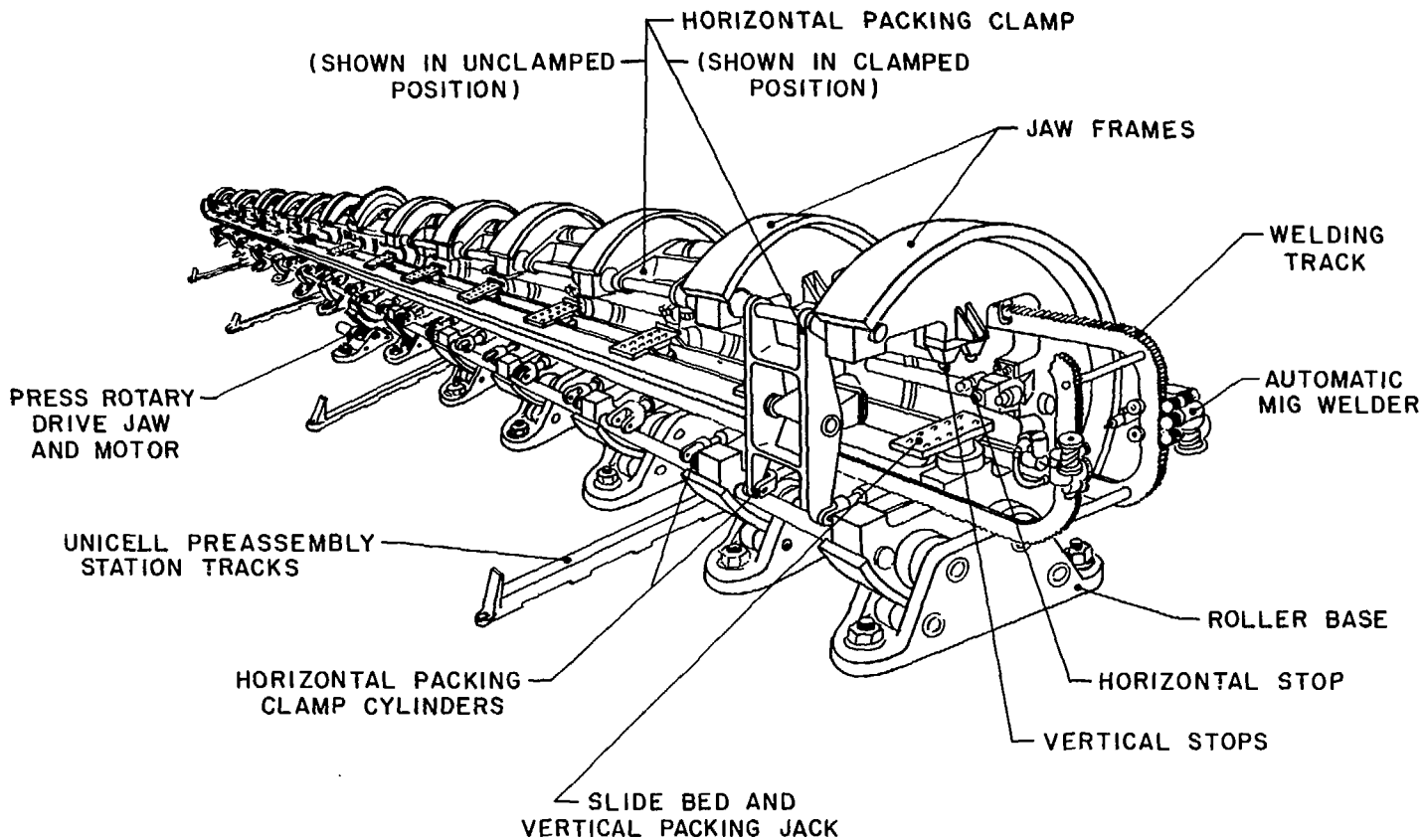

Figure A.4.9. Unicell assembly packing press.

The assembly press is designed to curve the dipole, bore tube, coil, and yoke inside the cryostat prior to welding. A unique advantage of the wind frame design is that this curvature is only two dimensional. This greatly simplifies the problem of providing slip planes, and is an essential feature of the unicell design. The resulting stress on the bore tube has been calculated to be less than 1,500 psi. The curved coil assembly, encased in the welded cryostat, becomes a very stable structure.

The assembly procedure includes electrical and magnetic testing at v stages. Later experiments may show that the scope of magnetic measurements pr ently planned can be reduced.

vi. Installation and Surveying

Electrical and mechanical interconnections are the most time consum installation operations. The long unicell design decreases the number of interconnections, which have been designed to be simple. A single lead bus is used to interconnect the unicell components. The bus interconnections and diodes are in one accessible cold lead pot located between the unicells.

Survey pads of precise thickness penetrating the cryostat wall are welded in contact with the laminations. These pads define the orbit centerli outside the cryostat. The cryostat and magnet assembly is rigid. This makes possible to fix the radial position of the unicell by lateral restraints at o two points. Vertical support structures are needed at seven pairs of points. fiducial external to the cryostat and dewar is provided at each of these four teen points.

Commercially available ball transfer units (Fig. A.4.10) are used t support the magnet and cryostat assembly within the dewar (see Fig. A.4.11). The ballbearing units allow free movement in the horizontal plane to accommo

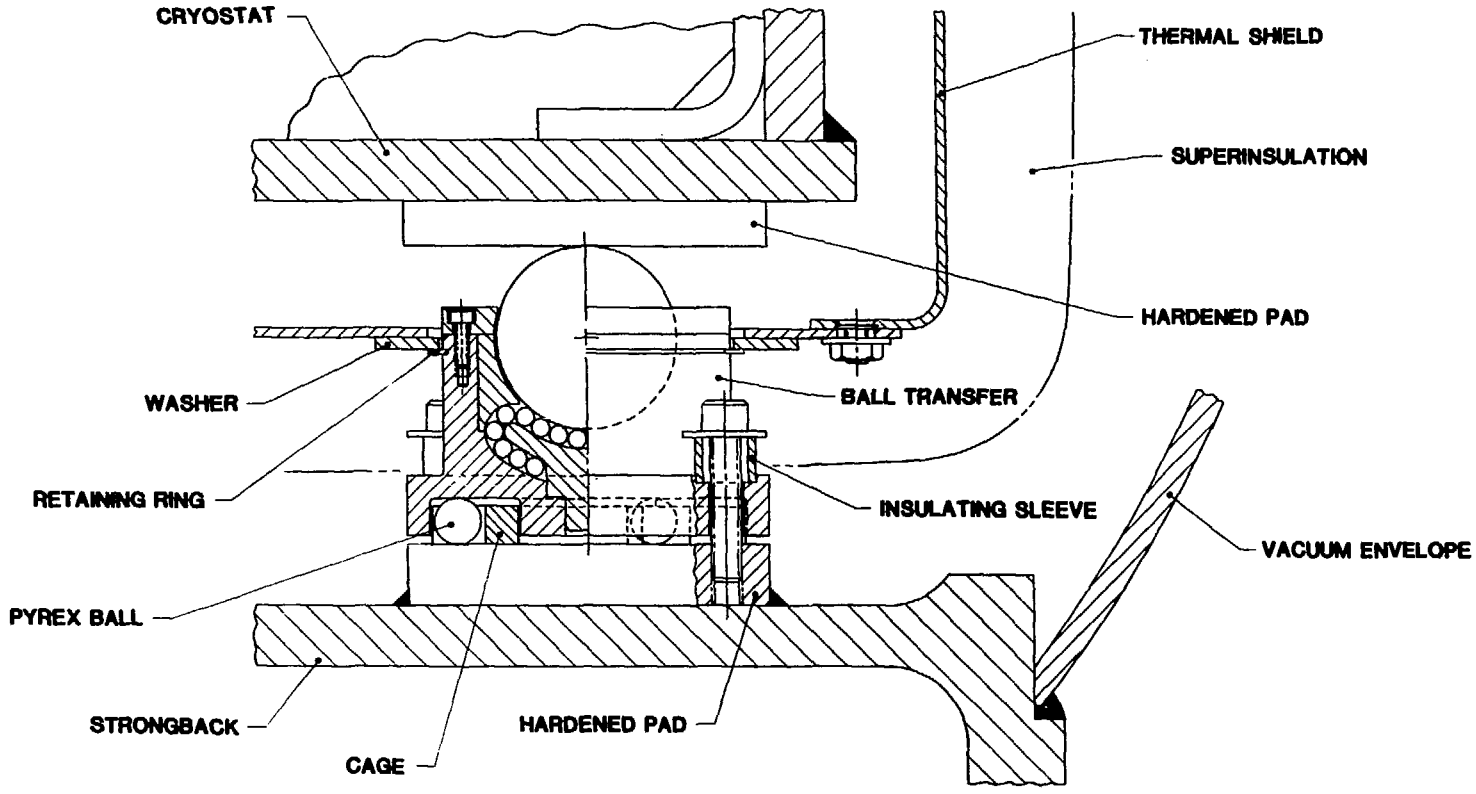

Figure A.4.10. Ball transfer assembly.

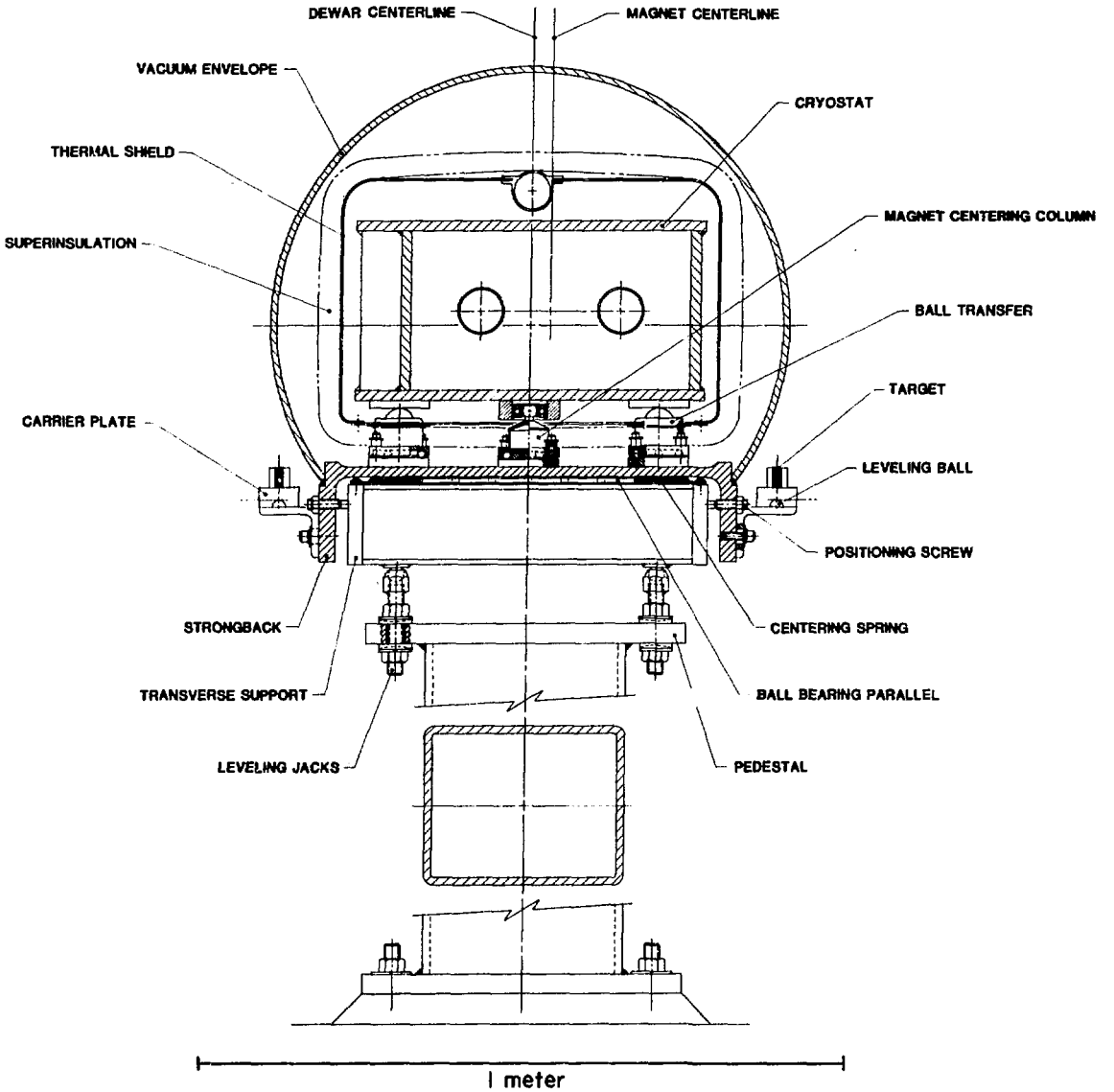

Figure A.4.11. *RHIC window frame dewar assembly midsection.*

the complex motion of the cryostat during cool down. They are efficient thermal insulators, since they offer approximately a point contact.

The vacuum envelope base is a wide-flange steel beam providing a strongback for the cryostat assembly. The lateral restraints are centering ball columns which key the cryostat to the strongback (Fig. A.4.12). These centering balls are fixed at one end of the unicell and ride in a longitudinal slot at the other end to allow for contraction during cooldown. External horizontal and vertical jacking screws fixed to the strongback provide the degrees of freedom required to locate the magnets precisely. Before the vacuum envelope is installed the cryostat is surveyed in position and the horizontal and vertical centerlines referenced to fourteen external fiducials fixed to the strongback. The survey is simple, since in the unicell design many of the accelerator components have been accurately prelocated.

A production scenario, a factory plan, and flowcharts for assembly and testing operations, including quality assurance, have been considered in detail. The mechanical and electrical designs of the window frame magnets are cost effective.

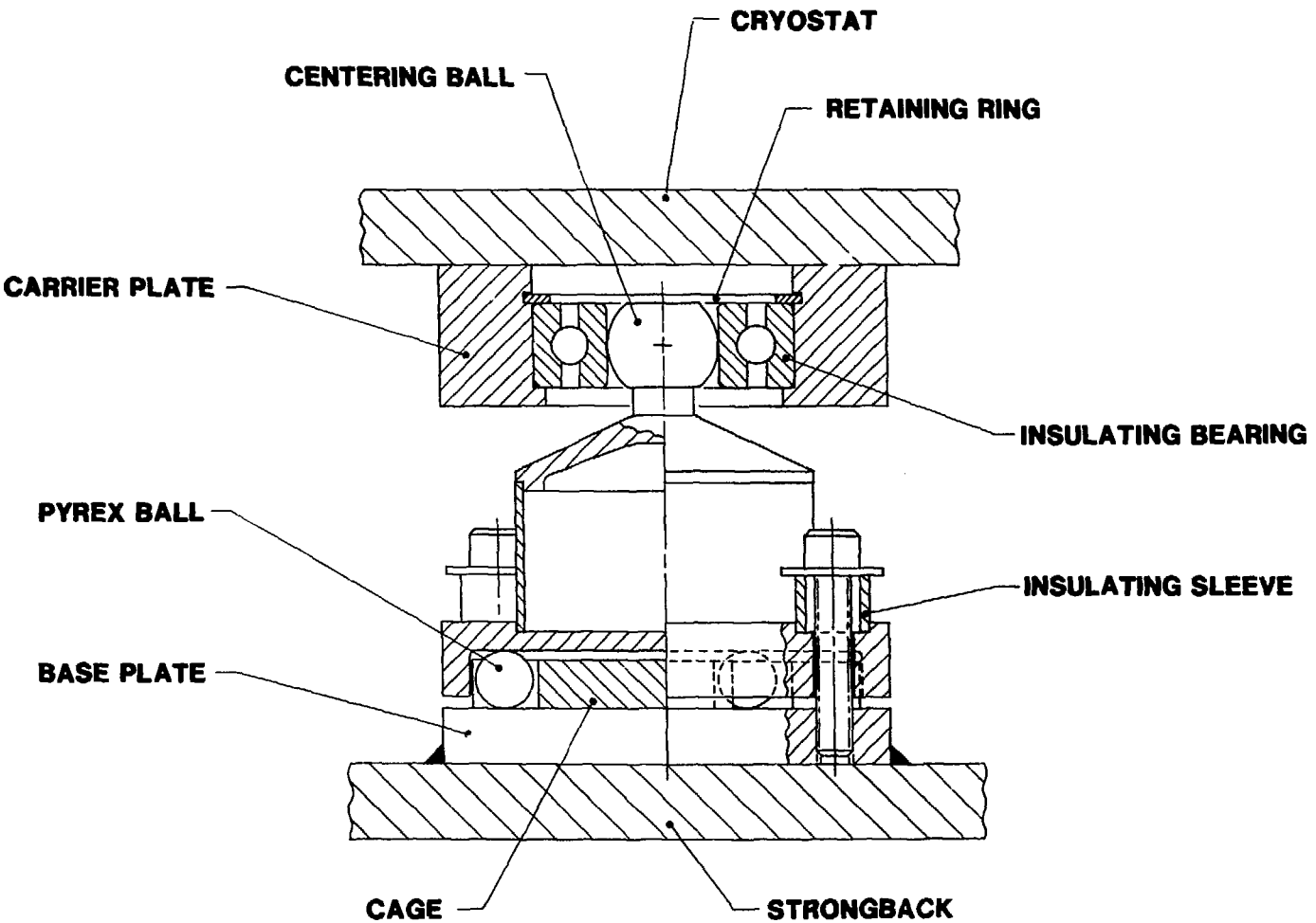

Figure A.4.12. Centering column assembly.